Error characterization and quantum control benchmarking in liquid state NMR using quantum information processing techniques

by

Martin Laforest

A thesis
presented to the University of Waterloo
in fulfillment of the
thesis requirement for the degree of
Doctor of Philosophy
in
Physics

Waterloo, Ontario, Canada, 2008

© Martin Laforest 2008

I hereby declare that I am the sole author of this thesis. This is a true copy of the thesis, including any required final revisions, as accepted by my examiners.

I understand that my thesis may be made electronically available to the public.

Martin Laforest

Abstract

Quantum information processing has been the subject of countless discoveries since the early 1990's. It is believed to be the way of the future for computation: using quantum systems permits one to perform computation exponentially faster than on a regular classical computer. Unfortunately, quantum systems that not isolated do not behave well. They tend to lose their quantum nature due to the presence of the environment. If key information is known about the noise present in the system, methods such as quantum error correction have been developed in order to reduce the errors introduced by the environment during a given quantum computation. In order to harness the quantum world and implement the theoretical ideas of quantum information processing and quantum error correction, it is imperative to understand and quantify the noise present in the quantum processor and benchmark the quality of the control over the qubits. Usual techniques to estimate the noise or the control are based on quantum process tomography (QPT), which, unfortunately, demands an exponential amount of resources.

This thesis presents work towards the characterization of noisy processes in an efficient manner. The protocols are developed from a purely abstract setting with no system-dependent variables. To circumvent the exponential nature of quantum process tomography, three different efficient protocols are proposed and experimentally verified. The first protocol uses the idea of quantum error correction to extract relevant parameters about a given noise model, namely the correlation between the dephasing of two qubits. Following that is a protocol using randomization and symmetrization to extract the probability that a given number of qubits are simultaneously corrupted in a quantum memory, regardless of the specifics of the error and which qubits are affected. Finally, a last protocol, still using randomization ideas, is developed to estimate the average fidelity per computational gates for single and multi qubit systems.

Even though liquid state NMR is argued to be unsuitable for scalable quantum information processing, it remains the best test-bed system to experimentally implement, verify and develop protocols aimed at increasing the control over general quantum information processors. For this reason, all the protocols described in this thesis have been implemented in liquid state NMR, which then led to further development of control and analysis techniques.

Acknowledgements

Although I would like to take all the credit, my five years journey in the world we call graduate school was made possible through the help and support of a countless number of people. People that help me through my academic path and people who had an influence on my personal life. This section is dedicated to them.

First and foremost, it is a requirement by most importantly an honor, to thank my supervisor Prof. Raymond Laflamme for giving me the opportunity to begin my research career in the exciting field of quantum information processing. His ridiculously broad knowledge of science was a great reference to understand the "big picture". He provided me with an extremely vibrant research atmosphere and has always been supportive in my endeavors. This vibrant atmosphere would certainly have been different having had different office mates. For that matter, I am grateful to Colm Ryan, with whom I did most of the work presented in this thesis and who always seemed to find the right idea at the right time. I also thank him for consistently having a different point of view than mine, hence sparking great discussions leading to even stronger ideas. I also thank Marcus Silva for countless hours spent discussing theoretical ideas and problems. Finally, thanks to Osama Moussa for being a great thinker and leading great discussions. To these three, I am proud to call you colleagues, and even prouder to call you friends. I also need to thanks Mike Ditty of helping me with my shortcomings with shimming a magnet, Camille Negrevergne for basically teaching me NMR QIP, Joseph Emerson for introducing me to randomization and Jonathan Baugh for many discussions about NMR. Finally, thanks to all the others I have worked with at one point or another. I will not risk listing names, by fear of forgetting somebody. Thanks to Prof. William Power, Prof. Michele Mosca, Prof. Gregor Weihs for being on my Ph. D. committee and not tearing me apart during my comprehensive exam. Thanks also to Prof. Frank Wilhelm, Prof. Joseph Emerson and Prof. Steffen Glaser for making me the honors to be on my Ph. D. defense committee. Thanks to all the administrative staff at IQC for the help throughout the years. Finally, I would like to thanks the government and private institutions for their financial support. It was nice to be a student and to be free of extra loans. Thanks to NSERC, FQRNT and the Bell family Foundation.

On a personal level, I need to thank my friends in Waterloo for, well, being my friends. Thanks to Mike Leamen, the brother I never had, J.-C. Boileau and Chris Erven. You have been great roommates and fantastic friends. Thanks to Casey Myers and Jamie Batuwantudawe for the good times. Thanks to the many great friends I met through the couchsurfing community. You guys turned my social life around and brought some more excitements. Thanks to all my volleyball, ultimate frisbee and rock climibing partners. I would also like to thanks Jen Muir, for being

who she is, for being a fantastically understanding girlfriend and for making me laugh during the rough times.

Je dois aussi remercier tous mes amis de Rivière-du-Loup: Guillaume, Sophie (pour votre soutien dans les temps durs et bien sûr, votre divan), Steve, Bégin, Carole, Marie-Hélène, Gauvin, Cox, Val, Nick, Catherine, Lafreux, Édith, Pierre-Luc et j'en oublie certainement. Rares sont les personnes qui peuvent se vanter d'avoir les mêmes amis depuis l'école secondaire et même primaire. Quand j'ai déménagé à 1000km de vous, la distance ne nous a pas séparés. Une amitié comme celle-là, ça n'a pas de prix.

Je veux aussi remercier Martin Francoeur, Benoît Gagnon et feu John Rice pour m'avoir enseigné les rudiments de la physique et de m'avoir transmis la passion.

Finalement, ma famille. Ma mère Aline et ma soeur Édith. Elles ne comprennent toujours pas ce que je fais dans la vie, mais je sais que j'ai leur appui inconditionnel. Édith, on a eu des moments difficiles dans notre jeune temps, mais je crois qu'aujourd'hui on peut affirmer qu'on s'en sort bien! Maman, tu m'as toujours encouragé dans toutes mes aventures, tant musicales, sportives que scolaires. Malgré toutes les sottises que mes professeurs ont pu te dire à mon sujet au cours des années, tu t'es entêtée et tu ne m'as jamais lâché. Je serai reconnaissant à jamais.

À Benoît et Alexandre

Contents

List of Tables

List of Figures

Preface

The birth of quantum information processing

Since the arrival of the digital computer in the early 1940's, nearly all the information we have digitally processed has been encoded in the most simplified mathematical model: binary calculus. To this day, information is still being processed using strings of 0's and 1's. In the early days of computation, computers used vacuum tubes as their electronic base and were typically the size of a large room. In 1948, the development of the transistor launched a race for the miniaturization of processors which ultimately led to the small and powerful personal computer we know today.

From the early days of the transistors (1965), the co-founder of IBM, Gordon E. Moore noticed that the size of transistors decreased by a factor of two every 18 months. Amazingly, Moore's law has held true since and makes people wonder: What will happen when the transistor will be the size of an atom? At this critical limit, the laws of physics are different and quantum mechanical effects need to be taken into consideration. A certain community decided to accept this fact and tried to build the smallest transistor possible: the single electron transistor [AL85, FD87]. Another community, lead by the legendary Richard P. Feynman, thought another venue might be of interest: redefine the entire scheme of computation as we know it and base the calculations not on the laws of electronics, but on the laws of quantum mechanics [Fey82, Fey84] . From there, a computer bit could not only be in the state 0 or in the state 1, but it could also exist in a quantum superposition of the two states. This quantum mechanical bit was later accepted as the *qubit* [Sch95]. Using quantum systems to perform calculations would not only open the door to quantum superposition, but also to other phenomena that do not have classical counterparts, such as quantum entanglement and wave-function collapse.

In 1985, Feynman demonstrated to the AT&T engineers how it would be possible to simulate many-body quantum mechanical systems using only a few qubits, as opposed to the exponential number of bits a classical computer would need to perform such a task. One of the first quantum algorithms was developed by David

Deutsch and Richard Jonza in 1992 [DJ92]. The algorithm permits one to determine whether a function of N numbers is constant or balanced using only one query to the function, as opposed to the $\frac{N}{2}+1$ queries needed classically. Although of little practical use, it showed that quantum computers could outperform classical computers. The first major discovery had to wait until 1994, when Peter Shor developed a quantum algorithm that could factorize an n bit number into its primes using only on the order of $\log(n)^3$ operation [Sho94]. Not only did this algorithm demonstrate the possible insecurity of many cryptosystems (which are usually based on hard mathematical problems that can be reduced to factoring of the discrete logarithm problem), but it also showed an algorithm that could exponentially outperform any known classical factoring algorithm [CP01].

This discovery then sparked the field of quantum computing (QC) and quantum information processing (QIP), which soon led to the development of other algorithms that outperform their classical counterparts, such as Grover's search algorithm [Gro96], the quantum random walk [CCD+02, FG98], etc.

Although there are many different models of quantum computation, such as the adiabatic quantum computer [FGG+01, FGGS00], the measurement-based quantum computer [RB01] and the topological quantum computer [Kit03], we will restrict ourselves to the original circuit model of quantum computation. Just as in the case of classical computing, a quantum computation typically implements a series of carefully chosen gates to a known initial state, after which the answer is retrieved from a measurement of the final state. Because the computational gates are to be implemented in a quantum mechanical fashion, they have to be reversible and unitary.

Computing with quantum mechanical systems

Soon after the discovery by Shor, theoretical and experimental physicists were then trying to answer the simplest of questions: How do we build a quantum computer? The answer have been partially formulated in 1995 by D. P. DiVincenzo and comes under a list of five criteria. To be considered as a potential QIP device, a system must:

1. Be a scalable physical system with well-defined qubits (two level systems).

2. Have a universal set of quantum gates that can implement any quantum computations.

3. Be initializable to a simple known fiducial state.

4. Permit reliable, qubit-specific measurements.

5. Have much longer decoherence times than the time to implement a gate.

A multitudes of system have been brought forward as fulfilling all the requirements. The list of systems includes, but is not limited to linear optics [KLM01], trapped ions [CZ95], parallel and vertical quantum dots [LD98], superconducting circuits [MOL+99, NPT99], optical cavity quantum electron dynamics [THL+95]and electron spins in diamond [WJ06]. One of the earliest proposals was to use the spins of the nuclei of a molecule placed in a large magnetic field [GC97, CFH97], also known as *Nuclear Magnetic Resonance*, or NMR. Though NMR has issues with the scalbility criterion [War97], it is known to be an excellent test-bed for the ideas of quantum computation and quantum control.

The natural dynamics of a quantum system is described through its natural, (usually) time independent Hamiltonian $\mathcal{H}_0$. To perform the computation, external elements must be brought in to create a control, (usually) time dependent, Hamiltonian $\mathcal{H}_c(t, \vec{\alpha})$ which depends on control parameters $\vec{\alpha}$. If we ignore noise and other sources of error, the evolution of a general density matrix ρ of the system follows Liouville's diffferential equation

$$\dot{\rho}(t) \quad = \quad -i[\mathcal{H}_0 + \mathcal{H}_c(t, \vec{\alpha}),\ \rho(t)], \tag{1}$$

where we have used the convention $\hbar = 1$ for simplicity. The solution to this equation takes the form

$$\rho(t) \quad = \quad U\rho(0)U^\dagger, \tag{2}$$

where

$$U \quad = \quad \hat{T}e^{-i\int_0^t dt'(\mathcal{H}_0+\mathcal{H}_c(t',\vec{\alpha}))} \tag{3}$$

and $\hat{T}$ is the time ordering operator. The operator U is unitary and corresponds to computational gates that are meant to implement a quantum algorithm. The evolution of a system under a given unitary evolution is also known as a *quantum channel*. In experimental QIP, the goal is to find the control Hamiltonians implementing the universal set of gates, while minimizing the effect of noise and control errors.

Completely isolated quantum systems do not exist in nature. Moreover, access to this system is important in order to drive the system and perform a computation through the control handles. Because the system is not isolated, it will interact with its environment and since we do not have access to the state of the environment, this interaction will effectively create a probabilistic evolution of the system and cause it

to lose its purity, i.e. it will introduce "noise" in the system. This phenomenon can also be describe as the system "losing" its quantum information to the environment, which cannot be retrieved deterministically. This is known as *decoherence* [Zur03, Sch07].

In QIP, and any other science exploiting the quantum mechanical properties of nature, uncontrollable decoherence is a sworn enemy. The probabilistic nature of the evolution causes the system to loose it purity and hence become a state with unknown, or random, information. Understanding and minimizing the effect of decoherence in a quantum system has been an active area of research since the early days of QIP, which led to novel ideas such as quantum error correction (QEC) [Sho95, Ste96] and fault-tolerant (FT) QIP [DS96, Got98]. The threshold theorems stipulate that if the error per gate in a system is below a given value, arbitrarily long computation can be achieve with an amount of resources that does not grow exponentially with the scale of the problem. Therefore, being able to quantify the level of noise and the quality of control in a system is of primary importance.

Quantum process tomography [CN97, PCZ97, THL+95] can allow one to gain complete knowledge about any quantum operations on a given system. Unfortunately, since it takes exponentially many parameters to fully describe a quantum process ($\mathcal{O}(4^{2n})$ for a n qubit process), an exponential amount of experiments needs to be performed and this becomes infeasible for more than five or six qubits. Moreover, imperfect state preparation and readout can introduce error in the reconstructed process and lead to process breaking quantum mechanical conditions [WHE+04, BEH+04]. For these reasons, efficient and reliable protocols to characterize the noise and control over a system are paramount to the realization of QIP.

The goal of this thesis

In the present thesis, we will survey our effort toward developing and testing *efficient tools* to increase the understanding and the quality of the control over open quantum systems. Our major contributions arise from the development of scalable protocols to characterize the noise present in a given system and also to benchmark the control one has over its qubits. These protocosl are developed from an abstract point of view and thus applicable to almost any QIP device. To demonstrate their viability, all the developed protocols are accompanied with experimental implementations on a liquid state NMR quantum information processor.

Toward this goal, background knowledge will be introduced in Chapters 1 and 2. Although the exact mechanism of decoherence is beyond the scope of this thesis,

Chapter 1 will be mostly concerned with how one can describe the effect of decoherence on the state of a system. Chapter 2 will briefly introduce NMR and how it can be used to implement QIP. We also give an overview of the tool we use and developed to achieve a high degree control in our systems [RNL+08] and briefly discuss the shortcomings of NMR as a scalable QIP device.

Our first implemented error characterization protocol will be introduced in Chapter 3. The dephasing noise model during free evolution of a liquid state NMR system and other systems is well known and well understood [Sli96]. Using an approach inspired from QIP, we developed a technique to extract the correlation in the dephasing affecting two near-identical qubits. Using a simple instance of three qubit quantum error correction, we designed a protocol whose goal was not to correct the errors introduced by the noise, but to probe properties of the noise and extract the correlation factor [LSB+07]. This technique is shown to be more effective than standard NMR protocols since, due to the correcting nature of the code used, the amount of coherence in the system survives longer and hence more statistics could be acquired. From the nature of the protocol, it can be generalized to a multitude of systems with different noise model.

In Chapter 4, we describe an efficient method to extract incomplete but relevant information about the noise present in the implementation of a quantum channel intended to implement an identity evolution, i.e. a quantum memory or a time-suspension sequence. In most FT quantum computing architectures, complete knowledge of a channel is unnecessary, but knowing the probability that a given number of qubits are corrupted at the same time is sufficient, thereby exponentially reducing the number of parameters required (if there are n qubit, there is only n different probabilities). The protocol uses efficient randomization and symmetrization to estimate those probabilities [ESM+07]. The core of this chapter relies on the implementation of the protocol on a two qubit processor under three different types of engineered noise. We also analyze and explain certain modifications to the usual control techniques in order to increase the precision of our results to within 0.5% of the expected results.

Finally, Chapter 5 describes the efficient randomized benchmarking of the quality of control on a given system. Inspired by previous work from Emerson et al. [EAZ05] and Knill et al. [KLR+08], we implemented a protocol on a single qubit processor to estimate the average fidelity per computational gate. At first, results were much different than expected, but careful modeling of the expected errors in the system accurately explained our results and gave us a way to modify our implementation technique to then successfully obtain a relevant result. We then attempt to generalize the latter protocol to be suitable to benchmark the control over a multi-qubit system. We argue several modifications to Emerson et al. protocol to permit a realistic implementation and also to permit a fair comparison between

systems of different sizes. This is followed by an implementation on a three qubit NMR processor [RLL08].

Notation

For the understanding of this thesis, we will list a summary of different notations used. Since this thesis includes work on quantum information theory and its implementation using NMR, the words "qubit" and "spin" are used interchangeably.

The Pauli matrices are defined as the generators of rotation on a qubit, i.e.

$$\mathbb{1} = \begin{pmatrix} 1 & 0 \\ 0 & 1 \end{pmatrix}, \quad X = \begin{pmatrix} 0 & 1 \\ 1 & 0 \end{pmatrix},$$
$$Y = \begin{pmatrix} 0 & -i \\ i & 0 \end{pmatrix}, \quad Z = \begin{pmatrix} 1 & 0 \\ 0 & -1 \end{pmatrix}. \tag{4}$$

Unless otherwise stated, the matrices are explicitly written in the *computational basis*, that is, the eigenvectors of the Z matrix, i.e. $Z|0\rangle = |0\rangle$ and $Z|1\rangle = -|1\rangle$. The NOT gate is defined as the X gates since it has the NOT action on the computational basis, i.e. $X|0\rangle = |1\rangle$ and $X|1\rangle = |0\rangle$. The $|\pm\rangle = \frac{1}{\sqrt{2}}(|0\rangle \pm |1\rangle)$ states are the eigenstates of the NOT gate, i.e. $X|\pm\rangle = \pm|\pm\rangle$. Other gates used are the Hadamard gate and the two-qubit controlled-NOT (CNOT) gate, i.e.

$$H = \frac{1}{\sqrt{2}} \begin{pmatrix} 1 & 1 \\ 1 & -1 \end{pmatrix}, \quad CNOT = \begin{pmatrix} 1 & 0 & 0 & 0 \\ 0 & 1 & 0 & 0 \\ 0 & 0 & 0 & 1 \\ 0 & 0 & 1 & 0 \end{pmatrix}. \tag{5}$$

It is easy to verify that $H|0\rangle = |+\rangle$ and $H|1\rangle = |-\rangle$. The CNOT is so named because a NOT gate will affect the second qubit if and only if the first qubit is in the state $|1\rangle$. The circuit description of a CNOT is shown in Fig. 1-a. Another important two qubit interaction is the J-coupling evolution, which has the effect $e^{-i\frac{\theta}{2}Z_1Z_2}$. The circuit description for a $\pi/2$ and a $\pi/4$ coupling is given in Fig. 1-b and c.

In circuit diagrams and in the text, $R_\phi(\theta)$ corresponds to a rotation of angle θ around an axis in the xy plane making an angle ϕ with the x axis, i.e.

$$\begin{aligned} R_\phi(\theta) &= e^{-i\frac{\theta}{2}(\cos\phi X + \sin\phi Y)} \\ &= \cos\frac{\theta}{2}\mathbb{1} - i\sin\frac{\theta}{2}(\cos\phi X + \sin\phi Y). \end{aligned} \tag{6}$$

Moreover, $R_x(\theta)$, $R_y(\theta)$ and $R_z(\theta)$ are short notations to represent a θ rotation about the x, y or z axis.

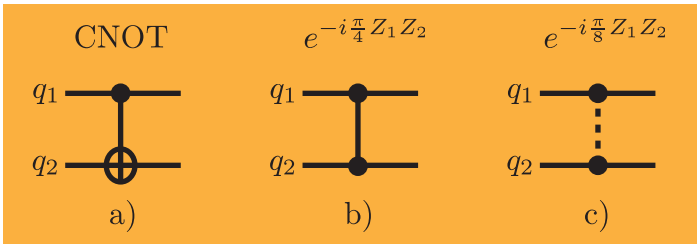

Figure 1: The quantum circuit representation of a) a CNOT b) a $\pi/2$ coupling c) a $\pi/4$ coupling.

When working with multi-qubit operators and states, e.g. $X \otimes X \otimes Z$ or $|0\rangle \otimes |1\rangle \otimes |1\rangle$, the $\otimes$ is often omitted and replaced by indices for the operators, i.e. $X_1X_2Z_3$, can compacted for the states, i.e. $|011\rangle$. When the situation is clear, the indices will also be omitted.

A $D \times D$ unitary matrix acting on the $D \times 1$ pure state vector of the system is denoted by an italic capital letter, i.e. U or V. The superoperator acting on the $D \times D$ density matrix of the system is denoted Λ. In the Liouville representation (Sec. 1.2.3), the $D^2 \times 1$ vector corresponding to a density matrix ρ is written as $|\rho\rangle\rangle$. The $D^2 \times D^2$ representation of U is denoted with a "hat", i.e. $\hat{U}$, just as the representation of Λ, i.e. $\hat{\Lambda}$. The superoperator Λ will also be referred as a *quantum channel* throughout the text.

Finally, we should note that we are using a set of units in which $\hbar = 1$ to simplify the presentation.

Additional information of the examining committee

This thesis presents *some* of the work carried out by the author during the course of his doctoral studies. In no way does the author claim the originality of all the work presented in this thesis and below are listed his contributions.

Chapter 1 only contains background information concerning some possible representations of decoherence superoperator needed for the comprehension of this thesis which can be found in the literature [NC00, Hav03, BP02].

Most of Chapter 2 also contains background information about liquid state NMR. The chapter is loosely based on the review article "Quantum information processing using nuclear and electron magnetic resonance: review and prospects" [BCC+07] written by the NMR group at the IQC and MIT. It is available as a

preprint at arXiv:0710.1447 and published in *Physics In Canada - Quantum Computing and Quantum Information Edition* **63**, no.4 (2007). The present author solely wrote the liquid state NMR part of the review. The original work about advanced control techniques presented in Sec. 2.6 have been mainly carried out by C. Negrevergne and C. A. Ryan based on earlier developments by E. Knill and R. Laflamme. The present author contributed to this work mostly through idea sharing and some programming. For this reason, little detail has been included in this thesis and only the main results used in later sections were given and explained. "Liquid State NMR as a Test-bed for Developing Quantum Control Methods" [RNL+08] is available at arXiv:0803.1982 and is published in *Physical Review A* **78**, 012328 (2008).

Chapter 3 in based on the article "Determining the noise model using error correction" [LSB+07], published in Physical Review A **75**, 012331 (2007) and available at arXiv:quant-ph/0610038. The work was initially carried out by J. Baugh and D. Simon as a summer project. J.- C. Boileau was then appointed to finish the experiment. Upon unsuccessful implementation due to the lack of control available at the time, the project was shelved. After glancing at the project report of D. Simon, the present author found irregularities in the noise simulation procedure and argued the sub-optimality of the pulse sequence used. He then redesigned the entire experiment using a different analysis method, different control techniques and a different molecule. Moreover, the mathematical justification of the Gaussian noise model presented in Sec. 3.2 was proven by the author whereas before, the noise was only *assumed* to be Gaussian.

Chapter 4 reports the author's participation in the collaborative work "Symmetrized characterization of noisy quantum processes", published in *Science*, **317**, p. 1893-1896 (2007) [ESM+07] and available at arXiv:0707.0685 . The protocol was proposed by J. Emerson and further developed by M. Silva and O. Moussa. Although the mathematical derivation of the protocol is reported, the author wanted to present his own derivation of the protocol, which is slightly different (and to the author's view, simpler) than the one available in the published manuscript. The author also participated in several discussions and mathematical derivations proving the invertability of the Ω matrix in Eq. 4.41. The designed and implementation of the experiment in Sec. 4.6 was carried entirely by the author, with some technical help of M. J. Ditty for remote control of the spectrometer and the help of O. Moussa for calculating the values of $\vec{p}$ given in Table 4.2 and 4.3 using the method of maximum likelihood. A three-spin solid-state NMR experiment was also conducted by C. A. Ryan and J. Baugh, and was not presented here as the author did not participate in its implementation. Finally, the SPICE simulator for the phase transient analysis presented in Sec. 4.6.3 was entirely built by the author. It was developed for a joint project with C. A. Ryan and J. S. Hodge at

MIT on the analytical (J. S. Hodges), simulated (present author) and experimental (C. A. Ryan) analysis of the phase transient occurring during the implementation of strongly modulated pulses. Details of the simulator and some simulation results are presented in Appendix C, but are yet unpublished.

The work presented in the final chapter reports the joint effort of the author and C. A. Ryan to benchmark the control on a single spin and the generalization and implementation of the protocol on a multiple spin processor. The original single qubit experiment was carried out by E. Knill et al. on a trapped ion processor [KLR+08], based on a protocol proposed by J. Emerson et al. [EAZ05] and presented in the author's own word in Sec 5.2. The generalization to multiple qubit presented in Sec. 5.3.2 is a joint effort by the author and C. A. Ryan. The simulations of 5.3.3 were carried by the author. The single qubit experiment was essentially implemented by C. A. Ryan, but the analytical model of the super-exponential decay described in Sec. 5.4.3 was developed solely by the present author. The three-spin experiment was carried by the author, with the help of C. A. Ryan for characterizing the molecule, finding, fixing and optimizing the GRAPE pulses. Moreover, the signal analysis carried in Sec. 5.5.2 was the author's work, initiated by discussion with C. A. Ryan. The manuscript, "Randomized benchmarking single and multi-qubit control in liquid state NMR quantum information processing" is submitted for peer-review and a preprint is available at arXiv:0808.3973.

The work presented in this thesis only corresponds to the effort of the author towards the characterization of decoherence and control. The author also participated in "Robust Quantum Communication Using A Polarization-Entangled Photon Pair" [BLLM04], initiated by J.- C. Boileau, by calculating the probability of success of the protocol under random unitary collective noise. This work is published in *Physical Review Letters* **93**, 220501 (2004) and available at arXiv:quant-ph/0406118. The author also initiated the work presented in "Experimental Implementation of Discrete Time Quantum Random Walk on an NMR Quantum Information Processor" [RLBL05]. The implementation was a joint effort by the author and C. A. Ryan, with the help of J.- C. Boileau. This work is published in *Physical Review A* **72**, 062312 and available at arXiv:quant-ph/0507267.

The article "Time-reversal formalism applied to maximal bipartite entanglement: Theoretical and experimental exploration" [LBL06] was initiated from an idea of Raymond Laflamme and some earlier thoughts by J. Baugh. The entirety of the theory and the experiment is the work of the author. The manuscript is available at arXiv:quant-ph/0510048 and published in *Physical Review A* **73** 032323 (2006). The work with C. A. Ryan and J. S. Hodges on "Protecting nuclear spins from electron relaxation" have been published in *Proceeding of the Asian Quantum Information Conference 2007*. Finally, the work in " Quantum Reference Frames and the Classification of Rotationally-Invariant Maps" [BSLB08] was carrier out

by J.- C. Boileau and L. Sheridan. The present author participated in initiating and helping with the proof of the representation of covariant maps. The article is published in *Journal of Mathematical Physics* **49**, 032105 (2008) and is available at arXiv:0709.0142v2. Finally, the author helped J. Zhang to find the control sequences used in "Direct observation of quantum criticality in Ising spin chains", available at arXiv:0808.1536.

Chapter 1

Decoherence in open quantum system

1.1 The effect of the environment

Standard introductory quantum mechanics textbooks (e.g. [Lib03, Sak85, Tow00]) describe the evolution of a quantum system using the Schrödinger equation or the Liouville equation (Eq. 1). The solution to these gives a unitary evolution. A key property of unitary evolution is that the system will not lose purity due to its internal dynamics. From a quantum information perspective, no quantum information "leaks" to the outside world, such that the evolution is a reversible process. For these reasons, the two equations are known as the equations of motion for a *closed* quantum system.

The presence of an environment, i.e. the surroundings over which we do not have any control, will introduce *noise* into the system and force it to possibly undergo dynamics different from the intended one. This noise will introduce a level of uncertainty in the quantum evolution. This probabilistic evolution will effectively make the system slowly lose its coherent quantum nature,hence the term *decoherence*, also known as *relaxation*. Therefore, a quantum state in a given superposition will decay to a statistical mixture of the initially superposed state. This effect of the environment is know as a *dissipative* evolution. Many efforts throughout the years have led to the development of master differential equations for the continuous time evolution of a given system under its internal coherent dynamics and the external dissipative noise. Such equations can be written in the Lindblad form [Lin76] or in the Bloch-Redfield from [Wei99], which give a differential equation for the continuous evolution of an open quantum system and can be quite involved. These equations are suitable to describe Markovian or semi-Markovian environment, that

is the environment has a very short memory, so that the system-environment interaction does not reintroduce information into the system.

In quantum computing, we are mostly interested in the effect of decoherence for a given amount of time, or for a fixed process. Just like we describe quantum computing as discrete unitary operators rather than a continuous Hamiltonian evolution, we describe decoherence as an operator acting on the system. Consider our system of interest to be in the initial state $\rho_s(0)$, with internal Hamiltonian $\mathcal{H}_s$. To describe its evolution as an open system, we can expand that system to include the environment so that the entire system in closed. Suppose the environment has an internal Hamiltonian $\mathcal{H}_\mathcal{E}$ and interacts with the system through an interaction Hamiltonian $\mathcal{H}_{int}$. It is commonly accepted, though some conditions apply as explained below, that the initial state of the system-environment is separable, i.e. there is initially no quantum correlation between them. Without loss of generality, and also for simplicity, the environment can be assumed to be in the state $|0_\mathcal{E}\rangle\langle 0_\mathcal{E}|$, so that $\rho(0) = \rho_s(0) \otimes |0_\mathcal{E}\rangle\langle 0_\mathcal{E}|$. After a time τ, the final state will be

$$\begin{aligned} \rho(\tau) &= e^{-i(\mathcal{H}_s+\mathcal{H}_\mathcal{E}+\mathcal{H}_{int})\tau} \left(\rho_s(0) \otimes |0_\mathcal{E}\rangle\langle 0_\mathcal{E}|\right) e^{i(\mathcal{H}_s+\mathcal{H}_\mathcal{E}+\mathcal{H}_{int})\tau} \\ &= U(\tau) \left(\rho_s(0) \otimes |0_\mathcal{E}\rangle\langle 0_\mathcal{E}|\right) U(\tau)^\dagger, \end{aligned} \tag{1.1}$$

where we defined $U(\tau)$ as being the unitary evolution of the system-environment for a time τ. Since we do not have access to the environment register, the evolution of the system can thus be described by the partial trace of the above state over the environment degree of freedom. Assuming the environment is a D dimensional system with basis states $|0_\mathcal{E}\rangle, \ldots |D-1_\mathcal{E}\rangle$, we have

$$\begin{aligned} \rho_s(\tau) &= \mathrm{Tr}_\mathcal{E}[\rho(\tau)] \\ &= \sum_{k=0}^{D-1} \langle k_\mathcal{E}| U(\tau) \left(\rho_s(0) \otimes |0_\mathcal{E}\rangle\langle 0_\mathcal{E}|\right) U(\tau)^\dagger |k_\mathcal{E}\rangle \\ &= \sum_{k=0}^{D-1} A_k \rho_s(0) A_k^\dagger, \end{aligned} \tag{1.2}$$

where we have defined the contracted operator

$$A_k = \langle k_\mathcal{E}| U(\tau) |0_\mathcal{E}\rangle, \tag{1.3}$$

acting on the Hilbert space of the system alone. From the above equation, we see that the evolution of the system is described as a statistical mixture of different operators acting on the initial state $\rho_s(0)$. Because of this probabilistic evolution, more uncertainty about the evolution will occur and the system will thus lose purity.

Since the above cannot be described by a simple unitary operator, we denote the operator Λ, defined as

$$\Lambda(\square) = \sum_k A_k \square A_k^\dagger \tag{1.4}$$

the *superoperator* describing the open system evolution. Λ can also be referred at a *quantum channel*.

Since the exact mechanism of open quantum system is beyond the scope of this thesis, we will only describe three different ways of representing the action of the noise on the state of the system.

1.2 Useful representation of decoherence

1.2.1 Kraus representation

Describing an open system evolution for a given time using a set of operators as in Eq. 1.2 is known as the Kraus representation of an evolution and the operators A_k are called the *Kraus operators*.

From Eq. 1.2 and using the fact that successively partially tracing out the environment and then the system is equivalent to a complete trace of the system-environment state, we see that

$$\mathrm{Tr}[\Lambda(\rho_s(0))] \;=\; 1, \tag{1.5}$$

that is that the evolution in Eq. 1.2 is *trace preserving*, which is a requirement for Λ to describe a quantum evolution operation. This also follows from the fact that

$$\begin{aligned}\sum_k A_k^\dagger A_k &= \sum_k \langle 0_\mathcal{E}|U(\tau)^\dagger|k_\mathcal{E}\rangle\langle k_\mathcal{E}|U(\tau)|0_\mathcal{E}\rangle \\ &= \mathbb{1}_s,\end{aligned} \tag{1.6}$$

where we have used the fact that $U^\dagger U = UU^\dagger = \mathbb{1}$ for any unitary operator. Moreover, since the state of a closed system is always a positive operator, i.e. $\langle\Psi|\rho(\tau)|\Psi\rangle \geq 0$ for any state $|\Psi\rangle$ of the system-environment, we also have that

$$\begin{aligned}\langle\psi_s|\rho_s(t)|\psi_s\rangle &= \sum_k \langle\psi_s k_\mathcal{E}|U(\tau)\left(\rho_s(0)\otimes|0_\mathcal{E}\rangle\langle 0_\mathcal{E}|\right)U(\tau)^\dagger|\psi_s k_\mathcal{E}\rangle \\ &\geq 0,\end{aligned} \tag{1.7}$$

so that the evolution is also *positive*.

Conversely, Kraus demonstrated that if any set of operators A_k satisfying Eq. 1.6 with the assumption that the system and the environment are initially uncorrelated, then Eq. 1.2 will necessarily describe a *trace-preserving and completely positive* (CPTP) map [Kra83]. Therefore, any possible quantum evolution on a given, initially isolated system, must be CPTP and can be described using Kraus

operators. Moreover, there is formal proof that any CPTP map can be described as a unitary evolution on a bigger system [Sti55], as intuitively explained above.

It can be shown that a CPTP map on a system of dimension D can be described using at most D^2 Kraus operators. The Kraus representation of a given process is not unique, but all sets of operators are related through a unitary transformation. Given $\{A_k\}$ and $\{B_k\}$, there exist a unitary operator V such that

$$B_j = \sum_i V_{ij} A_i. \tag{1.8}$$

For Kraus theorem to be true, one *must* make the assumption that the environment and the system are initially separable. It has been reported that the failure of such condition can in fact lead to a non-completely positive map [Pec94, SB01, JSS04, WHE+04].

1.2.2 χ matrix

The χ matrix representation is simply a way to describe the Kraus operators in a unique fashion. In quantum computing, an n qubit system has dimension $D = 2^n$ and an orthonormal basis for operators acting on such a systems is the set of all tensor product Pauli operators $\mathcal{P}_n$, since we know that $\mathrm{Tr}(P_i P_j) = D\delta_{ij}$. Therefore, given a set of Kraus operator $\{A_k\}$, each operator can be decomposed as

$$A_k = \sum_i \alpha_i^{(k)} P_i, \quad P_i \in \mathcal{P}_n, \tag{1.9}$$

where $\alpha_i^{(k)} = \frac{1}{D}\mathrm{Tr}(A_k P_i)$. The effect of the quantum channel on a state ρ is then written as

$$\begin{aligned} \Lambda(\rho) &= \sum_{ijk} \alpha_i^{(k)} \alpha_j^{(k)*} P_i \rho P_j \\ &= \sum_{ij} \chi_{ij} P_i \rho P_j, \end{aligned} \tag{1.10}$$

where we have defined $\chi_{ij} = \sum_k \alpha_i^{(k)} \alpha_j^{(k)*}$.

Because of the unitary equivalence between all the Kraus representations of a given channel, the elements χ_{ij} are identical for all representations. Therefore, the χ matrix gives us a representation of a CPTP map that is uniquely determined by the choice of operator basis.

From its definition, the χ matrix is a hermitian matrix. It can be shown to be positive, semi-definite with, $\mathrm{Tr}(\chi) = 1$ if and only if it represents a CPTP map [Eme07].

1.2.3 Liouville representation

One of the most practical ways of describing the action of a superoperator on a given state is through the Liouville representation [Blu96]. The superoperator described by the Kraus operators is a linear function on the space of $D \times D$ density matrices, i.e. a linear operation on a D^2 vector space. Therefore, there must exist a representation in which the state and the superoperator follow the traditional vectorial multiplication, i.e.

$$\Lambda(\rho) \quad \leftrightarrow \quad \hat{\Lambda}|\rho\rangle\rangle, \tag{1.11}$$

where $|\rho\rangle\rangle$ is a $D^2 \times 1$ vector representation of ρ and $\hat{\Lambda}$ is a $D^2 \times D^2$ matrix representation of Λ. It is a well known fact of matrix algebra [HJ91, Lüt96, Hav03] that if $|\rho\rangle\rangle$ is constructed by stacking the columns of ρ, then

$$\hat{\Lambda} \quad = \quad \sum_k A_k^* \otimes A_k, \tag{1.12}$$

where A_k^* is the complex conjugate of A_k in the chosen basis for the matrix representation. From the definition of $|\rho\rangle\rangle$, it can be shown that

$$\langle\langle \rho_1 | \rho_2 \rangle\rangle \quad = \quad \mathrm{Tr}(\rho_1^\dagger \rho_2). \tag{1.13}$$

It is possible to relate the Liouville operator $\hat{\Lambda}$ and the associated χ matrix since

$$\begin{aligned} \hat{\Lambda} &= \sum_k A_k^* \otimes A_k \\ &= \sum_{ijk} \alpha_i^{(k)*} \alpha_j^{(k)} P_i^* \otimes P_j \\ &= \sum_{ij} \chi_{ji} P_i^* \otimes P_j. \end{aligned} \tag{1.14}$$

1.3 Uncorrelated and correlated noise

In the above section, we presented some representations of the evolution of an arbitrary number of qubits. This was assuming that we had knowledge, for example, of all the Kraus operators acting on the system as a whole. In reality, one might only possess the action of the environment on a single qubit, e.g. dephasing (Sec. 2.7.1). If we assume that the noise is uncorrelated from qubit to qubit, that is, that the error happening on qubit a is not influenced, nor is influencing the noise on qubit b, then the noise operation on the two qubits commutes and can be described by conjugating the single qubit superoperators. If the noise introduced by the

environment is described by a single qubit superoperator Λ, then the cumulative noise Λ_{ab} on qubit a and b is described by

$$\Lambda_{ab} = \Lambda_b \circ \Lambda_a = \Lambda_a \circ \Lambda_b. \tag{1.15}$$

where $\circ$ denotes the composition of the maps.

For example, on a two qubit system with single qubit noise being described by the set of Kraus operators $\{A_i\}$, the cumulative noise on a joint density matrix ρ_{12} is given by

$$\begin{aligned} \Lambda_{12}(\rho_{12} &= \Lambda_2 \left(\Lambda_1(\rho_{12})\right) \\ &= \Lambda_2 \left(\sum_i A_i^{(1)} \rho_{12} A_i^{(1)\dagger} \right) \\ &= \sum_{ij} A_j^{(2)} A_i^{(1)} \rho_{12} A_i^{(1)\dagger} A_j^{(2)\dagger}. \end{aligned} \tag{1.16}$$

From this principle, the Liouville and χ matrix representation can be derived.

If there exists correlations between the noise affecting the qubits, this implies that if an error hapen on qubit a, an error will also affect qubit b. Because of this correlation, a full multi qubit representation of the noise is needed and cannot be inferred from the action on a single qubit alone without knowing the correlation operators (Chapter 3).

1.4 Coherent, incoherent and decoherent noise

Although we have classified any evolution of a system that includes unwanted interactions with an environment as decoherence, we can find in the literature further division in the semantics. If we extend the definition of noise to any operation or evolution that makes the system not perform the exact desired evolution, it can be argued that there are three different types of noise: decoherent, incoherent and coherent.

Decoherent noise

As mentioned so far, decoherent noise is the term associated with the unwanted quantum interaction of a system with its environment that causes the system to lose purity. Even if we assume a realistic situation of a non-Markovian environment (e.g. finite temperature bath), there will always be some information that will remain in the environment and never come back to the system. Hence, decoherence is the term used to described the intrinsic lost of purity.

Incoherent error

The term incoherent noise has been introduced to explain the loss of purity of a quantum system due to classical noise. It will effectively encode quantum information into classical degrees of freedom [PBE+03, BEH+04]. It will manifest itself as a statistical variation of the system's Hamiltonian [WHE+04]. Ultimately, the evolution will be described by an averaging of unitary operators over a distribution of the classical parameters $\vec{u}$, i.e.

$$\begin{aligned} \rho &\rightarrow \int d\vec{u} p(\vec{u}) e^{-i\mathcal{H}(\vec{u})t} \rho e^{i\mathcal{H}(\vec{u})t} \\ &= \int d\vec{u} p(\vec{u}) U(t,\vec{u}) \rho U(t,\vec{u})^\dagger \end{aligned} \tag{1.17}$$

Incoherent errors will also cause a loss of purity of an ensemble of systems, while each system retains its purity [HGW+07]. This loss of ensemble purity is usually recoverable by controlling the system appropriately. Examples of interest include the magnetic field inhomogeneity in NMR (Sec. 2.7.1), which can be refocused through a Hanh echo [Han50] or a CPMG sequence [CP54, MG58] or the space dependent control magnetic field in NMR (Sec. 5.4.3), which can be avoided using optimal control theory [PDR88, DPR90, FPB+02, KRK+05]

Coherent noise

As it name suggest, a coherent noise, or coherent error, make the system undergo a different evolution, but yet, this evolution does not introduce probabilistic uncertainty in the system and thus does not decrease the purity of the system. That is, the error can be represented as a single unitary operator. An example of such a noise could be a systematic calibration error that over rotates a qubit.

Chapter 2

Liquid state NMR

2.1 Using NMR for quantum information processing

The fundamental unit of quantum information is the qubit, which is a two-level quantum mechanical system. The spin-1/2 property of certain particles is an ideal candidate for multiple reasons. First of all, they represent a system whose observables are described using the Pauli matrices and hence are a two level quantum systems.

In the 1950's, Purcell, Bloch and their coworkers discovered that once placed in a magnetic field, the nuclear spins of molecules can be controlled by electromagnetic excitation at a given frequency, thus leading to nuclear magnetic resonance (NMR) [Blo46, PTP46]. Since then, NMR has been the subject of intensive research and development. The technology is now sufficiently advanced to allow accurate control of the state of nuclear spins. Being able to individually control the spins and also use their interactions gives the basis for universal control which is essential for QIP.

Finally, nuclear spins are naturally a good candidate for qubits as they do not significantly interact with other degrees of freedom of the system, such as the orbital and vibrational modes [Abr83]. At room temperature, the energy gap between the spin energies and the other degrees of freedom is too large to have an effect on each other. For these reasons, nuclear spins are naturally protected from decoherence and demonstrate relatively long coherence times.

As will be explained in more detail, liquid state NMR suffers from the major caveat of unscalability due to low polarization and the difficulty in creating a fiducial initial state from the thermal state of the system. Despite these limitations, NMR still remains to this day the QIP device with the highest degree of control and is a

perfect test-bed system for developing and benchmarking tools that then could be used by other scalable devices.

The ability to control liquid state nuclear spin systems has allowed implementation of a variety of benchmarking experiments and algorithms on small qubit registers. For example, sufficient control has been developed to implement quantum algorithms [JM98, CVZ+98, LBF98, WLC01, KLMT00, VSB+01, ZLD+04, RLBL05], quantum error correcting protocols [CMP+98, LSB+07, SCS+00, KLMN01, BVFC05], the simulation of quantum systems [CYC06, NSO+05, HSVC01, TSS+00, STH+99] and also the benchmarking of a 12 qubit quantum processor [NMR+06].

2.2 Summary of the magnetic interactions

In the semi-classical picture, the spin of a nucleus behaves like the dipolar moment of a magnet possessing angular momentum parallel to its magnetic moment. When placed in a constant magnetic field pointing along a certain direction (customarily defined as the z direction), the dipolar moment precesses around this axis. The frequency of this precession is called the *Larmor frequency* and is dependent on the external magnetic field, the nuclear isotope and its chemical environment within the molecule. For quantum information purposes, we can use any spin-1/2 nuclei (e.g. ^{1}H, ^{13}C, ^{15}N, ^{19}F, ^{29}Si and ^{31}P to name a few).

Placed in magnetic fields generated by modern superconducting magnets, different isotopes of nuclei have differences in Larmor frequency on the order of MHz. For example, the Larmor frequency of ^{1}H is about 700 MHz in a 16.4 Tesla magnet, while that of ^{13}C is about 175 MHz. Depending on the symmetry of the molecule, two nuclei of the same isotop can either have the same Larmor frequency, or can have a frequency difference ranging from a few Hz to several kHz. Typical liquid state NMR experiments involve an ensemble of around 10^{20} identical molecules dissolved in a deuterated solvent whose effect on the nuclear magnetic moments of the molecules can be neglected.

When two spins are spatially close, their dipolar moments interact with each other through their generated magnetic field. The strength of this coupling is dependent on the distance between the two spins and their relative orientation with respect to the external magnetic field. In a liquid, the molecules move and rotate around each other on a much shorter time scale than the interactions occurring between them. This causes the intermolecular and intra-molecular dipolar interactions to average to zero on the NMR time scale (i.e. the Larmor period time scale).

Within the same molecule, there are still interactions between the spins in the liquid state. If the wavefunctions of bonding electrons overlap spatially with a pair

of nuclear spins, the electron mediates an effective interaction between the nuclear spins. The average of this interaction is independent of the external magnetic field and the orientation of the molecule, which inspires its name: scalar coupling (also called indirect spin-spin coupling, or J-coupling).

2.3 The natural NMR Hamiltonian

As mentioned above, in liquid state NMR the intermolecular spin interactions are suppressed. This causes the molecules to be effectively isolated from each other, and therefore a description of the spin dynamics of an ensemble of identical molecules is well approximated by the spin dynamics of a single molecule. If we consider a molecule containing N spin-1/2 nuclei, then the natural Hamiltonian of this system in a large homogeneous magnetic field $\vec{B}_0$ pointing in the z direction is given by

$$\mathcal{H}_{nat} = \frac{1}{2}\sum_{i=1}^{N} 2\pi\nu_i^L Z_i + \frac{\pi}{2}\sum_{i<j} J_{ij} Z_i Z_j \tag{2.1}$$

where $2\pi\nu_i^L = \omega_i^L = \gamma_i(1+\delta_i)|\vec{B}_0|$ is the Larmor frequency of the i^{th} nucleus with gyromagnetic ratio γ_i (dependent on the isotope only) and chemical shift δ_i (dependent on the chemical environment), J_{ij} is the coupling strength between nucleus i and j and Z_i is the Z Pauli matrix of the i^{th} spin. More details about the different possible nuclear interactions is available in Appendix A

The first term in the Hamiltonian is the *Zeeman interaction* and describes the precession of the spins due to their coupling to the external magnetic field, while the second term describes the J-coupling between pairs of nuclei. This Hamiltonian corresponds to the weak coupling limit, where we assume that the difference in chemical shifts between coupled spins are much greater than their respective couplings, i.e. $|\nu_i^L - \nu_j^L| \gg J_{ij}/2$. If this approximation is not valid, we need to use the full exchange coupling operator $X_iX_j + Y_iY_j + Z_iZ_j$ in place of Z_iZ_j. The exact values of the Hamiltonian parameters can be determined by fitting experimental data (see Sec. 2.4.4).

2.4 DiVincenzo criteria in NMR

2.4.1 Defining the qubit

If we refer back to the Preface, the first criterion a potential system must fulfill to be a suitable quantum information processor candidate is to be a scalable system

with well-defined qubits. We have already argued that the nuclear spins are well defined two-level systems. To encode quantum information, we can associate the computational basis state $|0\rangle$ and $|1\rangle$ with the up or down projection of a spin along the z axis. An arbitrary qubit state $|\psi\rangle = \alpha|0\rangle + \beta|1\rangle$ can be experimentally described as

$$\alpha|0\rangle + \beta|1\rangle \quad \Leftrightarrow \quad \alpha|\uparrow\rangle + \beta|\downarrow\rangle. \tag{2.2}$$

The scalability criterion implies that one can potentially scale the quantum computer to virtually any size. Unfortunately, this capability is compromised in liquid-state NMR due to incapacity of efficiently initializing the system. A deeper discussion will follow in Sec. 2.5

2.4.2 Universal control

How to reach universality

In order for a quantum device to be deemed a universal quantum computer, it must be able to perform any possible algorithm. In the circuit model of QIP, this implies that it is possible to implement any desired unitary operation on a given system. Although there exist techniques based on optimal control theory to generate continuous control sequences for a given unitary (Sec. 2.6.2), it is preferable for scalability and for design purposes to possess a set of generating gates from which any operation can be performed. As a matter of fact, the optimal control technique will require optimization of the control handle each and every time an extra qubit is added or when the algorithm is slightly modified. On the other hand, having a set of generating gates permits one to determine the control on the system for each gate only once, and then apply them sequentially to implement the desired operation.

Unfortunately, decomposing an arbitrary unitary operation into an optimal sequence of generating gates is a very hard task, but it is known that given a unitary, it is always possible to approximate it to arbitrary precision using an efficient amount of gates [Kit97a, Sol00, HRC02]. Even though there is an infinite number of universal sets of gates (if fact, almost "any" set is universal [Llo95, DBE95]), NMR is best suited for the use of single qubit rotations and two-qubit entangling gates. It is known that if one can perform arbitrary rotation about any axis on any qubits, as well as performing a controlled-NOT (CNOT) gate between any two qubits, universal quantum computation is possible [BBC$^+$95].

Single-spin control

Consider an oscillating magnetic field applied to the sample perpendicular to the z axis and at the same frequency as the Larmor frequency of a given nucleus. In the rotating frame of the spin, that is, a reference frame rotating at the Larmor frequency, this oscillating field will appear constant and the spin will precess about this axis. Therefore, this will implement a rotation about an axis in the xy plane, where the effective angle of rotation will be determined by the duration and power of the pulse, while the phase of the axis of rotation is determined by the phase of the pulse. From the time scale of NMR (MHz), these pulses are at radio-frequencies (RF).

From a more mathematical approach, consider the application of a magnetic field $\vec{B}_1$ perpendicular to the z axis which oscillates at the angular frequency ω^{rf} with a given phase ϕ:

$$\vec{B}_1 = |\vec{B}_1| \left(\cos(\omega^{rf} t + \phi)\, \vec{x} + \sin(\omega^{rf} t + \phi)\, \vec{y}\right). \tag{2.3}$$

Since the RF pulse is a magnetic field, it will interact with the dipolar moment of the nuclear spins such that the Hamiltonian associated with this interaction will be

$$\begin{aligned} \mathcal{H} &= \mathcal{H}_{nat} + \mathcal{H}_{rf} \\ &= \mathcal{H}_{nat} + \sum_i \frac{\omega_i^{nut}}{2} \left[\cos\left(\omega^{rf} t + \phi\right) X_i + \sin\left(\omega^{rf} t + \phi\right) Y_i\right], \end{aligned} \tag{2.4}$$

where $\omega_i^{nut} = \gamma_i |\vec{B}_1|$ is the nutation frequency of the rotation.

After transforming to a rotating frame with angular frequency ω, the system will evolve, in that rotating frame, according to the rotating frame Hamiltonian given by

$$\mathcal{H}_r = R_z(-\omega t)\mathcal{H} R_z(\omega t) - \sum_i \frac{\omega}{2} Z_i. \tag{2.5}$$

If we consider the system in the rotating frame of the pulse ($\omega = \omega^{rf}$), the total Hamiltonian (pulse and natural) becomes

$$\begin{aligned} \mathcal{H}_r &= \sum_i \left[\frac{1}{2}(\omega_i^L - \omega^{rf}) Z_i + \frac{1}{2}\omega_i^{nut}(\cos\phi\, X_i + \sin\phi\, Y_i)\right] \\ &\quad + \frac{\pi}{2} \sum_{i<j} J_{ij} Z_i Z_j. \end{aligned} \tag{2.6}$$

Ignoring the coupling effect for the moment, if the RF pulse is at the same frequency as one of the spins, say $\omega^{rf} = \omega_k^L$, the spin k will see an effective constant field in

the xy plane making an angle ϕ with the x axis, and will precess about it. The rotation angle θ is determine by the interval τ during which the RF field is applied, according to $\theta = \omega_i^{nut}\tau$.

The other spins that are not exactly on resonance with the pulse will experience an additional non-zero z component to the magnetic field. This is called the *off-resonance* effect and will make the spins precess about an axis making an angle Θ_i with the z axis, such that

$$\tan\Theta_i = \frac{\omega_i^{nut}}{\omega_i^L - \omega^{rf}}. \tag{2.7}$$

The effective nutation frequency is now given by

$$\omega_i^{eff} = \sqrt{(\omega_i^{nut})^2 + (\omega_i^L - \omega^{rf})^2}. \tag{2.8}$$

From the above equation, we can conclude that in order to rotate a single spin k without rotating the other spins, we need $\omega_i^{nut} \ll |\omega_i^L - \omega^{rf}|$ so that $\Theta_1 \simeq 0$. This can be achieved by either considering heteronuclear spins, or by using very small pulse power. In this limit, Eq. 2.8 thus tells us that spin i will be affected by a shift in its Larmor frequency, Δ_{BS} given by

$$\Delta_{BS} = \frac{(\omega_i^{nut})^2}{2(\omega_i^L - \omega^{rf})}. \tag{2.9}$$

The above shift is known as the *transient Bloch-Siegert effect*, which will introduce a phase error on the other spins. Fortunately, such a shift can be calculated in advance and be accounted for by modifying the phase of subsequent pulses on the spin, as we will discuss in more detail in Sec. 2.6.1. For example, a nucleus that is off-resonant by 3kHz will undergo an extra phase shift of $\sim 15^\circ$ during a $1ms$ π rotation of the other spins.

From the above treatment, we conclude that pulses on a heteronuclear system can be achieved by a quick and powerful burst of RF power ("hard" pulse) due to the large difference in the gyromagnetic ratio. In commercially available spectrometers, nutation frequencies can attain 10's of kHz so that $\pi/2$ rotations are achievable in several μs. On this time scale, the coupling effects between the spins are negligible. On the other hand, for homonuclear systems with chemical shifts on the order of kHz, very small nutation frequencies are needed, which implies the need for very weak and long pulses ("soft" pulses). For a $\pi/2$ rotation, $\tau \gg 1/(\omega_i^L - \omega^k)$, hence introducing potentially large coupling errors. Since these error do not commute with the RF Hamiltonian, they will corrupt the state of the system and introduced intractable errors (unlike the Bloch-Siegert shift).

Fortunately, in the linear response regime, we know that frequency-selective excitation can be achieved through amplitude and phase modulation of a signal

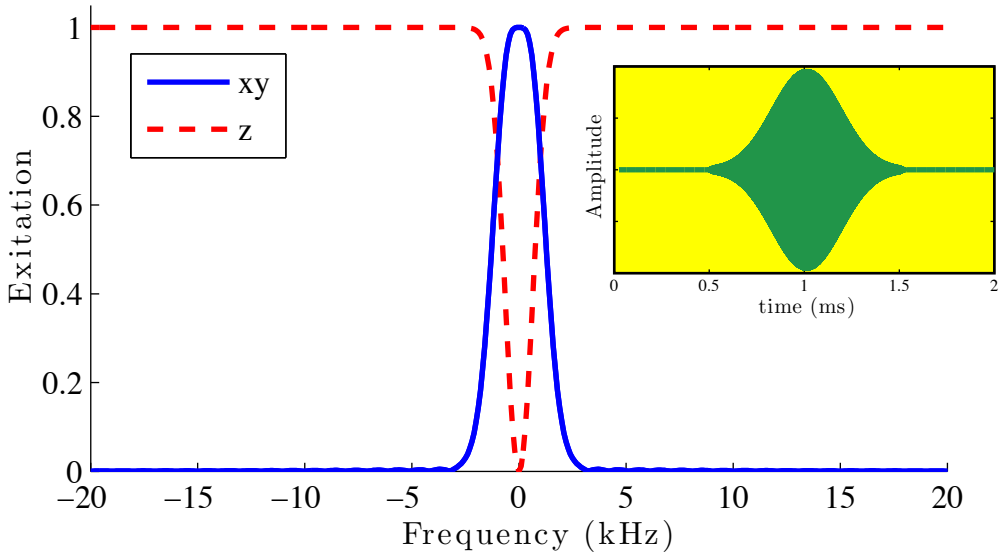

Figure 2.1: The excitation profile of a $1ms$ Gaussian shape pulse. The spectrum is centered at the carrier frequency of the pulse. The initial state of the spin was pointing along the z axis and the spectrum shows the z (dotted red) and the quadrature (solid blue) component of the spin after the pulse, with respect to the off-resonance of the spin.

(Fourier theorem). Even though the NMR excitation is sinusoidal in frequency (since the pulse Hamiltonian is exponentiated), the linear regime is a good zeroth order approximation to evaluate the excitation profile of simple shaped pulses. Since the Fourier transform of a Gaussian function is also Gaussian, we expect an RF pulse with a Gaussian amplitude envelope to have an almost Gaussian frequency excitation profile. The excitation profile of a $1ms$ Gaussian pulse is shown in Fig. 2.1. Using Gaussian shaped pulses, it is now possible to selectively excite a single spin using a pulse length of $\tau \sim 1/(\omega_i^L - \omega^k))$, and hence reduce the coupling errors. Unfortunately, there will still be a transient Bloch-Siegert shift on the other spins, but as mentioned before, it is possible to compensate for it.

For most liquid state experiments on a few spins, where chemical shifts are comparatively large and J-couplings are small, the use of Gaussian pulses is sufficient to achieve very high precision spin rotations. The situation becomes more complicated when there are more homonuclear spins (implying smaller chemical shift differences on average), or stronger coupling like in solid state [BMR+06] or liquid crystal environments [HRH+07]. It is still possible to overcome these drawbacks by considering more complicated pulse shapes and phase modulation as discussed in Sec. 2.6.2 where we describe how it is possible to find shaped pulses that can

implement any desired evolution by simulating the full quantum dynamics.

For calibration purposes, it is preferable to implement either a $\pi/2$ or a π pulse. Therefore, RF fields give us the set of all $\pi/2$ and π rotations about any axis in the xy plane. This set of single qubit rotations is sufficient to generate any desired single qubit rotations. For example, if a rotation of angle ξ is to be performed around the axis $\vec{n} = (\sin\theta\cos\phi, \sin\theta\sin\phi, \cos\theta)$, simple geometrical arguments can be made to show that

$$R_{\vec{n}}(\xi) = R_z(\xi)R_{\phi-\xi}(\pi/2)R_{\phi-\xi-\theta}(-\pi/2)R_{\phi-\theta}(\pi/2)R_{\phi}(-\pi/2), \tag{2.10}$$

The final z rotation can be implemented instantaneously by updating the phase of subsequent pulses, e.g.

$$R_{\phi}(\frac{\pi}{2})R_z(\theta) = R_z(\theta)R_{\phi-\theta}(\frac{\pi}{2}). \tag{2.11}$$

Such phase tracking also allows us to instantaneously implement z rotations of arbitrary angle and, through efficient phase tracking of the pulses, it is possible to commute all the z pulses to the end of the computation and cancel them during the post-processing of the measurements [MFM+00]. Since the implementation of the phase update of a pulse is usually much more accurate than the implementation of an RF pulse (the phase is updated digitally and is discretized to 1 part in 65536), it is preferable to modify any pulse sequence to include as many z rotations as possible, hence reducing the error introduced by the pulses.

To create an RF magnetic field at the sample, the sample is placed in the inductor (either solenoid or Helmholtz coil) of a resonant LC circuits. More details about resonant circuits will be described in 4.6.3.

The controlled-NOT operation and its implementation

To complement the selective arbitrary qubit rotation, one also needs a multi-qubit entangling operation. A useful and widely used two-qubit gate for quantum information processing is the controlled-NOT (CNOT), which acts on the computational basis

$$\begin{aligned} |00\rangle &\rightarrow |00\rangle, \qquad |10\rangle \rightarrow |11\rangle \\ |01\rangle &\rightarrow |01\rangle, \qquad |11\rangle \rightarrow |10\rangle. \end{aligned} \tag{2.12}$$

The operation must flip the target qubit (second qubit above) if and only if the first qubit is in the state $|1\rangle$. In NMR, $|0\rangle$ and $|1\rangle$ are associated with the state of the spin pointing up, $|\uparrow\rangle$ or pointing down $|\downarrow\rangle$ respectively. If we look at the Hamiltonian in Eq. 2.1 for a two-spin system and consider its effect on spin

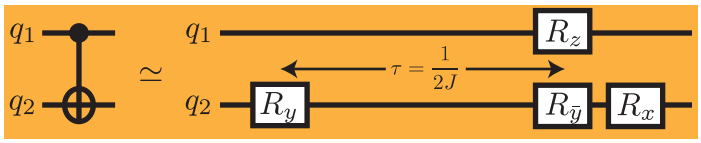

Figure 2.2: Implementation of a controlled-NOT gate in liquid state NMR. The CNOT is equivalent to a J-coupling evolution up to local operations.

2 depending on whether the state of spin 1 is up or down, we obtain an effective Hamiltonian for the second spin of the form

$$\mathcal{H}_{2,\uparrow} = \frac{1}{2}(\omega_2^L + \pi J_{12})Z_2 \tag{2.13}$$

$$\mathcal{H}_{2,\downarrow} = \frac{1}{2}(\omega_2^L - \pi J_{12})Z_2. \tag{2.14}$$

That is, spin 2 will rotate slower or faster depending on the state of spin 1. If the coupling evolves for a time $\tau = \frac{1}{2J_{12}}$, we obtain a controlled-Z rotation of $\pi/2$, which correspond to a relative difference in angle of rotation of π. This controlled rotation can then be transformed into a CNOT by a few single spin pulses applied before and after the free evolution (see Fig. 2.2 for the complete sequence to implement a CNOT). During the coupling evolution, the Zeeman interaction is also present, but since it commutes with the J-coupling, it is possible to calculate this phase evolution and include it in the phase-tracking scheme described above.

Once we consider a system with more than two spins, all the other spins will also couple during the free evolution period. These extra couplings can be refocused by implementing a series of cleverly chosen π pulses which would effectively create a time reversal motion for the spins not affected by the CNOT. For example, on a three spin system, a π pulse on the third spin half-way through and at the end of the free evolution will effectively decouple it from the rest, i.e.

$$\begin{aligned} U(t) &= R_{x3}^{\dagger}(\pi)e^{-i\mathcal{H}\tau/2}R_{x3}(\pi)e^{-i\mathcal{H}\tau/2} \\ &= (iX^3)e^{-i\frac{\pi\tau}{4}(J_{12}Z_1Z_2+J_{13}Z_1Z_3+J_{23}Z_2Z_3}(-iX^3)e^{-i\frac{\pi\tau}{4}(J_{12}Z_1Z_2+J_{13}Z_1Z_3+J_{23}Z_2Z_3)} \\ &= e^{-i\frac{\tau}{2}(J_{12}Z_1Z_2-J_{13}Z_1Z_3-J_{23}Z_2Z_3)}e^{-i\frac{\tau}{2}(J_{12}Z_1Z_2+J_{13}Z_1Z_3+J_{23}Z_2Z_3)} \\ &= e^{-i\frac{\pi\tau}{2}J_{12}Z_1Z_2}, \end{aligned} \tag{2.15}$$

where we have ignored the Zeeman term in the Hamiltonian. Note that the Zeeman evolution on spin 3 will also be refocused by such a scheme. In reality, the terminating π pulse does not need to be implemented and can be treated as a "virtual" pulse. Using the identity

$$\begin{aligned} R_\phi(\pi/2)R_\theta(\pi) &= R_z(\gamma)R_\delta(\pi/2) \\ \gamma &= 2(\phi-\theta) \\ \delta &= 2\theta - \phi - \pi, \end{aligned} \tag{2.16}$$

the virtual π pulse can be accounted for by updating the phase of subsequent pulses and performing phase tracking.

This scheme can be generalized to efficiently decouple m spins from an N spin system [JK99, LCYY00]. For systems involving up to a three or four spins, pulse phases and decoupling sequences are derived by hand, but for molecules containing a greater number of spins, these calculations become tedious and computer assisted techniques are used, as described in Sec. 2.6.1

2.4.3 State initialization

In order to implement quantum algorithms and extract relevant information, one must know the initial state of the quantum processor and that state should preferably be pure. Liquid state NMR does not offer this luxury due to its high temperature and ensemble nature, but techniques have been developed to partially overcome this limitation.

As already explained, all the molecules in a liquid sample are effectively decoupled from each other, so that the dynamics of the ensemble can be treated by considering only a single molecule. The thermal state ρ_{th} of the molecule is given by the Boltzmann thermal distribution

$$\rho_{th} = \frac{e^{-\beta \mathcal{H}_{nat}}}{\mathrm{Tr}(e^{-\beta \mathcal{H}_{nat}})}, \tag{2.17}$$

where $\beta^{-1} = k_B T$. At room temperature, the Zeeman energy of the nuclei is much smaller than $k_B T$ so that we can approximate the thermal state of an N spin molecule by

$$\rho_{th} \simeq \frac{1}{2^N}\mathbb{1} - \frac{1}{2^N}\frac{1}{k_B T}\sum_{i=1}^{N}\frac{\omega_i}{2}Z_i, \tag{2.18}$$

so that the thermal state in liquid state NMR is highly mixed. The non identity part of the thermal state is called the *deviation density matrix*. Since quantum information processing is concerned with the unitary evolution of a system, which does not affect the identity part of the state, and since this identity is unobservable, we can only consider the deviation matrix. As far as NMR is concerned, we can write the (renormalized) initial state as

$$\rho_{th} = \sum_{i=1}^{N}\omega_i Z_i. \tag{2.19}$$

To perform quantum algorithms, the system must be initialized in a fiducial pure state such as $\rho(0) = |0\rangle\langle 0|^{\otimes N}$. Since the initial state is highly mixed, we cannot

use standard NMR techniques to transform the thermal state into that state, but we can map the deviation matrix into such a state, hence the term *pseudopure state*. Several techniques have been developed in NMR to transform the initial deviation matrix into such a state. These techniques include temporal averaging [KCL98] and logical labeling [GC97, CGKL98, DAK00]. In our lab, we usually use the technique of spatial averaging [CFH97, CPH98, KLMT00] which consists of using spatially varying magnetic fields, or magnetic field gradients, to achieve the pseudopure state.

The first step is to keep polarization on only one spin, which can be done by rotating all but one of the spins, say the spin labeled 1, into the plane and using a strong magnetic field gradient. The initial state (up to normalization) is then

$$\rho_1 = Z_1. \tag{2.20}$$

In order to maximize the amount of signal during the readout (Sec. 2.4.4), it is desirable to keep the polarization on the spin of isotope with the largest Larmor frequency (typically ^{1}H).

If we consider a 3-spin molecule for example, applying the encoding part of the sequence of pulses in Fig. 2.3 will transform the initial state into

$$\begin{aligned} \rho_2 &= -X_1X_2X_3 \\ &= -I^+I^+I^+ - I^+I^+I^- - I^+I^-I^+ - I^+I^-I^- \\ &\quad -I^-I^+I^+ - I^-I^+I^- - I^-I^-I^+ - I^-I^-I^-, \end{aligned} \tag{2.21}$$

where $I^+ = |0\rangle\langle 1|$ and $I^- = |1\rangle\langle 0|$ and the spin raising and lower operators. This state comprises all possible coherence terms, where the *coherence number* is defined as the number of raising operators minus the number of lowering operators. The action of applying a magnetic field gradient along the z axis is to modify the Larmor frequency of a molecule depending on its spatial location in the sample, hence effectively creating a spatially dependent z rotation on all the spins. For a given spatial location the angle of rotation will be dependent on the strength of the gradient at that location and the gyromagnetic ratio of the spin. If we use a linearly dependent gradient, the rotation angle on spin i would be $\theta = \alpha z \gamma_i$ for a given proportionality constant α related to the strength of the gradient field. For a specific molecule at a given location z, its state after the gradient is

$$\begin{aligned} \rho_3 &= -e^{-\frac{3i\gamma\alpha z}{2}} I^+I^+I^+ - e^{-\frac{i\gamma\alpha z}{2}} I^+I^+I^- - e^{-\frac{i\gamma\alpha z}{2}} I^+I^-I^+ - e^{\frac{i\gamma\alpha z}{2}} I^+I^-I^- \\ &\quad -e^{-\frac{i\gamma\alpha z}{2}} I^-I^+I^+ - e^{\frac{i\gamma\alpha z}{2}} I^-I^+I^- - e^{\frac{i\gamma\alpha z}{2}} I^-I^-I^+ - e^{\frac{3i\gamma\alpha z}{2}} I^-I^-I^- \end{aligned} \tag{2.22}$$

where we have assumed that $\gamma_1 = \gamma_2 = \gamma_3 = \gamma$ for simplicity, but the generalization is straightforward. This gradient pulse is known as the *labeling gradient*. The two

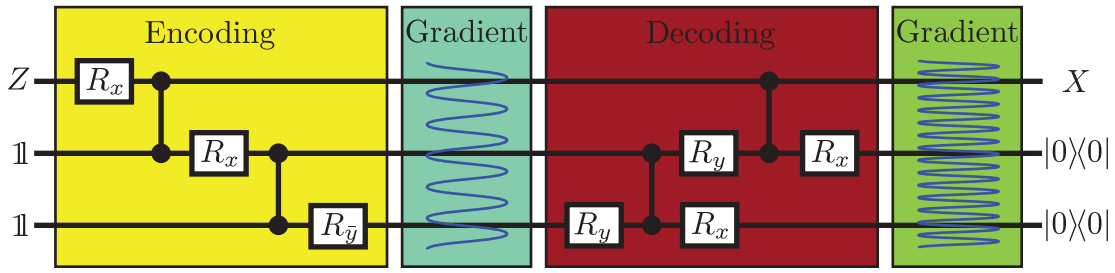

Figure 2.3: Circuit to create a three spin pseudopure state on spin 1 using spatial averaging. The gradients and the decoding part of the circuit are designed to select only the highest coherence terms generated after the implementation of the encoding part.

triple coherence terms actually rotate three times faster than the rest of the terms and we will use this fact to select those maximal coherence terms using the decoding part of the circuit in Fig. 2.3. After the pulse sequence, the state is

$$\begin{aligned}\rho_4 &= e^{-\frac{3i\gamma\alpha z}{2}} I^+|00\rangle\langle 00| + e^{-\frac{i\gamma\alpha z}{2}} I^+|01\rangle\langle 01| - e^{-\frac{i\gamma\alpha z}{2}} I^+|11\rangle\langle 11| - e^{\frac{i\gamma\alpha z}{2}} I^+|10\rangle\langle 10| \\ &\quad -e^{-\frac{i\gamma\alpha z}{2}} I^-|10\rangle\langle 10| - e^{i\frac{\gamma\alpha z}{2}} I^-|11\rangle\langle 11| + e^{\frac{i\gamma\alpha z}{2}} I^-|01\rangle\langle 01| + e^{\frac{3i\gamma\alpha z}{2}} I^-|00\rangle\langle 00|\end{aligned} \tag{2.23}$$

If the last step implements another gradient pulse of three times the strength (or for the appropriate value if the γ's are different) of the labeling gradient but with opposite direction, known as the *unlabeling gradient*, then once averaged over the entire sample, all the terms with remaining spatially dependent z rotation will be dephased, hence yielding the final state

$$\begin{aligned}\rho_{pp} &= I^+|00\rangle\langle 00| + I^-|00\rangle\langle 00| \\ &= X|00\rangle\langle 00|.\end{aligned} \tag{2.24}$$

Such a process is typically called a *gradient echo*.

We should recall that only the deviation density matrix of the state will have the form $X|00\rangle\langle 00|$. Effectively, this means that the state of the entire ensemble of molecules is still in a highly mixed state, but a tiny fraction of the molecules will have all the spins, minus one, pointing up.

The spatial diffusion of the molecules between the labeling and the unlabeling gradients causes an inexact cancelation of the z rotations performed by the labeling gradient, hence some signal loss is expected between the initial state ρ_1 and the final pseudopure state ρ_{pp}. In typical experiments in our lab, we where able to achieve pseudopure states with approximately 92% of the original signal on three spins (Chapter 3). NMR shortcoming for scalability essentially resides in the inability to create large pseudopure states and this fact is addressed in more detail in Sec. 2.5.

2.4.4 Readout process

Another criterion needed to perform quantum information processing using liquid state NMR is a way to perform reliable qubit specific measurements. Due to the ensemble nature of NMR, it is impossible to performed projective measurements. Fortunately, it is often possible to modify an algorithm to allow ensemble measurements [NKL98, SVC00].

From a semi-classical approach, since nuclei have magnetic moments, they create magnetic fields. Therefore, a spin that is in the xy plane will create a magnetic field that rotates around the z axis at the Larmor frequency of the spin. It will in turn induce an oscillating current in the coil used to produce RF bursts by Faraday's principle of magnetic induction. We can therefore detect and measure the current.

From a quantum mechanical approach, if the induction coil is along the (laboratory frame) x axis, it will detect the magnetization of the spins along the x axis, which is given by

$$M_x(t) = \mathrm{Tr}\left[\rho(t)\sum_i X_i\right]. \tag{2.25}$$

In commercially available spectrometers, quadrature detection is performed to infer the y magnetization. Careful analysis of quadrature detection [Lev01] shows that only the (-1)-coherence terms are detected so that the signal measured by the electronics, known as the *free induction decay* (FID), is proportional to the measurement

$$\begin{aligned} FID &\propto \sum_i \rho_{i-}(t) \\ &= \mathrm{Tr}\left[\rho(t)\sum_i I_i^+\right], \end{aligned} \tag{2.26}$$

where ρ_{i-} is the sum of all (-1)-coherence terms in the density matrix that has the coherence on spin i. Due to electronic limitations and the finite excitation bandwidth of the probe (see Sec. 4.6.3), the detection window rarely exceeds 1 MHz, so that normally only single isotopes can be recorded at once. Moreover, through signal processing (see Sec. 5.5.2), it is possible to restrict the window to any bandwidth and any center frequency, within the limitation of signal processing.

An experimental ^{1}H, or proton, FID after applying a $\pi/2$ pulse on the thermal equilibrium state ($T = 293K$) of the acetyl chloride molecule (Sec. 3.6.2) can be seen in red in Fig. 2.4. Since the three protons of the methyl group are magnetically equivalent, they generate the same FID as a single proton. The exponential decay of the signal is due to the dephasing present in NMR systems (see Sec. 2.7.1), which

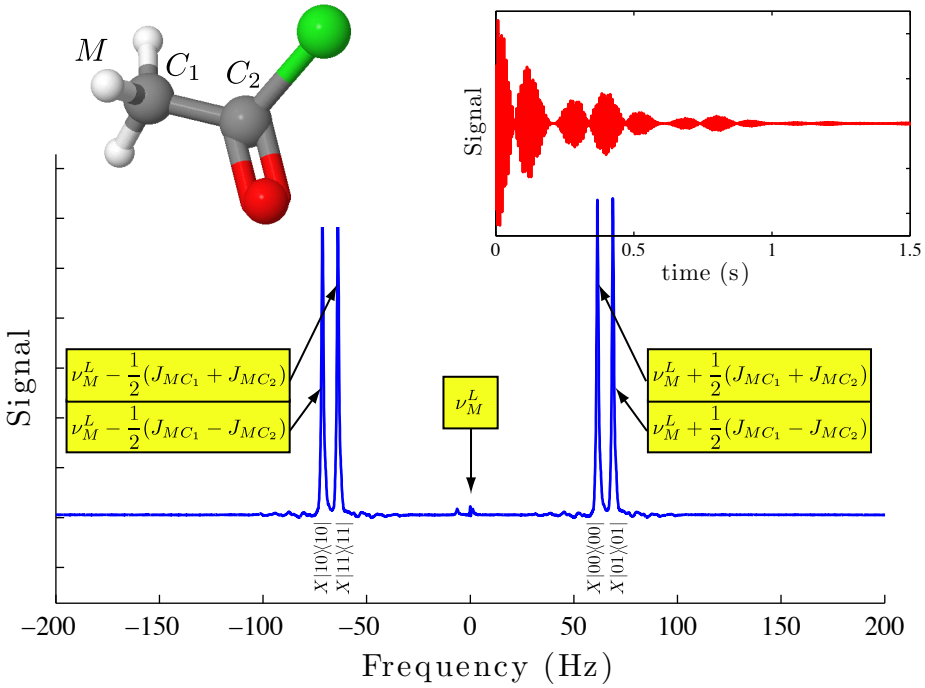

Figure 2.4: Experimental hydrogen FID and spectrum of the acetyl chloride. The spectrum is obtained by Fourier transforming the FID. Each peak of the spectrum can be associated with a computational state of the carbons.

causes the polarization to dampen and ultimately disappear. The polarization then rebuilds along the z axis through the thermalization procedure of amplitude damping (Sec. 2.7.2).

In practice, we study the Fourier transform of the FID which gives us the spectrum in blue in Fig. 2.4. Since the FID contained an exponentially decaying sinusoidal function, the Fourier transform gives complex Lorentzian peaks at each frequency in the FID. Since only the single coherence of the spin (proton here) is detected, it is possible to associate each peak of the spectrum to a state of the proton and the state of the other spins (carbons). In the weak coupling limit, a single coherence term on the proton means that all the other spins must either point up or down. As already discussed in Sec. 2.4.2, the effective magnetic field seen by the proton will depend on the state of the neighboring nuclei. Depending on the signs of the coupling, we can associate the signal of each peak to the state of the rest of the spins. Moreover, the state of the proton is determined through the phase of the real part of the Fourier transform, i.e. absorption Lorentzian (real part) for X (as shown in the figure) and dispersion Lorentzian (imaginary part) for Y.

Since the integral of an dispersion Lorentzian vanishes due to the oddness of the

function, the integral of a single peak s, say the right most peak in the acetyl choride spectrum, will therefore be proportional to the coefficient of the term $X|01\rangle\langle 01|$ in the density matrix at the moment the readout process starts, i.e.

$$s \quad \propto \quad \mathrm{Tr}[\rho(0)(X|01\rangle\langle 01|)]. \tag{2.27}$$

Therefore, in general, the integral of all the resonance peaks of spin i is equivalent to measuring the observable X_i. Any other Pauli observable in the plane, i.e. $\cos\theta X_i + \sin\theta Y_i$ can be measured by multiplying the spectrum by a phase $e^{i\theta}$ first and then integrating. By a clever choice of readout pulse [RLBL05], it is possible to completely reconstruct the original density matrix, which is known as *state tomography* [Jon94, VR89].

With today's technology, such detection is unable to detect single nuclear spins due to their small magnetic moments. This fact alone explains the need for an ensemble of molecules in order to amplify the signal to be recorded by the spectrometer. Even though more sensitive measurement techniques have been developed, such as resistive NMR [DKS+88, KDvK+99, GST+05] which can detect a signal for a few orders of magnitude less molecules. On the other hand, traditional NMR technologies are extremely reliable and permit us to record a spectrum with a high signal-to-noise ratio. Moreover, as far as quantum information processing is concerned, there is no major benefit in reducing the size of the ensemble, unless it can be reduced to a single molecule.

Finally, from Fig. 2.4, it is possible to extract the value of ω_M^L as well as the value of the couplings. By analysis and fitting the thermal spectrum of each nuclei, it is in principle possible to extract all the parameters of the natural Hamiltonian of a molecule. Unfortunately, it is not possible to extract the sign of the coupling from this technique alone and more involved techniques must be used. As a general rule, the one-bond coupling between nuclei with the same sign of gyromagnetic ratio will be positive and negative for that of opposite sign [Lev01]. A good rule of thumb for ^{1}H-^{13}C coupling signs is that it will be positive for an odd number of bonds, but negative for an even number of bounds. This rule remains true for acetyl chloride (Sec. 3.6.2) and crotonic acid [KLMT00], but does not hold for the tri-chloro-ethylene (TCE) [CMP+98].

Finally, as seen in Eq. 2.27, the amount of signal measured during acquisition is proportional to the state before the acquisition, i.e. the deviation matrix. Since the "size" of the thermal deviation matrix is proportional to the Larmor frequency of the nucleus (Eq. 2.17), it is preferable to create a pseudopure state starting with the polarization on a nucleus with high gyromagnetic ratio, such as ^{1}H of ^{19}F, in order to increase the signal-to-noise ratio of the output signal.

2.4.5 Decoherence time

A final requirement for implementing QIP using liquid state NMR is to have qubits that are long-lived. We thus need a system where the time to implement quantum gates is significantly shorter than the decoherence time of the system. As mentioned earlier, the low energies of nuclear spins naturally decouples them from other degree of freedom, hence isolating them well. To a high order, the only decoherence present in NMR arises from interactiosn with the other spins (Sec. 2.7.1) or by energy exchange with the surroundings (Sec. 2.7.2). In liquid state NMR, these processes are associated with a loss of coherence on the order of 100's of ms to seconds, while the longest quantum gates can be implemented on the order of 10's of ms.

These competing timescales allows us to implement 10's and even 100's of gates before decoherence greatly affects the system.

2.5 Summary and critique of NMR QIP

In the previous sections, we have demonstrated the liquid state NMR capabilities to implement quantum information processing tasks. Using nuclear spins as qubits is natural due to the two-level nature of spin-1/2 systems and also due to their weak couplings to the environment, which lead to long coherence times. RF technologies and the natural coupling between the spins allows us, in principle, to perform any unitary operation possible and finally magnetic detection allows us to perform high performance readout.

A major caveat in liquid state NMR, which is unfortunately fatal, is the scalability issues of such a system. As seen in section 2.4.3, there is very little thermal polarization available in the system due to the high temperature of the spins. Using spatial averaging technique to create a pseudopure state, we saw that one must discard all the different polarization combinations except for one, which means that all the peaks in Fig. 2.4 must be dephased and only one kept. As the number of peaks increases exponentially with the number of spins, there is thus an exponential loss of signal occurring during the state initialization procedure. If one chooses the temporal averaging technique instead, an exponential amount of experiment needs to be performed. Therefore, using these two techniques, it is exponentially hard to build larger and larger quantum computer.

L. Schulman and U. Vazirani [SV99] developed an efficient algorithm that could allow scalable NMR quantum information processing. They demonstrated that if the molecules have N spins with initial polarization $\epsilon \approx \frac{\omega}{k_B T} < 1$, it is possible to completely (within error) cool, or polarize, $\mathcal{O}(\epsilon^2 N)$ of them. Unfortunately, on typical available superconducting magnets, $\epsilon \sim 10^{-5}$ at room temperature, so

approximately 10^{12} spins would be needed to initialize a 100-qubit quantum computer. Such a molecule would be impractical due to the physical limitation on the addressability of each spins. Furthermore, such a molecule would require unphysically large coherence time to implement the control sequence necessary for the state initialization. By passing to solid state NMR quantum information processing [BMR+06], it is in principle possible to boost the initial polarization by cooling the sample to low temperature or by performing dynamic nuclear polarization [AG82]. Such an increase in the initial polarization to, say, $\epsilon = 0.1$ would permit us to create 100 fully polarized qubits using molecules with "only" 10^4 nuclei. Note that since Schulman and Vazirani's proposal, other type of algorithmic cooling protocols have been introduced, such as the heat-bath algorithmic cooling [BMR+02, BMR+05, SMW05, Kay07].

Another critique of NMR quantum information processing has to do with whether or not entanglement is present in the system. Because of the highly mixed nature of the state of the system at room temperature, the state will always be provably separable up to about 14 qubits [BCJ+99]. Therefore, even though entangling operations are performed, no entanglement is present in the system. For larger molecule, it is unfortunately unclear if entanglement will be present or not.

From the above argument, one could argue that none of the implemented algorithms in NMR was a demonstration of quantum computation. On the other hand, it is still unknown if entanglement is necessary to outperform classical computation. If we are computing on pure states, not only it is known that entanglement is necessary [JL03], but "large enough" entanglement in needed [Vid03]. The situation becomes more complex when considering mixed states. A typical example is the DQC1 algorithm [KL98], specifically designed for NMR-type systems, in which it is shown that a highly mixed state can be used to outperform any known classical algorithm, even though there is no entanglement present in the system.

2.6 Advance control techniques

2.6.1 Efficient error estimation and optimization

Pulse decomposition

As argued in Sec. 2.4.2, a major source of pulse errors are off resonance and coupling errors. Even though the use of Gaussian soft pulses permits us to perform spin selective rotation in a faster way, there still can be significant dynamics in the system. During a pulse, coupling errors occur on the targeted spins since the

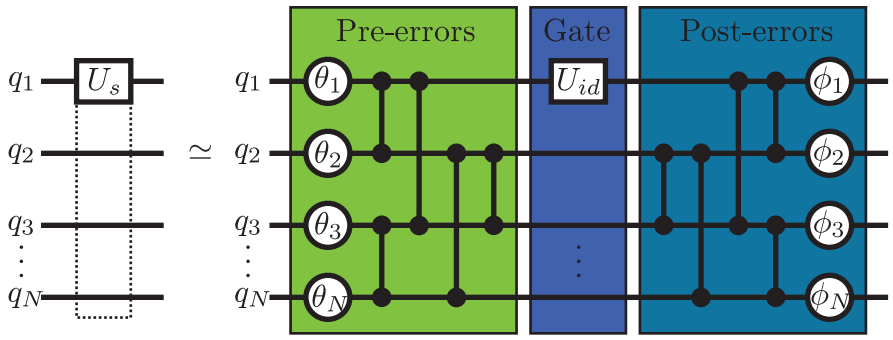

Figure 2.5: Representation of a realistic selective pulse by the ideal transformation and pre- and post-coupling and phase errors. In the limit of small errors, they can be efficiently estimated through single and pairwise spin simulations.

coupling Hamiltonian to the other spins does not commute with the control Hamiltonian, hence introducing errors on all the spins coupled to the target. Moreover, the other spins still evolve under the Zeeman Hamiltonian and the coupling Hamiltonian to the other non-targeted spins. Finally, as shown in Sec. 2.4.2, the action of pulsing on one spin will induce an extra phase shift on the other spins through the transient Bloch-Siegert effect.

Fortunately, it is possible to estimate and compensate for these errors by evaluating the first-order coupling and phase errors generated by a pulse [RNL+08]. This is done by assuming that the real pulse can be decomposed as the ideal pulse preceded and followed by phase and coupling errors (see figure 2.5). Since the error terms all commute with each other, they can be estimated using pairwise spin simulations, which requires a reasonable amount of computational resources. For a selective pulse, say on spin 1 of a N spin system, we know the ideal unitary evolution should be

$$U = V_1^{id} \otimes \mathbb{1}_2 \otimes \ldots \otimes \mathbb{1}_N. \tag{2.28}$$

where V_1^{id} is a rotation of the first spin. In practice, we keep track of all the evolution in a fixed reference frame (not necessarily that of the pulse) so that in general, the simulated gate has the form

$$U_s = U_1^{id} \otimes U_2^{id} \otimes \ldots \otimes U_N^{id}. \tag{2.29}$$

where U_1^{id} is related to V_1^{id} by a mere change of frame operation (z rotation) and $U_2^{id}, \ldots, U_N^{id}$ are the z-rotations corresponding to changing from the spins own rotating frame to the fixed rotating frame.

The zeroth order effect of the pulse on each spin is calculated by simulating the single spin terms in the full Hamiltonian, which gives a set of N single spin zeroth

order operator $U_1^{(0)}, \ldots, U_N^{(0)}$. At this point, it is assumed that only the spins of the same isotope as the targeted spin will be affected by the RF pulse. By modeling $U_i^{(0)} = U_i^{post} U_i^{id} U_i^{pre}$, where U_i^{pre} and U_i^{post} are z rotations, we can efficiently extract the pre and post zeroth order phase errors arising from the Bloch-Siegert and off-resonance effects. To extract the angle of each rotation, we optimize the function

$$\Phi \quad = \quad \text{real}\left[\text{Tr}(U_i^{(0)\dagger} U_i^{post} U_i^{id} U_i^{pre})\right]. \tag{2.30}$$

This function is sensitive to the global phase of the unitaries in order to permit a successful recombination of all the single spin operations into an N spin operation. The first order effect can now be calculated by simulating the Hamiltonian for all the pairs of spins and by finding the optimal pre and post phase and coupling errors using the same optimization procedure as for the zeroth order. Because most of the phase errors are already accounted for from the zeroth order approximations, only the difference in the found values to the zeroth order is added.

By performing pairwise simulations only, spin-mediated coupling between qubits is neglected, i.e. coupling between spin 1 and 3 through spin 2. On the other hand, we expect such a coupling to be minimal. By making the assumption that the phase and coupling errors approximately commute with the RF Hamiltonian, we are therefore assuming that the coupling between the targeted spin and the rest of the system is small during the time of the pulse, such that $\tau \ll \frac{1}{J}$. Since the direct coupling is small, we can also assume the spin-mediated coupling to be negligible. Therefore, the pairwise simulation will capture most of the errors introduced during a pulse.

We should mention that such a scheme is only valid for simple, spin selective pulses. It can be generalized if we consider subsystems of spins and extract the error by performing subsystem simulation [RNL+08] . In all cases, pairs of spins, or subsystems, are low dimensional and there is only a polynomial amount of pairs of spins (or subsystems). Therefore the above decomposition is efficient to compute and give an accurate representation of the pulse (with fidelity higher the 99.99% for the systems we normally use).

Once we have a representation for each pulse, we can use them as building blocks to optimize pulse sequences. The phase errors can be tracked through phase tracking and corrected by modifying the phase of pulses. Since the two-qubit gates are performed through natural ZZ evolution, the coupling errors can be either canceled through a cleverly chosen refocusing scheme or by absorbing the extra couplings during delays of free evolution.

Sequence compiler

All the techniques described so far to control a system (phase tracking, refocusing, virtual π pulses, coupling error absorbtion) have been implemented into a sequence compiler which takes as input a series of control commands and outputs a pulse sequence readable by the spectrometer.

The precompiled files comprise commands to be implemented and are described as a series of computational pulses, couplings and refocusing pulses. Before and after each computational pulse, the compiler sets goals for the couplings between the spins depending on previous commands received. By taking into account the coupling errors introduced by previous and subsequent pulses, it will optimize delays before and after the location of the refocusing pulses such that the coupling goals are attained with as little error accumulation as possible. It will also perform the phase tracking and virtual π cancellation by modifying the phase of the pulses accordingly.

The main advantages of using such a scheme is for the phase and coupling tracking. By tracking the phase of all the spins, chemical shift evolution does not need to be refocused during a coupling evolution, e.g. to implement a CNOT. The same argument applies for the couplings. For example, if the goal of a coupling on spin 1 is set to 0 before a pulse, only couplings to spin 1 have to be refocused, e.g. 0 coupling between 1 and 2 and between 1 and 3. The coupling between spin 2 and 3 does not need to be refocused and can be dealt with later.

Such a local optimization scheme is efficient since only pairs of qubits are considered.

2.6.2 Optimal control for strongly coupled spins

In some cases, spins are so strongly coupled that the approximations of phase and coupling errors used above is imprecise. In those cases, another technique can be used: strongly modulating pulses designed using numerical optimal control techniques [FPB+02, KRK+05]. For systems containing roughly less than ten qubits, we can find extremely high fidelity and robust control by applying optimal control principles. Quantum optimal control has been used for some time in the context of driving chemical reactions with shaped laser pulses [RdVRMK00]. There, the goal is to maximize the transfer from a known initial state to a known final state. In the context of quantum computing, we do not necessarily know what the input state will be, and so we must find unitary gates which will work correctly for any input state.

The Hamiltonian at any point in time can be written down as

$$\mathcal{H}_{tot}(t) \quad = \quad \mathcal{H}_{nat} + \mathcal{H}_{rf}(t, \vec{\alpha}), \tag{2.31}$$

where, as before, the (time-dependent) RF Hamiltonian is controlled via parameters $\vec{\alpha}$ (amplitude, phase and frequency of the pulse). The task is to find the sequence of control fields that will produce the correct unitary evolution. Using a numerical search algorithm, we can find control sequences with fidelities as high as 0.999999 on small systems.

By discretizing the parameters α into small intervals of constant amplitude, phase and frequency, it is possible to exactly compute the propagator of a given pulse by exponentiating the time-independent Hamiltonian (in the rotating frame of the pulse) of each interval and multiplying the unitaries together to obtain the simulated unitary U_{sim}. We can then compare it to the desired unitary U_{goal} with the Hilbert-Schmidt measure to obtain a fitness function

$$\Phi = \left| \mathrm{Tr} \left(U_{sim}^{\dagger} U_{goal} \right) \right|^2 . \tag{2.32}$$

Such a measure of gate fidelity is equivalent to measuring the state fidelity of the unitary $U_{sim}^{\dagger} U_{goal}$ ($= \mathbb{1}$ ideally) averaged over all input states [FPB+02]. By performing an optimization routine on Φ, we can achieve high gate fidelities, given that the Hamiltonian is well known. If there are uncertainties about either the natural or the RF Hamiltonian, or both, it is possible to optimize Φ over a distribution of Hamiltonians to make the pulse robust to the uncertainties in these parameters.

The first implementation of such an algorithm for QIP purposes was performed by Fortunato et al. [FPB+02], where they used a MATLAB built-in simplex search algorithm [Chv83] and cleverly chosen penalty functions on Φ, to avoid excessively high power for example. Inspired by optimal control technique, Khaneja et al. developed an algorithm in which the control parameters are modified in a way to move the fitness function in the steepest ascent direction, hence its name: GRadient Ascent Pulse Engineering, or GRAPE. They showed that the derivative of Φ with respect to the control parameter can be approximated solely from the information already acquired from the simulations, The derivative of Φ will depend on the derivative of the unitary operators at each time interval with respect to the control parameters. They showed that this derivative can be estimated by

$$\frac{\partial U_j}{\partial u_i(j)} \quad \approx \quad -i \Delta t \mathcal{H}_i U_j, \tag{2.33}$$

where Δt is the time of each interval, U_j is the propagator of the j^{th} interval and $u_i(j) (i = \{x, y\})$ is the nutation frequency of the spins due to the RF field along the

x or y direction during the time interval j. Notice that this differentiation does not involve finite differencing, nor extra matrix exponentiation, hence can be evaluated from matrices already calculated. We can connect to our previous pulse notation in Eq. 2.4 by $(\omega^{nut})^2 = u_x^2 + u_y^2$ and $\tan\phi = \frac{u_y}{u_x}$. From this information, it is possible to calculate the gradient of the fitness function and change the value of the control parameters accordingly.

Since each optimization step requires us to calculate the value of the propagator only once, such a search algorithm is much faster and thus allows for a greater number of time intervals to be considered, which can greatly improve the quality of the pulses and allows the identification of smoothly varying pulses, which are more spectrometer friendly (Sec. 4.6.3).

Strongly modulated pulses drive the state of the spins on a non-intuitive path on the Bloch sphere and can make use of all the dynamics of the system, i.e. chemical shift evolution, Bloch-Siegert shift, direct coupling, indirect coupling, etc. On the other hand, some constraints on the length of the pulses are imposed due to the natural Hamiltonian and the action of the desired unitary. For example, a selective pulse should take on the order of the inverse of the smallest chemical shift between the targeted spin and the others. A CNOT is also expected to take of the order $\tau \sim \frac{1}{2J}$.

Due to the nonintuitive dynamics of GRAPE pulses, the approximation done in Sec. 2.6.1 may break down and lead to incorrect representations of the pulse due to the use of the full dynamics. Fortunately, GRAPE can be used to find pulses on subsystems of strongly coupled spins, that are weakly coupled with each other. The effect of the other subsystems can then be approximated by pairwise subsystem simulations as described in 2.6.1 [RNL+08].

2.7 Noise and decoherence in NMR

2.7.1 Dephasing

One of the major sources of noise in NMR, as well as in many other quantum computing devices, is the interaction with the surroundings (see Capter 3 for a mathematical argument), which in turn causes *dephasing*. Dephasing, or *transverse relaxation*, is the phenomenon associated with the decay of the coherence terms (off-diagonals) in the density matrix. In NMR, since the signal is due to the ensemble of spins, a coherence term which lasts forever would require all the same spins of the different molecules to precess about the magnetic field at exactly the same rate. As previously mentioned, the frequency of a single spin depends on the local magnetic field, which depends on the external field, and on the field created by the

surrounding spins. Due to rapid tumbling, the average field over time is the same, but does vary across the sample at a particular given time. This instantaneous variation causes the identical spins of all the molecules to slowly desynchronize and therefore lose coherence across the sample.

From a more quantitative approach, dephasing noise Λ_d can be understood as small random z rotation across the sample, so that the state of the system can be described by a statistical average over a distribution of rotation angles $q(\theta)$:

$$\Lambda_d(\rho) = \int d\theta q(\theta) e^{-i\frac{\theta}{2}Z} \rho e^{i\frac{\theta}{2}Z}. \tag{2.34}$$

By directly evaluating the above integral, we find that

$$\begin{aligned} \rho &= \begin{pmatrix} \rho_{00} & \rho_{01} \\ \rho_{10} & \rho_{11} \end{pmatrix} \\ &\to \begin{pmatrix} \rho_{00} & \Gamma\rho_{01} \\ \Gamma^*\rho_{10} & \rho_{11} \end{pmatrix}, \end{aligned} \tag{2.35}$$

where $\Gamma = \langle e^{-i\theta} \rangle = \int d\theta q(\theta) e^{-i\theta}$. In liquid state, the environment is assumed to be isotropic, that is, the distribution $q(\theta)$ is symmetric about 0, so that $\Gamma = \langle \cos\theta \rangle$.

As already seen in Sec. 2.4.4, the FID envelope of a spin decays exponentially, and hence the single coherence terms do as well. The exponential decay for the coherences is true for any system with a Markovian environment [Kin63]. In liquid state NMR, the environment consists of the deuterated solvent and the other molecules. Due to the rapid tumbling and the high temperature of the spin bath, the environment is therefore highly incoherent and the memory effect of the environment can be neglected (Markovian). Therefore,

$$\Gamma = e^{-\gamma_2 t} = e^{-\frac{t}{T_2}}, \tag{2.36}$$

where we have defined the dephasing decay rate and decay time constant $\gamma_2^{-1} = T_2$.

From a different approach, if we explicitly expand and multiply the z rotations, we can also evaluate Eq. 2.34 as

$$\Lambda_d(\rho) = (1-p)|\psi\rangle\langle\psi| + pZ|\psi\rangle\langle\psi|Z, \tag{2.37}$$

where $p = \int d\theta q(\theta) \sin^2\frac{\theta}{2}$ is the probability of the state undergoing a phase flip. Therefore, dephasing can also be described by the Kraus operators

$$A_0 = \sqrt{1-p}\mathbb{1}, \qquad A_1 = \sqrt{p}Z. \tag{2.38}$$

By direct evaluation and comparison, we find that

$$p = \frac{1 - e^{-\gamma_2 t}}{2}. \tag{2.39}$$

We should note that dephasing channels are also described in the literature [NC00] using the Kraus operators

$$A'_0 = \begin{pmatrix} 1 & 0 \\ 0 & \sqrt{1-p'^2} \end{pmatrix} \qquad A'_1 = \begin{pmatrix} 0 & 0 \\ 0 & p' \end{pmatrix}, \tag{2.40}$$

for $p'^2 = 1 - e^{-\frac{t}{T_2}}$.

The uncorrelated dephasing of multiple spins can be evaluated by concatenating either the Kraus operators (as in Sec. 1.3) or by evaluating the direct integral of the random rotations, which gives, for example, a double spin coherence, either a zero or double coherence, to decay at the sum of the decay rate, e.g.

$$\Lambda_d(|00\rangle\langle 11|) \quad \rightarrow \quad e^{-\gamma_2^{(1)}t - \gamma_2^{(2)}t}|00\rangle\langle 11|. \tag{2.41}$$

If we use the integral approach, it is possible to evaluate the effect of correlated noise. If two spins have a correlated rotation angle distribution $q(\theta_1, \theta_2)$, the decay of their joint state will be evaluated as

$$\Lambda_d(\rho) \quad = \quad \int d\theta_1 d\theta_2 q(\theta_1, \theta_2) e^{-\frac{i}{2}(\theta_1 Z_1 + \theta_2 Z_2)} \rho e^{\frac{i}{2}(\theta_1 Z_1 + \theta_2 Z_2)}. \tag{2.42}$$

Even though dephasing of the coherence terms does not involve any energy exchange, it still increases the entropy of the system and since the lost of coherence is due to a Markovian environment, it is an irreversible process. On the other hand, since the dephasing of spins arises through the fluctuations of the local magnetic field created by the surrounding spins, it is also expected that inhomogeneities in the external magnetic field will also cause dephasing. Fortunately, this dephasing can be refocused using a series of π pulses. If the spins dephase due to the magnetic field inhomogeneities for a time $\tau/2$, then applying a π pulse will flip all the spins with respect to that axis and create a motion reversal of the spins. Therefore, the spins will undo their precession and evolve back to their original phase. This will work assuming the inhomogeneities are the same from t=$\tau/2$ to $t = \tau$. This is an example of incoherent noise (Sec. 1.4). In reality, the inhomogeneities fluctuate in time, but can still be refocused by applying pulses at shorter intervals during which the inhomogeneities are almost constant. Such a sequence is called a Carr-Purcell-Meiboom-Gill (CPMG) sequence [CP54, MG58].

Using the CPMG sequence, it is possible to measure the intrinsic value of T_2 by preparing the spin of a nuclei in the plane, refocusing the field inhomogeneities and recording the final signal. By plotting the signal as a function of time and fitting an exponential, one obtains the decay constant.

These two different dephasing phenomenon will induce two different time constants. T_2 is associated with the decay of the coherence due to the intrinsic irreversible dephasing, while T_2^* is associated with the dephasing from the unrefocused inhomogeneities. When recording an FID as in Fig. 2.4, the spins are typically not refocused so that the FID decays at the T_2^* rate. We can thus extract the value of T_2^* from the decay envelope of the FID or from the width of the resonant peak of the spectrum.

2.7.2 Amplitude damping

Dephasing is not the only source of decoherence in NMR. Amplitude damping, also known as the *longitudinal relaxation* or the spin-lattice relaxation, is the process through which the state of the nuclei returns to the thermal state given in Eq. 2.17. During the RF control sequence, energy is exchanged between the RF field and the nuclei to create coherences. Over time, this extra energy is then exchanged back to the environment causing the spins pointing down (high energy state) to emit energy and relax to the up state (low energy). Probabilistic laws obliged, the spins can also absorb energy from the environment, creating a up-down flip. The rethermalization of the system is achieved when the population of up ($p_\uparrow$) and down ($p_\downarrow$) states are in thermal equilibrium, i.e.

$$p_\uparrow - p_\downarrow \simeq \frac{\omega}{k_B T} \tag{2.43}$$

In an inversion recovery experiment, the thermal state of each spin is excited by a π pulse, hence inverting the population of up and down states. After letting the system relax for a time t, the spins are tipped into the plane and the signal recorded. By plotting the signal over time, one measures that the magnetization along the z axis relaxed according to

$$M_z(t) = M_{z,eq}(1 - 2e^{-\frac{t}{T_1}}), \tag{2.44}$$

where we have defined the longitudinal decay rate and time constant $\gamma_1^{-1} = T_1$. In a more general approach, if the initial magnetization was $M_z(0)$, the recovery process follows

$$M_z(t) = M_{z,eq} - (M_{z.eq} - M_z(0))e^{-\frac{t}{T_1}}. \tag{2.45}$$

A careful analysis of the master equation of longitudinal relaxation [BP02] leads to four Kraus operators [NC00] :

$$\begin{aligned} A_0 &= \sqrt{p}\begin{pmatrix} 1 & 0 \\ 0 & \sqrt{1-\eta} \end{pmatrix} \qquad A_1 = \sqrt{p}\begin{pmatrix} 0 & \sqrt{\eta} \\ 0 & 0 \end{pmatrix} \\ A_2 &= \sqrt{1-p}\begin{pmatrix} \sqrt{1-\eta} & 0 \\ 0 & 1 \end{pmatrix} \qquad A_3 = \sqrt{1-p}\begin{pmatrix} 0 & 0 \\ \sqrt{\eta} & 0 \end{pmatrix}, \end{aligned} \tag{2.46}$$

where $p \simeq \frac{1}{2}\left(1 - \frac{\omega}{2k_B T}\right)$ and $\eta = 1 - e^{-\frac{t}{T_1}}$. Intuitively, operators A_0 and A_1 describe the down-up flip while A_2 and A_3 the up-down flip. The probability of each flip p and $1-p$ is related to the thermal equilibrium of each population. By calculating the effect of the above operators on a density matrix, we see that amplitude damping also causes the coherence terms to decay, i.e.

$$\Lambda_a(\rho) = \begin{pmatrix} (\rho_{00} - \bar{\rho}_{00})e^{-\frac{t}{T_1}} + \bar{\rho}_{00} & \rho_{01}e^{-\frac{t}{2T_1}} \\ \rho_{10}e^{-\frac{t}{2T_1}} & (\rho_{11} - \bar{\rho}_{11})e^{-\frac{t}{T_1}} + \bar{\rho}_{11} \end{pmatrix}, \tag{2.47}$$

where $\bar{\rho}_{00}$ and $\bar{\rho}_{11}$ are the up and down equilibrium population.

2.7.3 General noise in NMR

From the two previous sections, we saw the effect of phase damping and dephasing separately, hence defining the decay time T_1 and T_2. In reality, both processes occur simultaneously. As shown in Appendix B, the complete relaxation of a single spin in time can be described as

$$\Lambda(\rho) = \begin{pmatrix} (\rho_{00} - \bar{\rho}_{00})e^{-\frac{t}{T_1}} + \bar{\rho}_{00} & \rho_{01}e^{-\frac{t}{T_2}} \\ \rho_{10}e^{-\frac{t}{T_2}} & (\rho_{11} - \bar{\rho}_{11})e^{-\frac{t}{T_1}} + \bar{\rho}_{11} \end{pmatrix}. \tag{2.48}$$

Since the decay of the off-diagonal elements is due to *both* dephasing and amplitude damping, the experimentally measured T_2 values thus correspond to the sum of the decay rate i.e. $T_2^{-1} = \frac{1}{2}\gamma_1 + \gamma_2$. Upon measuring the value of T_1 from an inversion recovery experiment, it is thus possible to infer the decay rate due to dephasing alone. Moreover, if dephasing would be completely absent from the system, the decay of the coherence would be only due to amplitude damping. We thus obtain a bound for the maximum value for T_2, i.e. $T_2 \leq 2T_1$. In real NMR system, field fluctuations and ensemble effects prevent the achievement of this bound, and we often have the situation $T_2 < T_1$ and $T_2^* \ll T_1$.

Chapter 3

Quantum error correction and noise correlation

3.1 The importance of knowing the behavior of the noise

Recall that quantum computation uses the properties of quantum mechanics to perform information processing and computation. Unfortunately, quantum mechanical systems are extremely fragile and tend to quickly lose their quantum nature because of noise and decoherence. Over time, decoherence pushes the quantum state of a system to decohere into a classical probabilistic mixture of quantum state. From a quantum computing point of view, this means that long and complex computations are extremely difficult to achieve and decoherence affects the carefully designed quantum algorithm to yield a random and often useless answer. Fortunately, the theory of quantum error correction (QEC) has been developed to circumvent this problem [Sho95, Ste96, BDSW96, KL97]. The basic idea of QEC is to encode the quantum information of k logical qubits into n physical qubits. The encoding is specifically designed so that once the encoded state is affected by the decoherence, it is still possible to recover the initial information through a series of measurements and quantum operations. The *threshold theorems* [ABO97, Kit97b, KLZ98] stipulate that if the decoherence, or the noise level, present in the system falls below a certain threshold value for given assumptions, arbitrarily long and complex quantum computation is possible. A detailed example of a QEC code will be given in Section 3.5.

One of the standard assumptions in developing a QEC code is that the noise is independent, or uncorrelated (Sec. 1.3), so that the probability of an error happening on a given qubit does not depend on the probability of an error happening

on one of the other qubits. Clearly, knowing if the noise present in a given system is correlated or uncorrelated is of crucial importance to performing precise, robust and reliable QIP. As a matter of fact, correlation in the noise can increase the probability of multi-qubit errors and therefore, jeopardize a computation scheme developed for a wrong threshold value.

The presence of noise correlation can be deduced by performing quantum process tomography (QPT) [THL+95, CN97, PCZ97], which is a method of determining for example, all the coefficients of the χ matrix (Sec. 1.2.2). Although QPT gives a complete description of the decoherence, it is also not scalable as the χ matrix has $\mathcal{O}(4^{2n})$ parameters and takes the same order of experiments to measure all these value [CCL01, WHE+04]. When the mechanism of the noise affecting a system is well understood (as in NMR [McC87]), complete QPT is often not needed to extract the parameters of the noise model and partial, but crucial, information can be extracted using scalable techniques.

In this section, we will demonstrate how QEC can be used, not to reduce decoherence, but to probe the correlations between the transverse relaxation of two homonuclear spins in liquid-state NMR (i.e. a T_2 relaxation). An experimental value was extracted from a three-spin processor, which was in accordance with the value extracted from a standard double coherence decay technique.

3.2 The noise model

As mentioned in the Section 2.7, the major source of decoherence in liquid state NMR is transverse and longitudinal relaxation (dephasing and amplitude damping). In a variety of molecules, especially molecules chosen for NMR QIP, the T_2 time-scale will be much shorter then T_1. Moreover, since the decay of the coherence terms of the density matrix are more affected by the dephasing than by the amplitude damping (γ_2 vs. $\frac{\gamma_1}{2}$), it is reasonable assume that for a short period of time, only dephasing is present in the system.

We mentioned that both intramolecular and intermolecular dipolar coupling average to zero on the NMR time scale due to isotropic molecular rotation. In high magnetic fields, the dipolar Hamiltonian has the from

$$\mathcal{H}_D = \frac{D_{ij}}{2}(1 - 3\cos^2\theta_{ij})(2Z_iZ_j - X_iX_j - Y_iY_j), \tag{3.1}$$

where θ_{ij} is the angle between $\vec{r}_{ij}$ and the z axis. D_{ij} is called the dipolar constant and is typically of the order of kHz. It depends on the magnetic moment of the spins and decays as r_{ij}^{-3} (see Appendix A).

Even though the $XX+YY$ part of the dipolar Hamiltonian averages to zero to high order in perturbation theory, the ZZ part can still create transverse relaxation due to the ensemble effect of neighboring molecules in the sample [Lev01]. As a simple example, consider a single qubit interacting with a single spin environment for a given time, yielding an interaction of strength b. Applying the standard assumption that the state of the system ρ_s, and the environment $\rho_{\mathcal{E}}$, are initially separable, i.e.

$$\rho = \rho_s \otimes \rho_{\mathcal{E}}, \tag{3.2}$$

the final state of the system is given by the partial trace of the global state over the environment, which gives

$$\begin{aligned}
\Lambda(\rho) &= \mathrm{Tr}_{\mathcal{E}}\left[e^{-ibZZ_{\mathcal{E}}}\rho_s \otimes \rho_{\mathcal{E}} e^{ibZZ_{\mathcal{E}}}\right] \\
&= \langle 0|_{\mathcal{E}} e^{-ibZZ_{\mathcal{E}}}\rho_s \otimes \rho_{\mathcal{E}} e^{ibZZ_{\mathcal{E}}}|0\rangle_{\mathcal{E}} \\
&\quad + \langle 1|_{\mathcal{E}} e^{-ibZZ_{\mathcal{E}}}\rho_s \otimes \rho_{\mathcal{E}} e^{ibZZ_{\mathcal{E}}}|1\rangle_{\mathcal{E}} \\
&= \langle 0|\rho_{\mathcal{E}}|0\rangle e^{-ibZ}\rho_s e^{ibZ} + \langle 1|\rho_{\mathcal{E}}|1\rangle e^{ibZ}\rho_{ini}e^{-ibZ},
\end{aligned} \tag{3.3}$$

We see that the qubit will undergo a phase rotation of $\frac{b}{2}$ with probability $|\langle 0|\rho_{\mathcal{E}}|0\rangle|^2$ and a rotation of $-\frac{b}{2}$ with probability $|\langle 1|\rho_{\mathcal{E}}|1\rangle|^2$, hence yielding uncertainty in the information about the phase of the state, thus giving rise to transverse relaxation.

In a more general case, consider a single spin interacting with an environment $\mathcal{E}$ of N spins. The propagator of the dipolar coupling between the spin and the environment is given by

$$\begin{aligned}
U &= \prod_{j\in\mathcal{E}} e^{-ib_j ZZ_j} \\
&= e^{-i\sum_j b_j ZZ_j},
\end{aligned} \tag{3.4}$$

where b_j is the interaction strength between the system spin and the j^{th} spin of the environment for a certain amount of time. Once we trace over the environment degrees of freedom, the final state of the single spin is

$$\begin{aligned}
\Lambda(\rho) &= \sum_{a\in\{0,1\}^N} \langle a|e^{-i\sum_j b_j ZZ_j}\rho_{ini}\otimes\rho_{\mathcal{E}}e^{i\sum_j b_j ZZ_j}|a\rangle \\
&= \sum_{a\in\{0,1\}^N} \langle a|\rho_{\mathcal{E}}|a\rangle e^{-i\xi_a Z}\rho_{ini}e^{i\xi_a Z} \\
&= \sum_{a\in\{0,1\}^N} \langle a|\rho_{\mathcal{E}}|a\rangle e^{-i\xi_a Z}\rho_{ini}e^{i\xi_a Z},
\end{aligned} \tag{3.5}$$

where we have defined $\xi_a = \sum_m b_m(-1)^{a_m}$, a_m being the m^{th} digit of a. In liquid state NMR using low viscosity solvents, we can assume the environment to be

isotropic. With this in mind, it is now possible to modify Eq. 3.5 by using $a = 0^{\otimes N}$ and by changing the sum over a to a sum over a symmetric and isotropic distribution of $\vec{b} = (b_1 \dots b_N)$. In the limit of large N, this sum becomes an integral. Moreover, in room temperature liquid state NMR, the deviation of the thermal state from the completely mixed state is of the order of 10^{-4}, so that $\langle a|\rho_{\mathcal{E}}|a\rangle \simeq \frac{1}{2^N}$. We finally have

$$\Lambda(\rho) = \int d\alpha q(\alpha) e^{-i\alpha Z} \rho_{ini} e^{i\alpha Z}, \tag{3.6}$$

where $\alpha = \sum_m b_m$ and $q(\alpha)$ is the distribution of α which takes into account the distribution of $\vec{b}$. By making the connection between the above equation and Eq. 2.34, we have physically argued the presence of dephasing in liquid state NMR due to dipolar interaction.

To determine more precisely the effect of the dephasing, we need to concentrate on the distribution of $\vec{b}$. First, all b_j's have the same distribution, and their values are given by the dipolar coupling to the single spin and the time of interaction. From Eq. 3.1, the strength of the couplings has an angular and a radial dependence. Since the environment is isotropic, the environment spins do not have a preferred alignment with the qubit. Therefore, by averaging the angular dependence, we conclude that the average value of b_j's must vanish. Since N is very large and by the summation property of α, we can invoke the central-limit theorem [Fel45, Spi92] and conclude that $q(\alpha)$ is well approximated by a Gaussian distribution with zero average, i.e.

$$q(\alpha) = \frac{1}{\sqrt{2\pi}} e^{-\frac{\alpha^2}{2\sigma^2}}, \tag{3.7}$$

with a given variance σ.

For the completely general case, i.e. for a system with M spins, the same argument applies and the model generalizes to

$$\Lambda(\rho) = \int d\vec{\alpha} q(\vec{\alpha}) e^{-i\vec{\alpha}\cdot\vec{Z}} \rho_{ini} e^{i\vec{\alpha}\cdot\vec{Z}}, \tag{3.8}$$

where $\vec{\alpha} = (\alpha_1, \dots, \alpha_M)$, $\vec{Z} = (Z_1, \dots, Z_M)$ and $p(\vec{\alpha})$ is the multivariate Gaussian distribution [Ton90]

$$q(\vec{\alpha}) = \frac{1}{\sqrt{(2\pi)^M |\hat{\Sigma}|}} e^{-\frac{1}{2}\vec{\alpha}^T \cdot \hat{\Sigma}^{-1} \cdot \vec{\alpha}}. \tag{3.9}$$

$\hat{\Sigma}$ is the covariant matrix, or the correlation matrix, and $|\Sigma|$ the determinant of the correlation matrix. This matrix takes the form

$$\hat{\Sigma}_{ii} = \langle \alpha_i^2 \rangle = \sigma_i^2 \tag{3.10}$$

$$\hat{\Sigma}_{ij} = \langle \alpha_i \alpha_j \rangle, \tag{3.11}$$

where σ_i^2 is the variance of α_i. From the Cauchy-Schwartz inequality, we know that

$$|\langle \alpha_i \alpha_j \rangle|^2 \leq \langle \alpha_i^2 \rangle \langle \alpha_j^2 \rangle, \tag{3.12}$$

so that we can write

$$\langle \alpha_i \alpha_j \rangle \quad = \quad c_{ij} \sigma_i \sigma_j, \tag{3.13}$$

where $-1 \leq c_{ij} \leq 1$ is the correlation factor between α_i and α_j, which is defined as

$$c_{ij} \quad = \quad \frac{\langle \alpha_i \alpha_j \rangle}{\sqrt{\langle \alpha_i^2 \rangle \langle \alpha_j^2 \rangle}}. \tag{3.14}$$

3.2.1 Single qubit case

In the case of a single qubit, the situation is simple due to the lack of correlation factors, and the fact that $\Sigma = \langle \alpha^2 \rangle = \sigma^2$ is only a scalar. In the computational basis, the density matrix of a single qubit is written as

$$\rho = \sum_{k,l=\{0,1\}} \rho_{kl} |k\rangle\langle l|. \tag{3.15}$$

The evolution of each terms goes as

$$\begin{aligned} \Lambda(|k\rangle\langle l|) \quad &= \quad \frac{1}{\sqrt{2\pi\sigma^2}} \int d\alpha e^{-\frac{\alpha^2}{2\sigma^2}} e^{-i\alpha Z} |k\rangle\langle l| e^{i\alpha Z} \\ &= \quad \begin{cases} \frac{1}{\sqrt{2\pi\sigma^2}} \int d\alpha e^{-\frac{\alpha^2}{2\sigma^2}} |k\rangle\langle l| & \text{If } k = l, \\ \frac{1}{\sqrt{2\pi\sigma^2}} \int d\alpha e^{-\frac{\alpha^2}{2\sigma^2}} e^{\pm 2i\alpha} |k\rangle\langle l| & \text{If } k \neq l. \end{cases} \\ &= \quad \begin{cases} |k\rangle\langle l| & \text{If } k = l, \\ e^{-2\sigma^2} |k\rangle\langle l| & \text{If } k \neq l \end{cases}. \end{aligned} \tag{3.16}$$

For a single qubit, such a noise model will thus affect the state as

$$|k\rangle\langle l| \quad \rightarrow \quad e^{-2\sigma^2(1-\delta_{kl})} |k\rangle\langle l|. \tag{3.17}$$

As explain in section 2.7.3, exponential transverse relaxation is described using the decay time constant $T_2^{-1} = \frac{1}{2}\gamma_1 + \gamma_2 := \gamma$. Therefore, we conclude that

$$\sigma^2 = \frac{\gamma t}{2}. \tag{3.18}$$

3.2.2 Two qubit case

In the case of 2 qubits, the calculation is slightly more cumbersome. As for the single qubit case, we will decompose the density matrix in the computational basis as

$$\rho = \sum_{\substack{k,l,\\ m,n=\{0,1\}}} \rho_{\substack{kl\\ mn}} |km\rangle\langle ln|. \tag{3.19}$$

The covariant matrix takes the form

$$\Sigma = \begin{pmatrix} \sigma_1^2 & c\sigma_1\sigma_2 \\ c\sigma_1\sigma_2 & \sigma_2^2 \end{pmatrix}, \tag{3.20}$$

and by using Gauss-Jordan elimination technique [Str03], we find that

$$\begin{aligned} \Sigma^{-1} &= \frac{1}{\sigma_1^2\sigma_2^2(1-c^2)} \begin{pmatrix} \sigma_2^2 & -c\sigma_1\sigma_2 \\ -c\sigma_1\sigma_2 & \sigma_1^2 \end{pmatrix} \\ &= \begin{pmatrix} \frac{1}{\sigma_1^2(1-c^2)} & \frac{-c}{\sigma_1\sigma_2(1-c^2)} \\ \frac{-c}{\sigma_1\sigma_2(1-c^2)} & \frac{1}{\sigma_2^2(1-c^2)} \end{pmatrix}. \end{aligned} \tag{3.21}$$

Actually, explicitly knowing the form of Σ^{-1} is not necessary to evaluate 3.8 if we use the integral identity of multivariate Gaussian integral with linear term, i.e.

$$\frac{1}{\sqrt{(2\pi)^q|A|}} \int d^q x e^{-\frac{1}{2}\vec{x}^T\cdot A^{-1}\cdot\vec{x}+\vec{s}^T\cdot\vec{x}} = e^{\frac{1}{2}\vec{s}^T\cdot A\cdot\vec{s}}, \tag{3.22}$$

By putting together Eq. 3.9 and 3.8 and analyzing the effect on an arbitrary term $|km\rangle\langle ln|$, we see that

$$\Lambda(|km\rangle\langle ln|) = \frac{1}{\sqrt{(2\pi)^2|\hat{\Sigma}|}} \int d\vec{\alpha} e^{-\frac{1}{2}\vec{\alpha}^T\cdot\hat{\Sigma}^{-1}\cdot\vec{\alpha}} \cdot e^{-i\vec{\alpha}\cdot\vec{Z}} |km\rangle\langle ln| e^{i\vec{\alpha}\cdot\vec{Z}}, \tag{3.23}$$

Here, we clearly have a direct analogy $A = \Sigma$, $\vec{x} = \vec{\alpha}$ and $q = 2$ and we only need to figure out the value of $\vec{s}$, which will depend on the action of the $\vec{\alpha}\cdot\vec{Z}$ operator on the matrix $|km\rangle\langle ln|$.

Out of the 16 terms in the density matrix of two spins, there are essentially five different cases that will yield inherently different $\vec{s}$, and those cases are listed in the Table 3.1. All together, we have that

$$\Lambda(|km\rangle\langle ln|) = e^{-2\sigma_1^2(1-\delta_{kl})-2\sigma_2^2(1-\delta_{mn})-4c\sigma_1\sigma_2\eta_{klmn}} |km\rangle\langle ln|, \tag{3.24}$$

Condition	# of terms	$\vec{s}^T$
$k = j,\ m = n$	4	$(0,\ 0)$
$k \neq j,\ m = n$	4	$(\pm 2i,\ 0)$
$k = j,\ m \neq n$	4	$(0,\ \pm 2i)$
$k \neq j,\ m \neq n,\ k \neq m$	2	$\pm(2i,\ 2i)$
$k \neq j,\ m \neq n,\ k = m$	2	$\pm(2i,\ -2i)$

Table 3.1: Different value of the linear term $\vec{s}$ for the multivariate Gaussian integral for different terms of the density matrix of a two qubit system.

where δ_{ab} is the usual Kronecker delta function and where we have defined the function η_{abcd} for $a,\ b,\ c,\ d \in \{0,\ 1\}$ as

$$\eta_{abcd} \quad = \quad \begin{cases} 0 & \text{If } a = b \text{ or } c = d \\ -1 & \text{If } a \neq b,\ c \neq d \text{ and } a = c\ (b = d) \\ 1 & \text{If } a \neq b,\ c \neq d \text{ and } a \neq c \end{cases} , \tag{3.25}$$

If we include the relations in Eq. 3.18, we have

$$\Lambda(|km\rangle\langle ln|) \quad = \quad e^{-\gamma^{(1)}t(1-\delta_{kl})-\gamma^{(2)}t(1-\delta_{mn})-2ct\sqrt{\gamma^{(1)}\gamma^{(2)}}\eta_{klmn}}|km\rangle\langle ln|. \tag{3.26}$$

From this equation, we can infer the effect of noise correlation on the error affecting a system. In the case where $c > 0$, a double coherence term, e.g. $|00\rangle\langle 11|$ or $|11\rangle\langle 00|$ will decay at a rate $2ct\sqrt{\gamma^{(1)}\gamma^{(2)}}$ faster than if the noise was uncorrelated. Therefore, if a quantum computing scheme is designed for independent errors using an error rate per qubit of $\Gamma = \max(\gamma^{(1)}, \gamma^{(2)})$, the whole computation could yield invalid results due to the fact that double coherence terms decay at a faster rate and this error might not be compensated for by the designed QEC scheme. Similarly, if $c < 0$, the zero coherence terms, e.g. $|01\rangle\langle 10|$ or $|10\rangle\langle 01|$, will decay faster.

3.2.3 Interpretation of correlation

Intuitive explanation

The correlation in the noise can be a very complex process to analyze [BP02, GZ04] and is beyond the scope of this thesis. On the other hand, one can make simple arguments to understand possible sources of correlation in NMR.

The correlation in the noise affecting two separate spins can be understood through the distinguishability of the spins. If two spins are indistinguishable, meaning that they have the same Larmor frequency and the same coupling to any other

surrounding spins in the molecule, then the environment will act identically on both of them. Therefore, if one spin undergoes a phase rotation due to an interaction with a spin from the environment, the other spin should undergo the exact same rotation. If two spins are completely distinguishable, say two different nuclear species, then the environment will couple differently to each spin and the noise will be completely uncorrelated. Spins of the same isotope but with different chemical shifts can be seen are "near distinguishable" and hence will yield a correlation factor of $-1 < c < 1$.

To put some mathematical modeling on the above argument, we will assume $\gamma^{(1)} = \gamma^{(2)} = \gamma$ for simplicity, but the same argument follows for $\gamma^{(1)} \neq \gamma^{(2)}$, and we will consider the case of $c = 0$ and $c = 1$ for the double coherence term $|00\rangle\langle 11|$.

Uncorrelated noise

If the two spins are completely uncorrelated, the probability distribution of $\vec{\alpha}$ will be separable,

$$p(\alpha_1, \alpha_2) = p(\alpha_1)p(\alpha_2). \tag{3.27}$$

Eq. 3.8 becomes

$$\begin{aligned}
\Lambda(|00\rangle\langle 11|) &= \int d\alpha_1 \alpha_2 p(\alpha_1)p(\alpha_2)e^{-2i\alpha_1 - 2i\alpha_2}|00\rangle\langle 11| \\
&= \left[\int d\alpha p(\alpha)e^{-2i\alpha}\right]^2 |00\rangle\langle 11| \\
&= \frac{1}{\sqrt{2\pi}}\left[\int d\alpha e^{-\frac{\alpha^2}{2\sigma^2} - 2i\alpha}\right]^2 |00\rangle\langle 11| \\
&= e^{-4\sigma^2}|00\rangle\langle 11| \\
&= e^{-2\gamma t}|00\rangle\langle 11|.
\end{aligned} \tag{3.28}$$

Therefore, a double coherence term will decay at twice the rate of a single coherence, which is intuitively sound, since each spin contributes a decay rate of γ.

Completely correlated noise

In the case of completely correlated noise, the spins undergo the same evolution due to the environment. Therefore the probability distribution now looks like

$$p(\alpha_1, \alpha_2) = p(\alpha_1)\delta(\alpha_2 - \alpha_1), \tag{3.29}$$

That is, the generator of error is now $\alpha(Z_1 + Z_2)$ and the evolution of the double coherence goes as

$$\begin{aligned}\Lambda(|00\rangle\langle 11|) &= \int d\alpha p(\alpha) e^{-4i\alpha}|00\rangle\langle 11| \\ &= e^{-8\sigma^2}|00\rangle\langle 11| \\ &= e^{-4\gamma t}|00\rangle\langle 11|, \end{aligned} \tag{3.30}$$

so that the completely correlated double coherence terms decay four times faster.

The above results are in agreement with Eq. 3.26 , which was derived in a much more abstract way.

3.3 Engineering the noise

3.3.1 Kraus form for correlated dephasing

For purposes that will become clear in Section 3.6.1, we need to experimentally engineer the above Gaussian noise model. If we explicitly expand Eq. 3.8 we obtain

$$\begin{aligned}\Lambda(\rho) &= \langle \cos^2\alpha_1 \cos^2\alpha_2\rangle \rho + \langle \cos^2\alpha_1 \sin^2\alpha_2\rangle Z_2\rho Z_2 \\ &\quad + \langle \sin^2\alpha_1 \cos^2\alpha_2\rangle Z_1\rho Z_1 + \langle \sin^2\alpha_1 \sin^2\alpha_2\rangle Z_1Z_2\rho Z_1Z_2 \\ &\quad + \langle \sin\alpha_1 \cos\alpha_1 \sin\alpha_2 \cos\alpha_2\rangle \left(Z_2\rho Z_1 + Z_1\rho Z_2 - \rho Z_1Z_2 \right. \\ &\qquad \left. - Z_1Z_2\rho\right), \end{aligned} \tag{3.31}$$

where we used the notation $\langle f(\alpha)\rangle = \int d\alpha p(\alpha) f(\alpha)$. In the Kraus operator formalism, the first four terms of the above equation tells us the probability that spins undergo no phase flip, single flips or a double flip. Unfortunately, it is hard to develop an intuition for the last terms. Actually, they are not even in the Kraus form (i.e. not of the form $A\rho A^\dagger$). On the other hand, it is possible to find the Kraus operators yielding such a term.

As seen in section 2.7.1, the Kraus operators for dephasing are $\{\sqrt{1-p^2}\mathbb{1}, \sqrt{p}Z\}$, with $p = \frac{1}{2}(1 - e^{-\gamma t})$. If the noise is independent from qubit to qubit, it is possible to determine the decohered state of multiple qubits by concatenating the action of the Kraus operators (Sec. 1.3). For two spins, we have

$$\begin{aligned}\rho &\to \Lambda_2\left(\Lambda_1(\rho)\right) \\ &= \Lambda_2((1-p_1)\rho + p_1 Z_1\rho Z_1) \\ &\to (1-p_2)[(1-p_1)\rho + p_1 Z_1\rho Z_1] + p_2 Z_2[(1-p_1)\rho + p_1 Z_1\rho Z_1]Z_2 \\ &= (1-p_1)(1-p_2)\rho + p_1(1-p_2)Z_1\rho Z_1 + (1-p_1)p_2 Z_2\rho Z_2 \\ &\quad + p_1p_2 Z_1Z_2\rho Z_1Z_2. \end{aligned} \tag{3.32}$$

Therefore, the first 4 terms in Eq. 3.31 describe the action of the uncorrelated part of the noise. The other terms are thus related to the correlation, which implies that the Kraus operators for those terms must be proportional to

$$B = e^{\theta_1 Z_1 + \theta_2 Z_2}. \tag{3.33}$$

It is straightforward to verify that if we take $B = e^{-i\frac{\pi}{4}(Z_1+Z_2)}$, we obtain

$$\begin{aligned} B\rho B^\dagger + B^\dagger \rho B &= \frac{1}{2}\left(\rho + Z_1\rho Z_1 + Z_2\rho Z_2 + Z_1Z_2\rho Z_1Z_2\right. \\ &\quad \left. + Z_1\rho Z_2 + Z_2\rho Z_1 - \rho Z_1Z_2 - Z_1Z_2\rho\right). \end{aligned} \tag{3.34}$$

It is therefore possible to rearrange Eq. 3.31 in the Kraus form:

$$\begin{aligned} \Lambda(\rho) &= p_1\rho + p_2 Z_1\rho Z_1 + p_3 Z_2\rho Z_2 + p_4 Z_1Z_2\rho Z_1Z_2 \\ &\quad p_5 e^{-i\frac{\pi}{4}(Z_1+Z_2)}\rho e^{i\frac{\pi}{4}(Z_1+Z_2)} + p_6 e^{i\frac{\pi}{4}(Z_1+Z_2)}\rho e^{-i\frac{\pi}{4}(Z_1+Z_2)}, \end{aligned} \tag{3.35}$$

where the coefficient p_i are given in Table 3.2.

A_i	p_i
$\mathbb{1}$	$\frac{1}{4}\left(1 + e^{-\gamma^{(1)}t} + e^{-\gamma^{(2)}t} + e^{-\gamma^{(1)}t-\gamma^{(2)}t-2ct\sqrt{\gamma^{(1)}\gamma^{(2)}}}\right)$
Z_1	$\frac{1}{4}\left(1 - e^{-\gamma^{(1)}t} + e^{-\gamma^{(2)}t} - e^{-\gamma^{(1)}t-\gamma^{(2)}t+2ct\sqrt{\gamma^{(1)}\gamma^{(2)}}}\right)$
Z_2	$\frac{1}{4}\left(1 + e^{-\gamma^{(1)}t} - e^{-\gamma^{(2)}t} - e^{-\gamma^{(1)}t-\gamma^{(1)}t+2ct\sqrt{\gamma^{(1)}\gamma^{(2)}}}\right)$
Z_1Z_2	$\frac{1}{4}\left(1 - e^{-\gamma^{(1)}t} - e^{-\gamma^{(2)}t} + e^{-\gamma^{(1)}t-\gamma^{(1)}t-2ct\sqrt{\gamma^{(1)}\gamma^{(2)}}}\right)$
$e^{-i\frac{\pi}{4}(Z_1+Z_2)}$	$\frac{1}{2}e^{-\gamma^{(1)}t-\gamma^{(2)}t}\sinh(2ct\sqrt{\gamma^{(1)}\gamma^{(2)}})$
$e^{i\frac{\pi}{4}(Z_1+Z_2)}$	$\frac{1}{2}e^{-\gamma^{(1)}t-\gamma^{(2)}t}\sinh(2ct\sqrt{\gamma^{(1)}\gamma^{(2)}})$

Table 3.2: Kraus decomposition for the correlated noise on two qubits. The left column gives the error operators and their respective probability is given in the right column.

For reasons that will become apparent in subsequent sections, we will ultimately need to engineer the noise on three spins such that the noise on the third spin is uncorrelated with the other spins. Since the added noise in uncorrelated to the existing noise, we only need to concatenate the Kraus operator as in Eq. 3.32. The new Kraus operator are given in Table 3.3.

3.3.2 Implementing the noise

From the above decomposition, it is now possible to engineer correlated noise on three qubits (one of them being uncorrelated) using twelve separate experiments.

A_i	p_i
$\mathbb{1}$	$\frac{1}{8}\left(1+e^{-\gamma^{(1)}t}+e^{-\gamma^{(2)}t}+e^{-\gamma^{(1)}t-\gamma^{(2)}t-2ct\sqrt{\gamma^{(1)}\gamma^{(2)}}}\right)\left(1+e^{-\gamma^{(3)}t}\right)$
Z_1	$\frac{1}{8}\left(1-e^{-\gamma^{(1)}t}+e^{-\gamma^{(2)}t}-e^{-\gamma^{(1)}t-\gamma^{(2)}t+2ct\sqrt{\gamma^{(1)}\gamma^{(2)}}}\right)\left(1+e^{-\gamma^{(3)}t}\right)$
Z_2	$\frac{1}{8}\left(1+e^{-\gamma^{(1)}t}-e^{-\gamma^{(2)}t}-e^{-\gamma^{(1)}t-\gamma^{(1)}t+2ct\sqrt{\gamma^{(1)}\gamma^{(2)}}}\right)\left(1+e^{-\gamma^{(3)}t}\right)$
Z_3	$\frac{1}{8}\left(1+e^{-\gamma^{(1)}t}+e^{-\gamma^{(2)}t}+e^{-\gamma^{(1)}t-\gamma^{(2)}t-2ct\sqrt{\gamma^{(1)}\gamma^{(2)}}}\right)\left(1-e^{-\gamma^{(3)}t}\right)$
Z_1Z_2	$\frac{1}{8}\left(1-e^{-\gamma^{(1)}t}-e^{-\gamma^{(2)}t}+e^{-\gamma^{(1)}t-\gamma^{(1)}t-2ct\sqrt{\gamma^{(1)}\gamma^{(2)}}}\right)\left(1+e^{-\gamma^{(3)}t}\right)$
Z_1Z_3	$\frac{1}{8}\left(1-e^{-\gamma^{(1)}t}+e^{-\gamma^{(2)}t}-e^{-\gamma^{(1)}t-\gamma^{(2)}t+2ct\sqrt{\gamma^{(1)}\gamma^{(2)}}}\right)\left(1-e^{-\gamma^{(3)}t}\right)$
Z_2Z_3	$\frac{1}{8}\left(1+e^{-\gamma^{(1)}t}-e^{-\gamma^{(2)}t}-e^{-\gamma^{(1)}t-\gamma^{(1)}t+2ct\sqrt{\gamma^{(1)}\gamma^{(2)}}}\right)\left(1-e^{-\gamma^{(3)}t}\right)$
$Z_1Z_2Z_3$	$\frac{1}{8}\left(1-e^{-\gamma^{(1)}t}-e^{-\gamma^{(2)}t}+e^{-\gamma^{(1)}t-\gamma^{(1)}t-2ct\sqrt{\gamma^{(1)}\gamma^{(2)}}}\right)\left(1-e^{-\gamma^{(3)}t}\right)$
$e^{-i\frac{\pi}{4}(Z_1+Z_2)}$	$\frac{1}{4}e^{-\gamma^{(1)}t-\gamma^{(2)}t}\sinh(2ct\sqrt{\gamma^{(1)}\gamma^{(2)}})\left(1+e^{-\gamma^{(3)}t}\right)$
$e^{i\frac{\pi}{4}(Z_1+Z_2)}$	$\frac{1}{4}e^{-\gamma^{(1)}t-\gamma^{(2)}t}\sinh(2ct\sqrt{\gamma^{(1)}\gamma^{(2)}})\left(1+e^{-\gamma^{(3)}t}\right)$
$e^{-i\frac{\pi}{4}(Z_1+Z_2)}Z_3$	$\frac{1}{4}e^{-\gamma^{(1)}t-\gamma^{(2)}t}\sinh(2ct\sqrt{\gamma^{(1)}\gamma^{(2)}})\left(1-e^{-\gamma^{(3)}t}\right)$
$e^{i\frac{\pi}{4}(Z_1+Z_2)}Z_3$	$\frac{1}{4}e^{-\gamma^{(1)}t-\gamma^{(2)}t}\sinh(2ct\sqrt{\gamma^{(1)}\gamma^{(2)}})\left(1-e^{-\gamma^{(3)}t}\right)$

Table 3.3: Kraus decomposition for the correlated noise on three qubits. The left column gives the error operators and their respective probability is given in the right column.

Initially, we prepare the state ρ. In each different experiment, the operator A_i is then applied so that $\rho \rightarrow \rho_i = A_i \rho A_i^\dagger$, and the experiment is finalized to yield the final state ρ_{fi} and final measurement m_i. The final state of the system under the influence of the fully correlated noise can now be simulated by summing the individual states with the appropriate weight defined by a choice of $\gamma^{(1)}$, $\gamma^{(2)}$, $\gamma^{(3)}$ and c:

$$\rho_f = \sum_{i=1}^{1} 2p_i\rho_{if}, \tag{3.36}$$

and by the linearity of quantum mechanics, the measurements follow the same relation:

$$m = \sum_{i=1}^{1} 2p_i m_i. \tag{3.37}$$

We should mention that this twelve experiment scheme only works if we desire to implement the noise at one time step of the computation. If we want to implement the noise at n time steps, it will require 12^n separate experiments.

3.4 Standard NMR technique to determine the correlation factor

The standard technique to measure T_2 in NMR, or in any other spin device, is to use a CPMG sequence of pulses [CP54, MG58]. This sequence consists of creating a single coherence state on the desired spin and then measuring the decay of such a state as a function of time (Sec. 2.7.1).

A similar sequence can be used to measure the noise correlation between two spins by measuring the decay of a double coherence state of the form

$$\begin{aligned} \rho_{ini} &= |00\rangle\langle 11| + |11\rangle\langle 00| \\ &= \hat{I}^+\hat{I}^+ + \hat{I}^-\hat{I}^-. \end{aligned} \tag{3.38}$$

It is possible to generate this state using phase cycling with two experiments by creating the state X_1X_2 and Y_1Y_2 and subtracting them. Using $X = \hat{I}^+ + \hat{I}^-$ and $Y = -i(\hat{I}^+ - \hat{I}^-)$, we have that

$$\begin{aligned} X_1X_2 - Y_1Y_2 &= \left(\hat{I}^+\hat{I}^+ + \hat{I}^+\hat{I}^- + \hat{I}^-\hat{I}^+ + \hat{I}^-\hat{I}^-\right) \\ &\quad + \left(\hat{I}^+\hat{I}^+ - \hat{I}^+\hat{I}^- + \hat{I}^-\hat{I}^- + \hat{I}^-\hat{I}^-\right) \\ &= \hat{I}^+\hat{I}^+ + \hat{I}^-\hat{I}^-. \end{aligned} \tag{3.39}$$

Two spins in a double coherence do not couple with each other, and therefore, there is no need to use π pulses to refocus the coupling. On the other hand, we still need to refocus the field inhomogeneities. A crucial observation is to notice that whenever we apply a single spin π pulse on a double coherence state, it becomes a zero coherence, e.g. $\pi_1|00\rangle\langle 11|\pi_1^\dagger = |10\rangle\langle 01|$. But from Eq. 3.26, if the correlated double coherence term decays faster than the uncorrelated one, the correlated zero coherence decays slower by the same amount. Hence, a refocusing scheme using selective π pulses will most likely yield an erroneous decay curve.

Consider the following pulse sequence:

$$\frac{\tau}{2} \rightarrow \pi_1\pi_2 \rightarrow \frac{\tau}{2}. \tag{3.40}$$

where τ is a certain time delay. The parallel π pulses will refocus the static field inhomogeneity, while always keeping the state in double coherence. Moreover, these pulses will decouple the two targeted spins from the rest of the spins in the molecule.

Applying the sequence for a series of time intervals τ and then measuring the final amount of signal will give a decay curve with exponential decay rate Γ given by

$$\Gamma = -\gamma^{(1)} - \gamma^{(2)} - 2ct\sqrt{\gamma^{(1)}\gamma^{(2)}}. \tag{3.41}$$

Since in NMR, only single coherence states can be directly detected, a final $\pi/2$ pulse is needed on one of the spins to detect such a state. Upon previously measuring $\gamma^{(1)}$ and $\gamma^{(2)}$ using a CP or CPMG sequence, it is posible to extract the value of c from the curve.

A caveat of this technique is that a double coherence signal decays exponentially at about twice the rate of a single coherence one. It is thus difficult to generate lots of statistics and often, significant amounts of signal averaging will be needed, rendering the measurement of the correlation factor long and cumbersome.

Finally, if the correlation between two spins is measured in a molecule with other spins present, these spins must be prepared in a non-coherent state, i.e. either Z or $\mathbb{1}$ so that their relaxation does not contribute to the decay curve.

3.5 Three qubit quantum error correction

3.5.1 The circuit and its effect

In the previous section, we saw that the standard technique to measure the correlation factor yields an exponential loss of signal. Since QEC is inherently built to reduce the effect of the noise, it is expected that a non-exponential decay curve will result, which could provide more statistics for determining the value of c.

Since the general theory of QEC [KLA+02, NC00, Got97, Kri06, KLM07] is beyond the scope of this thesis, we will only give the simplest example for a QEC correcting a single qubit error. The three qubit quantum error correction code (3QECC) [CMP+98] can correct any single qubit error about a single fixed Pauli axis. It is highly based on the classical repetition code.

The classical three bit repetition code, as its name suggest, encodes a logical bit by repeating it three times:

$$\bar{0} = 000, \qquad \bar{1} = 111. \tag{3.42}$$

If a single error (i.e. bit-flip) happens on any of the bits, the original value of the bit can be deduced by measuring the three bits and making a majority vote. Therefore, if the probability of error for a single qubit is p, then the probability of a single physical error is $p_1 = 3p(1-p)^2$, that of two simultaneous error is $p_2 = 3p^2(1-p)$ and that of there errors, $p_3 = p^3$.

On the other hand, using the repetition code, the probability of a logical qubit error is thus given by $p_2 + p_3$ which is of order $\mathcal{O}(p^2)$. The correction code decreases the error probability by one order.

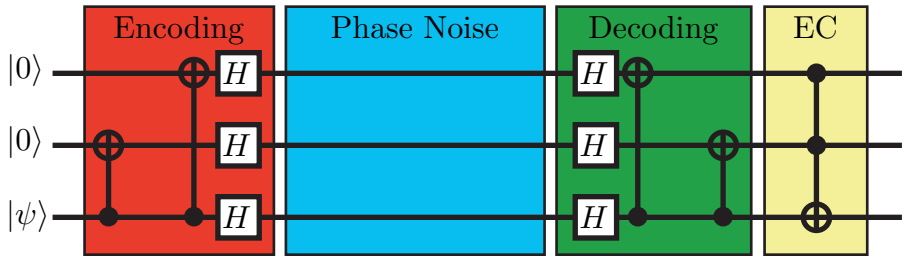

Figure 3.1: The quantum circuit of the three qubit quantum error correction code design to correct any single qubit phase errors.

The 3QECC is in direct analogy with the classical code. For our purposes, we are not interested in correcting for bit flips, but only for phase flip (or any z rotation). If we let $|\pm\rangle = \frac{1}{\sqrt{2}}(|0\rangle \pm |1\rangle)$ be the eigenvector of the X Pauli matrix, we see that $Z|\pm\rangle = |\mp\rangle$. Thus, the Z Pauli matrix acts as a bit flip in this basis. Therefore, let's define the encoded logical qubit basis as

$$\begin{aligned} |\bar{\psi}\rangle &= \alpha|\bar{0}\rangle + \beta|\bar{1}\rangle \\ &= \alpha|+++\rangle + \beta|---\rangle \end{aligned} \tag{3.43}$$

This state can be created from the initial state $|00\rangle(\alpha|0\rangle + \beta|1\rangle)$ using the encoding section of the circuit depicted in Fig. 3.1 . Since a generic arbitrary logical qubit will most likely be represented by an entangled superposition of the states of the physical qubits, we cannot apply the majority rule as in the classical case since it will collapse the superposition and hence lose the quantum information. On the other hand, by reversing the encoding sequence, one effectively disentangles the three qubits and stores information about the noise that has affected the system in the two top qubits. By measuring the top qubits, known as the *syndrome measurement* (which does not affect the superposition of information on the bottom qubit), we can deduce which error occurred and then apply the corresponding operation on the bottom qubit to recover the original quantum information. Knowing that measuring and then performing a classically controlled operation is equivalent to performing a quantum controlled operation and then measuring the qubit [NC00], it is possible to perform the error correction step using a Toffoli gate (controlled-controlled-NOT), as shown in the EC part of Fig. 3.1.

The evolution of a generic encoded state is documented in Table 3.4 for all possible phase flips considered here, where we have defined the states

$$\begin{aligned} |i\rangle &= \frac{1}{\sqrt{2}}(|0\rangle + i|1\rangle) \\ |\bar{i}\rangle &= \frac{1}{\sqrt{2}}(|0\rangle - i|1\rangle), \end{aligned} \tag{3.44}$$

as the eigenstates of the Pauli Y matrix. $\mathcal{E}(\rho_3)$ denotes the effective quantum operation on the state of the third qubit, i.e. $\rho_3 = |\psi\rangle\langle\psi|$. It is clearly seen that the state on the third qubit is the same as the original generic state if any single qubit phase error occurred (yellow part of the table), while it yields an erroneous state for more then two flips. We should also note that when the Kraus operators contain correlated $\pi/2$ phase errors, there is still a probability of recovering the original state (orange part of the table).

In conclusion, even though 3QECC does not correct for all errors, it will correct for any single phase error, hence reducing the effect of dephasing on a given system.

Error	Phase Noise	Decoding	Error Corrected	$\mathcal{E}(\rho_3)$
$\mathbb{1}\mathbb{1}\mathbb{1}$	$\alpha\|++\rangle + \beta\|--\rangle$	$\|00\rangle(\alpha\|0\rangle + \beta\|1\rangle)$	$\|00\rangle(\alpha\|0\rangle + \beta\|1\rangle)$	ρ_3
Z_1	$\alpha\|-+\rangle + \beta\|+-\rangle$	$\|10\rangle(\alpha\|0\rangle + \beta\|1\rangle)$	$\|10\rangle(\alpha\|0\rangle + \beta\|1\rangle)$	ρ_3
Z_2	$\alpha\|+-\rangle + \beta\|-+\rangle$	$\|01\rangle(\alpha\|0\rangle + \beta\|1\rangle)$	$\|01\rangle(\alpha\|0\rangle + \beta\|1\rangle)$	ρ_3
Z_3	$\alpha\|++\rangle + \beta\|--\rangle$	$\|11\rangle(\alpha\|1\rangle + \beta\|0\rangle)$	$\|11\rangle(\alpha\|0\rangle + \beta\|1\rangle)$	ρ_3
Z_1Z_2	$\alpha\|--\rangle + \beta\|++\rangle$	$\|11\rangle(\alpha\|0\rangle + \beta\|1\rangle)$	$\|11\rangle(\alpha\|1\rangle + \beta\|0\rangle)$	$X\rho_3X$
Z_1Z_3	$\alpha\|-+\rangle + \beta\|+-\rangle$	$\|00\rangle(\alpha\|1\rangle + \beta\|0\rangle)$	$\|01\rangle(\alpha\|1\rangle + \beta\|0\rangle)$	$X\rho_3X$
Z_2Z_3	$\alpha\|+-\rangle + \beta\|-+\rangle$	$\|10\rangle(\alpha\|1\rangle + \beta\|0\rangle)$	$\|00\rangle(\alpha\|1\rangle + \beta\|0\rangle)$	$X\rho_3X$
$Z_1Z_2Z_3$	$\alpha\|--\rangle + \beta\|++\rangle$	$\|00\rangle(\alpha\|1\rangle + \beta\|0\rangle)$	$\|00\rangle(\alpha\|1\rangle + \beta\|0\rangle)$	$X\rho_3X$
$e^{-i\frac{\pi}{4}(Z_1+Z_2)}$	$\alpha\|ii+\rangle + \beta\|\bar{i}\bar{i}-\rangle$	$\mathrm{i}\|ii\rangle(\alpha\|0\rangle + \beta\|1\rangle)$	$\|\Psi_1\rangle$	$\frac{3}{4}\rho_3 + \frac{1}{4}X\rho_3X$
$e^{i\frac{\pi}{4}(Z_1+Z_2)}$	$\alpha\|\bar{i}\bar{i}+\rangle + \beta\|ii-\rangle$	$-\mathrm{i}\|\bar{i}\bar{i}\rangle(\alpha\|0\rangle + \beta\|1\rangle)$	$\|\Psi_2\rangle$	$\frac{3}{4}\rho_3 + \frac{1}{4}X\rho_3X$
$e^{-i\frac{\pi}{4}(Z_1+Z_2)}Z_3$	$\alpha\|ii-\rangle + \beta\|\bar{i}\bar{i}+\rangle$	$\mathrm{i}\|ii\rangle(\alpha\|1\rangle + \beta\|0\rangle)$	$\|\Psi_3\rangle$	$\frac{3}{4}X\rho_3X + \frac{1}{4}\rho_3$
$e^{i\frac{\pi}{4}(Z_1+Z_2)}Z_3$	$\alpha\|\bar{i}\bar{i}-\rangle + \beta\|ii+\rangle$	$-i\|\bar{i}\bar{i}\rangle(\alpha\|1\rangle + \beta\|0\rangle)$	$\|\Psi_4\rangle$	$\frac{3}{4}X\rho_3X + \frac{1}{4}\rho_3$

Table 3.4: Evolution of a generic initial encoded state in the 3QECC circuit. The values for $|\Psi_i\rangle$ are given in Table 3.5. $\mathcal{E}(\rho_3)$ gives the final state of the third qubit after the ancilla qubits are discarded.

$\|\Psi_1\rangle$	$[i\|00\rangle - \|01\rangle - \|10\rangle](\alpha\|0\rangle + \beta\|1\rangle) - i\|11\rangle(\alpha\|1\rangle + \beta\|0\rangle)$
$\|\Psi_2\rangle$	$[-i\|00\rangle + \|01\rangle + \|10\rangle](\alpha\|0\rangle + \beta\|1\rangle) + i\|11\rangle(\alpha\|1\rangle + \beta\|0\rangle)$
$\|\Psi_3\rangle$	$[i\|00\rangle - \|01\rangle - \|10\rangle](\alpha\|1\rangle + \beta\|0\rangle) - i\|11\rangle(\alpha\|1\rangle + \beta\|0\rangle)$
$\|\Psi_4\rangle$	$i[-i\|00\rangle + \|01\rangle + \|10\rangle](\alpha\|0\rangle + \beta\|1\rangle) + i\|11\rangle(\alpha\|1\rangle + \beta\|0\rangle)$

Table 3.5: Error corrected states for correlated $\frac{\pi}{2}$ phase error.

3.5.2 Fidelity of the 3QECC circuit for correlated dephasing

In the above section, we saw the 3QECC can be used to correct single qubit phase errors but fails at correcting multi qubit errors. As Eq. 3.35 contains both single and multi-qubit errors and the noise correlation only affects multi-qubit errors, we expect to be able to extract information about the correlation factor if we can quantify the failure rate of the protocol. Therefore, we need a way to quantify how well the protocol preserves information. A useful measure often used in NMR and in quantum error correction is the *fidelity of entanglement*, which gives a lower bound on input-output state fidelity for any initial pure or mixed state [Sch96].

Given a mixed density matrix of a system ρ_S, it is always possible to extend this state to an entangled pure state $|\Psi_{SR}\rangle$ with a reference system R of the same dimension so that the reduce density matrix is given by ρ_S, i.e.

$$\mathrm{Tr}_R(|\Psi_{SR}\rangle\langle\Psi_{SR}|) \;=\; \rho_S. \tag{3.45}$$

If the final state of the system is given by $\mathcal{E}(\rho_S)$, then the entanglement fidelity is defined as

$$\begin{aligned} F_e &= \langle\Psi_{SR}|(\mathbb{1}\otimes\mathcal{E})[|\Psi_{SR}\rangle\langle\Psi_{SR}|]|\Psi_{SR}\rangle \\ &= \mathrm{Tr}(\rho_{SR}\rho'_{SR}), \end{aligned} \tag{3.46}$$

where $\rho'_{SR} = (\mathbb{1}\otimes\mathcal{E})[|\Psi_{SR}\rangle\langle\Psi_{SR}|]$, i.e. the initial system-reference state affected by the noise on the system alone. It can be shown that F_e is independent of the purification and depends only on the initial state ρ_S and the final state $\mathcal{E}(\rho_S)$. For one qubit of information, it is customary to use a standard initial Bell state as the initial entangled system-reference state [CPM+98, VFP+01, FVH+02]. If we use the singlet state $|\Psi_{RS}\rangle = \frac{1}{\sqrt{2}}(|01\rangle - |10\rangle)$ and the fact that the density matrix of the singlet is given by $\frac{1}{4}(\mathbb{1}_R\mathbb{1}_S + X_RX_S + Y_RY_S + Z_RZ_S)$, we find that

$$\begin{aligned} F_e &= \frac{1}{16}\mathrm{Tr}\left([\mathbb{1}\mathcal{E}(\mathbb{1}) + X\mathcal{E}(X) + Y\mathcal{E}(Y) + Z\mathcal{E}(Z)]\right. \\ &\quad \left.\times[\mathbb{1}\mathbb{1} + XX + YY + ZZ]\right) \\ &= \frac{1}{8}\left[\mathrm{Tr}\left(\mathbb{1}\mathcal{E}(\mathbb{1})\right) + \mathrm{Tr}\left(X\mathcal{E}(X)\right) + \mathrm{Tr}\left(Y\mathcal{E}(Y)\right) + \mathrm{Tr}\left(Z\mathcal{E}(Z)\right)\right] \\ &= \frac{1}{4}\left(f_{\mathbb{1}} + f_X + f_Y + f_Z\right), \end{aligned} \tag{3.47}$$

where we define $f_A = \frac{1}{2}\mathrm{Tr}\left(A\mathcal{E}(A)\right)$, i.e., the fidelity of entanglement is equal to the average polarization left along all the Pauli axes and depends only on the channel $\mathcal{E}$. To relate to the 3QECC, ρ_S is the qubit state we want to preserve (third qubit in Fig. 3.1) and $\mathcal{E}(\rho_S)$ is the final state, once the ancilla qubits are discarded (qubit 1 and 2).

For the 3QECC, it is possible to evaluate F_e using four separate experiments, with initial states $|00\rangle\langle 00|X$, $|00\rangle\langle 00|Y$, $|00\rangle\langle 00|Z$ and $|00\rangle\langle 00|\mathbb{1}$. From the action of $\mathcal{E}$ given in Table 3.4 , we see that if the qubit is initially in the state $|\psi\rangle = |0\rangle$, then the outcome will be an equal mixture of $|0\rangle$ and $|1\rangle$; similarly for $|\psi\rangle = |1\rangle$. We thus conclude that $f_{\mathbb{1}} = 1$. Also, the states $|\pm\rangle\langle\pm|$ will be map to themselves. Since $|\pm\rangle\langle\pm| = \frac{1}{2}(\mathbb{1} \pm X)$, we also have that $f_X = 1$. By symmetry of the noise and of the encoded logical state, we also have that $f_y = f_z$, so we only have to derive the expression for one of them. Looking at the last column of Table 3.4 and referring to Table 3.3, we have that

$$\begin{aligned} f_Z &= p_1 + p_2 + p_3 + p_4 - p_5 - p_6 - p_7 - p_8 + \frac{1}{2}(p_9 + p_{10} - p_{11} - p_{12}) \\ &= \frac{1}{2}\left[e^{-\gamma^{(1)}t} + e^{-\gamma^{(2)}t} + e^{-\gamma^{(3)}t} - e^{-\gamma^{(1)}t-\gamma^{(2)}t-\gamma^{(3)}t}\cosh(2ct\sqrt{\gamma^{(1)}\gamma^{(2)}})\right], \end{aligned} \tag{3.48}$$

The full fidelity of entanglement thus evolves as

$$\begin{aligned} F_e(t) &= \frac{1}{4}\left[2 + e^{-\gamma^{(1)}t} + e^{-\gamma^{(2)}t} + e^{-\gamma^{(3)}t} - e^{-\gamma^{(1)}t-\gamma^{(2)}t-\gamma^{(3)}t}\cosh(2ct\sqrt{\gamma^{(1)}\gamma^{(2)}})\right] \\ &\simeq 1 - \frac{1}{2}\left(\gamma^{(1)}\gamma^{(2)} + \gamma^{(1)}\gamma^{(3)} + \gamma^{(2)}\gamma^{(3)} + 2c^2\gamma^{(1)}\gamma^{(2)}\right)t^2 + \mathcal{O}(t^3). \end{aligned} \tag{3.49}$$

The above equation shows that the short time expansion of the fidelity is of order t^2, showing that the error correction scheme did suppress the noise by one order and as expected, the correlation factor does appear in the rate of success (or failure) of the QECC.

3.6 Experimental details

3.6.1 Strategy

The goal of the experiments is to extract the noise correlation factor between two spins using the 3QECC and compare the results with the factor obtained using double coherence decay. As seen in Section 3.3, once the T_2's of a system are known it is possible to engineer the correlated phase noise for any correlation factor on three qubits using twelve separate experiments.

The strategy will be to first obtain a "real noise" fidelity of entanglement curve; that is, by letting the system evolve freely during the "Phase Noise" part of the circuit in Fig. 3.1, and measuring fidelity of transmission f_A for the initial states $|00\rangle\langle 00|X$, $|00\rangle\langle 00|Y$ and $|00\rangle\langle 00|Z$ (we assume $|00\rangle\langle 00|\mathbb{1}$ will have perfect transmission.

Once the real noise curve is obtained, we need to build the engineered noise fidelity curve. Instead of a period of free evolution, a phase operation will be performed during the noisy part of the circuit and then the fidelity measured for each input state, and this process will be repeated for each Kraus operator in Table 3.3. By the linearity of quantum mechanics, the total fidelity will be given by the weighted sum of all the fidelities.

Finally, it will be possible to extract the value of c by finding the optimal value for which the engineered noise curve matches the real noise curve.

3.6.2 The molecule

All the theory developed in this chapter assumes we have three qubits, two of which experience correlated noise while the third one experiences an independent noise. It has been hinted that such a system could be found in a molecule containing two spins of the same isotope and a third one of a different isotope. One such molecule that has been used before for quantum information processing experiments is the trichloroethylene (TCE) [NKL98, RLBL05, CPM+98, FLMR04] which contains two carbon and one hydrogen. Even though the couplings are high ($H - C_1 \sim 200$ Hz and $C_1 - C_2 \sim 100$ Hz, the chemical shift difference of the carbons is comparatively small (~ 1200 Hz on a 16.4T magnet), thus rendering the selective carbon pulses hard to accomplish. Even though methods using periods of chemical shift evolution have been developed for creating selective pulses [RLBL05], sizable coupling errors are introduced when using them.

Also, the large coupling-small chemical shift difference breaks the condition of validity for the weak-coupling regime, implying imperfect refocusing of carbon coupling using π pulses and making the use of the sequence compiler described in Sec. 2.6.1 less precise. Finally, we should note that at the time of this experiment, the GRAPE pulse finding algorithm was not developed yet and only square and Gaussian shaped pulses were used. For these reasons, TCE was discarded as a potential spin system.

Instead, the acetyl chloride molecule, a previously unused molecule for NMR QIP, which also contains two carbons and one hydrogen, was used which offers large carbon chemical shift difference and significantly large coupling. The structure, chemical shift, couplings and relaxation times for this molecule on a 16.4T magnet can be found in Fig. 3.2. The T_1 times were measured using an inversion recovery experiment and the T_2's using CPMG. The T_1 times in acetyl chloride are significantly larger than the T_2, hence neglecting the longitudinal relaxation during the duration of the experiments is justified.

The methyl group in the molecule rotates along its axis at a rate much faster

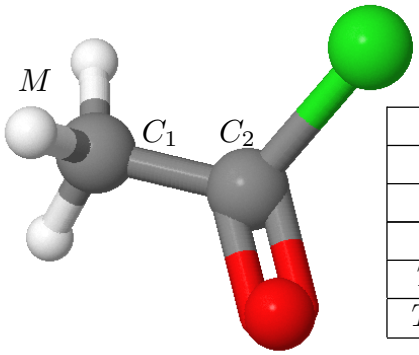

M	-1884.63		
C_1	132.72	-5949.48	
C_2	-7.44	56.2	-29998.18
	M	C_1	C_2
T_1 (s)	4.0 ± 0.1	7.9 ± 0.4	15.2 ± 0.8
T_2 (s)	1.2 ± 0.1	2.1 ± 0.1	0.24 ± 0.03

Figure 3.2: Structural and magnetic characteristics of acetyl chloride. The diagonal elements give the chemical shift with respect to the base frequency of the isotope (∼700MHz for the hydrogens and ∼176MHz for the carbons), and the off-diagonals gives the coupling constants in Hz.

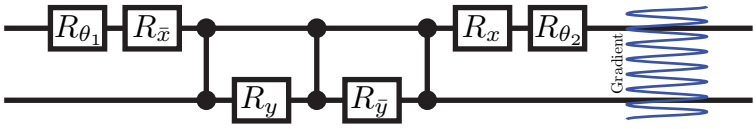

Figure 3.3: Pulse sequence to select the spin-$\frac{1}{2}$ subspace of a methyl group. After the implementation of this pulse sequence, the state of the protons have a vanishing probability to be found in the spin-3/2 subspace.

than the NMR time-scale, so that the three hydrogens composing it are magnetically identical, hence forming a spin-$\frac{3}{2}$ and a spin-$\frac{1}{2}$ subspace among the three protons. Using the pulse sequence depicted in Fig. 3.3, it can be shown [BY03] that the spin-$\frac{3}{2}$ subspace is annihilated, while the spin-$\frac{1}{2}$ subspace is mapped to itself.

3.6.3 Experimental implementation

In order to implement the 3QECC, each gate in the circuit in Fig. 3.1 had to translated into a series of $\pi/2$ pulses around specific axis in the xy plane, z-pulses of any angle and J-coupling evolutions. The methyl group protons act as qubit 3, while C_1 and C_2 are qubit 2 and 1 respectively. The pulse sequence obtained was then manually optimized to minimize the number of pulses and the number of couplings. Recall from section 2.4.2 that z pulses are free to implement by changing the phase of subsequent pulses. Since the coupling between M and C_2, i.e. qubit 3 and 1, is small, the second CNOT is impractical to perform. On the other hand, the fidelity of the 3QECC is independent of which qubit is used as initial and final

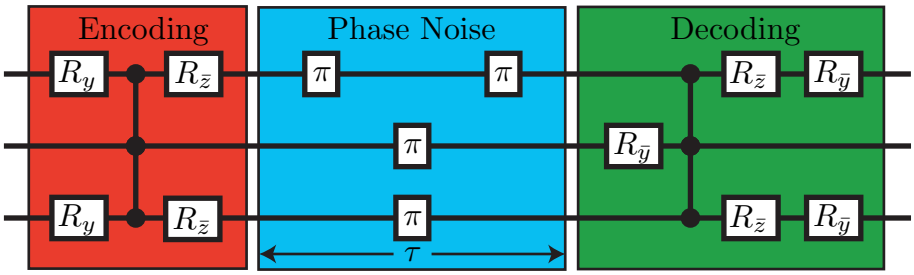

Figure 3.4: NMR pulse sequence to implement the encoding and decoding part of the 3QECC. The refocusing scheme during the Phase Noise part ensure that the protons do not couple to the carbons and that the carbons state remains in the same coherence number throughout. It also allows for the field inhomogeneities to be refocused on all the spins.

qubit of information. Therefore, we used C_1 as the physical qubit and M and C_2 as the ancilla. The only difference is that the CNOT's in Fig. 3.1 are all controlled from the middle qubit. Moreover, Hadamard gates usually take four $\pi/2$ pulses to achieve. In term of the action on the computational basis, the Hadamard is essentially the same as a $\pi/2$ pulse along the y axis.

In the implementation of the engineered noise, no pulses were actually performed during the noise part of the circuit, but only the phase of subsequent pulses was changed, depending on which Kraus operator was implemented. During the real noise delays, for the same reasons explained in Sec. 3.4, the carbon's field inhomogeneity and chemical shift evolution needed to be refocused simultaneously, so that double coherence terms and zero-coherence terms remained during the whole duration of the noise. The methyl evolution needed to be refocused too, which can be done using two π pulses before and after the refocusing of the carbons.

Finally, the Toffoli gate (controlled-controlled-X) is extremely complex to implement [NC00] using only single and two qubit gates. On the other hand, 3QECC does not need the exact Toffoli gate and still works for a controlled-controlled-iX, which can be implemented with much fewer gates. Using the commutation relation intrinsic to the Pauli operators, one can translate the 3QECC circuit into the pulse sequences depicted in Fig. 3.4 and 3.5.

Contrary to the standard NMR technique of double coherence decay, the carbon's state also contains single coherence terms during the noisy part of the experiment which would couple. As the J-coupling could be hard to refocus without risking transforming a double coherence into a zero coherence, the duration τ of the noisy evolutions was chosen so that $\tau = \frac{1}{J_{C_1C_2}}$, i.e. a multiple of a π coupling evolution.

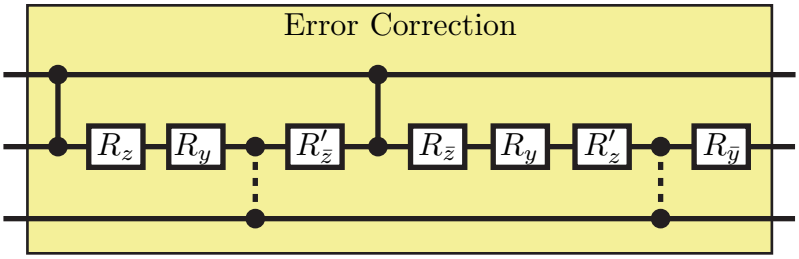

Figure 3.5: NMR pulse sequence to implement a modified version of the Toffoli gate. This sequence will implement a controlled-controlled-iX gate instead of a controled-controled-X gate (Toffoli).

Due to the large chemical shift difference between the carbons, the available hard pulses did not have a large enough bandwidth to refocus both carbons simultaneously (even for composite pulses). Instead, simultaneous Gaussian pulses were performed at each frequency. Because of the transient Bloch-Siegert shift, each carbon experiences a frequency shift due to the RF field applied on the other carbon and it has been reported that the frequency of each pulse needs to be adequately changed to perform high-precision control [SVC00]. Fortunately, simulations showed that the pulse representation in Sec. 2.6.1 were highly accurate without any frequency update.

Since the couplings during the encoding and decoding part of the pulse sequence commute with each other, they were implemented simultaneously in order to decrease the effect of decoherence. As a matter of fact, performing the couplings sequentially would take $\tau \sim \frac{1}{2J_{MC_1}} + \frac{1}{2J_{C_1C_2}}$ and would require the refocusing of C_2 and then of M. To save time and pulses, the two coupling were initiated. Since M and C_1 have a higher coupling constant, the desired evolution was achieved first, after a time of $\tau \sim \frac{1}{2J_{MC_1}}$. C_1 and C_2 then continue to couple until finished, while refocusing M. This way, the two couplings were implemented in $\tau \sim \frac{1}{2J_{MC_1}} + \frac{1}{2J_{C_1C_2}}$.

Finally, to ensure the noisy delays and the refocusing scheme was of the exact length and was not tampered with by the optimization procedure of the pulse sequence compiler, we forced it to finish all the operations related to the encoding part of the circuit before beginning the noise delays, and also forced it to start the decoding part once the delay is finished. This way, the spins started and finished the noise delays with no ongoing coupling between them. We did however allow freedom in the chemical shift evolution, since it does not tamper with the decay of the coherence terms.

The initial states $X_{C_1}|00\rangle\langle 00|_{MC_2}$, $Y_{C_1}|00\rangle\langle 00|_{MC_2}$ and $Z_{C_1}|00\rangle\langle 00|_{MC_2}$ were created starting with the methyl polarization, followed by the spin-1/2 subspace pulse

sequence and then using spatial averaging pseudo-pure state pulse sequence as explained in Section 2.3.

To evaluate the fidelities f_A, we needed to measure the correlation between the initial state of information A_{C_1} with the final state of information $\mathcal{E}(A_{C_1})$, where $\mathcal{E}$ is defined as the quantum channel implemented by the 3QECC circuit, the measurement and the discarding of the ancilla spins (partial trace). In NMR, discarding qubits is impossible. On other hand, measuring the observable A on C_1 while discarding M and C_2 is equivalent to measuring the observable $A_{C_1}\mathbb{1}_M\mathbb{1}_{C_2}$ [NC00]. Therefore, if we denote Λ_τ the full action of the 3QECC for a noise delay of τ and without measurements on the three spins, we have

$$\begin{aligned} f_X(\tau) &= \frac{1}{2}\mathrm{Tr}\left[\Lambda_\tau(X_{C_1}|00\rangle\langle 00|_{MC_2})X_{C_1}\right] \\ f_Y(\tau) &= \frac{1}{2}\mathrm{Tr}\left[\Lambda_\tau(Y_{C_1}|00\rangle\langle 00|_{MC_2})Y_{C_1}\right] \\ f_Z(\tau) &= \frac{1}{2}\mathrm{Tr}\left[\Lambda_\tau(Z_{C_1}|00\rangle\langle 00|_{MC_2})Z_{C_1}\right]. \end{aligned} \tag{3.50}$$

As seen in Sec. 2.4.4, the observable X_{C_1} will be proportional to the full integral of the C_1 spectrum. If we denote $s_X(\tau)$ the amount of signal (the integral of the spectrum) measured for a noise delay of τ and initial state $X_{C_1}|00\rangle\langle 00|_{MC_2}$, then

$$s_X(\tau) = \mathcal{N}\mathrm{Tr}\left[\Lambda_\tau(X_{C_1}|00\rangle\langle 00|_{MC_2})X_{C_1}\right], \tag{3.51}$$

where $\mathcal{N}$ is the proportionality constant relating the integral and the measurement. If the 3QECC is not implemented, $\Lambda(X_{C_1}|00\rangle\langle 00|_{MC_2}) = X_{C_1}|00\rangle\langle 00|_{MC_2}$ so that s_{X0}, the amount of signal of the pseudopure state is $2\mathcal{N}$. Therefore,

$$f_X(\tau) = \frac{s_X(\tau)}{s_{X0}}. \tag{3.52}$$

Using the appropriate readout pulses, it is also possible to measure $f_Y(\tau)$ and $f_Z(\tau)$ by ensuring that the final state of C_1 is along X. Therefore, the fidelity of each input state can be measured by comparing the signal of each experiment to the initial experiment, where no delays are implemented. Using such a scheme also allows one to quantify the fidelity of the implementation of the 3QECC, which is given by $F_e(0)$

3.6.4 Experimental results

The experiments were conducted on a 16.4T Bruker Avance spectrometer using a TCI cryogenic probe. By placing the resonant circuit of the probe in liquid helium, while keeping the sample at room temperature, the cryprobe provide an enhance

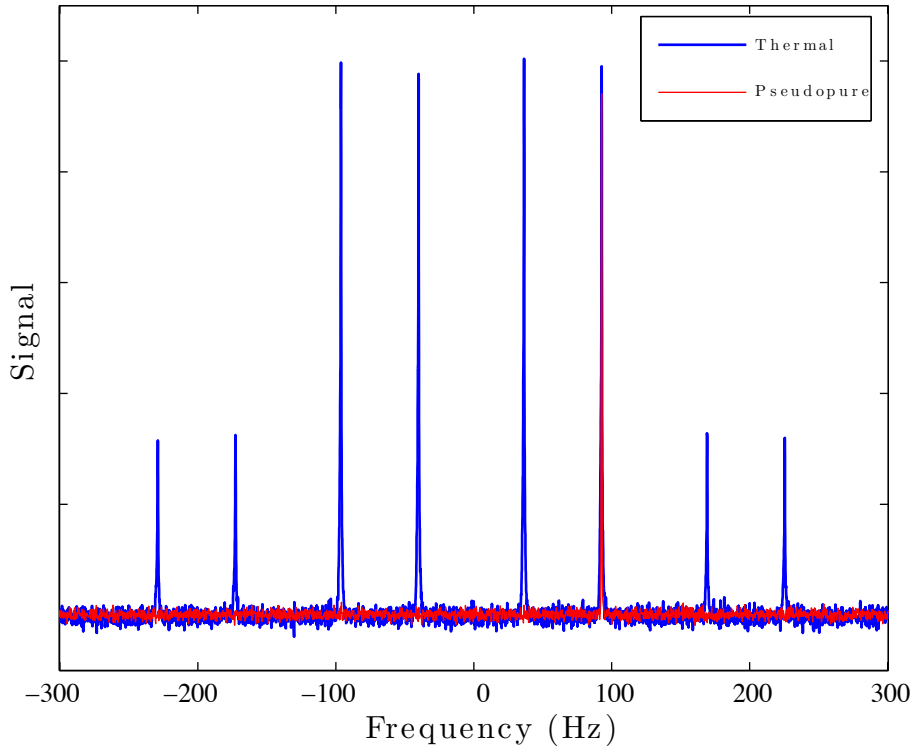

Figure 3.6: The thermal equilibrium state spectrum of C_1 of acetyl chloride compared to the pseudopure state spectrum. The spectra are centered at $\nu^L_{C_1}$.

signal-to-noise ratio and allow for the use of more diluted samples. The creation of the pseudopure state on C_1 is shown in Fig. 3.6 and is compared to the thermal state of C_1. Since the pseudopure sequence started with the methyl polarization, and since there is signal loss due to molecular diffusion during the labelling gradients of the pulse sequence, there is no readily available fair comparison for the spectrum, so they have both been normalized for the sake of qualitative comparison. The presence of the four satellite peaks on the far right and far left of the thermal spectrum is due to the spin-3/2 subspace of the methyl group in the thermal state (before the sequence in Fig. 3.3 is implemented), which creates a 1:3:3:1 peak intensity pattern [Lev01] (each peak being further split due to the coupling to C_2).

The spectrum for implementing the 3QECC with no noise compared to the input pseudopure state is shown in Fig. 3.7. The fidelity of entanglement for the pulse sequence implementation is 0.92 ± 0.01. According to the complete simulation of initial state preparation and pulse sequence implementation, including T_2 relaxation but not the spatial diffusion of the molecules during the pseudopure state preparation, the fidelity should be 0.94 and the simulation spectra is shown in the

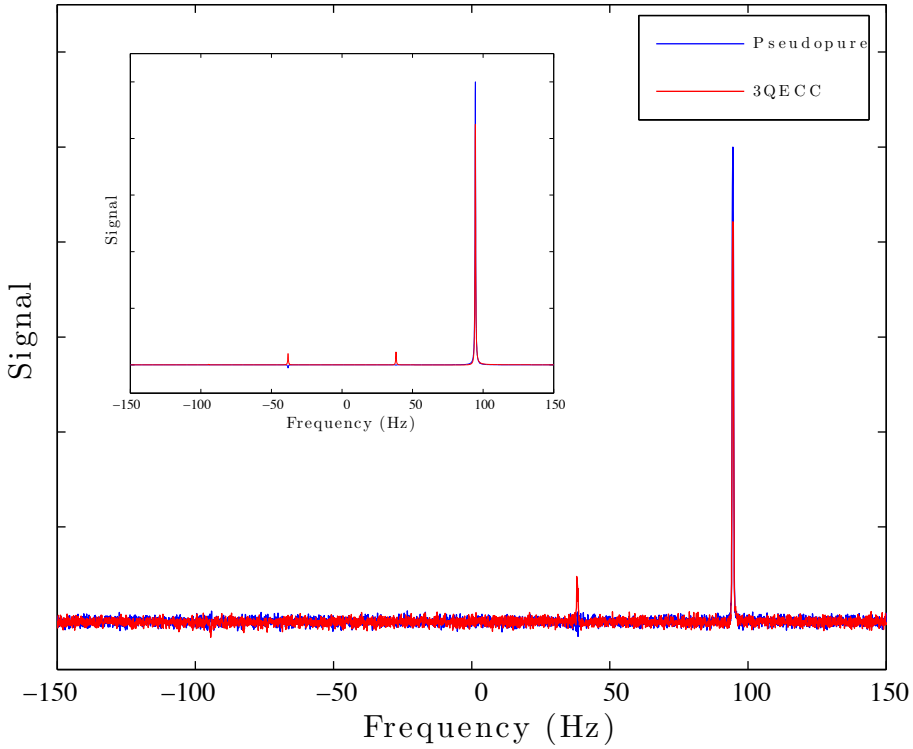

Figure 3.7: Comparison of the initial pseudopure state and the final state spectra after the implementation of the 3QECC with no noise delay.

inset of Fig. 3.7. The experimental spectrum is qualitatively and quantitatively comparable to the simulated spectrum, hence we can conclude that our control was precise and understood to a high degree.

The 3QECC pulse sequence has been implemented on the three initial states with noisy delay of $1, \ldots, 9$ complete J-coupling evolutions between the carbons and the fidelities recorded. After averaging the fidelities, we obtained the entanglement fidelity decay curve shown by the black dots in Fig. 3.8. To integrate the spectra, we first fitted the peaks with Lorentzians and then added the amplitudes. The error bar are the 68% confidence level on the fit.

The twelve experiments needed to engineer to noise were then implemented and the fidelities added using the appropriate coefficient (Table 3.3) for $c = 0$ (blue curve) and $c = 1$ (red curve). Using a least square fit optimization approach, we found that $c = 0.5 \pm 0.2$ corresponds best to the experimental curve obtained for the noisy delays.

By implementing the sequence described in Sec. 3.4, we obtained the double coherence decay curve. By fitting the decay rate given in Eq. 3.41 using the T_2 for

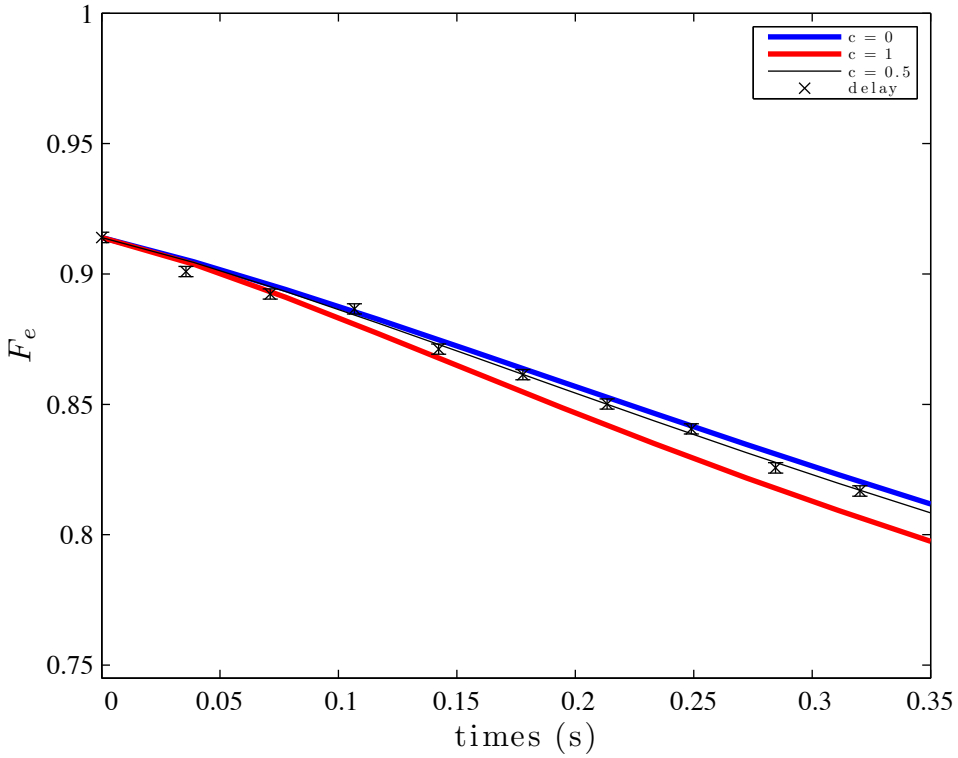

Figure 3.8: Experimental results for the implementation of the 3QECC for various noisy delays and engineered noise. The lines correspond to the fidelity decay for noise correlation factors of 0, 0.5 and 1 as a function of time simulated from the measured T_2's and the experimental fidelities obtained by implementing engineered noise. The points are the fidelities when the system is affected by natural noise for a various amount of time.

C_1 and C_2 previously measured, we extracted a value of $c = 0.3 \pm 0.2$ which is, within error, in agreement with the correlation factor found with this new method.

3.7 Analysis and conclusion

The noise correlation factor obtained using quantum error correction is in agreement, within error, to the factor found using standard NMR techniques. One could argue that the confidence interval on the values found are too large to really conclude anything. The present exercise actually served a wider purpose than just extracting the correlation between the carbons and can be extended beyond what we reported here.

First of all, by looking at Fig. 3.8, the largest fidelity difference between the

independent noise and the fully correlated noise is at most 2%. Being able to successfully implement such an experiment demonstrates the level of control achievable in liquid state NMR quantum computing. The entire pulse sequence contained at least 20 operations, which implies that each operation must be precise to within 0.1%, which was a level unequalled in the QIP literature at the time the experiment was performed. Therefore, the sensitivity of the protocol explained the large uncertainty on the value of c. On the other hand, the much simpler NMR technique does not show any indication of being more precise. Another contribution to the uncertainty on c comes from the signal to noise ratio in the spectra. If we integrate the square of the noise over a region corresponding to the width of a peak, we find the uncertainty on integrating each peak is about 1%, hence contributing to the uncertainty of F_e.

Moreover, an advantage of using the QEC protocol instead of the double coherence decay protocol comes from the intrinsic nature of QEC: as it is designed to detect and correct the single qubit error, the measured signal then decays at a slower rate, hence permitting the acquisition of fidelity for a larger amount of time and thus developing more complete statistics.

Another advantage of the QEC protocol is that it is universal for any QIP processor. One of the requirements for a scalable QIP device is the ability to perform fault-tolerant quantum computation, which relies on QEC. Therefore, this protocol could be implemented in any QIP device to probe their noise.

The strength of this protocol relies on the generalization possibilities. The protocol implemented here was assuming that only two of the three qubits were noise correlated. On the other hand, the protocol is still usable to determine the pairwise qubit noise correlation for a fully correlated system, by redesigning the refocusing scheme during the noisy part of the protocol. As already mentioned, every time a single qubit π pulse is applied on a double coherence, it turns it into a zero coherence, which decays at a different rate than the double coherence. By referring to Eq. 3.26, if the qubit spends as much time in a zero than in a double coherence, the part of the decay rate due to the correlation factor cancels out. For example, if we are trying to measure c_{23}, the correlation factor between spin 2 and 3, we need to refocus spin 1 as in Fig. 3.4 to cancel the possible effect of c_{12} and c_{13}.

Once the three c's are found, it will then be possible to verify the validity of the Gaussian noise model. By assuming the noise is Gaussian, it ensures that the correlation is pairwise and any higher order correlations, e.g. $\langle \alpha_1 \alpha_2 \alpha_3 \rangle \propto c_{123}$, vanish. Once a QEC decay curve using a refocusing scheme that would not refocus such a correlation factor is obtained, we can then infer if this assumption is valid if the curve can be parametrized by the T_2's and the c_{ij} only. We should note that such a curve could also be obtained through triple coherence decay but again, the

signal-to-noise ratio will become a problem as such a coherence term decays triply exponentially.

A final generalization could be to analyze the correlation present within a more general noise. In this chapter, we only considered the case of dephasing noise, which already corresponds to noise present in many systems. The more general single qubit noise can be described as a mixture of error about any Pauli axis. To probe the correlations in such a noise, it should be possible to apply the theory developed here using QEC codes that correct any single qubit error, such as the five bit code [LMPZ96, BBP+96], Steane's seven qubit code [Ste96] or Shor's nine qubit code [Sho95]

Chapter 4

Noise characterization through symmetrization

4.1 Why rely on symmetrization

In the previous chapter, we already argued the importance of knowing the behavior of the noise model in order to successfully develop quantum error correction codes that will allow for arbitrarily long computations. The protocol was applicable to a well understood noise model and a specific noise parameter was probed. New efficient techniques need to be developed in order to extract even more relevant information about the noise, without the overhead of requiring an exponential amount of resources, or number of experiments, e.g. quantum process tomography.

Active symmetrization of a noise process allows for the characterization of relevant information about the noise by corse-graining the noise into families of independent parameters, hence possibly diminishing the amount of experiments needed to obtain information about the noise.

By identifying a symmetry associated with the families of parameters of interest, one can operationally conjugate the noise map by the appropriate unitary group and monitor the action of the effective quantum process on a certain set of initial states. Information about the coarse-grained parameters can then be extracted through an appropriate measurement process. Such an average over a unitary group is known as a *twirl* [BDSW96, DCEL06].

In this chapter, we will describe how one can coarse-grain the noise using Clifford twirling and extract information about the weights of the errors. We then report our effort toward the implementation of such a protocol on a heteronuclear two-spin NMR processor for three different types of engineered noise. Along the way, we also

describe and analyze the arguments against the use of hard pulses and point out the benefits of longer and smoother Gaussian pulses.

4.2 Measuring the weight of the noise

A family of parameters that is of great importance in fault-tolerant quantum computation is the weight w of the errors affecting a system. We define the weight of a noise operator as being the number of qubits acted on by that operator. Typical QECCs are described using the notation $[n,\ k,\ d]$, which corresponds to a distance d code encoding k logical qubits using n physical qubits. A distance d code is capable of detecting and correcting any error of weight $t = \frac{1}{2}(d-1)$ or less on any qubit. Therefore, the probability of failure p_f of a given code is given by

$$p_f \ = \ \sum_{w=t+1}^{n} p_w \tag{4.1}$$

where p_w is the probability of any error of weight w occuring on any set of qubits. If $p_f < p_{th}$, the threshold error rate, fault-tolerant quantum computation is feasible.

In the spirit of fault-tolerant QIP, being able to *efficiently* estimate the value of p_w is of great interest and great practicality. Moreover, as we will discuss in Sec. 4.4, knowing the p_w's can also permit one to determine whether the noise is correlated or independent. Recall from Sec. 3.1 that most fault-tolerant QIP schemes assume independent noise from qubit to qubit or between blocks of qubits, so knowing whether or not the noise is correlated is of fundamental importance.

4.3 Clifford twirling of a single qubit superoperator

We will see in this section that symmetrizing a noisy map Λ such that the weight parameters of the noise operators are coarse-grained can be achieved through a twirling of the channel by a subset of the single qubit Clifford operations. To twirl a given channel, the twirling operation must be applied before and after the action of Λ, and averaged over the entire group. Therefore, we need to assume that the noise Λ is not associated with the implementation of the Clifford operators. For example, Λ can characterize the decoherence happening in a quantum memory, or during the transmission of photonic qubits in an optical fiber, such that the Cliffords could be implemented before the qubit is stored, or sent, and after is it retrieved.

Operationally, a channel Λ is said to be twirled over subgroup of unitaries $\mathcal{G}$ if, given an initial state ρ, we evaluate

$$\begin{aligned} \rho &\rightarrow \frac{1}{|\mathcal{G}|}\sum_i \hat{G}_i^\dagger \Lambda\left(G_i \rho G_i^\dagger\right) G_i \\ &= \Lambda_{ave}(\rho), \end{aligned} \tag{4.2}$$

for $G_i \in \mathcal{G}$ and $|\mathcal{G}|$ being the cardinality of the group. In the Liouville space, we can write the averaged superoperator as

$$\begin{aligned} \hat{\Lambda}_{ave} &= \frac{1}{|\mathcal{G}|}\sum_i \hat{G}^\dagger \hat{\Lambda} \hat{G} \\ &= \frac{1}{|\mathcal{G}|}\sum_i (G_i^T \otimes G_i^\dagger)\hat{\Lambda}(G_i^* \otimes G_i). \end{aligned} \tag{4.3}$$

The one qubit Clifford group is defined as the subgroup of the unitary operations that are in the normalizer of the one qubit Pauli group $\mathcal{P}_1 = \{\pm\mathbb{1},\ \pm X,\ \pm Y,\ \pm Z\}$, that is

$$\mathcal{C}_1 = \left\{C \in \mathcal{U}(2) \mid CPC^\dagger \in \mathcal{P}_1\right\}. \tag{4.4}$$

In the case of a single qubit, a full Clifford twirl is equivalent to a symplectic twirl followed by a Pauli twirl [BDSW96], i.e.

$$\mathcal{C}_1 \cong \mathcal{P}_1\mathcal{S}_1 \tag{4.5}$$

where

$$\mathcal{S}_1 = \left\{e^{\pm i\frac{\pi}{4}Q} \mid Q \in \{X,\ Y,\ Z\}\right\}. \tag{4.6}$$

The entire single qubit Clifford group contains 48 elements. Due to redundancy, such as global phase and identical action on the Pauli operators, only 12 carefully chosen Clifford operations are necessary to implement a full Clifford twirling. In the Pauli-symplectic equivalence, those 12 elements can be chosen as

$$\left\{PS \mid P \in \bar{\mathcal{P}}_1,\ S \in \bar{\mathcal{S}}_1\right\} \tag{4.7}$$

$$\simeq$$

$$\left\{e^{-i\frac{\pi}{2}P}e^{-i\frac{\pi}{4}Q} \mid P \in \bar{\mathcal{P}}_1,\ Q \in \{X,\ Y,\ Z\}\right\} \quad , \tag{4.8}$$

where the last equality is up to a global phase and we have defined the sets

$$\bar{\mathcal{P}}_1 = \{\mathbb{1},\ X,\ Y,\ Z\} \tag{4.9}$$

$$\bar{\mathcal{S}}_1 = \left\{e^{-i\frac{\pi}{4}Q} \mid Q \in \{X,\ Y,\ Z\}\right\} \tag{4.10}$$

Using this equivalence, the full twirling effect can be written as

$$\begin{aligned}\hat{\Lambda}_{ave} &= \frac{1}{12}\sum_{P\in\bar{\mathcal{P}}_1}\sum_{S_i\in\bar{\mathcal{S}}_1}\hat{S}_i^\dagger\hat{P}_j^\dagger\hat{\Lambda}\hat{P}_j\hat{S}_i \\ &= \frac{1}{3}\sum_{i=1}^{3}(S_i^T\otimes S_i^\dagger)\left(\frac{1}{4}\sum_{j=1}^{4}(P_j^T\otimes P_j^\dagger)\hat{\Lambda}(P_j^*\otimes P_j)\right)(S_i^*\otimes S_i). \quad (4.11)\end{aligned}$$

As we saw in Sec. 1.2.3, any channel can be decomposed in the Pauli basis as

$$\hat{\Lambda} = \sum_{kl}\chi_{kl}P_l^*\otimes P_k, \quad (4.12)$$

so that

$$\hat{\Lambda}_{ave} = \frac{1}{3}\sum_{i}(S_i^T\otimes S_i^\dagger)\left(\frac{1}{4}\sum_{j,k,l}\chi_{kl}(P_j^\dagger P_l P_j)^*\otimes(P_j^\dagger P_k P_j)\right)(S_i^*\otimes S_i). \quad (4.13)$$

Using the property that $P_i^2=\mathbb{1}$, and that any given non trivial Pauli matrix (X, Y or Z) only commutes with itself and the identity and anti-commutes with the two others, all the off-diagonal of the χ matrix representing the Pauli twirled channel must then vanish, i.e.

$$\begin{aligned}\hat{\Lambda}_{ave} &= \frac{1}{3}\sum_{i}(S_i^T\otimes S_i^\dagger)\left(\sum_k\chi_{kk}(P_k^*\otimes P_k)\right)(S_i^*\otimes S_i) \\ &= \sum_k\chi_{kk}\left(\frac{1}{3}\sum_i(S_i^\dagger P_k S_i)^*\otimes(S_i^\dagger P_k S_i)\right) \quad (4.14)\end{aligned}$$

A channel represented by a diagonal χ matrix (in the Pauli basis) is called a *Pauli channel*. To evaluate the last line of the above equation, let us first consider the case $P_k=\mathbb{1}$. In this case, the sum obviously returns $\mathbb{1}$ back. For the non-trivial Paulis, the situation will be symmetric, so we only need to consider $P_k=X$ for example, which transforms as

$$X^*\otimes X \rightarrow \begin{cases} X^*\otimes X & \text{if } Q_k=X \\ Y^*\otimes Y & \text{if } Q_k=Z \\ Z^*\otimes Z & \text{if } Q_k=Y \end{cases}, \quad (4.15)$$

which allows us to conclude that

$$\hat{\Lambda}_{ave} = \chi_{11}\mathbb{1}+\frac{1}{3}\left(\sum_{k=2}^{4}\chi_{kk}\right)(X^*\otimes X+Y^*\otimes Y+Z^*\otimes Z). \quad (4.16)$$

which is a depolarizing channel (see Sec. 5.2). The action of the above channel on a state ρ can be represented in the Kraus form as

$$\Lambda_{ave}(\rho) \;=\; \chi_{11}\rho + \frac{1}{3}\left(\sum_{k=2}^{4}\chi_{kk}\right)\left(X\rho X + Y\rho Y + Z\rho Z\right). \tag{4.17}$$

From this simple exercise, we see that performing a single qubit Clifford twirling has the effect of diagonalizing the χ matrix and averaging the parameters corresponding to different error weights, i.e. $p_0 = \chi_{11}$, describing the probability of undergoing no error, and $p_1 = \sum_{k=2}^{4}\chi_{kk}$, the average probability of any single qubit error.

We can already see a hint on how to extract p_0 and p_1. If we probe the channel with the state $\rho = |0\rangle\langle 0|$, the twirled output state ρ_{out} is given by

$$\begin{aligned}\rho_{out} &= p_0|0\rangle\langle 0| + \frac{1}{3}p_1\left(|1\rangle\langle 1| + |1\rangle\langle 1| + |0\rangle\langle 0|\right)\\ &= = \left(p_0 + \frac{p_1}{3}\right)|0\rangle\langle 0| + \frac{2}{3}p_1|1\rangle\langle 1|.\end{aligned} \tag{4.18}$$

By acquiring statistics on the measurements in the computational basis, it is therefore possible to directly evaluate p_0 and p_1.

4.4 Multi-qubit Clifford twirling

It is possible to define the Clifford group on any number of qubits from a simple generalization. If we denote the n qubit Pauli group by $\mathcal{P}_n$, which is defined as qubit as

$$\mathcal{P}_n \;=\; \left\{\bigotimes_{i=1}^{n} P_i \;\middle|\; P_i \in \{\pm\mathbb{1},\ \pm X,\ \pm Y,\ \pm Z\}\right\}, \tag{4.19}$$

the n qubit Clifford group $\mathcal{C}_n$ is defined as the subgroup of the $2^n \times 2^n$ unitary matrices that is the normalizer of the Pauli group, i.e.

$$\mathcal{C}_n \;=\; \left\{C \in \mathcal{U}(2^n) \;\middle|\; CPC^\dagger \in \mathcal{P}_n,\ \forall\ P \in \mathcal{P}_n\right\}. \tag{4.20}$$

As we will see in Chapter 5, Clifford twirling is a unitary 2-design, implying that the averaged channel corresponds to a depolarizing channel, which essentially gives only two independent parameters: the probability of no error, and the probability of any error of any weight happening on any qubit. Such twirling coarse-grains the noise too much and we wish to extract more information.

On the other hand, it is intuitive to observe that if we perform single qubit twirling on each qubit, the resulting channel should be coarse-grained according to the weight of the errors. Since we want to characterize the errors by their weights independent of which qubit is affected, qubit permutations will also be needed to ensure that, if the noise if stronger on a certain qubits, it will be distributed to the others.

To show this fact, we only need to generalize the single qubit procedure. We will denote the *symmetrized* single qubit Clifford twirling on n qubits as a $\widetilde{\mathcal{C}}^{\otimes n}$ twirling, where we define

$$\begin{aligned} \widetilde{\mathcal{C}}^{\otimes n} &= \mathcal{C}^{\otimes n}\Sigma_n \\ &= \left\{ \left(\bigotimes_{i=1}^{n} \hat{C}_i \right) \sigma \;\middle|\; C_i \in \mathcal{C}_1,\ \sigma \in \Sigma_n \right\}. \end{aligned} \tag{4.21}$$

Σ_n is the n qubit permutation group and $\mathcal{C}^{\otimes n}$ is the tensor product of all the single qubit Cliffords. A $\widetilde{\mathcal{C}}^{\otimes n}$ twirling is therefore a single qubit Clifford twirling on each qubit, preceded by a permutation twirl of the qubits. The cardinality of $\widetilde{\mathcal{C}}^{\otimes n}$ grows exponentially since $|\widetilde{\mathcal{C}}^{\otimes n}| = n!48^n$, but we will see that with randomization, full twirling is unnecessary. Moreover, since only twelve operations are needed to twirl a single qubit, $n!12^n$ should be enough to separately depolarize each n qubits.

As in the one qubit case, the $\mathcal{C}^{\otimes n}$ twilring will be equivalent to a symplectic twirl followed by a Pauli twirl, so that

$$\widetilde{\mathcal{C}}^{\otimes n} \;\cong\; \bar{\mathcal{P}}_n \bar{\mathcal{S}}_n \Sigma_n, \tag{4.22}$$

where $\bar{\mathcal{S}}_n$ and $\bar{\mathcal{P}}_n$ are defined as all the tensor products of $\bar{\mathcal{S}}_1$ and $\bar{\mathcal{P}}_1$ operations respectively. Therefore, a minimum fully symmetrized Clifford twirl of a n qubit channel can be expressed as

$$\begin{aligned} \hat{\Lambda}_{ave} &= \frac{1}{|\Sigma_n||\bar{\mathcal{P}}_n||\bar{\mathcal{S}}_n|} \sum_{\sigma\in\Sigma_n} \sum_{P\in\bar{\mathcal{P}}_n} \sum_{S\in\bar{\mathcal{S}}_n} (\hat{\sigma}^\dagger \hat{S}^\dagger \hat{P}^\dagger) \hat{\Lambda} (\hat{P}\hat{S}\hat{\sigma}) \\ &= \frac{1}{n!4^n 3^n} \sum_{\sigma\in\Sigma_n} \sum_{P\in\bar{\mathcal{P}}_n} \sum_{S\in\bar{\mathcal{S}}_n} (\hat{\sigma}^\dagger \hat{S}^\dagger \hat{P}^\dagger) \hat{\Lambda} (\hat{P}\hat{S}\hat{\sigma}) \end{aligned} \tag{4.23}$$

The key observation is that, as in the single qubit case, given a Pauli matrix in $\mathcal{P}_n$, it will commute with half the Pauli group and anti-commute with the other half. This fact is easily provable by induction. Therefore, a multi qubit Pauli twirl

will still transform Λ_{ave} into a Pauli channel (diagonal), such that

$$\begin{aligned}\hat{\Lambda}_{ave} &= \frac{1}{n!3^n}\sum_{\sigma\in\Sigma_n}\sum_k \chi_{kk}\hat{\sigma}^\dagger\left(\sum_{S\in\bar{\mathcal{S}}_n}(S^T\otimes S^\dagger)(P_k^*\otimes P_k)(S^*\otimes S)\right)\hat{\sigma} \\ &= \frac{1}{n!3^n}\sum_k \chi_{kk}\left(\sum_{\sigma\in\Sigma_n}\sum_{S\in\bar{\mathcal{S}}_n}\hat{\sigma}^\dagger\hat{S}^\dagger\hat{P}_k\hat{S}\hat{\sigma}\right). \end{aligned} \tag{4.24}$$

In order to evaluate the effect of the symmetrized symplectic twirl on the channel, we will consider its effect on an arbitrary Pauli operator P_k such that $w(P_k) = w_k$. Under the simplectic twirl, P_k will be *explicitly* (with no addition and substraction) mapped to 3^n terms. These terms will have all possible Pauli operators on the qubits that P_k had a non-trivial action on. Since there are only 3^{w_k} such terms, it is expected to have recurrence in the explicit expression. Moreover, the sum over all the permutations will map each term to $n!$ other terms, so that the explicit expression of the symmetrized twirling will have $n!3^n$ terms.

This twirling will therefore map P_k to all possible Pauli operator with weight w_k. There are $3^{w_k}\binom{n}{w_k}$ different such terms, so that, in the explicit expression, each different terms will occur $\frac{n!3^n}{3^{w_k}\binom{n}{w}}$ times. Therefore

$$\sum_{\sigma\in\Sigma_n}\sum_{S\in\bar{\mathcal{S}}_n}\hat{\sigma}^\dagger\hat{S}^\dagger\hat{P}_k\hat{S}\hat{\sigma} = \frac{n!3^{n-w_k}}{\binom{n}{w_k}}\sum_{l\in\mathcal{I}_{w_k}}\hat{P}_l, \tag{4.25}$$

where we define $\mathcal{I}_{w_k}$ as the set of indices such that $w(P_l) = w_k\ \forall l \in \mathcal{I}_{w_k}$. Eq. 4.24 can thus be written has

$$\hat{\Lambda}_{ave} = \sum_k \chi_{kk}\frac{1}{3^{w_k}\binom{n}{w_k}}\sum_{l\in\mathcal{I}_{w_k}}\hat{P}_l. \tag{4.26}$$

By regrouping the terms with respect to their weight, it is possible to rewrite the above equation as

$$\hat{\Lambda}_{ave} = \sum_w \frac{1}{3^w\binom{n}{w}}\left(\sum_{k\in\mathcal{I}_w}\chi_{kk}\right)\left(\sum_{l\in\mathcal{I}_w}\hat{P}_l\right). \tag{4.27}$$

Observing that the probability of having any error of weight w affecting any qubit can be extracted from the χ matrix as

$$p_w = \sum_{k\in\mathcal{I}_w}\chi_{kk}, \tag{4.28}$$

we can therefore write the full expression for the symmetrized Clifford twirled channel as

$$\hat{\Lambda}_{ave} = \sum_{w} \frac{p_w}{3^w \binom{n}{w}} \left(\sum_{l \in \mathcal{I}_w} \hat{P}_l \right). \tag{4.29}$$

Therefore, the twirled channel can be described using only $n+1$ parameters, which is exponentially less than the original channel.

In order to be able to have an estimate of p_ω, we can probe the channel with the fiducial initial state $|0\rangle^{\otimes n}$ and perform a projective measurement of the outcome in the computational basis. As a matter of fact, the twirl channel will map the initial state to a mixture of states with different Hamming weights ((number of ones in the state), depending on which error operator affected the qubits. By gathering statistics on the measurements, we can infer the probability of errors of a given weight occuring.

Because the computational basis states are eigenstates of the Z_i operators, the measurement of an output state with Hamming weight m only gives the amount of X and Y operators present in the noise that affected the qubits. Therefore, the probability q_m of measuring any state with Hamming weight m will be a combination of all the probabilities p_w that have exactly m non-Z operators, so that

$$q_m = \sum_{\omega=0}^{n} R_{m\omega} p_\omega. \tag{4.30}$$

Since $m \leq w$, we know that R will be an upper triangular matrix and since none of the diagonal entries vanishes, it is also invertible. For a given w, there is $\binom{n}{w}$ locations for an error to happen. There will be $2^m \binom{w}{m}$ different terms with m X or Y error and the remaining $\omega - m$ will be Z errors. Therefore,

$$R_{m\omega} = \frac{2^m \binom{w}{m}}{3^w} p_w. \tag{4.31}$$

Once the $\vec{q}$ values are experimentally measured, it is then possible to recover $\vec{p}$ by

$$\vec{p} = R^{-1} \vec{q}. \tag{4.32}$$

Since the initial state is symmetric, the initial permutation operations are no longer necessary. Moreover, the final permutations can also be ignored if we only measure the Hamming weight of the output state, regardless of the location of the 1's.

As we already mentioned before, a complete $\mathcal{C}^{\otimes n}$ twirling requires an exponential number of experiments, i.e. $n! 12^n$. On the other hand, one can invoke the Chernoff

inequality to show that it is possible to estimate the value of q_m within a precision of δ using only $\frac{\log(2)}{\delta^2}$ experiments. Since the amount is logarithmic in the number of qubits, this protocol is efficient.

In practice, for a given QECC of distance d, we are only interested in knowing the probability of an error of weight greater than $t = \frac{1}{2}(d-1)$ to happen. Therefore, we only need to estimate the value of $p_0 \dots p_t$ to estimate a upper bound on the probability of failure of the QECC.

As a final point, we should mention that knowing the value of $\vec{p}$ can provide us with a test to determine if noise correlations are present in the system. For example, if the noise is completely uncorrelated (Markovian), then the p values should satisfy

$$p_\omega = p_1^\omega \tag{4.33}$$

4.5 Modifications for the NMR implementation

In NMR, we do not have access to projective measurements. On the other hand, NMR being a case of ensemble quantum computing, it is still possible to evaluate q_m. As explained in Sec. 2.4.4, the signal of each absorption Lorentzian peak of a given spectrum corresponds to the probability of measuring a given computational basis state on the other spins. By the properties of the twirled channel, the readout spin should be along the z axis. After the pulse applied on the readout nucleus, the normalized integral of a given peak (with respect to the thermal state), will also give us information about the state of the readout nucleus.

For example, on a $N+1$ spin molecule, if we consider the output signal of the peak corresponding to the $X|0\rangle\langle 0|^{\otimes N}$ state, there will be a positive contribution from the term in which the nucleus points up ($+X|0\rangle\langle 0|^{\otimes N}$ readout), and a negative contribution from the term where it points down ($-X|0\rangle\langle 0|^{\otimes N}$ readout). Therefore, since initially the readout nucleus was pointing up, the normalized integral of the output peaks will give us the probability of the all 0 state minus the probability of all zero state except for the readout nucleus. Since there is only one state of Hamming weight 0 and $n+1$ states of Hamming weight 1, the normalized signal s will give us the value

$$s_0 = q_0 - \frac{q_1}{N+1}. \tag{4.34}$$

This example generalizes easily. If we measure the signal of a peak corresponding a state of the other nuclei of weight m, then the normalized signal corresponds to

$$s_m = \frac{q_m}{\binom{N+1}{m}} - \frac{q_{m+1}}{\binom{N+1}{m+1}}. \tag{4.35}$$

It is therefore possible to extract enough independent values from a spectrum to solve for $\vec{q}$ and thus find $\vec{p}$. Performing the implementation this way might not be the most practical route for an increasing number of spins. For example, every peak corresponding to a given Hamming weight w of the remaining spins (there are $2^{\binom{N}{w}}$ of them) will have the same signal. Preprocessing will be needed to define which peak should be used, or an average of all of them will be done. In all cases, an exponential number of peak will have to be processed.

On the other hand, the initial state of the protocol on n qubit is chosen to be all 0 state. This fiducial state can be decomposed as

$$|0\rangle\langle 0|^{\otimes n} = \frac{1}{2^n}\sum_{w=0}^{n}\bar{Z}_w, \tag{4.36}$$

where $\bar{Z}_w$ is the sum of all the Pauli operators containing w Z and $n-w$ identities, which is equivalent

$$\bar{Z}_w = \sum_{\sigma\in\Sigma_n}\sigma^\dagger\left(Z^{\otimes w}\otimes \mathbb{1}^{\otimes(n-w)}\right)\sigma, \tag{4.37}$$

for all the permutation operations σ. Using again the fact that Pauli operators either commute or anti-commute with each other, we know that for any Pauli channel,

$$\Lambda(P) = \alpha_P P, \text{ for any } P\in\mathcal{P}_n, \tag{4.38}$$

This says that every Pauli matrix is an eigenoperator of the channel. The value of α_P is given by

$$\alpha_P = \Pr(\mathrm{C}) - \Pr(\mathrm{A}) \tag{4.39}$$

where $Pr(C)$ and $Pr(A)$ is the probability that an operator of the channel commutes or anti-commutes with P respectively.

By the symmetric property of the twirled channel, α_P must be the same for any Pauli input state of the same weight. If we define the coefficient c_w by

$$\begin{aligned} c_w &= \left\langle\bar{Z}_w\right\rangle \\ &= \mathrm{Tr}\left[\Lambda_{ave}\left(\bar{Z}_w\right)\bar{Z}_w\right], \end{aligned} \tag{4.40}$$

one can show that the c's and p's are related via an invertible matrix such that

$$\vec{p} = \Omega^{-1}\vec{c}. \tag{4.41}$$

The proof of this fact is beyond the scope of this thesis, but the matrix Ω is given by

$$\Omega_{ww'} = -1 + \sum_{L=\max(0,w+w'-n)}^{\min(w,w')} \frac{\binom{n-w}{w'-L}\binom{w}{L}}{\binom{n}{w'}} \frac{3^L + (-1)^L}{3^L} \tag{4.42}$$

$$\Omega^{-1}_{ww'} = \frac{3^{w+w'}\binom{n}{w}\binom{n}{w'}}{4^n}\Omega_{ww'} \tag{4.43}$$

As an example, for the two qubit case, we have

$$\Omega = \begin{pmatrix} 1 & 1 & 1 \\ 1 & \frac{1}{3} & -\frac{1}{3} \\ 1 & -\frac{1}{3} & \frac{1}{9} \end{pmatrix} \tag{4.44}$$

$$\Omega^{-1} = \frac{1}{16}\begin{pmatrix} 1 & 6 & 9 \\ 6 & 12 & -18 \\ 9 & -18 & 9 \end{pmatrix} \tag{4.45}$$

Each c_w can be estimated to within precision δ using only $\frac{\log(2(n+1))}{\delta^2}$. It can also be shown that estimating the values of all c_w leads to an uncertainty on the values of p_w that grows only polynomially in n and the degree of the polynomial is linear in w. This implies that the uncertainties on $\vec{c}$ do not propagate badly to the value of $\vec{p}$, as long as we estimate the values for $w \leq t$, for fixed t.

The advantage of such a scheme is that, in NMR, the preparation of the computational state $|0\rangle^{\otimes n}$ can be challenging (Sec. 2.3). On the other hand, the preparation of $Z^{\otimes w} \otimes \mathbb{1}^{\otimes n-w}$ can be easily done through a series of simple pulses and J-couplings (essentially the same as the encoding part of the pseudo-pure state preparation). The average over the permutation operations at the beginning and the end of the protocol will effectively create the initial state $\bar{Z}_w$. The final permutation will ensure that the readout state will be of the form $c_w Z^{\otimes w} \otimes \mathbb{1}^{\otimes n-w}$.

4.6 Experimental details

4.6.1 The experiment

To demonstrate the feasibility of the twirling protocol, we designed a two qubit experiment probing three different sources of error. The protocol was tested on the standard heteronuclear 2-spin molecule used in many other QIP experiments [CVZ+98, LVZ+99, ZLSD02]: carbon-13 labeled chloroform ($CHCl_3$). The molecule and its magnetic properties can be seen in Fig. 4.1. Chloroform is an ideal choice

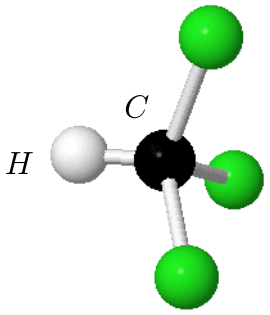

H	-5627.02	
C	215.2	-13790.17
	H	C

Figure 4.1: Chemical structure and relevant magnetic properties of chloroform ($CHCl_3$). The diagonal elements gives the chemical shift of the nuclei with respect to the carrier frequency of the spectrometer for that particular isotope. The off-diagonal element gives the H-C coupling.

for NMR QIP as it possesses long coherence times (well over $1s$). For the following sections, we will label H as qubit 1 and C as qubit 2.

The protocol will be tested for the three different engineered noises given by the Kraus operators

$$\{A_k^{(1)}\} = \frac{1}{\sqrt{2}}\{Z_1,\ Z_2\} \tag{4.46}$$

$$\{A_k^{(2)}\} = \{Z_1 Z_2\} \tag{4.47}$$

$$\{A_k^{(3)}\} = e^{-i\frac{\pi}{4}(Z_1+Z_2)}. \tag{4.48}$$

The first engineered noise corresponds to a $1/2$ probability for each spin to undergo a phase flip and the second corresponds to a certainty of having a two spin phase flip. The third engineered noise will induce a coherent error of a $\pi/2$ rotation around the z-axis. If we expand this error, we have

$$\begin{aligned} e^{-i\frac{\pi}{4}(Z_1+Z_2)} &= e^{-i\frac{\pi}{4}Z_1} \otimes e^{-i\frac{\pi}{4}Z_2} \\ &= \frac{1}{2}\left(\mathbb{1} - iZ_1 - iZ_1 - Z_1Z_2\right), \end{aligned} \tag{4.49}$$

which will induce a single spin phase flip twice as often as a double, or no, phase flip. The summary of the expected values of $\vec{c}$ and $\vec{p}$ is available in Table 4.1.

In order to achieve a good proof of principle, a complete twirling of the noise was performed. Since 12 operations are needed to depolarize each qubit, 144 operations are needed to perform a $\mathcal{C}^{\otimes 2}$ twirl. Since there are only 2 permutations (no-operation and a swap), a complete twirling will require 288 experiments.

exp. #	p_0	p_1	p_2	c_0	c_1	c_2
1	0	1	0	1	$\frac{1}{3}$	$-\frac{1}{3}$
2	0	0	1	1	$-\frac{1}{3}$	$-\frac{1}{9}$
3	$\frac{1}{4}$	$\frac{1}{2}$	$\frac{1}{4}$	1	$\frac{1}{3}$	$\frac{1}{9}$

Table 4.1: Expected value of $\vec{p}$ and $\vec{c}$ for the different engineered noises described in Eq. 4.46.

4.6.2 Pulse sequences

The goal of the experiments is to demonstrate a proof of principle. Since two-qubit NMR QIP experiments are easily implemented, the ultimate goal of this work was to demonstrate the quality of the control possible in NMR by achieving the highest precision possible. The first step toward this realization was to enable a systematic way of obtaining and comparing the values of c_w.

To extract $\vec{c}$ from each experiment, three different input states needed to be created:

$$\rho_0 = \mathbb{1}_1 \otimes \mathbb{1}_2 \tag{4.50}$$

$$\rho_1 = Z_1 \otimes \mathbb{1}_2 \tag{4.51}$$

$$\rho_2 = Z_1 \otimes Z_2 \tag{4.52}$$

Since ρ_0 is undetectable in any NMR experiment, we had to assume that $c_0 = 1$ in all cases. When dealing with ρ_1 as an input state, the protocol stipulates that we had to implement a permutation before and after the Clifford operations in order to create the effective initial state $Z_1 + Z_2$. Unfortunately, this permutation requires pulses and J-coupling evolutions which might introduce state preparation control errors. Because of this, measuring the signal when there is a permutation might lead to a smaller residual signal compared to when no permutation was applied, which in turn will affect the averaged value of c_1. Similarly, ρ_2 is already a symmetric state and the permutation operations are not needed. On the other hand, the obtained values of c_2 would also not take into account the possible errors introduced from the permutations needed to extract c_1.

The solution to this problem was to always concretely apply a permutation pulse sequence. If no swap was needed, the pulse sequence will effectively implement the identity. This way, all the different sub-experiments contained the same number of pulses and any introduced errors were thus, on average, normalized with respect to each other.

Finally, as in the case of the preceding chapter, since the implemented noise corresponds to phase flips, the engineered noise was implemented through virtual

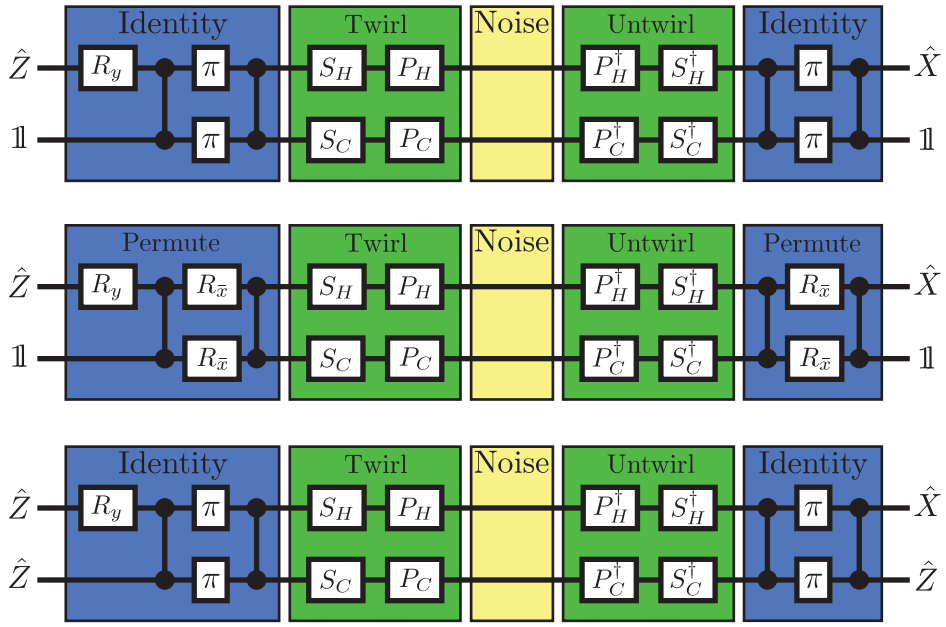

Figure 4.2: Different pulse sequences for the two qubit twirling experiments depending on the desired initial state.

z-rotations, which can be implemented by modifying the phase of subsequent pulses and possibly the phases of the receiver during the recording of the FID. To create the random error in experiment #1, the noise was implemented by applying a phase shift on H for half the experiments and on C for the other half. To be consistent with the random nature of this noise, the experiments were chosen at random.

The final pulse sequence for the three different sub-experiments (i.e. initial state ρ_1 with and without permutation, and ρ_2) can be seen in Fig. 4.2. By implementing these three different pulse sequences, the initial state preparation and state readout part of the pulse sequence had the exact same number of pulses and J-couplings; hence the results of all these sub-experiments can be fairly compared.

Finally, it should be noted that, in order to minimize the number of pulses, the identity operations and the permutations actually left the state of the spins in $X_1\mathbb{1}_2$, $\mathbb{1}_1X_2$ and X_1Z_2. Since the twirling protocol is entirely symmetric with respect to the Pauli axes, the modified protocol developed in Sec. 4.5 could have used any state $\bar{X}_\omega$, $\bar{Y}_\omega$, or any symmetric mixture of X, Y or Z with weight ω.

4.6.3 Electronic analysis

In the previous section, we described a method to treat all the sub-experiments on the same footing. Unfortunately, as we will shown in Sec. 4.6.4, this was not

enough to give highly precise results. One major source of error that was previously ignored was the imperfection of the pulse generation at the sample.

Since chloroform is a heteronuclear 2-spin system, hard pulses are usable for selective control of the spins. A hard pulse consists of a short burst of RF power at the frequency of the targeted spin, i.e. a square shaped pulse. As explained is Sec. 2.4.2, commercially available NMR probehead consist of a LC circuit, where the RF magnetic field is created at the inductor (L). A resonant circuit has a finite response to excitation, i.e. since it has a finite resonance frequency bandwidth. Short, square pulses, which have a wide Fourier spectrum, are never completely sharp and have a finite rise time.

To implement the twirling experiment, we used a cryo-probe with a very narrow bandwidth, which leads to large distortions of the square pulses. This probehead has a double coil that is triple resonant, but the details of the LC circuit are unavailable due to intellectual property protection. For the sake of analysis and to verify our claim, we performed signal analysis using a standard single resonance circuit [FR86]. A typical RF resonance circuit is depicted in Fig. 4.3. With commercially available NMR spectrometers, commands about the frequency, length and shape of the pulses are digitally sent to the spectrometer, which in turn create the wave form using a frequency generator and an arbitrary waveform generator. The final wave is then amplified and sent to the probehead. For simplicity, we will assume that the signal the spectrometer sends is exactly the shape desired, such that we only analyze the effect of the RLC circuit.

In the present circuit, L_s is the coil where the RF magnetic field is created, hence where the sample is located. r is its associated resistance. From basic electronic circuit analysis [NR04], we know the parallel LC_T circuit has a complex impedance of

$$\mathcal{Z} = \frac{i\omega L_s + r}{1 - \omega^2 L_s C + i\omega C_T r}. \tag{4.53}$$

The condition for resonance will be given when the imaginary part of the impedance vanishes, which gives the resonance condition

$$\omega_0 = \sqrt{\frac{L_s - r^2 C_T}{L_s^2 C_T}} = 2\pi f_0. \tag{4.54}$$

Since the induction of L_s is fixed during the building of the probe, C_T is therefore a variable capacitor used to tune the resonance frequency. As a matter of fact, when changing from one sample to another, the impedance of the sample can modify the value of L_s and slightly change f_0.

In order to achieve matching conditions, the probe must have an impedance of 50Ω (just as the spectrometer). Since the parallel RLC circuit has a non-zero

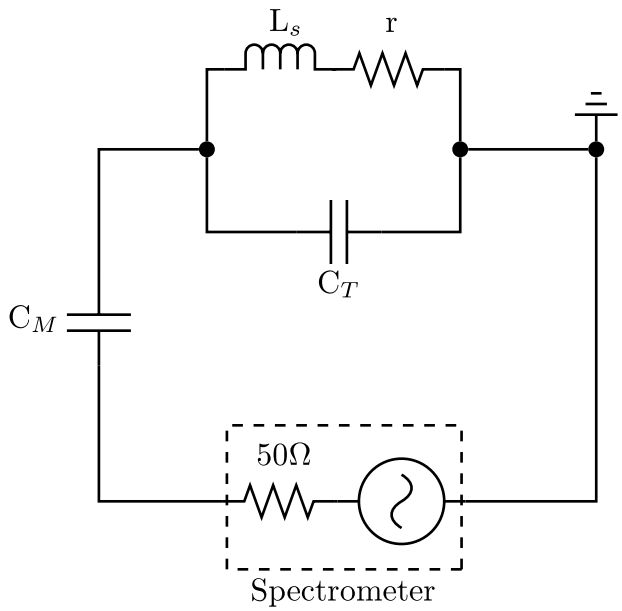

Figure 4.3: Single resonance RLC circuit. The resonant frequency can be tuned by varying C_T and the impedance of the circuit can be matched to that of the spectrometer (50Ω) by adjusting C_M.

resistance, its impedance is complex-valued. Therefore, an extra active circuit element (capacitor or inductor) is needed to achieve a real impedance. Although transmission lines can also be used [LE74], it is customary to use an extra variable matching capacitor C_m.

The quality factor of a resonant circuit is given as the amount of energy stored in the resonant part of the circuit over the dissipation power, i.e.

$$Q = 2\pi \frac{\text{Energy stored}}{\text{Energy dissipated per cycle}}. \tag{4.55}$$

For any simple linear circuit, the energy is stored in the active elements, i.e. inductors and capacitors, and dissipated by resistors. Since the current through an inductor is $\pi/2$ out of phase with the current through a capacitor, the energy stored in the LC circuit is given by the maximal energy stored in the inductor so that

$$\text{Energy stored} \;=\; \frac{1}{2}LI^2 \tag{4.56}$$

The power dissipated by a resistor is $P = vi = ri^2$, where v and i are the instantaneous potential difference and current in the resistor. On resonance, $i = I\sin(\omega_0 t + \phi)$ for a given phase ϕ. The energy dissipated per cycle is given by the

time integral of the dissipation power over an entire cycle of length $T = \frac{2\pi}{\omega_0}$:

$$\begin{aligned} \text{Energy dissipated per cycle} &= \int_0^T ri^2 dt \\ &= rI^2 \int_0^T \sin^2(\omega_0 t + \phi) \\ &= \frac{1}{2} rI^2 T \\ &= \frac{\pi}{\omega_0} rI^2 \end{aligned} \tag{4.57}$$

Therefore

$$Q = \frac{\omega_0 L}{r}. \tag{4.58}$$

Full simulations of the probe response to a given driving source have been conducted using a free version of SPICE [NP73], a general purpose simulation program for electronic circuits. Some details of the simulator are given in Appendix C.

The Bruker spectrometer software, XWin-NMR, has the capability to measures the reflected power (under a given frequency excitation, of the resonant circuit in real time. If we plot this reflection as a function of a frequency sweep, a dip is expected at the resonance frequency. In terms of electric properties of the circuit, the reflected power takes the expression

$$\text{Reflected Power} = \left| \frac{\mathcal{Z}_c - \mathcal{Z}_{sp}}{\mathcal{Z}_c + \mathcal{Z}_{sp}} \right|, \tag{4.59}$$

where $\mathcal{Z}_c$ is the complex impedance of the LC circuit and $\mathcal{Z}_{sp} = 50\Omega$ is the impedance of the source, i.e. the spectrometer. From the reflected power function of a given circuit, the value of Q can be extracted using

$$Q = \frac{f_0}{\text{FWHM}}, \tag{4.60}$$

where the FWHM is the full width of the reflected power dip at half the minimum.

For the simulations, we choose values of L, r, C_T and C_m that approximated the best the conditions of the hydrogen channel on our cryoprobe:

$$\begin{aligned} f_0 &= 700 \text{ MHz} \\ Q &\approx 700 \\ \mathcal{Z} &= 50\ \Omega. \end{aligned} \tag{4.61}$$

The value of the circuit elements and the simulation of the reflected power as a function of the frequency can be seen in Fig. 4.4.

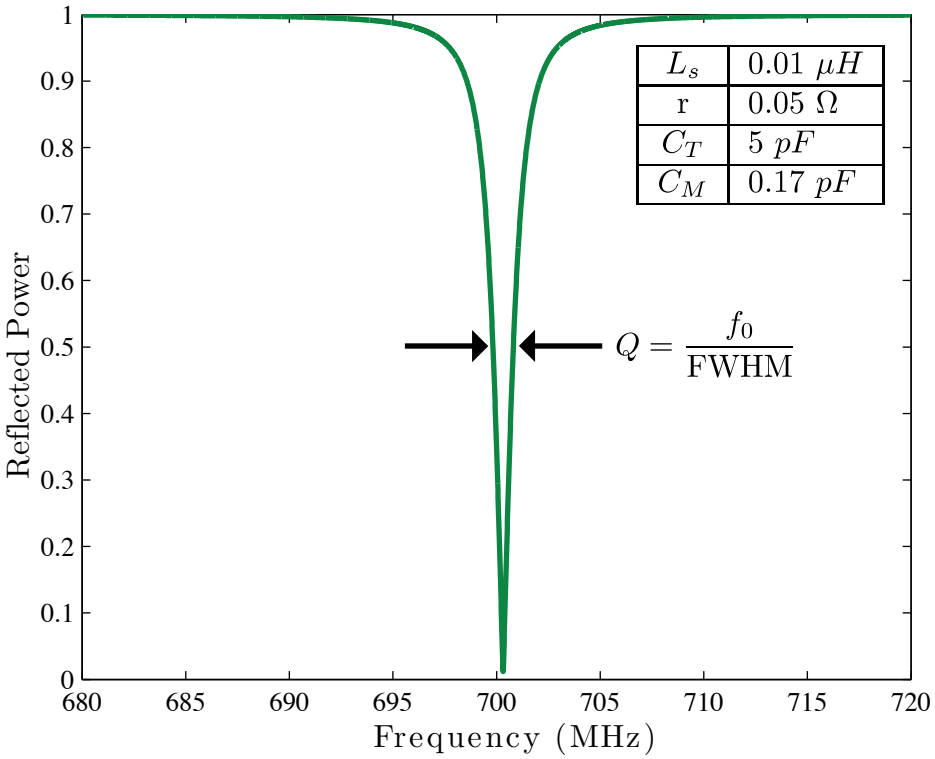

Figure 4.4: Approximated lumped element values and simulated reflected power as a function of excitation frequency for the cryoprobe resonant circuit depicted in Fig. 4.3.

One can verify that if we use the values of the lumped elements in Eq. 4.54 and 4.60, we do not obtain the values claimed in Eq. 4.61, but a value somewhat similar. Although ignored, the presence of the matching capacitor C_m does have a small effect on the resonance frequency and on the quality factor of the circuit, phenomenon that we actually observe experimentally.

Using SPICE, we first created a square pulse of 10 μs in length with an arbitrary power and recorded the voltage across the inductor L_s. Since the magnetic field inside an inductor is directly proportional to the voltage across it, we could reconstruct the RF field at the sample. By demodulating the simulated field with the same carrier frequency as that of the input pulse, we were able to analyze the quadrature components of the field at the sample. The input pulse only had an amplitude in the x quadrature and the simulated hard pulse out of the source is shown in black in Fig. 4.5. The demodulated x and y components measured at the sample are in blue and red.

Due to the high quality factor of the probe, the electric circuit takes a long time to react to a driving voltage, hence explaining the low rise of the pulse. For the

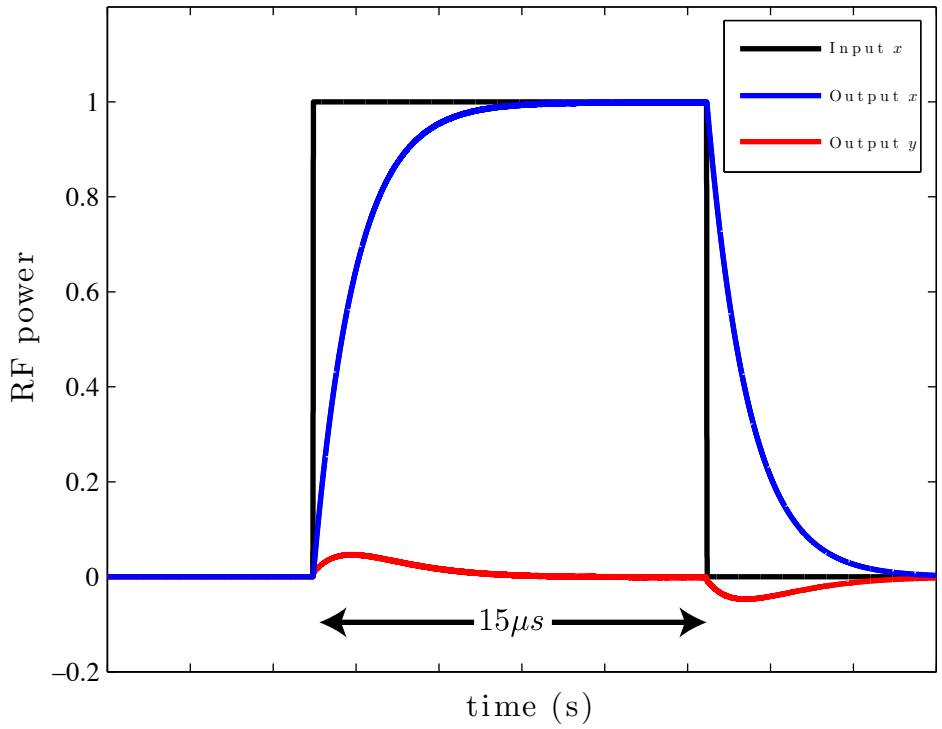

Figure 4.5: Simulated quadrature components of a short hard pulse measured at the probehead. Due to the finite response time of the circuit, the pulse at the probe will contain unwanted quadrature components.

same reason, once the input voltage is turned of, the circuit keeps resonating and the current dissipates in a finite amout of time. From a Fourier analysis argument, the high Q of the probe means that it does not resonate as well for frequencies away from f_0. Since high and low frequencies are responsible for shaping the edges of a pulse, the measured signal is expected to be smoother than the input. The extra signal in the y quadrature is known as the *phase transients* and is a well documented phenomenon in the NMR community [VES+72, AHT76, BMW91, Veg04].

The major problem arising from phase transients is that it will not create exactly the desired unitary operation. That is, if we want to implement a $\pi/2$ degree pulse around, say, the x-axis, in reality, the unitary transformation will be different. In an experimental setting, these effects can be hidden during the calibration process. As a matter of fact, the usual calibration technique is to apply the pulse on a known initial state and optimize the phase and power of the pulse to maximize the signal of the final known state. For example, we calibrate a $\pi/2$ y pulse by first defining the x axis. To do so, we apply the possibly mis-calibrated y pulse to the thermal state Z and rephase the obtained spectrum so that it shows absorption Lorentzian

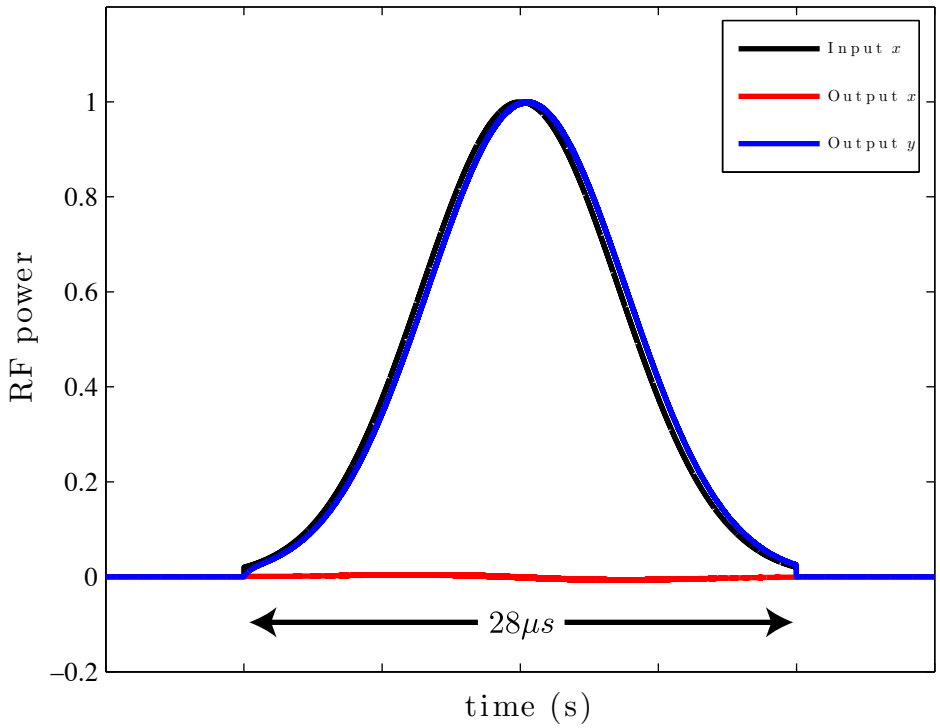

Figure 4.6: Simulated quadrature component of a short hard pulse measured at the probehead. The smoothness of a Gaussian pulse does not require high frequency components to generate the pulse and no phase transients are observed.

peaks only, hence defining the set of axes for the xy plane. The power is then optimized to maximize the signal.

Since a pulse with phase transients does not rotate the spins along a constant axis, the choice of xy could be erroneous. Therefore, using different types of pulses at different phases for a given sequence will introduce calibration and phase errors, hence diminishing the fidelity of the operations.

Following the above Fourier argument, we thus expect that a smoother, slowly varying pulse should have fewer phase transients. Indeed, this conclusion is verified from the simulation of a $28us$ Gaussian shaped pulse, discretized over 40 points with a 3% cut-off. The quadrature component of the input and output pulse can be seen in Fig. 4.6.

As expected, the measured pulse at the sample is essentially identical to the input pulse. As a final remark, we should point out that the above simulation does not exactly correspond to reality. As already mentioned, we do not have access to the actual electronic circuit of our high Q cryoprobe. We did however, measure and demodulate the magnetic field at the sample by placing a small coil in a

test tube and recording the induced voltage using the receiver of the spectrometer. For hard pulses, we still measured phases transients, but they were much less pronounced than in Fig. 4.5. Nevertheless, the search for high fidelity control forces us to reconsider the use of hard pulses and migrate towards softer pulses, even for heteronuclear systems. Unfortunately, soft pulses usually takes longer to implement and thus errors coming from the natural evolution of the system can jeopardize the improvements. Ultimately, we want to reach the optimal trade-off between phase transient effects and unwanted evolution errors.

4.6.4 Experimental results

The reason why the above signal analysis was performed was because the first successful implementation of the protocol led to results that were close to the expected values, but given that the experiment was only on two qubits, we expected much better results. Once the value of $\vec{c}$ was measured by averaging the spectra of all the 288 experiments, they were fitted with absorption and dispersion Lorentzian functions and integrated. The uncertainties of the c's were estimated from the fitting of the spectra and the signal to noise ratio. The propagation of these errors to $\vec{p}$ was then calculated using the method of maximum likelihood [vdV98]. The original results are given in Table 4.2.

exp. #	p_0	p_1	p_2	c_0	c_1	c_2
1	$0.000^{+0.026}_{-0.000}$	$1.000^{+0.000}_{-0.025}$	$0.000^{+0.006}_{0.000}$	1	0.36 ± 0.01	-0.36 ± 0.02
2	$0.00^{+0.04}_{-0.00}$	$0.00^{+0.06}_{-0.00}$	$1.00^{+0.00}_{0.07}$	1	-0.31 ± 0.02	0.121 ± 0.03
3	$0.25^{+0.03}_{-0.03}$	$0.44^{+0.06}_{-0.06}$	$0.30^{+0.05}_{0.04}$	1	0.30 ± 0.02	0.14 ± 0.03

Table 4.2: First set of experimental value of $\vec{p}$ and $\vec{c}$ obtained by performing the experiment using hard square pulses. The large deviation of the experimental values for $\vec{c}$ from the expected values yield unacceptably large uncertainties on the derived $\vec{p}$.

Although a quick glance at the results might lead to the conclusion that $\vec{p}$ was correctly evaluated (at least for the two first experiments), analysis of the value of $\vec{c}$ does show the imprecision of the implementation. The reason the $\vec{p}$'s are correctly derived is simply due to the bounds imposed to their values, which also explained the large uncertainties. For example, if we use the value of $\vec{c}$ for experiment 1 and the inversion matrix in Eq. 4.44, we obtain the value $\vec{p} = (-0.005,\ 1.05,\ -0.045)$. Since all those values are outside the permitted interval $[0,\ 1]$, the maximum likelihood method would then change them to $(0,\ 1,\ 0)$.

The imprecision becomes more obvious when analyzing the third experiment. In this situation, none of the expected p_w were at the boundaries of the allowed interval, and the value of $\vec{p}$ is clearly far from correct.

By changing from hard pulses to slightly longer, Gaussian shaped pulses, we have been able to measure the $\vec{p}$ and $\vec{c}$ vectors shown in Table 4.3. This table shows the improvement on the uncertainties on all the $\vec{p}$'s and most notably on the precision of the values for the third experiment .

exp. #	p_0	p_1	p_2	c_0	c_1	c_2
1	$0.000^{+0.004}$	$0.991^{+0.009}_{-0.015}$	$0.009^{+0.017}_{-0.009}$	1	0.32 ± 0.01	-0.34 ± 0.01
2	$0.001^{+0.006}_{-0.001}$	$0.004^{+0.011}_{-0.004}$	$0.996^{+0.004}_{-0.011}$	1	-0.330 ± 0.005	0.11 ± 0.01
3	$0.254^{+0.010}_{-0.010}$	$0.495^{+0.021}_{-0.020}$	$0.250^{+0.019}_{-0.019}$	1	0.336 ± 0.009	0.117 ± 0.009

Table 4.3: Final set of experimental value of $\vec{p}$ and $\vec{c}$ obtained using soft Gaussian pulses. The precise $\vec{c}$ and $\vec{p}$ demonstrate the positive consequences of using smooth pulses (no phase transients) over hard pulses.

From the final results, we see that the largest uncertainties happen for experiment 1. This larger error is actually due not to more control errors, but actually to statistical errors. As a matter of fact, the 288 experiments completely twirled the noise in experiment 2 and 3, while it only twirled within an error ϵ for experiment 1. The error model in experiment 1 is expressed a

$$\rho \quad \rightarrow \quad \frac{1}{2} Z_1 \rho Z_1 + \frac{1}{2} Z_2 \rho Z_2, \tag{4.62}$$

which means that in order to engineer such a noise, two separate experiments needed to be performed (one applying a Z_1 error and the other a Z_2 error). Since we were still performing 288 twirling experiments, choosing randomly whether qubit 1 or 2 is flipped, the final channel was just an average of two partially twirled channels.

4.7 Conclusion

In retrospect, we have explained the existence of a scheme that can extract relevant information about a given quantum channel without the necessity of performing inefficient quantum process tomography. By performing an approximate $\widetilde{\mathcal{C}}^{\otimes n}$ twirl on a n qubit channel, it is possible to measure the probabilities of errors of any given weight. This knowledge is necessary and mostly sufficient for developing QECCs, vital to fault-tolerant quantum computation. The experimental implementation on a 2 qubit quantum information processor led to three important conclusions:

1. The theoretically derived protocol is implementable and leads to the expected results.

2. Smoothly varying pulses should be used for high fidelity control due to the presence of phase transients in hard pulses.

3. The precision of the results demonstrates the quality of the control and hence the understanding of the system in liquid state NMR.

As mentioned previously, this scheme is perfect for probing channels that are intended to perform the identity, such as the time suspension sequences used in NMR homonuclear decoupling experiments [MG75, CLSW85, CMG90] or the control sequences used in a quantum memory [MJN+02, FL02, TML03, JSC+04]. In these cases, the value of p_0 would give the fidelity of the implementation of the identity. A generalization of this protocol can be used to benchmark the quality of non-trivial, fully coherent quantum operations, such as any computational gates in a given quantum computation. This protocol will be the subject of the next chapter.

Chapter 5

Benchmarking single and multi-qubit control

5.1 The paradox of benchmarking computational gates

In chapter 3, we developed a scalable technique for estimating important information concerning the behavior of the noise in a given system. In chapter 4, we described and implemented a protocol based on symmetrization and randomization to extract parameters of a noisy channel affecting, for example, quantum data storage. In retrospect, these two protocols are excellent for probing the sources of error when no computation is performed. Simply put, we assumed that the operation performed in the protocol were perfect so that the only source of noise was that of the channel.

The same type of assumption was made in the theory of quantum error correction, until somebody asked: what happens when the operations performed are themselves faulty? This simple but deep question led to the theory of fault-tolerant quantum computation [Sho96, Kit97b, CPZ96, ZL96]. Therefore, it is important to be able to characterize the control one has over their quantum information processing devices in such a way that errors in the implementation of the probing protocol do not influence the precision of the answer. As already mentioned in previous sections, quantum process tomography not only suffers from the exponential amount of resources, but also from errors in state preparation and readout that seriously affect the analysis and makes it difficult to reconstruct a completely positive map [BHPC03].

Therefore, if the goal of a probing experiment is to quantify the quality of the computational gates, we must ensure that errors in state preparation and readout

are much smaller than the errors per gate. As seen in section 2.3, initial state preparation can involve many computational gates and is thus considered noisy. Ultimately, we have the bootstrapping problem of benchmarking noisy computational gates using noisy computational gates and a protocol is needed to either overcome the paradoxical situation situation, or to embrace it.

Fortunately, Emerson and colleagues [EAZ05] showed that, under certain conditions, applying noisy but random gates effectively turns the noise into a depolarizing channel, which can be described using a single parameter. Based on this protocol, Knill et al. [KLR+08] developed a slightly modified single qubit experiment and implemented the protocol on a single qubit based on a trapped ion. We also directly applied the protocol using NMR on a single spin molecule to compare our results to theirs.

In this Chapter, we report our effort toward the implementation of the single qubit experiment in liquid-state NMR. Moreover, we discuss a possible generalization of the protocol for the benchmarking of multi qubit control, which would permit a fair comparison between processors of all sizes. This protocol was implemented on a three qubit liquid-state NMR processor.

5.2 Benchmarking protocol

5.2.1 Haar unitary randomization

In order to quantify the quality of the implementation of a given unitary U, we must define the concept of *average gate fidelity*. If we could write only the noise portion of the implementation as a superoperator, it is intuitive to defined the average gate fidelity as $\chi_{11} = p_0$, which gives the probability of Λ to affect no qubits. The strategy of the protocol will be to extract as efficiently as possible this value.

Suppose we wish to implement an ideal gate U. In reality, due to decoherence, mis-calibration and other sources of error, a faulty, completely positive map, Γ will be implemented, whose action on a given state ρ can be described using Kraus operators as

$$\Gamma(\rho) = \sum_k B_k \rho B_k^\dagger. \tag{5.1}$$

If we define the operators A_k as

$$A_k = B_k U^\dagger, \tag{5.2}$$

and we perform a motion reversal on $\Gamma(\rho)$, we have

$$\begin{aligned} U^\dagger \Gamma(\rho) U &= \sum_k U^\dagger A_k U \rho U^\dagger A_k^\dagger U \\ &= U^\dagger \Lambda \left(U \rho U^\dagger \right) U, \end{aligned} \tag{5.3}$$

where we have defined $\Lambda(\square) = \sum_k A_k \square A_k^\dagger$. From the form of the above equation, we can associate Λ with the superoperator corresponding to the cumulative noise in the implementation of U. If we choose $\rho = |\psi\rangle\langle\psi|$, the state fidelity of the gate U for this arbitrary state is

$$F(\Lambda, U, \psi) = \langle\psi| U^\dagger \Lambda \left(U|\psi\rangle\langle\psi| U^\dagger \right) U |\psi\rangle. \tag{5.4}$$

In order to make the fidelity independent of the input state and hence have an average gate fidelity, we can simply average over all the pure input states with the Fibini-Study metric $d\psi$, i.e.

$$\begin{aligned} F(\Lambda, U) &= \int d\psi \langle\psi| U^\dagger \Lambda \left(U|\psi\rangle\langle\psi| U^\dagger \right) U |\psi\rangle \\ &= \sum_k \int d\psi \left| \langle\psi| U^\dagger A_k U |\psi\rangle \right|^2. \end{aligned} \tag{5.5}$$

The Fubini-Study metric is an invariant metric over the pure states. For example, for a one qubit system, the metric is invariant over the Bloch sphere, meaning that if the Bloch sphere undergoes a given rotation R, the metric is the same, i.e. $dR\psi = d\psi$ [BH01, BZ06]. It has been shown that under the invariant metric, the average gate fidelity only depends on the noise and not on the gate itself as it takes the form [BOS+02, HHH99, Nie02]

$$F_\Lambda = F(\Lambda, U) = \frac{\sum_k |\mathrm{Tr}(A_k)|^2 + D}{D^2 + D}. \tag{5.6}$$

If we go back and analyze Eq. 5.5 from a different perspective, since the columns (or rows) of any unitary operator also correspond to pure quantum states, averaging over the states $|\psi\rangle$ for a given fixed U is equivalent to averaging over the unitary operators for a fixed state $|\psi\rangle$. Therefore, if we assume that the error Λ is *gate-independent*, we have

$$\begin{aligned} F(\Lambda, \psi) &= F(\Lambda, U) \\ &= \int dU \langle\psi| U^\dagger \Lambda \left(U|\psi\rangle\langle\psi| U^\dagger \right) U |\psi\rangle \\ &= \langle\psi| \left[\int dU U^\dagger \Lambda \left(U|\psi\rangle\langle\psi| U^\dagger \right) U \right] |\psi\rangle. \end{aligned} \tag{5.7}$$

The invariant metric on the unitary operators is known as the Haar measure and is invariant in the sense $dU = d(R_1 U R_2)$ for fixed unitaries R_1 and R_2 [Haa01]. If we rewrite the integral portion of Eq. 5.7 in the Liouville space, we obtain

$$\begin{aligned} \int dU U^\dagger \Lambda \left(U|\psi\rangle\langle\psi|U^\dagger \right) U &\cong \int d\hat{U} \hat{U}^\dagger \hat{\Lambda} \hat{U} |\psi\rangle\rangle \\ &= \hat{\Lambda}_{ave} |\psi\rangle\rangle, \end{aligned} \tag{5.8}$$

where we have defined the superoperator

$$\hat{\Lambda}_{ave} = \int d\hat{U} \hat{U}^\dagger \hat{\Lambda} \hat{U}. \tag{5.9}$$

By invoking the invariance of the Haar measure and Schur's lemma, Emerson et al. [EAZ05] proved that the averaged operator must cause a depolarizing action, i.e.

$$\Lambda_{ave}(\rho) = (1 - p_\Lambda)\rho + p_\Lambda \frac{\mathbb{1}}{D}, \tag{5.10}$$

that is, the noise either does not affect the state of the system with probability $p_0 = 1 - p_\Lambda$, or returns a completely mixed state with probability p_Λ. The value of p_Λ depends on the noise and an explicit formulation will be given below.

We can finally write, for any state $|\psi\rangle\langle\psi| = \rho$ that the average gate fidelity is given by

$$\begin{aligned} F_\Lambda &= \langle\psi|\Lambda_{ave}(|\psi\rangle\langle\psi|)|\psi\rangle \\ &= \mathrm{Tr}\left[|\psi\rangle\langle\psi|\Lambda_{ave}(|\psi\rangle\langle\psi|)\right] \\ &= \mathrm{Tr}\left[\rho\Lambda_{ave}(\rho)\right] \\ &= (1 - p_\Lambda)\mathrm{Tr}(\rho^2) + \frac{p_\Lambda}{D} \qquad (5.11) \\ &= p_0 + \frac{1 - p_0}{D}, \quad \text{for pure states.} \qquad (5.12) \end{aligned}$$

The last line confirmed our intuitive approach. The average gate fidelity is given by $\chi_{11} = p_0$, but since measuring a maximally mixed state will give the right answer with probability $\frac{1}{D}$ for any measurement, the average gate fidelity is further enhanced by p_Λ. The above equation essentially tells us that estimating the average gate fidelity is equivalent to estimating the depolarizing factor of the noise averaged over randomly chosen unitaries.

Using the fact that all operators in the n qubit Pauli group are traceless except the identity operator, and given that $\mathcal{P}_n$ is a complete set of basis operators for the $2^n \times 2^n$ matrices, we can thus decompose any state ρ as

$$\rho = \frac{\mathbb{1}}{D} + \sum_{P_j \neq \mathbb{1}} \rho_j P_j. \tag{5.13}$$

Moreover, since Pauli operators commute with half of the Pauli group and anti-commute with the other half, we have, for any given $P \neq \mathbb{1}$

$$\sum_k P_k P P_k = 0. \tag{5.14}$$

while

$$\sum_k P_k \mathbb{1} P_k = D^2 \mathbb{1}. \tag{5.15}$$

so that

$$\frac{1}{D^2} \sum_k P_k \rho P_k = \frac{\mathbb{1}}{D}. \tag{5.16}$$

The Liouville representation of a depolarization operator can thus be written

$$\hat{\Lambda}_{ave} = (1 - p_\Lambda)\mathbb{1} \otimes \mathbb{1} + \frac{p_\Lambda}{D^2} \sum_k P_k^* \otimes P_k, \tag{5.17}$$

which implies that

$$\mathrm{Tr}(\hat{\Lambda}_{ave}) = D^2(1 - p_\Lambda) + p_\Lambda. \tag{5.18}$$

The depolarizing factor is thus related to the original noise by

$$\begin{aligned} p_\Lambda &= \frac{D^2 - \mathrm{Tr}(\hat{\Lambda}_{ave})}{D^2 - 1} \\ &= \frac{D^2 - \mathrm{Tr}(\hat{\Lambda})}{D^2 - 1} \\ &= \frac{D^2 - \sum_k |\mathrm{Tr}(A_k)|^2}{D^2 - 1}, \end{aligned} \tag{5.19}$$

where we used the fact that

$$\begin{aligned} \mathrm{Tr}(\hat{\Lambda}_{ave}) &= \mathrm{Tr}\left(\int d\hat{U} \hat{U}^{-1} \hat{\Lambda} \hat{U} \right) \\ &= \int dU \mathrm{Tr}\left(\hat{U}^{-} 1 \hat{\Lambda} \hat{U} \right) \\ &= \int dU \mathrm{Tr}(\hat{\Lambda}) \\ &= \mathrm{Tr}(\hat{\Lambda}) \\ &= \sum_k \mathrm{Tr}\left(A_k^* \otimes A_k \right) \\ &= \sum_k \mathrm{Tr}(A_k) \mathrm{Tr}(A_k)^* \\ &= \sum_k |\mathrm{Tr}(A_k)|^2. \end{aligned} \tag{5.20, 5.21}$$

The above results can also be obtained by directly comparing Eq. 5.6 with 5.11.

Under the same assumption of gate independent noise, let us analyze a series of faulty gates averaged over the Haar measure, i.e. given an initial state in the Liouville representation $|\rho\rangle\rangle$, the final state after n randomly chosen gates will be

$$|\rho(n)\rangle\rangle = \int \left[\Pi_i d\hat{U}_i\right] \hat{\Lambda}\hat{U}_n \ldots \hat{\Lambda}\hat{U}_2\hat{\Lambda}\hat{U}_1|\rho(0)\rangle\rangle. \tag{5.22}$$

Since the gates are randomly chosen, we can always write $U_i = U_i' U_{i-1}^\dagger$ so that the above averaging reduce to

$$\begin{aligned} |\rho(n)\rangle\rangle &= \int \left[\Pi_i d\hat{U}_i\right] \hat{R}\hat{U}_n'^{-1}\hat{\Lambda}\hat{U}_n' \ldots \hat{U}_2'^{-1}\hat{\Lambda}\hat{U}_2' U_1^{-1}\hat{\Lambda}\hat{U}_1|\rho(0)\rangle \\ &= \hat{R}^\dagger \left[\int d\hat{U}\hat{U}^{-1}\hat{\Lambda}\hat{U}\right]^n |\rho(0)\rangle \\ &= \hat{R}^\dagger \hat{\Lambda}_{ave}^n |\rho(0)\rangle, \end{aligned} \tag{5.23}$$

where $R^\dagger$ corresponds to the overall effect of the ideal pulse sequence, i.e. $R^\dagger = U_n U_{n-1} \ldots U_1$, so that R is the time-reversal gate, i.e. the recovery gate.

Simple proof by induction shows that the effect of Λ_{ave}^n on any state ρ is given by

$$\Lambda_{ave}^n(\rho) = (1-p_\Lambda)^n \rho + (1-(1-p_\Lambda)^n)\frac{\mathbb{1}}{D}. \tag{5.24}$$

From the expression in Eq. 5.11, the average gate fidelity F_n after n gates can be measured by evaluating the average state-to-state fidelity of the random self-reversed sequences for a generic initial state $\rho(0)$, i.e.

$$\begin{aligned} F_n &= \mathrm{Tr}\left[\rho(0) R\rho(n)R^\dagger\right] \\ &= \mathrm{Tr}\left[\rho(0)\Lambda_{ave}^n\left(\rho(0)\right)\right] \\ &= (1-p_\Lambda)^n \left[\mathrm{Tr}(\rho(0)^2) - \frac{1}{D}\right] + \frac{1}{D}. \end{aligned} \tag{5.25}$$

This shows us that the function $F_n - \frac{1}{D}$ is an exponentially decaying function in the number of gates.

In the light of the above theory, the protocol to extract the average fidelity per gate becomes clear:

1. Generate n_g sets of N random unitaries.
2. Select a set of numbers of truncation to be implemented $l_1 < l_2 < \ldots < l_N = N$.

3. For each truncation l_i, calculate the recovery gate $R_{ik} = U_1^{(k)\dagger} \dots U_{l_i}^{(k)\dagger}$, $k = 1, \dots, n_g$.

4. For each truncation, implement each n_g sequences for a fixed initial state, implement the recovery gate record the state fidelity and average the fidelities over the n_g sequences.

5. Plot the average fidelity as a function of the number of gates l_i.

6. Extract the exponential factor p_Λ.

In reality, there will be errors in the state preparation Λ_p and in the implementation of the recovery gate Λ_R. Since the n_g sequences are randomly chosen for a given l_i, averaging over the sequence will effectively depolarize the preparation and recovery errors. If p_p and p_R are associated with the depolarizing factor of the initial state preparation and recovery gate respectively, that channel is then described by

$$\begin{aligned} \Lambda_{R,ave} \circ \Lambda_{ave}^n \circ \Lambda_{p,ave}(\rho) &= (1-p_p)(1-p_R)(1-p_\Lambda)^n \rho \\ &\quad + (1-(1-p_p)(1-p_R)(1-p_\Lambda)^n)\frac{\mathbb{1}}{D}. \end{aligned} \tag{5.26}$$

The average gate fidelity is now given by

$$F_n = (1-p_p)(1-p_R)(1-p_\Lambda)^n \left[\mathrm{Tr}(\rho(0)^2) - \frac{1}{D}\right] + \frac{1}{D}, \tag{5.27}$$

so that $F_n - \frac{1}{D}$ is still exponential in n, but with a different value at $n = 0$.

The most important fact about this protocol is that due to the concentration of measure in large Hilbert spaces [EWLC02], the fidelity decay of a single sequence becomes exponentially close to the true average as a function of the number of qubits. Therefore, only a few random sequences needs to be implemented to estimate the depolarizing factor. The advantage of measuring the depolarizing factor as part of a long sequence of gates reside in the fact that we only need to undo the computation at the very end of the sequence, hence potentially canceling less coherent, possibly pulse dependent, errors, as we will explained in more detail in Sec. 5.3.2.

5.2.2 Clifford randomization

The main concern the experimental implementation of the protocol has to do with the generation of the unitary matrices. Unitary matrices are a continuous set of

gates and requires an exponential amount of parameters to describe them. Therefore, from an experimental point of view, random unitary operators are impractical and inefficient to implement. There are, on the other hand, ways to efficiently generate pseudo-random unitary operators by iterating a series of single qubit random unitaries and fixed two qubit gates [EWS+03], which converge to a Haar distributed set of gates exponentially fast (in the length of the circuit) [ELL05]. These methods still use a continuous set of gates (single qubit unitaries) and are not ideal for experiments, though feasible.

As seen from Eq. 5.7, the average gate fidelity is given by a polynomial of second degree in U and second degree in $U^\dagger$, also known as a $(2,2)$ polynomial. The average over the set of all unitaries can therefore be performed using a unitary 2-design, that is, a finite set of operators such that the average over the finite set will yield the same result as the average over the continuous set of Haar distributed unitaries. It has been shown [DLT02] that averaging over the Clifford operations is an exact 2-designed, that is

$$\int d\hat{U}\, \hat{U}^{-1}\hat{\Lambda}\hat{U} = \frac{1}{|\mathcal{C}_n|}\sum_{\hat{C}\in\mathcal{C}_n} \hat{C}^{-1}\hat{\Lambda}\hat{C}. \tag{5.28}$$

Using a finite set of gates is now more realizable experimentally, but there are still exponentially many, as a function of the number of qubits, Clifford operations. Fortunately, Dankert et al. [DCEL06] showed that to evaluate the average to within precision ϵ, only $\mathcal{O}(n \log \epsilon^{-1})$ Clifford operations are needed. Therefore, only a few randomly chosen Clifford gates will be needed to obtain a fidelity decay curve.

Another strong argument to use the Clifford operations instead of the unitaries is in the calculation of the recovery map R. For a sequence of random unitaries, it takes an exponential amount of resources to calculate the overall transformation. On the other hand, it is known that Clifford operations are efficiently tractable on a classical computer [Got97] and we know that any Clifford gate can be decomposed into a scalable number of known one and two qubit gates [AG04, DDM03]. Therefore, the use of a Clifford randomization will enable us to undo the computation in very few steps.

Moreover, being able to benchmark the quality of the Clifford gates is of great importance to measure the ability for a device to implement fault-tolerant QIP based on stabilized codes [Got97]. Such codes perform their error correction mainly using Clifford operations. The universality of such an architecture can be completed by preparing "magic-states", e.g. states of the form $\cos\frac{\pi}{8}|0\rangle + \sin\frac{\pi}{8}|1\rangle$. The preparation of a faulty magic-state can be purified solely from the use of Clifford operations [BK05, Rei05]. Therefore, the performance of a quantum computation can be significantly increased by the use of higher precision Clifford operations.

Finally, by extracting the value of the depolarizing factor, we obtain concrete information about the noise present in the implementation of computational gates. One could argue that the average gate fidelity is not an appropriate figure of merit for fault tolerant quantum computation since these schemes have to work in all scenarios. Instead, the perfect number to use would be the worst case fidelity, i.e. the minimal state fidelity over the entire Hilbert space. Even though such fidelity can be evaluated for a known unitary operator [HJ85], it is not clear how to measure it for a general CP map. On the other hand, since we are measuring the fidelity of computational gates, we are assuming that those gates have a non-trivial effect on the state of the system, meaning that during an actual computation the system will most likely visit different regions of the Hilbert space and be equally affected by worst case and best case scenarios. Moreover, for most experimental errors any given device has to deal with, e.g. mis-calibration, dephasing, amplitude damping, etc., the action of this noise is smoothly distributed across the Hilbert space. Therefore, the average gate fidelity will never greatly differ from the worst case fidelity and therefore it is a relevant quantity to know so that the quality of the control on a system can be assessed.

5.3 Modifications for implementation

5.3.1 Modifying the assumptions

The theory and mathematics leading to the development of the above protocol rely on a very constrictive assumption: the noise present is independent of the unitary implemented. Since we are trying to evaluate the control on our system, that is, how well we are able to implement a given gate, this assumption conflicts with what we are trying to evaluate.

For example, typical gate independent errors could come from dephasing or amplitude damping, which are essentially only dependent on the system and its environment. But when we are implementing a given gate, e.g. a $\pi/2$ pulse about the x axis, miscalibration will introduce a small error corresponding to an over or under rotation around the x axis. If the pulse would have been about the y axis, then the error would have been around the y axis. Also, residual couplings can introduce errors. During a pulse on a qubit coupled to, say, one other qubit, the error introduced will be different than that introduced if we were implementing the exact same pulse, but on a qubit coupled to two other qubits.

Simply said, the cumulative error of a given sequence of gates will be strongly correlated with the particular sequence implemented. In their work, Emerson et. al. conjectured, based on the fact that the depolarizing factor depends only on the

strength of the noise measured by $\mathrm{Tr}(\hat{\Lambda})$, that the strength of the noise for a specific, yet random gate sequence will concentrate around the average value depending only on the length of the sequence, as long as all the noise has the same strength, i.e. if the residual noise coming from applying U is Λ_U, then for a specific self-reversed sequence $RU_n \dots U_1$

$$\hat{R}\hat{\Lambda}_{U_n}\hat{U}_n \dots \hat{\Lambda}_{U_1}\hat{U}_1 \quad \simeq \quad \hat{\Lambda}_{ave}^n, \text{ for large } n, \tag{5.29}$$

where, as before

$$\hat{\Lambda}_{ave}(\rho) \quad = \quad (1-p_\Lambda)\rho + p_\Lambda \frac{\mathbb{1}}{D}, \tag{5.30}$$

and

$$p_\Lambda \quad = \quad \frac{D^2 - \mathrm{Tr}(\hat{\Lambda}_{U_i})}{D^2-1}, \tag{5.31}$$

where Λ_{U_i} is any gate noise, since they are assumed to all have the same strength. This conjecture therefore tells us that the noise does not need to be the same for each gate, but as long as each gate is equally good, or bad, independent of the action of the noise, the protocol will work. In such a case of gate dependent errors, we are expecting the asymptotic error to approach the true average value.

5.3.2 Modifying the protocol

Reducing further the set of gates

Using the argument of unitary 2-design theory, we have been able to reduce the set of gates to average over from a continuous set to a discrete set. Unfortunately, for more than two qubits, the Clifford operations are still impractical since there are exponentially many of them, hence an exponential amount of operations to perform experimentally. We report here our effort toward further reducing the amount of multi-qubit gates necessary to implement the protocol, while still extracting relevant information.

On the other hand, we know that only a small number of gates are necessary to generate any Clifford operation, hence we should be able to generate random Cliffords using an efficient amount of generating gates. One set of generating gates is all the single qubit Hadamard and phase gates, and a set of CNOTs affecting all qubits. The Hadamard gate has been previously defined in Eq. 5, and the phase gate corresponds to a $\pi/4$ rotation about the z axis, i.e.

$$P = e^{-i\frac{\pi}{4}Z} = \begin{pmatrix} e^{-i\frac{\pi}{4}} & 0 \\ 0 & e^{i\frac{\pi}{4}} \end{pmatrix} \simeq \begin{pmatrix} 1 & 0 \\ 0 & i \end{pmatrix}. \tag{5.32}$$

There are maximally $\mathcal{O}(n^2)$ such operations. Multiplying a reasonable amount of randomly chosen generating Clifford gates together (polynomially many) is known to produce uniformly distributed random Cliffords [HL08]. For example, on three qubits, numerical simulations shows that multiply five randomly chosen generators will yield a random Clifford gate.

The practical limitation of such an approach relies on the fact that each randomly chosen Clifford will now contain, say, m physical gates, so that the noise on that random gate will be the cumulative noise of all the physical gates. By invoking the theory of unitary 2-design for large sequences and large amounts of sequence averaging, the cumulative noise will converge to the same depolarizing noise. Therefore, each randomly chosen generating gate can be counted as a random Clifford operation. This claim will be numerically verified in the next section.

The advantage of using the generating set of gates containing only single and two qubit operations relies on the fact that we now have a meaningful connection to the fault-tolerance thresholds. Indeed, fault-tolerance relies on the error per single and two qubit gates and also the error per wait step. That is, the usual assumption is that a faulty gate affecting qubit a will only create an error on qubit a, while the errors on the other qubits will be classified as a wait step error. As argued above, a gate on a given qubit, or pair of qubits, is likely to induce errors on the other qubits. In the present work, we decided to eliminate the wait step error category and include them as part of the error per gate. Therefore, by implementing the benchmarking protocol using only one and two qubit gates, we quote an average error per one *or* two qubit gate that also contains the possible wait step errors. These errors per gate will therefore correspond to an "average worst case scenario" compared to quoting three different numbers. Obviously, such a method could be hiding information about the error as, for example, in the situation where the one qubit gates are near perfect and most of the errors are from the two qubit gates, our protocol would not make the distinction. We will explain later how we can modify the present protocol to extract more coarse-grained information about the noise.

Changing the initial state

To evaluate Eq. 5.25, we assume that the initial state is a quantum state, i.e. $\mathrm{Tr}(\rho) = 1$. In order to minimize the error due to state preparation, we should use a state easily obtainable from the thermal state. As explained before, the initial thermal state in liquid state NMR is highly mixed and we only care about the deviation matrix. Using gradient techniques or phase cycling, it is possible to

transform the initial thermal state into

$$\begin{aligned} \rho &= \frac{1}{D}\mathbb{1} - \epsilon Z_1 \\ &= \frac{1}{D}\mathbb{1} - \epsilon\sigma, \end{aligned} \tag{5.33}$$

with virtually no error, so that we can assume that $p_p = 0$ for the liquid state NMR implementation. Since $\mathrm{Tr}(\sigma) = 0$, the deviation does not describe a quantum state per say. On one end, we have from before that

$$\begin{aligned} \Lambda_{ave}^n(\rho) &= (1-p_R)(1-p_\Lambda)^n\rho + (1-(1-p_R)(1-p_\Lambda)^n)\frac{\mathbb{1}}{D} \\ &= \frac{\mathbb{1}}{D} + \epsilon(1-p_R)(1-p_\Lambda)^n\sigma. \end{aligned} \tag{5.34}$$

By the linearity of quantum mechanics we have

$$\begin{aligned} \Lambda_{ave}^n(\rho) &= \frac{1}{D}\Lambda_{ave}^n(\mathbb{1}) + \epsilon\Lambda_{ave}^n(\sigma) \\ &= \frac{1}{D} + \epsilon\Lambda_{ave}^n(\sigma), \end{aligned} \tag{5.35}$$

so we can conclude that

$$\Lambda_{ave}^n(\sigma) = (1-p_R)(1-p_\Lambda)^n\sigma. \tag{5.36}$$

We can extract the depolarizing factor using $p_\Lambda^n = \mathrm{Tr}\left[\sigma\Lambda_{ave}^n(\sigma)\right]$. If we use $\sigma = Z_1$ for example, $(1-p_\Lambda)^n$ will be measurable in NMR by comparing the final amount of signal with the initial amount of signal (Sec. 2.4.4). Since the initial signal is constant, we can extract the depolarizing parameter by fitting the graph of the final signal versus the number of gates implemented.

5.3.3 Simulating the protocol

Before going ahead and experimentally implementing the protocol, we decided some simulations were needed to verify the validity of the conjectures mentioned above, as well as the viability of the protocol under the estimated error in our NMR system.

First, to analyze the convergence of the scheme and the viability of the Clifford 2-design option, we simulated the fidelity decay curve for a gate-independent noise on three qubits. The most common such noise, also present in NMR, is the phase flip noise (similar to dephasing). Given a state ρ,

$$\Lambda(\rho) = (1-d)\,\rho + \frac{d}{3}(Z_1\rho Z_1 + Z_2\rho Z_2 + Z_3\rho Z_3), \tag{5.37}$$

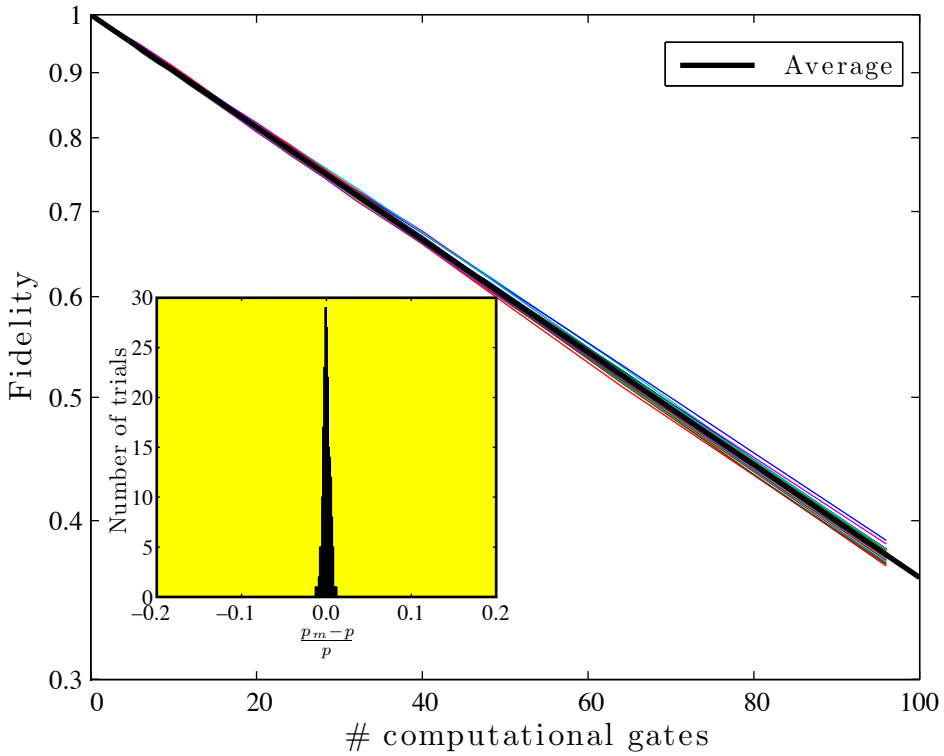

Figure 5.1: Fidelity decay curve of a phase flip noise under Haar unitary randomization. Each different curve represents the fidelity of a given sequence of N randomly chosen unitary gates. The inset histogram gives the distribution of the measured depolarizing factor for 200 different complete simulations.

where we used the arbitrary value of $d = 0.01$. Once the noise is depolarized, Eq. 5.19 tells us that we should measure a depolarizing factor of $p = 0.010158$, yielding an average gate fidelity of 0.991111. Fig. 5.1 shows the fidelity decay for $n_g = 32$ different computational gate sequences recorded at $l_i = \{2, 4, 6, 8, 10, 12, 16, 20, 24, 28, 32, 40, 48, 64, 80, 96\}$. We see that there is very little variation from one sequence to another, verifying the conjecture in Eq. 5.29. The asymptotic average (neglecting $n_i = \{2, 4, 6, 8, 10, 12, 16\}$) of the curves shown fit to a measured factor of $p_m = 0.01010 \pm 0.00008$, which is very close to the expected value for the simulated noise. The inset histogram actually shows the fitted depolarizing factor compared to the expected value for 200 different simulations, i.e. $\frac{p_m - p}{p}$. The distribution has virtually no variance, hence demonstrating the concentration of measure even for a Hilbert space of small dimension.

Fig. 5.2 demonstrates the same simulation, but using random Clifford gates to depolarize the noise. We see that the fidelity curve for each sequence is more dispersed, yet followd the right tendency. The simulation shown produced a fitted

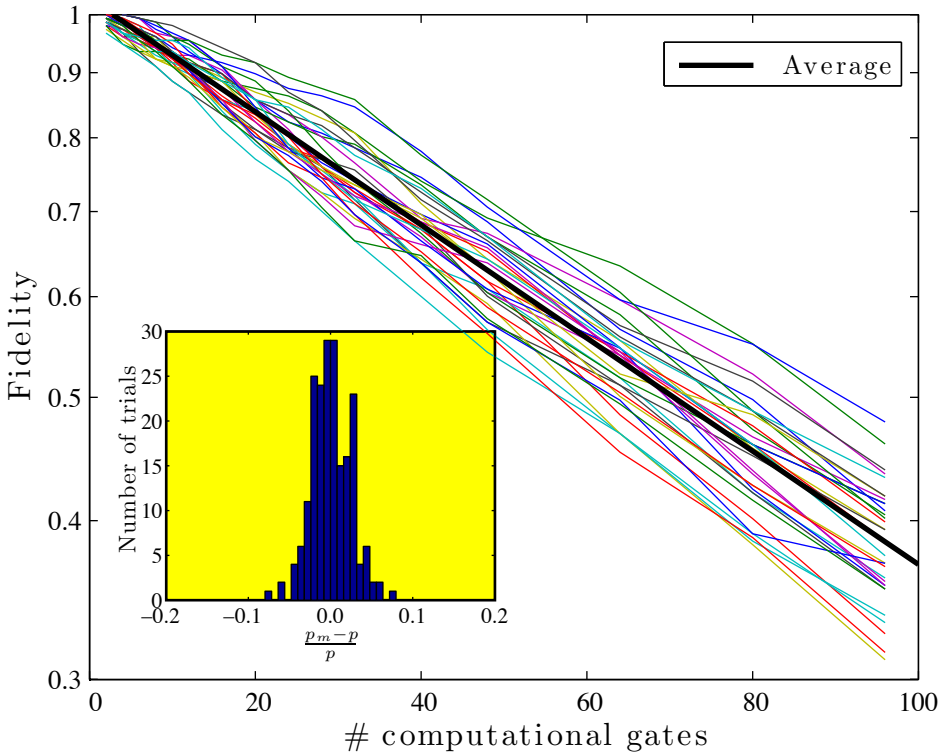

Figure 5.2: Fidelity decay curve of a dephasing noise under Clifford randomization. Even though the true average curve should be the same, the separate fidelity curves are more dispersed for a Clifford randomization than a Haar unitary randomization. It has consequences to yield a less sharp distribution of the measured depolarizing value over 200 different experiments (inset).

$p = 0.0102 \pm 0.0002$. The inset histogram shows that even for minimal averaging ($n_g = 32$), the Clifford average will still depolarize the noise to the expected value, but with a larger variance. The theory of 2-design stipulates that the average will be the same, but does not specify anything about the moment of the distribution of the average when performing estimates. Since we are averaging over a smaller set of gates, it is expected that more averaging will be needed to approach the true value, but the present simulations shows that, at worst, the value measured will be away from the true average by 10%. The analysis of the moments of the estimates is presently under investigation [ME08].

In our recent experiments, we typically designed our pulses using the GRAPE search algorithm described in Sec. 2.6.2. If we specify to the search engine to terminate when the simulated gate has, say, a 99.75% gate fidelity with the ideal gate, then we know that all the gates implemented should have similar strengths of error.

The claim by Emerson et al. [EAZ05] is only a conjecture and no numerical support has been given, so it is important to ensure that such a claim holds for the noise model we are expecting to encounter. Since the noise model for single qubits will be analyzed in detail in the next section, we will only verify the conjectures for a three qubit system. For purposes of analysis, we will assume that the search terminates when the gate fidelity, with respect to the Hilbert-Schmidt measure, is 99.75%, i.e.

$$0.9975 \quad = \quad \frac{1}{D^2}|\mathrm{Tr}(U_{id}U_{sim}^{\dagger})|^2. \tag{5.38}$$

We can assume that $U_{sim} = VU_{id}$, where V corresponds to the error in the simulated gate, so that

$$0.9975 \quad = \quad \frac{1}{D^2}|\mathrm{Tr}(V)|^2. \tag{5.39}$$

Since V is unitary, it can be written as $V = We^{-i\frac{\theta}{2}Z_1}W^{\dagger}$ for a given unitary W. This shows that any unitary operation is essentially a rotation of angle θ about a certain axis of the D-dimensional hyper-sphere. Therefore,

$$\begin{aligned} 0.9975 \quad &= \quad \frac{1}{D^2}|\mathrm{Tr}(V)|^2 \\ &= \quad \frac{1}{D^2}|\mathrm{Tr}(e^{-i\frac{\theta}{2}Z})|^2 \\ &= \quad \cos^2\frac{\theta}{2} \\ &\Rightarrow \quad \theta = 0.1. \end{aligned} \tag{5.40}$$

For the sake of simulation, each computational gate was assigned a random error of the above strength by randomly generating the unitary V. The random unitaries were generated from the eigenvectors of a random Gaussian unitary hermitian matrix [Haa01]. The expected depolarizing value is $p = 0.002537$, yielding an average gate fidelity of 0.997780. Anecdotally, this shows the close relation between the average gate fidelity and the Hilbert-Schmidt measure. Though the latter is a well suited figure of merit for the unitary implementation of gates, the former extends for general CPTP implementation. Fig. 5.3 and 5.4 shows the simulated experiments for a unitary and a Clifford randomization.

Surprisingly, there is little difference between the unitary and Clifford randomizations, suggesting that coherence noise is hard to depolarize and that even a continuous set cannot do it properly for a small amount of sequences.

For the final simulation, each random Clifford was replaced by a randomly chosen generating gate. The histogram for 200 different measured depolarization values is shown in Fig. 5.5. We can observe that the variance of the distribution

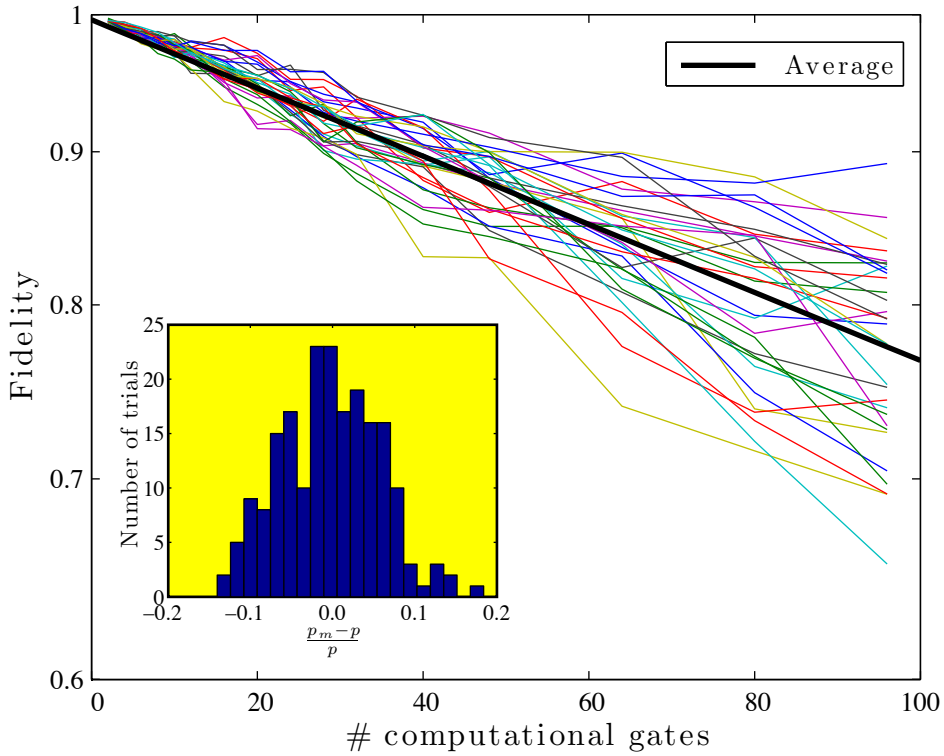

Figure 5.3: Fidelity decay curve of a gate dependent unitary noise under Haar unitary randomization. As expected, even for Haar unitary randomization, coherent noise is harder to depolarize, as indicated by the dispersion in each separate curve and by the histogram in the inset showing the depolarizing factor measured in 200 different experiments.

is essentially similar to that of Fig. 5.4, so that using randomly chosen Clifford generators has the same depolarizing power as random Cliffords. On the other hand, the average value measured tends to be about 5% greater than the true depolarizing value. This discrepancy is not very alarming since the present protocol serves to estimate the average error per gate and the most important information is not necessarily the number itself, but the order of that number. Therefore, measuring a number that is within 5 or 10% of the true value is still a very valid number. Moreover, it is expected that more averaging over longer sequences would improve the asymptotic convergence of the extracted depolarizing factor to the true value.

From the simulations above, a general observation can be made: it is harder to depolarize unitary, coherent noise. This is expected since coherent noise is "stronger" than decoherent noise. If we look at the action of different noises on the Bloch sphere, we see that a depolarizing noise reduces the sphere in all dimensions. Decoherent noise reduces the Bloch sphere in some dimensions while coherent noise

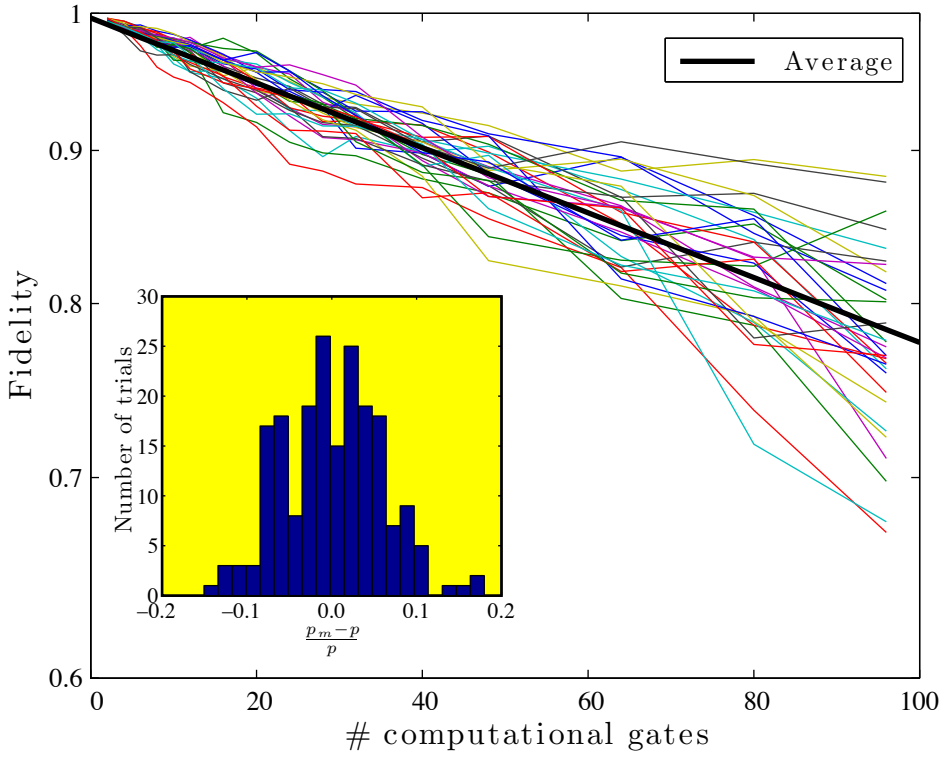

Figure 5.4: Fidelity decay curve of a gate dependent unitary noise under Clifford randomization. Surprisingly, in the case of coherent noise, the Clifford randomization appears to have a similar convergence rate than a Haar unitary randomization.

only rotates the sphere. Said in another way, depolarizing and decoherent noise reduce the purity of a state while coherent noise does not. Therefore, it is expected to need more averaging to depolarize a coherent noise, since a larger amount of purity needs to be lost by the averaging.

5.4 1 qubit experiment

5.4.1 The procedure

The first implementation of the protocol of Emerson et al. [EAZ05] was carried out by Knill et al. on a single qubit consisting of a single trapped ion [KLR+08]. They reported an average error per gate of $1 - F = 4.82 \pm 0.17 \times 10^{-3}$. In order to compare their system to ours, we decided to first implement the identical protocol. Since the single qubit Clifford set only contains 48 gates, they decided to use the entire set and not only the generators as we argued above. As mentioned in Sec. 4.3, one qubit Clifford gate randomization is isomorphic to a Pauli twirl followed by a

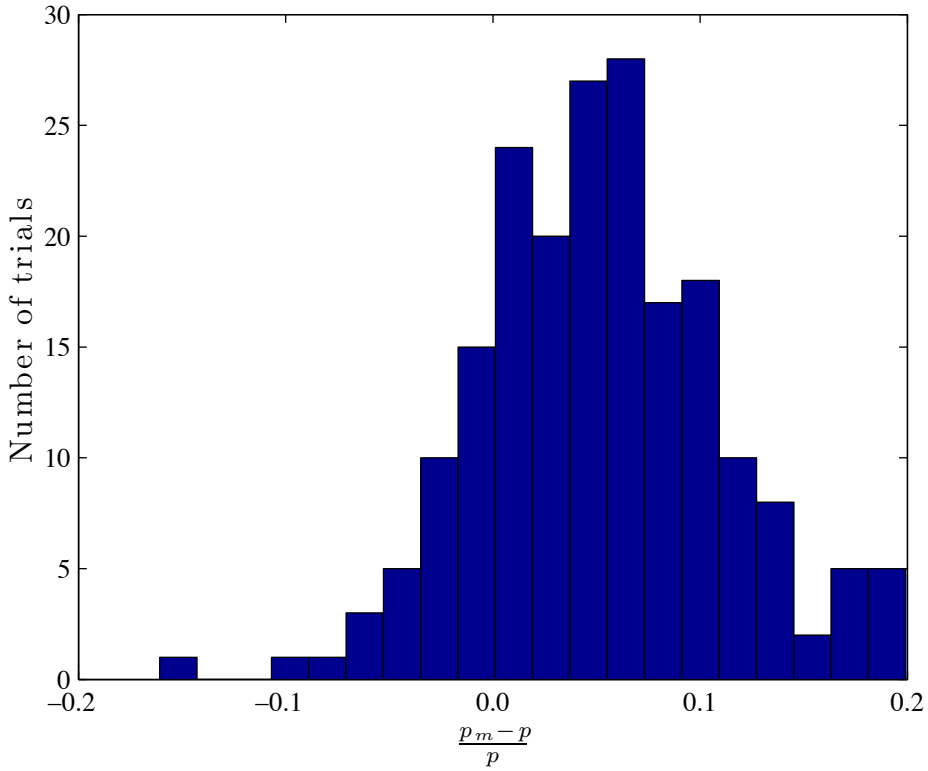

Figure 5.5: Fitted depolarizing value compared to the expected one for Clifford generators randomization. The use of random Clifford generators over-estimate the depolarizing factor by about $5 - 10\%$ on three qubits. Such a biased number is still significant since, in the worst case, it corresponds to an over-estimation of the average error per gates.

simplectic twirl or vice-versa, i.e.

$$\begin{aligned} \mathcal{C}_1 &\cong \mathcal{S}_1\mathcal{P}_1 \\ &\simeq \left\{ e^{\pm i\frac{\pi}{4}Q} e^{\pm i\frac{\pi}{2}P} \mid Q \in \{X, Y, Z\},\ P \in \{\mathbb{1}, X, Y, Z\} \right\}. \end{aligned} \tag{5.41}$$

That is, each Clifford operation consists of a π pulse (or Pauli operation) followed by a $\pi/2$ pulse (simplectic operation). The simplectic operations are deemed the "computationally relevant" operations that advance the computation while the Pauli operations serve only to redefine the Pauli frame.

The circuit implemented is shown in Fig. 5.6. To perform an approximate averaging, 4 sequences of 192 computational gates were chosen at random and truncated at different lengths $l = \{2,\ 4,\ 6,\ 8,\ 12,\ 16,\ 20,\ 24,\ 32,\ 40,\ 48,\ 64,\ 80,\ 96,\ 128,\ 160,\ 192\}$. Random Pauli operations were then inserted between each computational gate. Therefore, each dyad of a $\pi/2$ and π pulse was considered a random gate. In their analysis, Knill et al. [KLR+08] did not really address

Figure 5.6: Pulse sequence to benchmark the control on a single qubit.

the problem of cumulative noise and were assuming that the error on the Pauli operations were vanishing. Being true or not, the simulations from above argue for the validity of their experiment.

The state of the system was tracked through the computational gates. Since we were using only the simplectic gates as computational gates, the final state of the system could only be $\pm X$, $\pm Y$ or $\pm Z$. The $\pi/2$ recovery gate R was easily determined and chosen to return the state to either $+Z$ or $-Z$ with equal probability. The state was then read out with a $\pi/2$ readout pulse and the fidelity measured by comparing the integral of the signal to a reference spectrum as argued in Sec. 5.3.2. For each truncation and sequence, the Pauli operations were randomized 8 times, giving a number of sequences of $n_g = 32$, and the average fidelity recorded.

5.4.2 The implementation

Chloroform was the molecule chosen to implement the experiment, as used in the experiments in Chapter 4, but with only the natural abundance ($\sim 1\%$) of ^{13}C. The measured T_1 and T_2 of the proton were 7 and $4.5s$ respectively, while the T_2^* was estimated to be $0.45s$ from the linewidth of the spectrum. As previously argued, the pulses were implemented using $24\mu s$ Gaussian shaped pulse to avoid the phase transient effects of the high Q cryo-probe.

Cryoprobes are well known to have bad RF-profiles [KSK+04], that is, the molecules throughout the sample do not see the same RF-field, thus leading to incoherent noise throughout the sample. For this reason, we decided to implement each pulse using the BB1 family of composite pulses which are known to be robust against RF-inhomogeneity [Wim94]. If the RF-field inhomogeneities cause a simple pulse to implement a rotation with angle ϵ away from the intended angle, BB1 pulses will implement the same rotation with a reduced error of ϵ^6. The pulses consist of a compensating block followed by the desired pulse so that a rotation by an angle θ about the x axis can be replaced by,

$$R_x(\theta) \quad = \quad (180)_{\phi_1} (360)_{\phi_2} (180)_{\phi_1} R_x(\theta). \tag{5.42}$$

ϕ_1 and ϕ_2 depend on the pulse flip angle according to,

$$\phi_1 = \frac{1}{3}\phi_2 = \arccos\left(\frac{-\theta}{4\pi}\right). \tag{5.43}$$

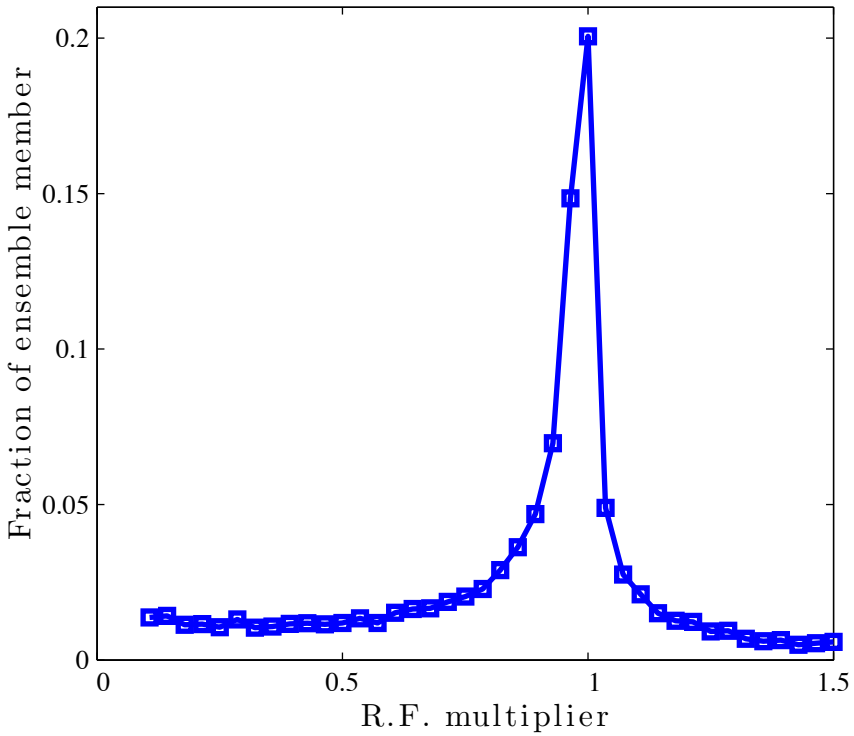

Figure 5.7: The RF-profile of the TCI cryoprobe.

Such a composite pulse relies on the fact that phase modulation can dramatically improve the exitation bandwidth of a pulse [TPC94] .

The RF-profile in our sample is shown in Fig. 5.7 which has been measured through in a Rabi oscillation experiment. The results for the first round of simulations can be seen on the semi-log graph in Fig. 5.8. As seen, the experimental curve does not even follow an exponential trend (linear on a semi-log graph) and the fidelity decays very quickly. To ensure that this misbehavior was not attributed to experimental problems, such as spectrometer defects or amplifier drifting, we simulated the entire experiment over the distribution of RF-field in the sample. The simulation curve in Fig. 5.8 demonstrates that the major source of non-exponential decay came from the RF-inhomogeneity, even though the pulses were robust against it. A detailed analysis of the situation will follow in the next section.

To overcome the effect of inhomogeneity in our probe, it is possible to design pulse sequences that physically select only the spins seeing the appropriate RF field to, say, 2% of the actual value and completely depolarize all the other spins [SKBF85, Lev86, Cor93]. In our case, such a pulse has been developed using the GRAPE algorithm so that all the spins seeing a RF field larger then 2% were rotated to the xy plane, while the "good" spins were kept along the z axis. The rotated

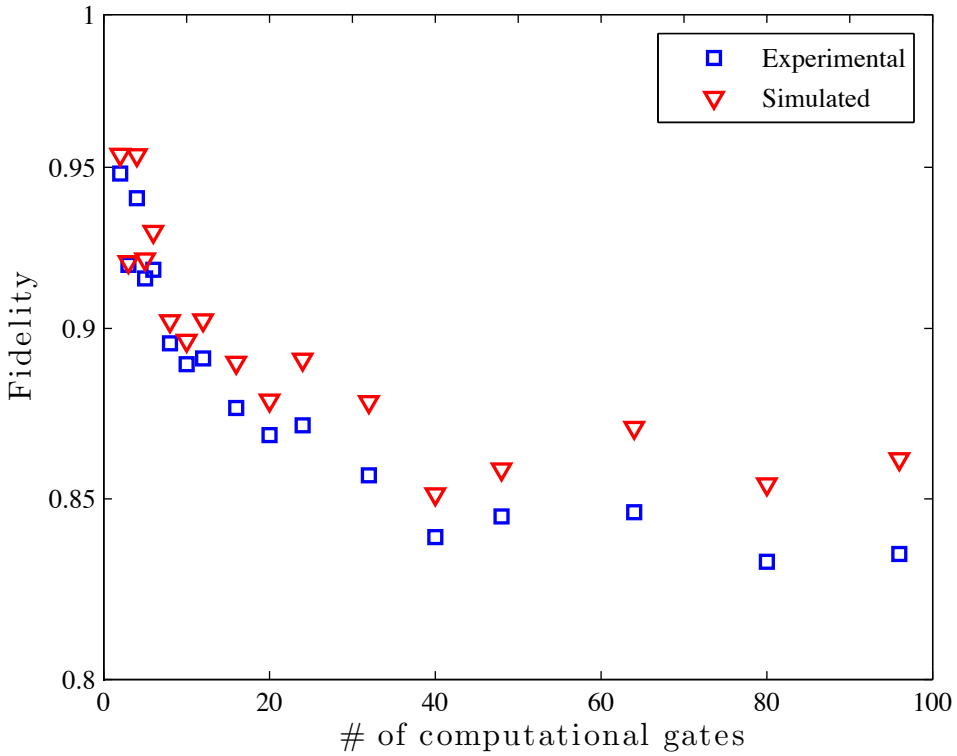

Figure 5.8: Semi-log graph of the first set of results of the 1 qubit benchmarking experiment. The presence of RF-inhomogeneities across the sample yield a superexponential decay due to badly behaving spins that depolarize quickly.

spins were then completely depolarized using a pulsed magnetic field gradient pulse.

To eliminate the errors arriving from the fluctuation of the signal, each experiment was referenced to its own initial signal using stroboscopic observation and signal processing. The procedure went as followed:

1. Tip the polarization along the x axis.
2. Open the receiver and record the signal for $10ms$ and close it.
3. Tip the spin back along the z axis.
4. Implement the pulse sequence.
5. Record the remaining signal.

The final FID was then post-processed. Since there is only a single spin and the receiver acquired the magnetization in the rotating frame of the spin, the reference signal was essentially flat. The remaining amount of signal was then Fourier transformed and the integral of the spectrum was then divided by the reference signal.

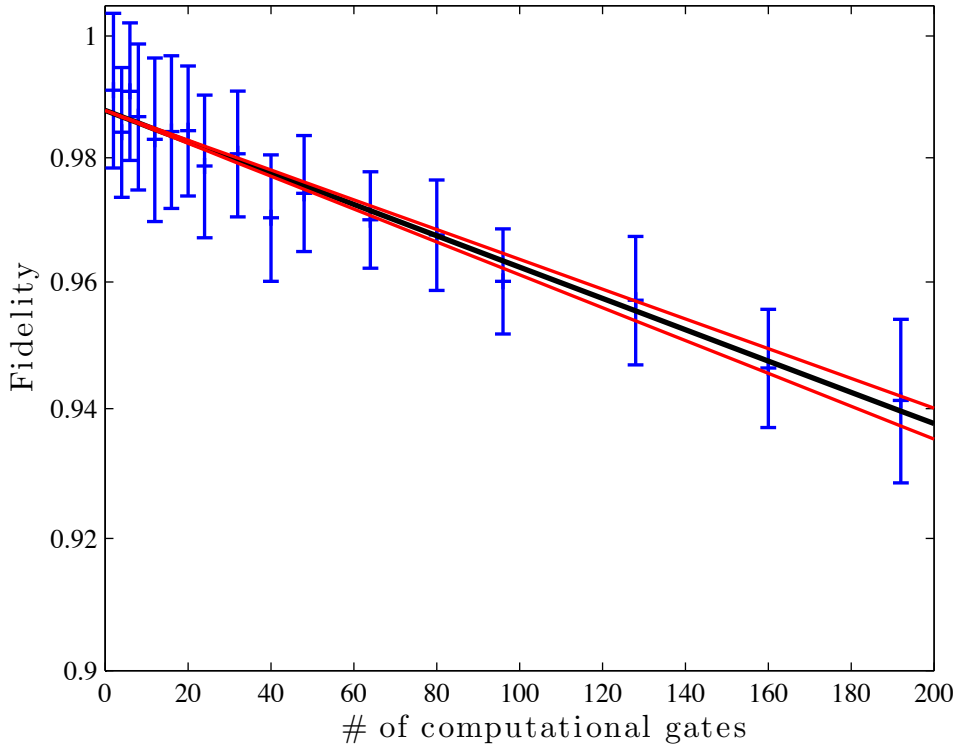

Figure 5.9: Semi-log graph of the final set of results of the 1 qubit benchmarking experiment using RF-selection and the BB1 composite pulses. By initially depolarizing the bad spins (RF-selection), the remaining spins could be depolarized at the same rate under the randomize sequences, hence yielding an exponential decay.

The fidelity was then obtained by dividing the obtained ratio by the average reference signal of all the experiments. Digital filtering was also manually implemented to reduce the noise, but more details will be given in Sec. 5.5.2 and in Appendix D.

By applying the RF-selection pulse first and then running the experiment, we obtained the results shown in Fig. 5.9, which fitted nicely to an exponential, yielding a depolarizing factor of $2.6 \pm 0.2 \times 10^{-4}$ and hence an average error per gate of $1.3 \pm 0.1 \times 10^{-4}$. The black line is the exponential fit and the red lines are the 68% confidence fit. The error bars on the graph correspond to the 68% confidence level of the statistical fluctuation of the measured fidelities. Due to the high sensitivity of the cryo-probe, the fluctuation due to the sensitivity of the probe was less then 0.5%.

Two more experiments have been conducted using simple pulses and GRAPE optimized pulses. The average error per computational gate was measured to be $2.1 \pm 0.1 \times 10^{-4}$ and $1.8 \pm 0.1 \times 10^{-4}$ respectively. The results obtained are one order of magnitude smaller that the number obtained for a single trapped ion, hence

demonstrating again the quality of control in liquid state NMR.

5.4.3 Discussion and analysis

Effects of RF-inhomogeneity

The unexpected results from the experiment without RF-selection have a very intuitive explanation. Namely, the spins that see a field much different than the intended one are basically seeing the intended gates, followed by a big calibration error. As the sequence of pulses continues, these spins will depolarize very quickly and after only a few gates, their state fidelity will approach 0, hence explaining the fast initial decay. We would thus expect the decay curve to level-off after a large number of gates as only the spins seeing a near-ideal field will still be polarized.

From a more quantitative point of view, if we apply a RF-field calibrated to rotate the spins by an angle $\pi/2$ about the u-axis ($u \in \{x, y, z\}$), the density matrix describing the state averaged across the sample in initial state ρ is:

$$\rho \rightarrow \int d\epsilon g(\epsilon) \Lambda_{P_u}(\epsilon) \left(e^{-i\frac{\pi}{4}P_u} \rho e^{i\frac{\pi}{4}P_u} \right), \tag{5.44}$$

where $\Lambda_{P_u}(\epsilon)$ is the superoperator describing the error for the spins experiencing a field ϵ away from the ideal field ($\Lambda_{P_u}(\epsilon)(\rho) = e^{-i\epsilon\frac{\pi}{4}P_u}\rho e^{i\epsilon\frac{\pi}{4}P_u}$), $g(\epsilon)$ is the RF-distribution and P_u the appropriate rotation matrix. This is an example of incoherent noise discussed in Sec. 1.4. The error model arising from RF-field inhomogeneity is therefore an over- or under-rotation along the same axis as the actual rotation. With this notation the superoperator describing a specific sequence of the single qubit experiment is written as (ignoring the recovery gate and assuming the sequence is self-inverting for simplicity):

$$\begin{aligned} \hat{\Lambda}_i(n) &= \int d\epsilon g(\epsilon) \hat{\Lambda}_{S_{i_n}}(\epsilon) \hat{S}_{i_n} \hat{\Lambda}_{P_{i_n}}(\epsilon) \hat{P}_{i_n} \ldots \hat{\Lambda}_{S_{i_2}}(\epsilon) \hat{S}_{i_2} \hat{\Lambda}_{P_{i_2}}(\epsilon) \hat{P}_{i_2} \hat{\Lambda}_{S_{i_1}}(\epsilon) \hat{S}_{i_1} \hat{\Lambda}_{P_{i_1}}(\epsilon) \hat{P}_{i_1} \\ &= \int d\epsilon g(\epsilon) \hat{\Lambda}_{i_n}(\epsilon) \hat{S}_{i_n} \hat{P}_{i_n} \ldots \hat{\Lambda}_{i_2}(\epsilon) \hat{S}_{i_2} \hat{P}_{i_2} \hat{\Lambda}_{i_1}(\epsilon) \hat{S}_1 \hat{P}_{i_1}, \end{aligned} \tag{5.45}$$

where $\Lambda_{S_{i_j}}(\rho) = e^{-i\epsilon\frac{\pi}{4}Q_{i_j}} \rho e^{i\epsilon\frac{\pi}{4}Q_{i_j}}$, $\Lambda_{P_{i_j}}(\rho) = e^{-i\epsilon\frac{\pi}{2}P_{i_j}} \rho e^{i\epsilon\frac{\pi}{2}P_{i_j}}$. $\Lambda_{i_j}(\epsilon)$ is the cumulative error due to sequentially applying faulty S_{i_j} and P_{i_j}. In the present case, the strength of the noise can be parameterized by the tipping angle of $\Lambda_{i_j}(\epsilon)$ and it can be easily verified that there are three relevant strengths, depending on whether S_{i_j} and P_{i_j} are along parallel, anti-parallel or perpendicular axes, as enumerated in Table 5.1.

Strength	Axis	Probability
$\frac{3\pi}{2}\epsilon$	Parallel	1/8
$\frac{\pi}{2}\epsilon$	Anti-parallel	3/8
$\Gamma = 2\cos^{-1}[\cos(\frac{\pi}{4}\epsilon)\cos(\frac{\pi}{2}\epsilon)]$	Perpendicular	1/2

Table 5.1: Three possible strength parameters and their probability of occurrence for the cumulative error of a π pulse followed by $\pi/2$ pulse due to RF inhomogeneity.

In terms of the depolarizing action, Eq. 5.45 is equivalent to

$$\begin{aligned}\hat{\Lambda}_i(n) &= \int d\epsilon g(\epsilon)\hat{P}_{i_n}^\dagger \hat{S}_{i_n}^\dagger \hat{\Lambda}_{i_n}(\epsilon)\hat{S}_{i_n}\hat{P}_{i_n}\ldots\hat{P}_{i_2}^\dagger \hat{S}_{i_2}^\dagger \hat{\Lambda}_{i_2}(\epsilon)\hat{S}_{i_2}\hat{P}_{i_2}\hat{P}_{i_1}^\dagger \hat{S}_{i_1}^\dagger \hat{\Lambda}_{i_1}(\epsilon)\hat{S}_{i_1}\hat{P}_{i_1} \\ &= \int d\epsilon g(\epsilon)\prod_j \hat{P}_{i_j}^\dagger \hat{S}_{i_j}^\dagger \hat{\Lambda}_{i_j}(\epsilon)\hat{S}_{i_j}\hat{P}_{i_j}. \end{aligned} \tag{5.46}$$

The key observation to make is that each subset of S and P yielding a given noise strength parameter is sufficient to depolarize that given noise, e.g.

$$\frac{1}{|\mathcal{I}_{\frac{3\pi}{2}\epsilon}|}\sum_{S,P\in\mathcal{I}_{\frac{3\pi}{2}\epsilon}} \hat{P}^\dagger\hat{S}^\dagger\hat{\Lambda}_{\frac{3\pi}{2}\epsilon}\hat{S}\hat{P} = \hat{\Lambda}_{ave,\frac{3\pi}{2}\epsilon}, \tag{5.47}$$

where $\mathcal{I}_{\frac{3\pi}{2}\epsilon} = \{SP \mid S \text{ and } P \text{ are along a parallel axis}\}$ and $\hat{\Lambda}_{ave,\frac{3\pi}{2}\epsilon}$ is the depolarized channel associated with the cumulative noise of strength $\frac{3\pi}{2}\epsilon$ with depolarizing factor

$$p_{\frac{3\pi}{2}\epsilon} = \frac{4-4\cos^2(\frac{3\pi}{4}\epsilon)}{3}, \tag{5.48}$$

obtained from Eq. 5.19. Once the randomization is performed, each $\hat{\Lambda}_{i_j}$ in Eq. 5.46 will be randomized to a channel given by a weighted sum of the three different

depolarizing channels, i.e.

$$\begin{aligned}
\hat{\Lambda}_{ave}(n) =& \frac{1}{|\mathcal{P}|^n|\mathcal{S}|^n}\sum_i \int d\epsilon g(\epsilon) \prod_{j=1}^{n} \hat{P}_{i_j}^\dagger \hat{S}_{i_j}^\dagger \hat{\Lambda}_{i_j}(\epsilon)\hat{S}_{i_j}\hat{P}_{i_j} \\
=& \int d\epsilon g(\epsilon) \prod_{j=1}^{n} \frac{1}{|\mathcal{P}||\mathcal{S}|}\sum_{i_j} \hat{P}_{i_j}^\dagger \hat{S}_{i_j}^\dagger \hat{\Lambda}_{i_j}(\epsilon)\hat{S}_{i_j}\hat{P}_{i_j} \\
=& \int d\epsilon g(\epsilon) \Bigg[\frac{1}{|\mathcal{I}_{\frac{\pi}{2}\epsilon|}} \sum_{\hat{P},\hat{S}\in\mathcal{I}_{\frac{\pi}{2}\epsilon}} \hat{P}^\dagger\hat{S}^\dagger\hat{\Lambda}_\epsilon\hat{S}\hat{P} + \frac{1}{|\mathcal{I}_{\frac{3\pi}{2}\epsilon|}} \sum_{\hat{P},\hat{S}\in\mathcal{I}_{\frac{3\pi}{2}\epsilon}} \hat{P}^\dagger\hat{S}^\dagger\hat{\Lambda}_{\frac{3\pi}{2}\epsilon}\hat{S}\hat{P} \\
&+ \frac{1}{|\mathcal{I}_\Gamma|} \sum_{\hat{P},\hat{S}\in\mathcal{I}_\Gamma} \hat{P}^\dagger\hat{S}^\dagger\hat{\Lambda}_\Gamma\hat{S}\hat{P} \Bigg]^n \\
=& \int d\epsilon g(\epsilon) \left[\frac{3}{8}\hat{\Lambda}_{ave,\frac{\pi}{2}\epsilon} + \frac{1}{8}\hat{\Lambda}_{ave,\frac{3\pi}{2}\epsilon} + \frac{1}{2}\hat{\Lambda}_{ave,\Gamma} \right]^n . \\
=& \int d\epsilon g(\epsilon) \hat{\Lambda}_{ave}^n .
\end{aligned} \tag{5.49}$$

Therefore, the effective averaged channel action is given by

$$\begin{aligned}
\Lambda_{ave}(\rho) &= \bar{p}\rho + (1-\bar{p})\frac{\mathbb{1}}{2} \\
\bar{p} &= \frac{3}{8}p_{\frac{\pi}{2}\epsilon} + \frac{1}{8}p_{\frac{3\pi}{2}\epsilon} + \frac{1}{2}p_\Gamma,
\end{aligned} \tag{5.50}$$

The gate fidelity obtained by numerically integrating Eq. 5.49 using a given RF distribution is compared to an extensive numerical simulation of the gate sequences in Fig. 5.10, which clearly demonstrate the super-exponential behavior of the decay. From this figure, we see that our calculation from above justifies this super-exponential decay in the presence of incoherent noise arriving from RF-inhomogeneity. The slight variation of the simulated curve to the analytical curve is most likely due to incomplete averaging and a complete simulation would take too many resources to be evaluated.

We should mentioned that such a noise model is not restricted to ensemble effects. For example, it could apply to a system in which a given parameter, say a laser power in an ion trap, for the time of a single experiment, but fluctuates from one experiment to the other.

Analyzing the other sources of errors

Once RF-selection is implemented, one could hope that the source of miscalibration is gone and only intrinsic decoherence in left in our system. From Sec. 2.7, we know

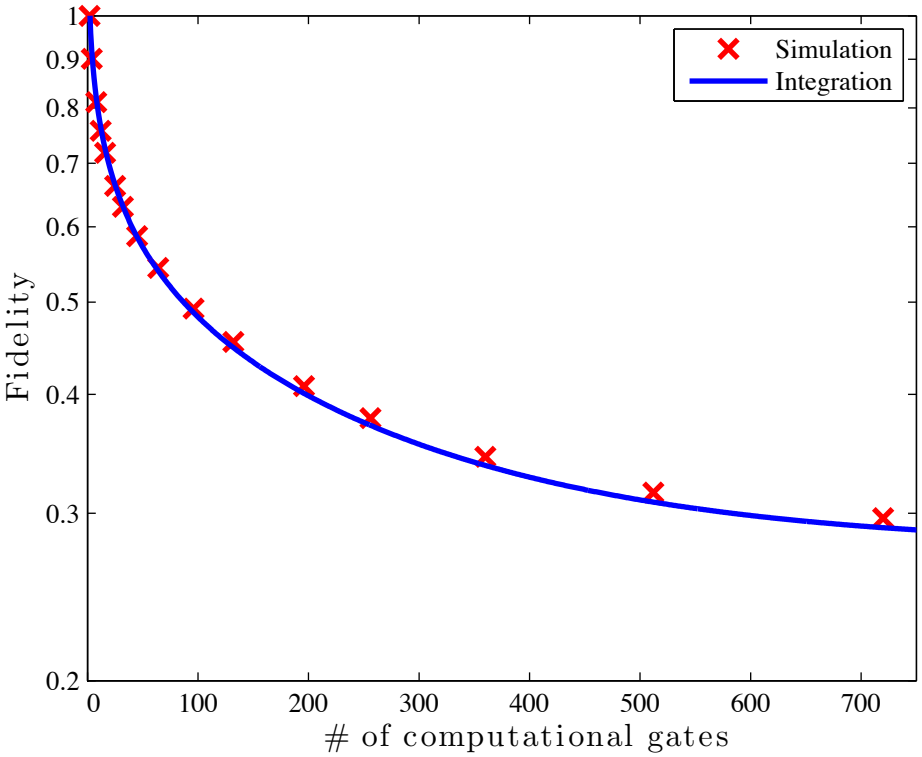

Figure 5.10: Numerical simulation and analytical prediction of the RF-inhomogeneity error model. RF-inhomogeneities will creates varying calibration errors across the sample, hence yielding an average of the depolarizing factor over the RF profile.

that intrinsic decoherence in NMR is due to amplitude damping (T_1) and dephasing (T_2). The state of a single spin ρ will relax according to

$$\begin{aligned}\rho &= \begin{pmatrix}\rho_{00} & \rho_{01}\\ \rho_{10} & \rho_{11}\end{pmatrix}\\ &\rightarrow \begin{pmatrix}(\rho_{00}-\bar{\rho}_{00})e^{-\frac{t}{T_1}}+\bar{\rho}_{00} & \rho_{01}e^{-\frac{t}{T_2}}\\ \rho_{10}e^{-\frac{t}{T_2}} & (\rho_{11}-\bar{\rho}_{11})e^{-\frac{t}{T_1}}+\bar{\rho}_{11}\end{pmatrix}.\end{aligned} \tag{5.51}$$

where $\bar{\rho}_{00}$ and $\bar{\rho}_{11}$ are the equilibrium value of the population, so that $\bar{\rho}_{00}-\bar{\rho}_{11}\simeq\frac{\hbar\omega}{k_BT}$. Using the fact that $\rho_{00}+\rho_{11}=1$, we can rewrite the above density matrix as

$$\begin{pmatrix}\rho_{00}[e^{-\frac{t}{T_1}}+\bar{\rho}_{00}(1-e^{-\frac{t}{T_1}})]+\rho_{11}\bar{\rho}_{00}(1-e^{-\frac{t}{T_1}}) & \rho_{01}e^{-\frac{t}{T_2}}\\ \rho_{10}e^{-\frac{t}{T_2}} & \rho_{11}[e^{-\frac{t}{T_1}}+\bar{\rho}_{11}(1-e^{-\frac{t}{T_1}})]+\rho_{00}\bar{\rho}_{11}(1-e^{-\frac{t}{T_1}})\end{pmatrix} \tag{5.52}$$

By columnizing the above state in the Liouville space, we see that the superoperator for intrinsic decoherence can be written as

$$\hat{\Lambda} = \begin{pmatrix}e^{-\frac{t}{T_1}}+\bar{\rho}_{00}(1-e^{-\frac{t}{T_1}}) & 0 & 0 & \bar{\rho}_{00}(1-e^{-\frac{t}{T_1}})\\ 0 & e^{-\frac{t}{T_2}} & 0 & 0\\ 0 & 0 & e^{-\frac{t}{T_2}} & 0\\ \bar{\rho}_{11}(1-e^{-\frac{t}{T_1}}) & & & e^{-\frac{t}{T_1}}+\bar{\rho}_{11}(1-e^{-\frac{t}{T_1}})\end{pmatrix}. \tag{5.53}$$

We can thus conclude that T_1 and T_2 noise alone will yield a depolarizing factor of

$$p = 1-\frac{e^{-\frac{t}{T_1}}+2e^{-\frac{t}{T_2}}}{3}. \tag{5.54}$$

For the experiment with composite pulses, each random gate composed of a computational gate and a Pauli gate were $516.8\mu s$ long, including pre- and post-delay, as well as the delays in between the simple pulses used to build the composite pulse. For this amount of time and using the relaxaton time measured in chloroform, the expected depolarizing factor should have been 1×10^{-4}, yielding an error per gate of 5×10^{-5}. If we use T_2^* instead of the intrinsic T_2, the average error per gate climbs up to 4×10^{-4}. On the other hand, this value corresponds to an over-estimate since a sequence of random pulses is more likely to refocus the external field inhomogeneity [VK05]. Since the intrinsic relaxation in our system only accounts for half of our measured errors per gate, we can conclude that our control is not decoherence limited and we should seek control and hardware improvements.

Some possible reasons explaining this discrepancy could arise from the instability of the amplifier. We know the BB1 pulses are robust for systematic miscalibration. But it is known that the amplifier power can fluctuate on a very short time

scale, so that the mis-calibration error on a spin can vary on the time scale of the duration of the pulse, hence inducing coherent error in the sample.

The fact that the main sources of error are still the control and hardware become obvious when the expected depolarizing factor is calculated for the simple pulse. Since the total duration of a random pulse was $95\mu s$, the error per gate due to decoherence only should have been 1×10^{-5}, which is an order of magnitude away from the measured value. Since the RF-inhomogeneity was mostly discarded through RF-selection, it gives an extra argument that the source of error arises from the pulse power fluctuations.

A last surprising observation is that the GRAPE pulses cannot match the result of the much longer BB1 pulses, even though they were optimized for $100\mu s$ at a fidelity over 99.999% over a range of RF inhomogenity of $\pm 3\%$. As for the BB1, GRAPE pulses are robust for systematic power miscalibration, but more sensitive to fluctuations. But since GRAPE pulses are modulated both in phase and amplitude, there are twice as many possibilities of amplifier fluctuations, hence explaining the lower fidelity per gate.

5.5 3 qubit experiment

5.5.1 The procedure

For the single qubit experiment, we implemented the exact same protocol as Knill et al. Since there are only 48 Clifford operations on a single qubit, we could easily implement each of them. For three qubits, the set of Cliffords is much larger. Moreover, our spectrometer only allows us to define at most 30 different pulse shapes (to which we can add any global implementation phase). For this reason, we relied on the arguments presented in Sec. 5.3.2 for benchmarking the control on three qubits.

Working with more qubits than before, more averaging is needed, so we decided to go with $n_g = 48$ different random sequences of gates drawn from the set of all the single qubit Hadamard and $PHP^\dagger$ and all the nearest neighbor CNOTs. The reason to use the $PHP^\dagger$ gates instead of phase gates will become apparent below. The procedure to implement the protocol went according to the following steps:

1. 48 different sequences of 120 gates were generated by randomly choosing any single qubit gates with a probability of 2/3 and any CNOTs with a probability of 1/3. The spectrometer limitation prevented us from going over 120 gates for reasons mentioned below.

2. Each sequence was then truncated to $l = \{10, 20, 40, 60, 80, 100, 120\}$ and the state-to-state evolution of the initial $Z\mathbb{1}\mathbb{1}$ state under each truncated sequence was efficiently tracked down using the simplectic notation [Got97].

3. The recovery gate was calculated for each sequence to undo the entire evolution. The gate was automatically calculated using a home-made state-to-state evolution algorithm. To design the recovery step, Hadamard or $PHP^\dagger$ gates were applied to each qubit such that their individual state was either $\mathbb{1}$ or along the z axis, i.e. using the property that $HXH = Z$ and $(PHP^\dagger)Y(P^\dagger HP) = Z$. This state was then transformed into the final $Z\mathbb{1}\mathbb{1}$ by finding the minimal amount of CNOTs needed to transfer all the polarization. The constructed algorithm is efficient and general for any number of qubits and any architecture.

4. The truncated sequences were then parallelized using a simple iterative algorithm checking whether a given gate can be compressed with the next gate. Such a parallelization will allow a fair comparison between a 3 and 50 qubit computer. More will be discussed in Sec. 5.6

5. The sequence were implemented and the final amount of $X\mathbb{1}\mathbb{1}$ signal was compared to the original signal. By plotting the average signal as a function of the number of gates in the sequence, the average fidelity for one and two qubit is then extracted by fitting an exponential to the fidelity decay curve.

5.5.2 The implementation

For the processor, we chose a selectively labeled ^{13}C - tris(trimethylsilyl)silane - acetylene (TMMS) dissolved in deuterated chloroform [HGW+07]. The molecule's structure and its Hamiltonian properties can be found in Fig. 5.11. The experiment was again performed on a 16.4T Bruker Avance spectrometer with a TCI cryoprobe.

The control was achieved through GRAPE optimized pulses. We optimized all the generating pulses, as well as all their combinations, over a range of RF power of $\pm 3\%$ from the ideal power, to a fidelity of 99.95%. To achieve this degree of precision while keeping the average power relatively low to avoid over-heating, pulses performing single spin gates were $1.2ms$ long, pulses having a CNOT between H and C_1 (and any gate on C_2) were $2.4ms$ and pulses with a CNOT between C_1 and C_2 were $4ms$ long.

For each experiment, the spectrometer could only handle 30 different shape files and can only receive no more then 1 MB of data. Since each pulse needed two shape files (one for the proton channel and one for the carbon channel), we could not independently define the 39 pulses from our generating set and their

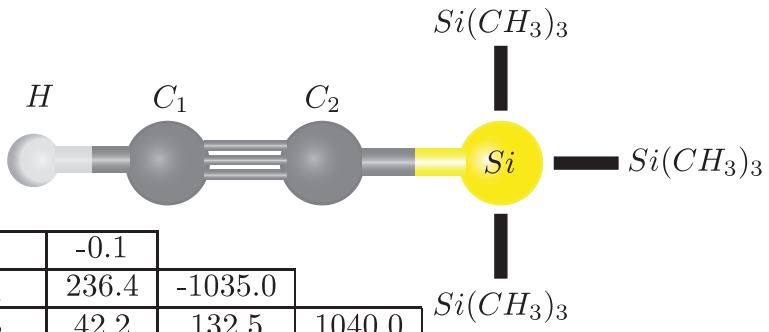

H	-0.1		
C_1	236.4	-1035.0	
C_2	42.2	132.5	1040.0
	H	C_1	C_2
T_1 (s)	2.4	5.3	5.3
T_2 (s)	2.0	2.0	2.4

Figure 5.11: Structure and chemical properties of selectively labeled ^{13}C tris(trimethylsilyl)silane-acetylene. The diagonal give the chemical shift with respect to the spectrometer base frequency of the isotope and the off-diagonals gives the coupling constant in Hz.

possible combinations. Pre-processing was thus performed to concatenate all the pulse shapes of a given sequence into one pulse file for the proton and one for the carbon. To limit the file size of a pulse, while keeping them smooth, a discretization of $2us$ per point was chosen. With this procedure, a maximum of 120 consecutive pulses could be implemented before the spectrometer was overloaded.

As mentioned in Sec. 4.6.3, the pulse implemented at the probe can vary from the desired shape. Even though the GRAPE pulses were designed to be slowly varying and thus limit the effect of phase transients, non-linearity in the pulse generation and amplifier heating can still cause distortion from the ideal shape. A simple feedback loop was performed by detecting the signal at the probe using a pick-up coil and then correcting those discrepancies. Only single pulse shapes were optimized to avoid re-optimizing the concatenated file every time a new set of experiments was run. By analyzing the shape of the concatenated pulses, we observed a systematic inverse droop in the rf. power over the time scale of tens of ms. Since it is a systematic change of power, we expect the RF-robustness of our pulses to correct for this droop.

The entire experiment was run several times, each time using a different set of 48 sequences. The outcome was highly reproducible and we measured the average error per gate in our three qubit system to be $4.7 \pm 0.3 \times 10^{-3}$. The decay curve of a typical run of the experiment is shown in Fig. 5.12 with the exponential fit. Once again, the error bars are due mostly to statistical fluctuations of an incomplete averaging and hardware instabilities.

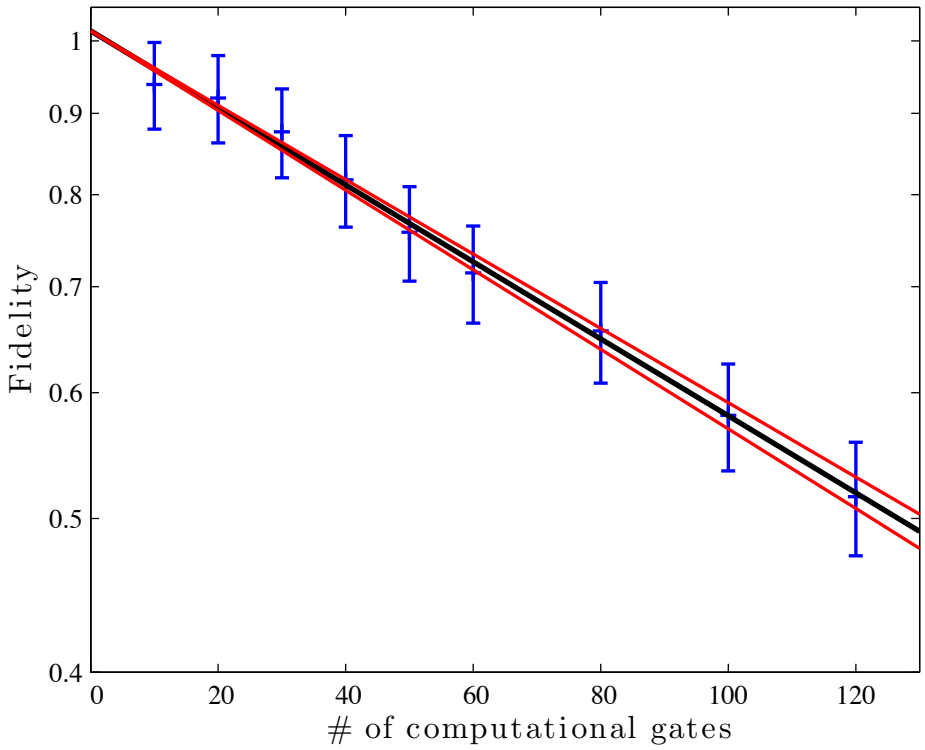

Figure 5.12: Fidelity decay curve for the control benchmarking of three spin control using randomly chosen Clifford generators. The error bars are due to the statistical fluctuation due to an incomplete randomization of the noise and hardware instabilities.

We mentioned in the one qubit experiment that, to avoid the signal fluctuations due to hardware instabilities, the signal was referenced to itself using stroboscopic observation. The fluctuation of the thermal state signal can be seen in Fig. 5.13, where 500 spectra were sequentially recorded over a period of more than 5 hours. The signals are normalized to the average amount of signal. One can clearly see both a short time and long time fluctuation of $\pm 8\%$ hence encouraging us to develop a readout technique to diminish this effect. Such variations in the amount of signal is most likely due to the fluctuations of the resonance frequency of our cryoprobe. Since it has a very sharp resonance frequency, tiny variations in the tuning will greatly affect the response of the probe, and hence the amount of signal recorded.

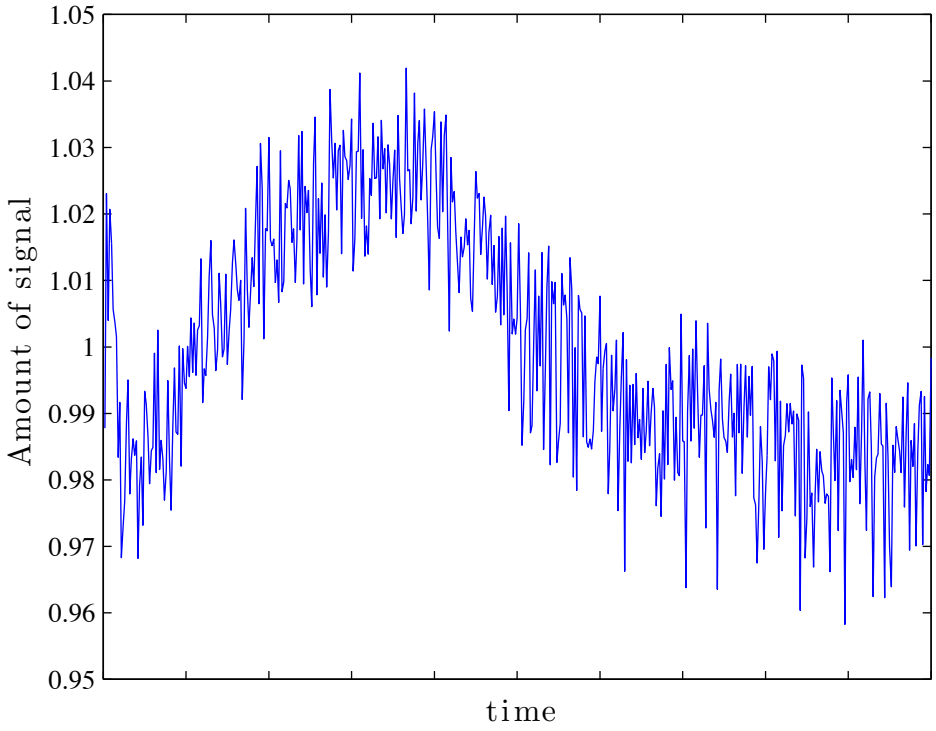

Figure 5.13: Fluctuations of the thermal equilibrium state signal as a function of time. This variation is most likely due to the fluctuation in the resonance frequency of the high Q cryoprobe.

In the single spin case, the stroboscopic observation and referencing was a fairly simple task since there is no evolution during the reference signal acquisition and the signal is essentially flat. Applying the same procedure to multiple spins is slightly more involved since the state of the spins do evolve during the stroboscopic observation of the reference signal. Details of the signal processing methods used to treat the three spins stroboscopic observation are available in Appendix D.

By normalizing each experiment with respect to the initial signal, we are removing the signal fluctuation (assuming the tuning does not change in the course of a single experiment) and are now expecting results with smaller error bars. The results are shown in Fig. 5.14 and they fit an exponential decay of $4.6 \pm 0.2 \times 10^{-3}$. As expected, the error bars on each averaged fidelity are much smaller as the fluctuations are now mostly due to the statistical fluctuations arising from an approximate averaging.

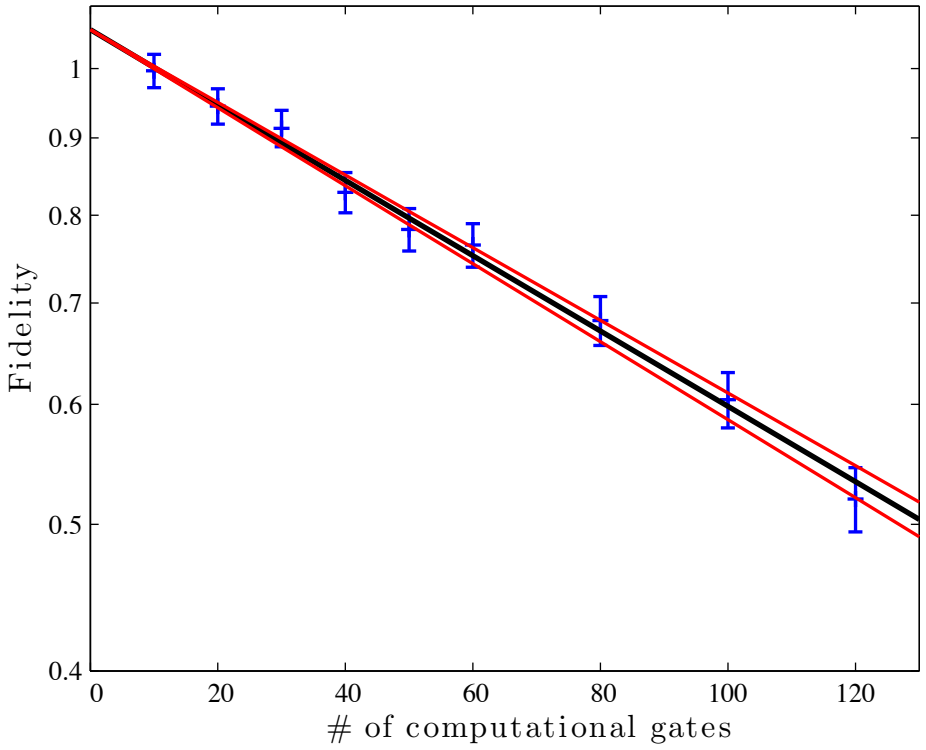

Figure 5.14: Fidelity decay curve for the control benchmarking of three spin control using stroboscopic observation. In this manner, is was possible to normalize most of the hardware instabilities, so that the error bars are now mostly due to statistical fluctuations.

On the other hand, we see that the signal now extrapolates to a fidelity of about 1.1 for no implemented gate. For yet unexplained reasons, the FID part of the experiments implementing 10 or 20 gates had more signal than the reference FID. We were able to observe a return of the solvent and other unidentified chemicals signal, but those should have been removed by the applied digital filtering. We unsuccessfully tried to apply different and/or stronger filters, such as a Butterworth filter and a custom design low pass filter. The increase of signal still remains a mystery.

5.5.3 Discussion and analysis

As in the single qubit case, some lower bounds on the value of p were expected due to intrinsic decoherence. Since our control was implemented using GRAPE pulses that were optimized to 99.95%, we knew from Eq. 5.40 that this corresponded to a "rotational error" of 0.0447 rad, hence yielding an error per gate of 4.4×10^{-4}, which is an order of magnitude smaller. Therefore, the control errors cannot be attributed solely to the search algorithm that designed our pulses.

To estimate the error in implementation due to intrinsic T_1 and T_2 relaxation, we can apply the same procedure as in the one qubit case. If we make the assumption that the noise is independent and uncorrelated, we can write the relaxation on the three qubits as

$$\begin{aligned} \rho &\rightarrow \Lambda_{C_2} \circ \Lambda_{C_1} \circ \Lambda_H(\rho) \\ &\Rightarrow |\rho\rangle\rangle \rightarrow \hat{\Lambda}_{C_2} \cdot \hat{\Lambda}_{C_1} \cdot \hat{\Lambda}_H |\rho\rangle\rangle. \end{aligned} \tag{5.55}$$

Since each superoperator only acts on a specific spin, we can thus rewrite, up to permutations in the representation,

$$\begin{aligned} \hat{\Lambda}_{C_2} \circ \hat{\Lambda}_{C_1} \circ \hat{\Lambda}_H &= \hat{\Lambda}_{C_2} \otimes \hat{\Lambda}_{C_1} \otimes \hat{\Lambda}_H \\ &\Rightarrow \mathrm{Tr}(\hat{\Lambda}) = \mathrm{Tr}(\hat{\Lambda}_{C_2})\mathrm{Tr}(\hat{\Lambda}_{C_1})\mathrm{Tr}(\hat{\Lambda}_H). \end{aligned} \tag{5.56}$$

From the probability distribution for choosing our random gates and after the compression algorithm, we estimated that the average time to implement a gate was around $2.25ms$, which would yield an error per gate of 1.75×10^{-3}, hence contributing to about half the signal loss, just as in the case of the single qubit.

Once again, we conclude that the control over our system is not decoherence limited and there are still improvements to be made, either on the stability of the hardware, or by finding ways to design more robust and spectrometer friendly control pulses.

5.6 Conclusion and outlook

The goal of this work was to develop a protocol to efficiently characterize the quality of the control one has over their system. The ultimate goal is to provide a simple experiment that could allow comparison between different types of QIP devices. A first step toward this direction has been put forward by Knill et al. to benchmark a single qubit processor, while leaving the door open for generalization.

The multi-qubit protocol developed and implemented here should allow a generalization of the previous protocol. By limiting the random gates to single and

double qubit gates, this allows us to quote errors per up to two qubit gates. Moreover, with parallelization, it allows a fair comparison between a 5 and a 50 qubit processor. As a matter of fact, gates are expected to be more faulty for bigger architectures due to more leakage and more degrees of freedom, but they are also expected to be able to perform more gates during a single time step.

Finally, more detailed information about the noise could be obtained by concatenating the present protocol with the twirling protocol presented in Sec. 4. For example, to benchmark the single qubit control on a multi-qubit processor, one could apply a train of Cliffords on a given qubit, while performing a $\widetilde{\mathcal{C}}^{\otimes n-1}$ twirling before and after the train on the remaining qubit. The sequence of Cliffords will dynamically decouple the qubit from the rest of the processor, hence preventing any non-Markovian effects. By recording the average gate fidelity on that qubit, this should provide us an estimate for the average gate fidelity on this qubit. The information arising from twirling the remaining qubits will give us information about the "wait step" error. This procedure can then be applied to all single qubits to obtain the worst single gate average error. We can also apply these same steps for two qubit gates on any pair of qubits. Already having an estimate for the error per single qubit gate, it should be possible to extract the error per two qubit gates. Although such a protocol might necessitate more experiments, it is still efficient in the number of qubits. We are currently investigating such a protocol.

Appendices

Appendix A

The NMR Hamiltonians

A.1 Zeeman Hamiltonian

The spin of a nucleus can be regarded as a quantum mechanical dipolar moment $\vec{u} = \gamma(X,\ Y,\ Z)$, where X, Y and Z are the Pauli matrices and γ is the *gyromagnetic ratio*, which is an intrinsic property of the nuclear isotope. Placed in a magnetic field $\vec{B}$, the Hamiltonian associated with the dipolar moment, known as the Zeeman Hamiltonian, is

$$\begin{aligned} \mathcal{H}_Z &= -\vec{u} \cdot \vec{B} \\ &= -\frac{\gamma}{2}(B_x X + B_y Y + B_z Z) \end{aligned} \tag{A.1}$$

The field $\vec{B}$ is the local field at the nucleus and is comprised of two parts: the external applied field along z, i.e. $\vec{B}_{ext} = B_0\hat{z}$, and the magnetic field created by the movement of the surrounding electrons participating in the chemical bonds, $\vec{B}_e$. To a good approximation,

$$\begin{aligned} \vec{B}_e &= \overleftrightarrow{\delta} \cdot \vec{B}_{ext} \\ &= \delta_{xz} B_0 \hat{x} + \delta_{yz} B_0 \hat{y} + \delta_{zz} B_0 \hat{z}, \end{aligned} \tag{A.2}$$

where $\overleftrightarrow{\delta}$ is known as the *chemical shift tensor* and is dependent on the orientation of the molecule with respect to the external field. δ_{ij} can be understood as the induced magnetic field at the nuclei in the i direction when a field in the j direction is applied. In isotropic liquids, rapid tumbling of the molecule creates a motional averaging on the induced fields so that

$$\vec{B}_e \simeq \delta B_0 \hat{z}, \tag{A.3}$$

where $\delta = \frac{1}{3}(\delta_{xx} + \delta_{yy} + \delta_{zz})$ is the isotropic part of the chemical shift tensor.

The Zeeman interaction is thus given by

$$\begin{aligned}\mathcal{H}_Z &= -\frac{\gamma}{2}(1+\delta)B_0 Z \\ &= \frac{\omega^L}{2}Z \end{aligned} \tag{A.4}$$

Since the Hamiltonian is the generator of rotation around the z axis, ω^L is thus the angular frequency of the spin and defines the *Larmor frequency* $\omega^L = 2\pi\nu^L$. For magnetic fields on the order of 10 T, $\frac{1}{2\pi}\gamma B_0$ is on the order of MHz and the chemical shift $\frac{1}{2\pi}\delta B_0$ is on the order of Hz to kHz.

A.2 Dipolar Hamiltonian

Since a spin i possess a dipolar moment, it will also generate a magnetic field in its surrounding. Another spin j at distance r_{ij} will thus experience a magnetic field created by both the external field and the presence of spin i. The direction and strength of a magnetic field of a magnetic dipole depends on the orientation of the moment. Therefore, the effective field seen by spin j will depend on the orientation of spin i, hence creating a coupling between the two spins. This interaction is called the direct spin-spin coupling, or *dipolar* coupling. In high $\vec{B}$ field, the dipolar Hamiltonian takes the form

$$\begin{aligned}\mathcal{H}_D &= \frac{u_0\gamma_i\gamma_j\hbar}{16\pi r_{ij}^3}(1-3\cos^2\theta_{ij})(2Z_iZ_j - X_iX_j - Y_iY_j) \\ &= \frac{D_{ij}}{2}(1-3\cos^2\theta_{ij})(2Z_iZ_j - X_iX_j - Y_iY_j), \end{aligned} \tag{A.5}$$

where u_0 is the vacuum permeability and θ_{ij} is the angle between $\vec{r}_{ij}$ and the external applied magnetic field axis. D_{ij} is called the dipolar constant and is typically of the order of kHz of directly bounded nuclei. In the liquid state, the molecules move around each other and also rotate on a time scale that is much shorter then the coupling timescale (ns vs. ms). There is thus a motional averaging of the Hamiltonian, i.e. on the NMR time scale, the spins will experience the average of the Hamiltonian over all orientations of the molecule, i.e. the angular dependence of the Hamiltonian will average to

$$\begin{aligned}\int d\omega(1-3\cos^2\theta) &= \int_0^{2\pi}\int_0^{\pi} d\phi d(\cos\theta)(1-3\cos^2\theta_{ij}) \\ &= 4\pi - 2\pi\cos\theta|_0^{\pi} \\ &= 0 \end{aligned} \tag{A.6}$$

Since the angular average of the dipolar Hamiltonian vanishes, there is no coherent dipolar coupling effect in liquid state NMR. Sec. 3.2 demonstrates how the dipolar coupling can induce decoherence.

A.3 J-coupling Hamiltonian

Even though the direct coupling has no coherent intramolecular and intermolecular effect in NMR, spins of the same molecule will still interact with each other. The bonding electrons in a molecule mediate interactions between nuclear spins by carrying information from one spin to another. The J-coupling Hamiltonian between spin i and j takes the form

$$\mathcal{H}_J = \frac{\pi}{2} J(X_i X_j + Y_i Y_j + Z_i Z_j). \tag{A.7}$$

J is called the *J-coupling* constant and is generally less then 300 Hz for ^{1}H and ^{13}C. If the two spins have a large difference in Larmor frequency, the above Hamiltonian can be simplified using a *secular* approximation. By considering the Zeeman and the J-coupling Hamiltonian, we can explicitly write

$$\begin{aligned} \mathcal{H} &= \mathcal{H}_Z + \mathcal{H}_J \\ &= \begin{pmatrix} \frac{\omega_1^L}{2} + \frac{\omega_2^L}{2} + \frac{\pi}{2}J & 0 & 0 & 0 \\ 0 & \frac{\omega_1^L}{2} - \frac{\omega_2^L}{2} - \frac{\pi}{2}J & \pi J & 0 \\ 0 & \pi J & -\frac{\omega_1^L}{2} + \frac{\omega_2^L}{2} - \frac{\pi}{2}J & 0 \\ 0 & 0 & 0 & \frac{\omega_1^L}{2} + \frac{\omega_2^L}{2} - \frac{\pi}{2}J \end{pmatrix} \end{aligned} \tag{A.8}$$

From the above explicit form of the Hamiltonian, we see that the state $|\uparrow\uparrow\rangle$ and $|\downarrow\downarrow\rangle$ are still energy eigenstates, but the two remaining energy eigenstates will be a superposition of $|\uparrow\downarrow\rangle$ and $|\downarrow\uparrow\rangle$. If the condition $|\omega_i^L - \omega_j^L| \ll \pi J_{ij}$ holds, this mixing will be minimal, e.g.

$$\begin{aligned} \mathcal{H}|\uparrow\downarrow\rangle &= \left(\frac{\omega_1^L}{2} - \frac{\omega_2^L}{2} - \frac{\pi}{2}J\right)|\uparrow\downarrow\rangle + \pi J|\downarrow\uparrow\rangle \\ &\simeq \left(\frac{\omega_1^L}{2} - \frac{\omega_2^L}{2} - \frac{\pi}{2}J\right)|\uparrow\downarrow\rangle \end{aligned} \tag{A.9}$$

Therefore assuming $|\nu_i^L - \nu_j^L| \ll J_{ij}/2$, which happen for either two different isotopes, or two homonuclear spins with large difference in chemical shift, the J-coupling Hamiltonian can be approximated by

$$\mathcal{H}_j \simeq \frac{\pi}{2} J Z_i Z_j. \tag{A.10}$$

Such an approximation is known as the *secular approximation* and the reduced Hamiltonian is known as the *weak coupling* Hamiltonian.

A.4 Electric Quadrupolar Hamiltonian

A final interaction to consider is the energy shift associated with the interaction of the nuclei with the electric field gradient generated by the bonding electron cloud. The electric field gradient (EFG) is a second rank tensor $\overleftrightarrow{V}$, where V_{ij} correspond the to the gradient if the i direction of the electric field component in the j direction. The principal axis system (PAS) is the set of axes in which the $\overleftrightarrow{V}$ is diagonal. In high field, a secular aproximation can be performed such that the quadrupolar Hamiltonian is given by

$$\mathcal{H}_Q \simeq \frac{3eQ}{4S(2S-1)}[V_{zz}(3S_z^2 - S(S+1)\mathbb{1})], \tag{A.11}$$

where S if the spin of the nucleus, S_z is the generalized-spin z matrix, i.e. a diagonal matrix with value $\{S, S-1, ..., -S\}$. Q is the *electric quadupole moment*. From this Hamiltonian, we see that for $S = 1/2$, $S_z^2 = \frac{1}{4}\mathbb{1} = S^2\mathbb{1}$, therefore

$$\mathcal{H}_Q = \frac{3eQV_{zz}}{4S}, \tag{A.12}$$

which is constant, and thus providing only a constant shift in all energy state, Therefore, in high fields, spin-1/2 nuclei do not have a quadrupolar interaction.

Appendix B

Lindblad equation and general noise in NMR

B.1 Master Equation in Lindblad form

The Lindblad equation is the general form in which every master equation describing a Markovian dynamical map can be written [Lin76]. The effect of the environment on a quantum system is said to be Markovian if it is assumed that the environment has no correlation time, i.e. no memory. If the environment has residual effect on the system described by Λ_τ for a time τ, then a Markovian map will satisfy

$$\Lambda_{\tau_1+\tau_2} = \Lambda_{\tau_2} \circ \Lambda_{\tau_1}. \tag{B.1}$$

Therefore, if the environment is Markovian, then the reduced dynamics on the system can be written as

$$\begin{aligned} \frac{\partial \rho}{\partial t} &= -i[\mathcal{H}, \rho] + \sum_k \left(L_k \rho L_k^\dagger - \frac{1}{2}\{L_k^\dagger L_k, \rho\} \right) \\ &= -i[\mathcal{H}, \rho] + \mathcal{D}(\rho), \end{aligned} \tag{B.2}$$

where $[\square, \square]$ denotes the commutator and $\{\square, \square\}$ the anti-commutator. L_k's are called the *Lindblad operators* and $\mathcal{D}$ the *dissipator*. The solved dynamics can be obtained by solving B.2 directly or is given in the Liouville representation (Sec. 1.2.3) by the superoperator [Hav03]

$$\hat{\Lambda} = e^{-i\hat{\mathcal{H}}+\hat{D}}, \tag{B.3}$$

where

$$\hat{\mathcal{H}} = \mathcal{H}^* \otimes \mathbb{1} - \mathbb{1} \otimes \mathcal{H} \tag{B.4}$$

$$\hat{\mathcal{D}} = -\sum_k L_k^* \otimes L_k - \frac{1}{2}\mathbb{1} \otimes L_k^\dagger L_k - \frac{1}{2} L_k^T L_k^* \otimes \mathbb{1} \tag{B.5}$$

B.2 Lindblad operator for dephasing

In Sec. 2.7.1, we saw that the action of dephasing on a given state ρ was

$$\Lambda_d(\rho) \;=\; (1-p)\rho + pZ\rho Z, \tag{B.6}$$

where $p = \frac{1}{2}(1-e^{-\gamma_2 t})$. If we let Λ_d act for a small interval Δt, then $p \simeq \frac{\gamma_2 \Delta}{2}$ so that we can write the above equation as

$$\begin{aligned}\Lambda_d(\rho) &= \rho - \frac{\gamma_2 \Delta t}{2}\rho + \frac{\gamma_2 \Delta t}{2} Z\rho Z \\ &= \rho + \frac{\gamma_2 \Delta t}{2}\left(Z\rho Z - \frac{1}{2}\{ZZ,\rho\}\right),\end{aligned} \tag{B.7}$$

since $Z^2 = \mathbb{1}$. Therefore, the time derivative of the density matrix is given by

$$\begin{aligned}\frac{\partial \rho}{\partial t} &\simeq \frac{\Lambda_d(\rho)-\rho}{\Delta t} \\ &= \frac{\gamma_2}{2}\left(Z\rho Z - \frac{1}{2}\{ZZ,\rho\}\right).\end{aligned} \tag{B.8}$$

We conclude that $\sqrt{\frac{\gamma_2}{2}}Z$ is the Lindblad operator for dephasing.

B.3 Lindblad operator for amplitude damping

From Sec. 2.7.2, the T_1 process by itself can be described using the Kraus operators

$$\begin{aligned} A_0 &= \sqrt{p}\begin{pmatrix}1 & 0\\ 0 & \sqrt{1-\eta}\end{pmatrix} \qquad A_1 = \sqrt{p}\begin{pmatrix}0 & \sqrt{\eta}\\ 0 & 0\end{pmatrix} \\ A_2 &= \sqrt{1-p}\begin{pmatrix}\sqrt{1-\eta} & 0\\ 0 & 1\end{pmatrix} \qquad A_3 = \sqrt{1-p}\begin{pmatrix}0 & 0\\ \sqrt{\eta} & 0\end{pmatrix},\end{aligned} \tag{B.9}$$

where $p \simeq \frac{1}{2}\left(1-\frac{\omega}{2k_BT}\right)$ and $\eta = 1-e^{-\gamma_1 t}$. Using the notation $I^+ = |0\rangle\langle 1|$ and $I^- = |1\rangle\langle 0|$ and expanding the operators for short time Δt, we have

$$\begin{aligned} A_0 &\simeq \sqrt{p}\mathbb{1} - \sqrt{p}\frac{\gamma_1\Delta t}{2}\hat{I}^- I^+ \qquad A_1 \simeq \sqrt{p}\gamma_1\Delta t I^+ \\ A_2 &\simeq \sqrt{1-p}\mathbb{1} - \sqrt{1-p}\frac{\gamma_1\Delta t}{2} I^+ I^- \qquad A_3 \simeq \sqrt{1-p}\gamma_1\Delta t I^-.\end{aligned} \tag{B.10}$$

By expanding the transformation of a general state to the first order in Δt, we find

$$\begin{aligned}\Lambda_a(\rho) &= p\left(\rho - \frac{\gamma_1\Delta t}{2}I^-I^+\rho - \frac{\gamma_1\Delta t}{2}\rho I^+I^- + \gamma_1\Delta t I^+\rho I^-\right) \\ &\quad +(1-p)\left(\rho - \frac{\gamma_1\Delta t}{2}I^+I^-\rho - \frac{\gamma_1\Delta t}{2}\rho I^-I^+ + \gamma_1\Delta t I^-\rho I^+\right),\end{aligned} \tag{B.11}$$

so that the time derivative of the density matrix can be written as

$$\begin{aligned}\frac{\partial\rho}{\partial t} &\simeq p\gamma_1\left(I^+\rho I^- - \frac{1}{2}\{I^-I^+,\rho\}\right)\\ &\quad +(1-p)\gamma_1\left(I^-\rho I^+ - \frac{1}{2}\{I^+I^-,\rho\}\right).\end{aligned} \tag{B.12}$$

The Lindblad operators for amplitude damping are therefore given by $\sqrt{p\gamma_1}I^+$ and $\sqrt{(1-p)\gamma_1}I^-$.

B.4 Solving for the general noise

Since dephasing and amplitude damping are two different processes, we can now combine both their Lindblad operators into the same master equation. Therefore, a state ρ of an NMR system, under the influence of dephasing and longitudinal relaxation, will undergo a dynamic governed by

$$\begin{aligned}\frac{\partial\rho}{\partial t} &= \frac{\gamma_2}{2}\left(Z\rho Z - \frac{1}{2}\{ZZ,\rho\}\right) + p\gamma_1\left(I^+\rho I^- - \frac{1}{2}\{I^-I^+,\rho\}\right)\\ &\quad +(1-p)\gamma_1\left(I^-\rho I^+ - \frac{1}{2}\{I^+I^-,\rho\}\right)\end{aligned} \tag{B.13}$$

If we explicitly evaluate the above superoperator on an arbitrary single qubit state, we find that

$$\begin{pmatrix}\dot{\rho_{00}} & \dot{\rho_{01}}\\ \dot{\rho_{10}} & \dot{\rho_{11}}\end{pmatrix} = \begin{pmatrix}-(1-p)\gamma_1\rho_{00} + p\gamma_1\rho_{11} & -(\frac{\gamma_1}{2}+\gamma_2)\rho_{01}\\ -(\frac{\gamma_1}{2}+\gamma_2)\rho_{10} & -p\gamma_1\rho_{11} + (1-p)\gamma_1\rho_{00}.\end{pmatrix} \tag{B.14}$$

The two off diagonal terms are easily solved to give

$$\rho_{01} = e^{-(\frac{\gamma_1}{2}+\gamma_2)t}\rho_{01} \tag{B.15}$$

$$\rho_{10} = e^{-(\frac{\gamma_1}{2}+\gamma_2)t}\rho_{10}. \tag{B.16}$$

For the diagonal, we can use the fact that $\rho_{00}+\rho_{11}=1$. Also, by multiplying the equation by $e^{\gamma_1 t}$, we have

$$\begin{aligned}e^{\gamma_1 t}\frac{\partial\rho_{00}(t)}{\partial t} + e^{\gamma_1 t}\rho_{00} &= e^{\gamma_1 t}p\\ \frac{\partial}{\partial t}\left(e^{\gamma_1 t}\rho_{00}(t)\right) &= e^{\gamma_1 t}p\\ e^{\gamma_1 t}\rho_{00}(t) &= e^{\gamma_1 t}p + C\\ \rho_{00}(t) &= p + Ce^{-\gamma_1 t}.\end{aligned} \tag{B.17}$$

At $t = 0$, $\rho_{00}(0) = \rho_{00}$, so that $C = \rho_{00}$. Moreover, $\rho_{00}(t \to \infty) \equiv \bar{\rho}_{00}$, which implies $p = \bar{\rho}_{00}$. Therefore,

$$\rho_{00}(t) \;=\; \bar{\rho}_{00} + (\rho_{00} - \bar{\rho}_{00})e^{-\gamma_1 t}. \tag{B.18}$$

The same procedure applies in the solution for the evolution of ρ_{11}. The final density matrix of the system under the full decoherence in NMR is thus given by

$$\Lambda(\rho) \;=\; \begin{pmatrix} (\rho_{00} - \bar{\rho}_{00})e^{-\gamma_1 t} + \bar{\rho}_{00} & \rho_{01}e^{-(\frac{\gamma_1}{2}+\gamma_2)t} \\ \rho_{10}e^{-(\frac{\gamma_1}{2}+\gamma_2)t} & (\rho_{11} - \bar{\rho}_{11})e^{-\gamma_1 t} + \bar{\rho}_{11} \end{pmatrix}. \tag{B.19}$$

Appendix C

SPICE simulation of RLC circuit

C.1 Overview of SPICE

The SPICE simulator is dedicated to the simulation of lumped circuit elements in direct (DC) and alternative current (AC). In this appendix, we will describe how SPICE was used to simulate strongly modulated pulses (SMP) [FPB+02].

SMPs are known to have sharp modulation in phase and iamplitude. Even though they were simulated with a fidelity above 99.9%, the experimental implementation of the pulses yielded a loss in fidelity. The goal of the simulations was to analyze the phase transients due to the finite response time of the probe's resonant circuit.

SPICE is a command line simulator that takes an input file describing the circuit and commands concerning the type of simulation and measurements desired. The circuit is described by giving the characteristics of the lumped elements and how they are connected together. For example, the circuit in Fig. C.1 is supposed to be resonant at 75MHz (carbon Larmor frequency in a 7T magnet) with a quality factor of $Q \sim 40$. It can be written in circuit file as

```
Vacin 10 0 AC 1 0
Rvacin5 10 1 50
Cmatch 1 2 6.49p
Rmatch 1 2 100MEG
Ctune 2 0 38.66p
Rtune 2 0 100MEG
Lsample 2 3 0.1u
Rsample 3 0 1
.ac lin 10K 50MEG 105MEG
```

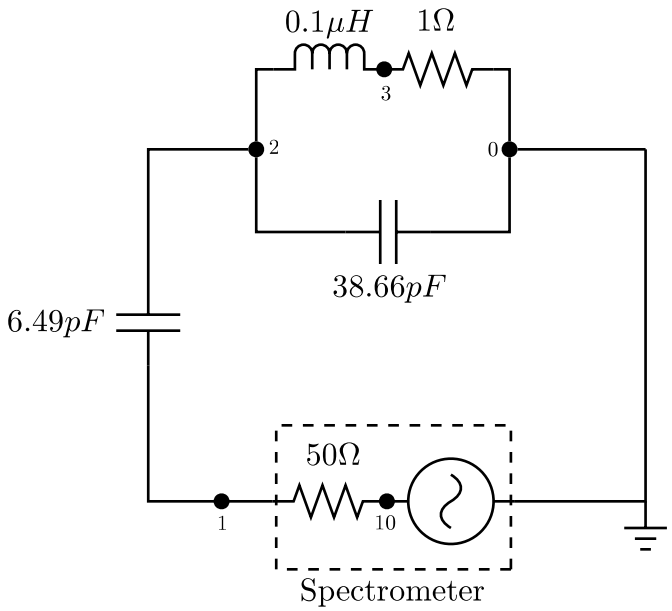

Figure C.1: RLC circuit resonant at 75 MHz with $Q \sim 40$

```
.print ac v(1) I(Vacin)
.end
```

This circuit file indicates that the circuit has an AC voltage source with amplitude 1V and phase 0. The large resistors in parallel with the capacitors are there because SPICE require the capacitors to "leak". The two last commands of the file tell the simulator to perform a frequency sweep between 50 MHz and 105 MHz by increments of 10 kHz, and to print the voltage at node 1 and the current out of the source. From this knowledge, we can use Eq. 4.59 to verify the tuning and matching conditions of the circuit and also extract Q.

C.2 Building an arbitrary RF pulse source

During the AC simulation, SPICE only records the amplitude of the voltage and current. To obtain the voltage or current as a function of time, both the source and the type of simulation must be changed. For example

```
Vsin 10 0 sin(0 1 75MEG)
Rvacin5 10 1 50
Cmatch 1 2 6.49p
Rmatch 1 2 100MEG
```

```
Ctune 2 0 38.66p
Rtune 2 0 100MEG
Lsample 2 3 0.1u
Rsample 3 0 1
.tran 20ps 4us 0 20ps
.print tran I(Lsample)
.end
```

will simulate a sinusoidal source of amplitude 1 with 0 DC component at 75MHz. It will record the current through the inductor every $20ps$ for $0 \leq t \leq 4\mu s$. In order to create shaped pulses, a little imagination is needed. SPICE allows you to add, subtract, multiply or divide different voltage sources. Using this freedom, and the other types of voltage sources available, one can create virtually any shaped voltage possible.

In a SMP, there are only time intervals of constant amplitude and of linearly varying phase. Therefore, we must create the source, namely

$$V(t) = A(t)\sin(\omega t + \phi(t)) \tag{C.1}$$

for $A(t)$ and $\phi(t)$ being piece-wise linear. SPICE has a function to create a piece-wise linear source

```
V na nb PWL(T1 V2 T2 V2 . . . Tn Vn)
```

will create a source between node a and node b that has voltage V1 at time T1, voltage V2 at time T2, and so on. For example, is we define the source part of the circuit file as

```
Vamp 100 0 PWL(0 0 4u 0 4u 1 8u 1 8u 0 12u 0)
Vsin 200 0 sin(0 1 75MEG)
Bin 10 0 V(100)*V(200)
```

Vamp and Vsin are grounded and attached to a node that does not influence the resonant circuit. Vamp corresponds to a $12us$ DC pulse with square amplitude between $4us$ and $8us$. Bin is a non-linearly dependent source controlled by the voltage of Vamp and Vsin. Therefore, Bin corresponds to a $4us$ long square pulse at 75Mhz and constant phase.

If the phase is piece-wise linear too, we cannot use the above trick as there is no way of controlling the phase. Instead, we can do this:

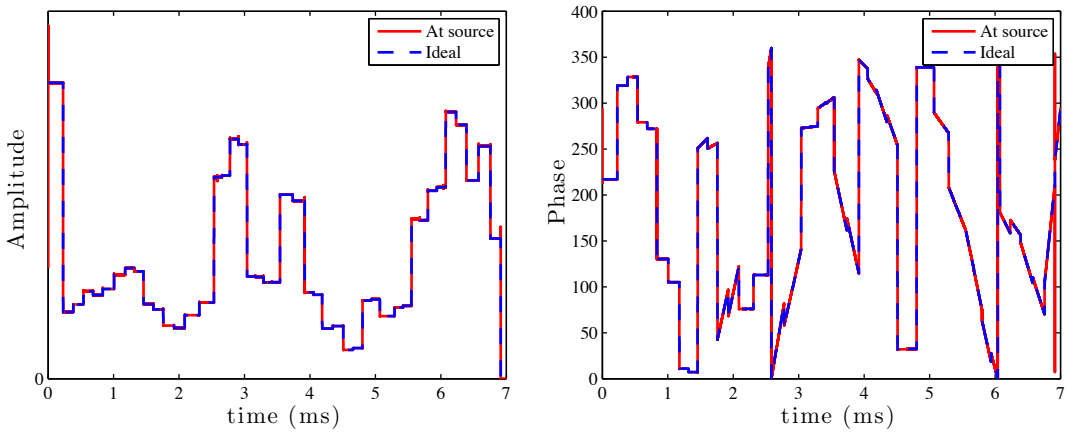

Figure C.2: The voltage generated at the source of the resonant circuit compared to the ideal pulse shape. The figure on the left shows the amplitude profile and the phase modulation is shown on the right.

```
Vamp 100 0 PWL(0 0 4u 0 4u 1 8u 1 8u 0 12u 0)
Vphase 200 0 PWL(0 0 4u 0 8u 2pi 8u 0 )
Vtime 300 0 PWL(0 0 12u 12u)
Bin 10 0 V(100)*sin(2pi*75e+06*V(300)+V(200))
```

Vphase linearly varies from 0 to 2π over the course of the pulse (between $4\mu s$ and $8\mu s$). Vtime is just a trick to create a time variable so we can use the non-linear source to create the actual desired source. With this method, we have been able to create any shape possible.

By recording the voltage at the sample (V(3)), it is possible to obtain the phase and the amplitude by demodulating the voltage using the MATLAB function "demod" with the "qad" option. Upon previously simulating the transfer function at the sample on resonance, i.e. $V(100)/V(1)$ for a simple square pulse, it was possible to compare the input voltage with the sample voltage. Since the voltage across an inductor is proportional to the magnetic field inside it, the recorded voltage was an exact representation of the RF pulse at the sample.

C.3 Simulating the response of a SMP

The shape file of a strongly modulated pulse performing a controlled-controlled-NOT on the three carbons of malonic acid [BMR+06] compared to the voltage at Bin, i.e. V(10) from the SPICE simulation, is shown in Fig. C.2, and the voltage

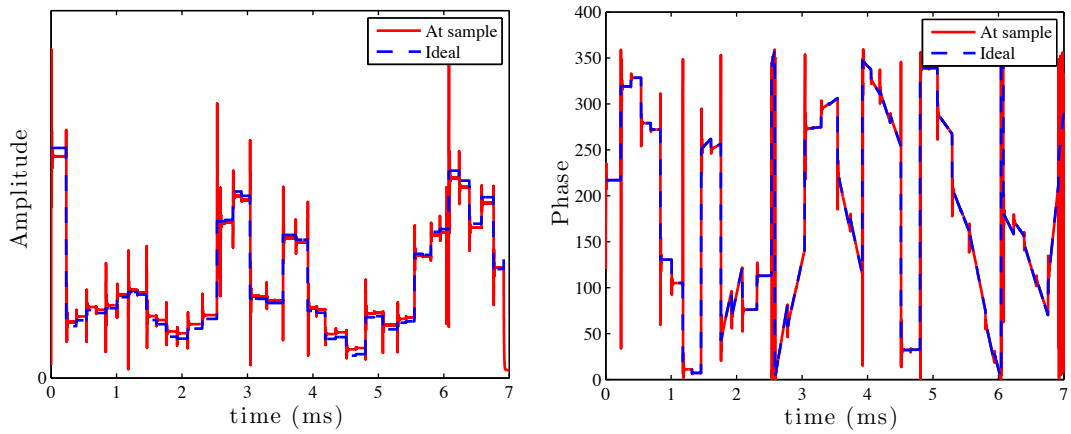

Figure C.3: The voltage at the sample from the excitation of a SMP pulse. The amplitude and phase modulation are shown on the left and right respectively. The phase transients introduce error in both the amplitude and the phase.

measured at the sample in shown in Fig. C.3. As shown, the finite-time response of the probe causes the sharp transitions of the pulse to be more noisy due to phase transient effects. Moreover, there is a clear tendency of the low power to be overshot and the high power undershot. For this reason, it is important to create the pulses so they are robust to power variation (RF inhomogeneity).

Since the arrival of the GRAPE algorithm [KRK+05], the search in the parameter space of the pulse has been accelerated significantly, so that the period of constant amplitude and phase can be reduced to one discretization point. By implementing a penalty function forcing the algorithm to smoothly vary the shape of the amplitude and phase, it is now possible to find smooth pulses which suffer less from the finite response time of the circuit.

Appendix D

Signal processing of an FID

D.1 A new readout scheme

The idea of stroboscopic reading is to normalize the fluctuations of the measured signal over time. Before implementing a given pulse sequence, the readout spin is rotated in the xy plane and its FID is recorded for a given time (then refocused). After the implementation, the recorded FID can be normalized by the amount of initial signal. Typical pulse sequences last on the order of 10's to 100's of ms, compared to severals second between each experiments. Therefore, the large fluctuation in the signal will be normalized and only the rapid and small fluctuations will remain.

Using the above procedure, we now have all the tools necessary to acquire and analyze a stroboscopically acquired FID of the TMMS molecule. The implementation of a pulse sequence now goes as follows:

1. Remove the unwanted signal outside the desired frequency window by using pulses and gradients.
2. Flip the hydrogen in the xy plane, and open the receiver for $50ms$ and sample every $10\mu s$ (bandwidth of ± 5 kHz).
3. Apply a π pulse on the hydrogen and wait another $50ms$ to refocus the free evolution and refocus the chemical shift dispersion.
4. Perform the pulse sequence.
5. Record the remainder of the FID.

Typical advanced acquisition software in commercially available spectrometers have built-in digital filters so that the processed spectrum from an acquired FID

does not contain any artifacts from the signal outside the desired windows of frequencies. Unfortunately, such filtering leaves transient effects at the beginning of the FID as seen in Fig. D.1, which can then corrupt our initial referencing signal. To overcome this problem, we decided to bypass the spectrometer filtering by performing an analog acquisition followed by our own signal processing.

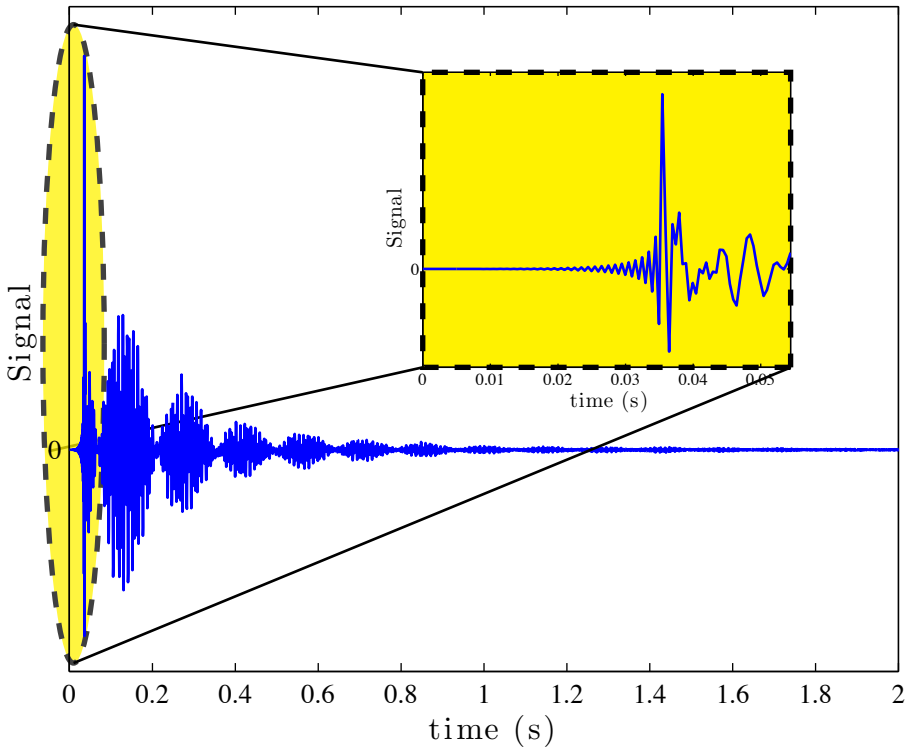

Figure D.1: The transient effects on an FID due to digital filtering.

The Nyquist-Shannon sampling theorem stipulates that in order to perfectly recover a signal that contains no frequencies higher than ω, the signal needs to be sampled at a rate of 2ω [Sha49]. On the other hand, if the signal contains frequencies higher then ω, the fast Fourier transform of the sampled signal (spectrum in the interval $[-\omega, \omega]$) will contain peaks at the mirror frequencies. For example, if the original signal contains a component at 1.1ω, then the discretized spectrum will show a peak at 0.9ω. Artifacts due to discretizing a continuous signal are known as *aliasing* and the particular problem explained here is known as *folding* [Lat98]. Due to the possible presence of signal from the solvent or water in the sample, we needed to perform the analog acquisition using a high sampling frequency (large spectrum window) so that we do not suffer from aliasing. Ultimately, we wanted to compare the amount of signal in the reference part of the FID to that of the output state FID. Therefore, we needed to eliminate all possible contribution to the FID

from other sources of signal.

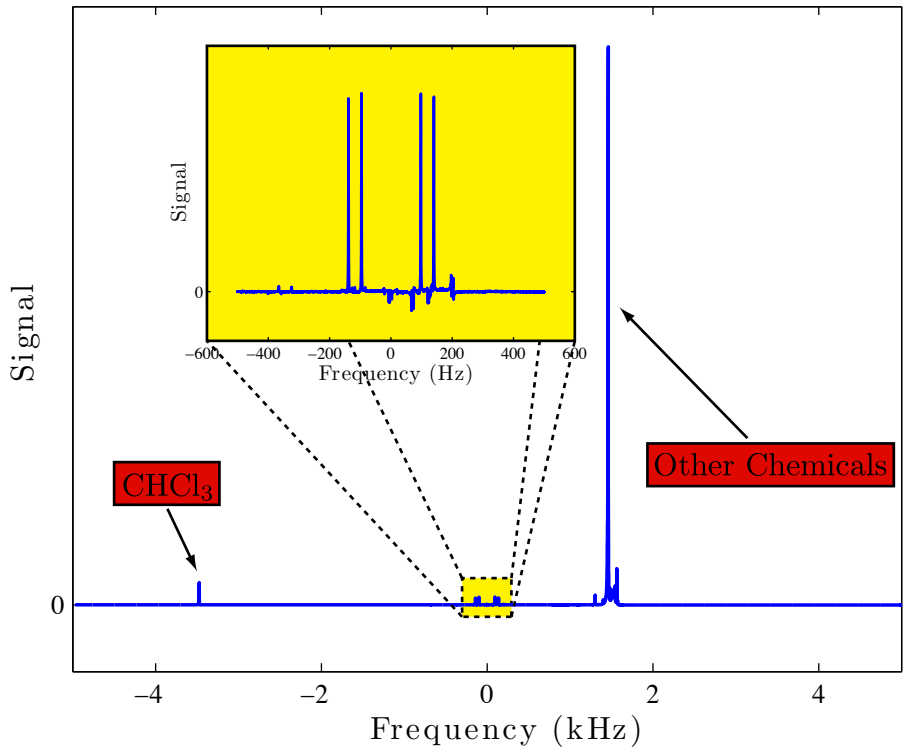

Figure D.2: Thermal equilibrium state ($T = 293K$) wide spectrum of the TMMS sample in deuterated chloroform ($CDCl_3$). The inset shows the zoomed region of the signal of TMMS

D.2 Processing a TMMS FID

By Fourier transforming the thermal equilibrium state ($T = 293K$) FID obtained from the hydrogen and acquiring at a high rate, the spectrum now contained an enormous amount of signal due to the presence of the chloroform and other unidentified chemicals most likely arising from the reaction of the TMMS with the solvent and the air present in the test-tube (see Fig.D.2). Such signals can be partially eliminated by performing $\pi/2$ pulses at those frequencies and then crushing the signal using gradient pulses (see the inset of Fig. D.3). Since the remaining signal is of the same strength as the TMMS, we can now use smooth digital filtering to get rid of it, which can be done using MATLAB's built-in infinite-impulse response (IIR) notch filters at frequencies 1461.6, 1565.5 and -3474.38 Hz (with respect to the TMMS Larmor frequency). After applying these filters to the FID, the edited spectrum can be seen in Fig. D.3.

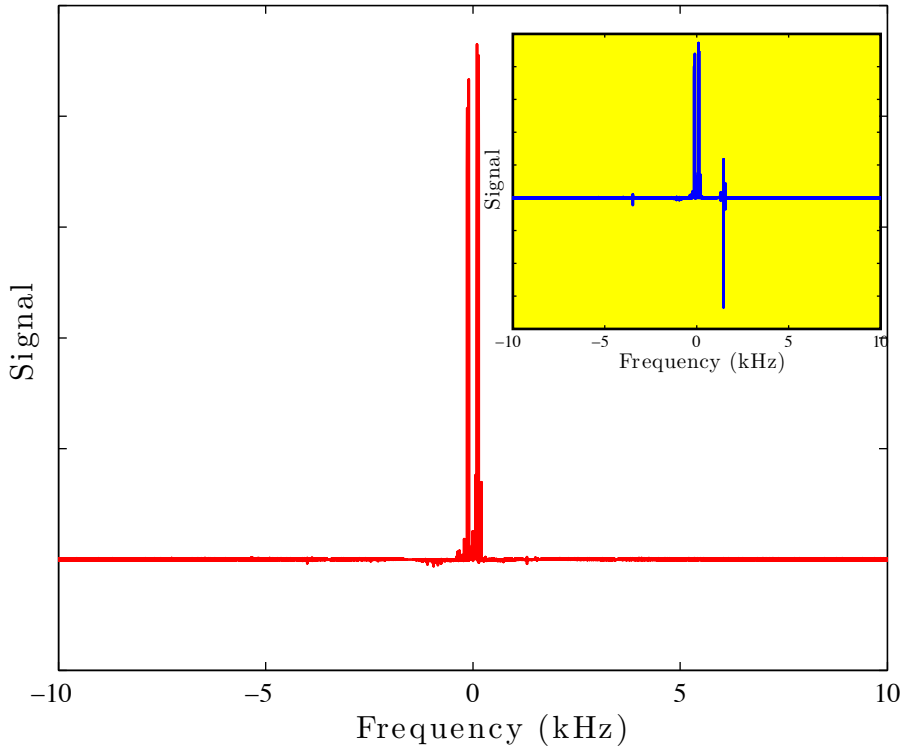

Figure D.3: Applying IIR notch digital filter to the acquired FID. The TMMS part of the processed spectrum is unaffected, while the unwanted signal have been filtered.

By resampling the signal at a different rate, we narrowed the frequency windows to that of importance. The built-in decimation function in MATLAB also implements a low-pass filter, which will filter all the other signal left outside the windows. Decimation is also known to increase the signal-to-noise ratio.

Unlike the single qubit case, the reference signal is no longer a constant, but is a periodic function with virtually no decay. We will thus have to "fit" a function to the reference part of the FID. Although we could fit a theoretical FID from our knowledge of the hamiltonian, we decided to take reference spectra (same procedure, but the pulse sequence only contained a $\pi/2$ readout pulse) every 50 experiments and use the first portion of these spectra as a basis of comparison. Once all the experiments were run, the analysis went as follows:

1. For each reference FID, separate the first 5000 points ($50ms$) and the rest of the FID.

2. For each obtained pair of FIDs, apply the notch filters and the decimation.

3. Average all the FIDs of the reference spectra. This will give us a reference 5000 points FID and the Fourier transform of the remaining points gives us a reference spectrum.

4. For each pulse sequence output FID, apply the above separation, filtering and decimation.

5. For each pulse sequence, find the appropriate multiplicative factor that maximizes the overlap of the first part of the FID to the reference FID. Multiply the remaining part of the outcome FID by this factor, Fourier transform it and appropriately rephase it.

6. Integrate the obtained spectrum and divide the amount of signal by the integral of the reference spectrum

7. Average over all the 48 experiments for each sequence truncation.

8. Fit an exponential decay.

The reference FID fit perfectly to the first part of the outcome FID from the random gate sequences, as seen in Fig. D.4. A final point to mentioned is that, after applying the fast Fourier transform to the second part of the FID, the spectrum obtained needed to be rephased. It is well known from signal processing that every time a point at the beginning of the FID is ignored, the spectrum acquires a phase of 2π linearly distributed across it. Since we had an FID in two parts, we could only find the linear rephasing parameter by trial and error (although we

attempted to build automated phasing algorithm). If S_0 is the spectrum obtained by transforming the FID, then the linearly rephased spectrum S is given by

$$S = S_0 e^{i\theta_0 + i\theta_1(\omega + \frac{\Omega}{2})}, \tag{D.1}$$

where $-\frac{\Omega}{2} \leq \omega \leq -\frac{\Omega}{2}$. By rephasing the second part of the reference FIDs, we found that $\theta_0 = 0.95$rad and $\theta_1 = 3.32$rad were optimal.

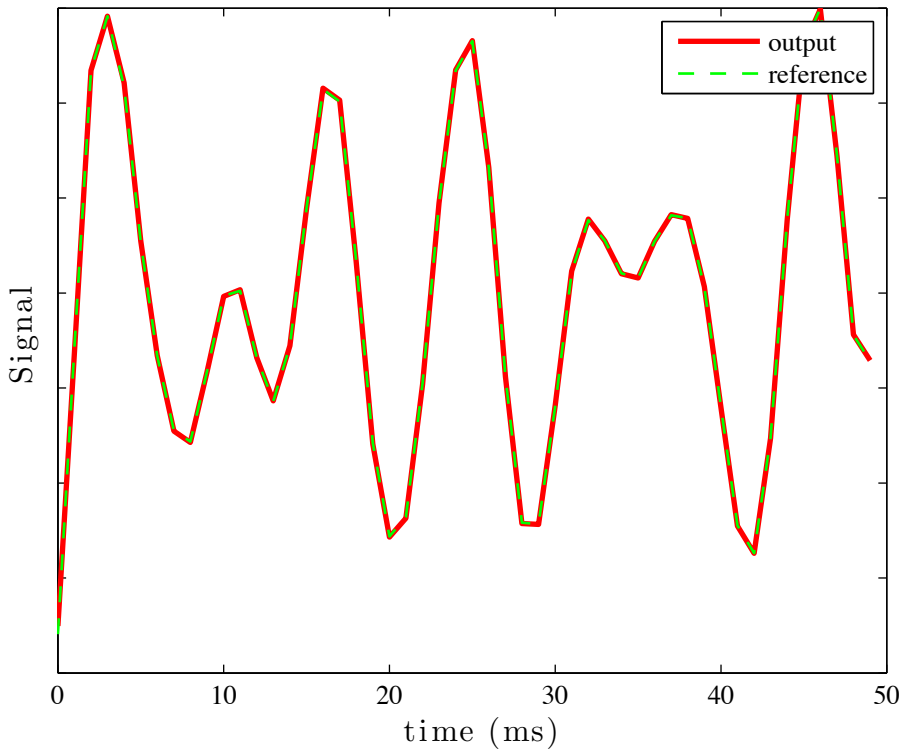

Figure D.4: The first part of the reference FID was properly fitting to the first part of the pulse sequence outcome FIDs.

References

[ABO97] D. Aharonov and M. Ben-Or. Fault-tolerant quantum computation with constant error. In *Proceeding of the 29th Annual ACM Symposium on Theory of Computing*, pages 176–188, 1997.

[Abr83] A. Abragam. *The Principles of Nuclear Magnetism*. Oxford University Press, 1983.

[AG82] A. Abragam and M. Goldman. *Nuclear Magnetism: Order and Disorder*. Oxford University Press, 1982.

[AG04] S. Aaronson and D. Gottesman. Improved simulation of stabilizer circuits. *Physical Review A*, 70:052328, 2004.

[AHT76] D. J. Adduci, P. A. Hornung, and D. R. Torgeson. Extremely fast recovery-time receiver for pulsed NMR. *Review of Scientific Instruments*, 47(12):1503–1505, 1976.

[AL85] D. V. Averin and K. K. Likharev. Coulomb blockade of single-electron tunneling, and coherent oscillations in small tunnel junctions. *Journal of Low Temperature Physics*, 62:3–4, 1985.

[BBC$^+$95] A. Barenco, C. H. Bennett, R. Cleve, D. P. DiVincenzo, N. Margolus, T. Sleator, J. A. Smolin, and H. Weinfurter. Elementary gates for quantum computation. *Physical Review A*, 52:3457, 1995.

[BBP$^+$96] C. H. Bennett, G. Brassard, S. Popescu, B. Schumacher, J. A. Smolin, and W. K. Wootters. Purification of noisy entanglement and faithful teleportation via noisy channels. *Physical Review Letters*, 76(5):722–725, 1996.

[BCC$^+$07] J. Baugh, J. Chamilliard, C. M. Chandrashekar, M. Ditty, A. Hubbard, R. Laflamme, M. Laforest, D. Maslov, O. Moussa, C. Negrevergne, M. Silva, S. Simmons, C. A. Ryan, D. G. Cory, J. S. Hodges, and C. Ramanathan. Quantum information processing using nuclear and electron magnetic resonance: review and prospects.

Physics in Canada - Quantum Information and Quantum Computing Edition, 63(4), 2007.

[BCJ+99] S. L. Braunstein, C. M. Caves, R. Jozsa, N. Linden, S. Popescu, and R. Schack. Separability of very noisy states and implications for NMR quantum computing. *Phys. Rev. Lett*, 83(5):1054–1057, 1999.

[BDSW96] C. H. Bennett, D. P. DiVincenzo, J. A. Smolin, and W. K. Wotters. Mixed-state entanglement and quantum error correction. *Physical Review A*, 54(5):3824–3851, 1996.

[BEH+04] N. Boulant, J. Emerson, T. F. Havel, D. G. Cory, and S. Furuta. Incoherent noise and quantum information processing. *Journal of chemical physics*, 121(7):2955–2961, 2004.

[BH01] D. C. Brody and L. P. Hughston. Geometric quantum mechanics. *Journal of Geometry and Physics*, 38:19–53, 2001.

[BHPC03] N. Boulant, T. F. Havel, M. A. Pravia, and D. G. Cory. Robust method for estimating the lindblad operators of a dissipative quantum process from measurements of the density operator at multiple time points. *Physical Review A*, 67(4):042322, 2003.

[BK05] S. Bravyi and A. Kitaev. Universal quantum computation with ideal clifford gates and noisy ancillas. *Physical Review A*, 71(2), 2005.

[BLLM04] J.-C. Boileau, R. Laflamme, M. Laforest, and C. R. Myers. Robust quantum communication using a polarization-entangled photon pair. *Physical Review Letters*, 93:220501, 2004.

[Blo46] F. Bloch. Nuclear induction. *Physical Review*, 70:460–485, 1946.

[Blu96] K. Blum. *Density Matrix Theory and Application*. Springer, 1996.

[BMR+02] P. O. Boykin, T. Mor, V. Roychowdhury, F. Vatan, and R. Vrijen. Algorithmic cooling and scalable NMR quantum computers. *Proceedings of the National Academy of Sciences*, 99(6):3388–3393, 2002.

[BMR+05] J. Baugh, O. Moussa, C. A. Ryan, A. Nayak, and R. Laflamme. Experimental implementation of heat-bath algorithmic cooling using solid-state nuclear magnetic resonance. *Nature*, 438:470–473, 2005.

[BMR+06] J. Baugh, O. Moussa, C. A. Ryan, R. Laflamme, C. Ramanathan, T. F. Havel, and D. G. Cory. Solid-state NMR three-qubit homonuclear system for quantum-information processing: Control and characterization. *Physical Review A*, 73(2), 2006.

[BMW91] T. M. Barbara, J. F. Martin, and J. G. Wurl. Phase transients in nmr probe circuits. *Journal of Magnetic Resonance*, 93(3):497–508, 1991.

[BOS+02] M. D. Bowdrey, D. K. L. Oi, A. J. Short, K. Banaszej, and J. A. Jones. Fidelity of single qubit maps. *Physics Letters A*, 294:258, 2002.

[BP02] H.-P. Breuer and F. Petruccione. *The theory of open quantum systems*. Oxford University Press, 2002.

[BSLB08] J.-C. Boileau, L. Sheridan, M. Laforest, and S. D. Bartlett. Quantum reference frames and the classification of rotationally-invariant maps. *Journal of Mathematical Physics*, 49:032105, 2008.

[BVFC05] N. Boulant, L. Viola, E. M. Forunato, and D. G. Cory. Experimental implementation of a concatenated quantum error-correcting code. *Physical Review Letters*, 94:130501, 2005.

[BY03] T. R. Beals and C. E. Young. Spin-$\frac{1}{2}$ selection. Technical report, Institute for Quantum Computing, University of Waterloo, 2003.

[BZ06] I. Bengtsson and K. Zyczkowski. *Geometry of Quantum State - An introduction to quantum entanglement*. Cambridge University Press, 2006.

[CCD+02] A. M. Childs, R. Cleve, E. Deotto, E. Farhi, S. Gutmann, and D. A. Spielman. Exponential algorithmic speedup by quantum walk. In *Proceedings of the 35th annual ACM symposium on Theory of computing*, 2002.

[CCL01] A. M. Childs, I. L. Chuang, and D. W. Leung. Realization of quantum process tomography in nmr. *Physical Review A*, 64:012314, 2001.

[CFH97] D. G. Cory, A. F. Fahmy, and T. F. Havel. Ensemble quantum computing by NMR spectroscopy. *Proceedings of the National Academy of Sciences*, 94(5):1634–1639, 1997.

[CGKL98] I. L. Chuang, N. Gershenfeld, M. G. Kubinec, and D. W. Leung. Bulk quantum computation with nuclear magnetic resonance: theory and experiment. In *Proceedings of the Royal Society of London A*, volume 454, pages 447–467, 1998.

[Chv83] V. Chvatal. *Linear Programming*. W. H. Freeman and Company, 1983.

[CLSW85] H. M. Cho, C. J. Lee, D. N. Shyking, and D. P. Weitekamp. Nutation sequences for magnetic-resonance imaging in solids. *Physical Review Letters*, 55(18):1923–1926, 1985.

[CMG90] D. G. Cory, J. B. Miller, and A. N. Garroway. Time suspension multiple-pulse sequences - application to solid-state imaging. *Journal of Magnetic Resonance*, 90(1):205–213, 1990.

[CMP+98] D. G. Cory, W. Maas, M. Price, E. Knill, R. Laflamme, W. H. Zurek, T. F. Havel, and S. S. Somaroo. Experimental quantum error correction. *Physical Review Letters*, 81:2152–2155, 1998.

[CN97] I. L. Chuang and M. A. Nielsen. Prescription for experimental determination of the dynamics of a quantum black box. *Journal of Modern Optics*, 44:2455–2467, 1997.

[Cor93] D. G. Cory. A dante based method for radiofrequency field selection. *Journal of Magnetic Resonance A*, 103(1):23–26, 1993.

[CP54] H. Y. Carr and E. M. Purcell. Effects of diffusion on free precession in nuclear magnetic resonance experiments. *Physical Review*, 94(3):630–638, 1954.

[CP01] R. Crandall and C. Pomerance. *Prime Numbers: A Computational Perspective (2001)*. Springer, 2001.

[CPH98] D. G. Cory, M. D. Price, and T. F. Havel. Nuclear magnetic resonance spectroscopy: An experimentally accessible paradigm for quantum computing. *Physica D*, 120(1-2):82–101, 1998.

[CPM+98] D. G. Cory, M. D. Price, W. Maas, E. Knill, R. Laflamme, W. H. Zurek, T. F. Havel, and S. S. Somaroo. Experimental quantum error correction. *Physical Review Letters*, 81(10):2152–2155, 1998.

[CPZ96] J. Cirac, T. Pellizzari, and P. Zoller. Enforcing coherent evolution in dissipative quantum dynamics. *Science*, 273:1207–1210, 1996.

[CVZ+98] I. L. Chuang, L. M. K. Vandersypen, X. Zhou, D. W. Leung, and S. Lloyd. Experimental realization of a quantum algorithm. *Nature*, 393:143–146, 1998.

[CYC06] Z. Chen, J. Yepez, and D. G. Cory. Simulation of the Burgers equation by NMR quantum-information processing. *Physical Review A*, 74(4), 2006.

[CZ95] J. Cirac and P. Zoller. Quantum computations with cold trapped ions. *Physical Review Letters*, 74:4091–4094, 1995.

[DAK00] K Dorai, Arvind, and A Kumar. Implementing quantum-logic operations, pseudopure states, and the Deutsch-Jozsa algorithm using noncommuting selective pulses in NMR. *Physical Review A*, 6104(4), 2000.

[DBE95] D. Deutsch, A. Barenco, and A. Ekert. Universality in quantum computation. In *Proceedings of the Royal Society of London A*, volume 449, pages 669–677, 1995.

[DCEL06] C. Dankert, R. Cleve, J. Emerson, and E. Levine. Exact and approximate unitary 2-designs: Constructions and applications. *arXiv:quant-ph/0606161*, 2006.

[DDM03] J. Dehaene and B. De Moor. Clifford group, stabilizer states, and linear and quadratic operations over gf(2). *Physical Review A*, 68:042318, 2003.

[DJ92] D. Deutsch and R. Jozsa. Rapid solution of problems by quantum computation. In *Proceedings of the Royal Society of London A*, volume 439, pages 553–558, 1992.

[DKS+88] M. Dobers, K. v. Klitzing, J. Schneider, G. Weimann, and K. Ploog. Electrical detection of nuclear magnetic resonance in $gaas-alxga1-xas$ heterostructures. *Physical Review Letters*, 61(14):1650–1653, 1988.

[DLT02] D. P. DiVincenzo, D. W. Leung, and B. M. Terhal. Quantum data hiding. *IEEE Transactions on Information Theory*, 48(3):580–598, 2002.

[DPR90] M. A. Dahleh, A. P. Peirce, and H. Rabitz. Optimal-control of uncertain quantum-systems. *Physical Review A*, 42(3):1065–1079, 1990.

[DS96] D. P. DiVincenzo and P. W. Shor. Fault-tolerant error correction with efficient quantum codes. *Physical Review Letters*, 77:3260–3263, 1996.

[EAZ05] J. Emerson, R. Alicki, and K. Zyczkowski. Scalable noise estimation with random unitary operators. *Journal of Optics B: Quantum and Semiclassical Optics*, 7:S347, 2005.

[ELL05] J. Emerson, E. Livine, and S. Lloyd. Convergence conditions for quantum random circuits. *Physical Review A*, 72:060302, 2005.

[Eme07] J. Emerson. Open quantum systems. Lecture Notes, AMATH876, University of Waterloo, 2007.

[ESM+07] J. Emerson, M. Silva, O. Moussa, C. Ryan, M. Laforest, J. Baugh, D. G. Cory, and R. Laflamme. Symmetrized characterization of noisy quantum processes. *Science*, 317(5846):1893–1896, 2007.

[EWLC02] J. Emerson, Y. S. Weinstein, S. Lloyd, and D. G. Cory. Fidelity decay as an efficient indicator of quantum chaos. *Physical Review Letters*, 89(28):284102, 2002.

[EWS+03] J. Emerson, Y. Weinstein, M. Saraceno, S. Lloyd, and D. Cory. Pseudo-random unitary operators for quantum information processing. *Science*, 302:2098, 2003.

[FD87] T. A. Fulton and G. J. Dolan. observation of single-electron charging effects in small tunnel junctions. *Physical Review Letters*, 59(1):109, 1987.

[Fel45] W. Feller. The fundamentals limit theorems in probability. *Bulletin of the American Mathematical Society*, 51:800–832, 1945.

[Fey82] R. P. Feynman. Simulating physics with computers. *International Journal of Theoretical Physics*, 21:467, 1982.

[Fey84] R. P. Feynman. Quantum-mechanical computers. *Journal of the Optical Society of America B*, 1:464, 1984.

[FG98] E. Farhi and S. Gutmann. Quantum computation and decision trees. *Physical Review A*, 58:915–928, 1998.

[FGG+01] E. Farhi, J. Goldstone, S. Gutmann, J. Lapan, A. Lundgren, and D. Preda. A quantum adiabatic evolution algorithm applied to random instance of and np-complete problem. *Science*, 292:474–476, 2001.

[FGGS00] E. Farhi, J. Goldstone, S. Gutmann, and M. Sipser. Quantum computation by adiabatic evolution, 2000.

[FL02] M. Fleischhauer and M. D. Lukin. Quantum memory for photons: Dark-state polaritons. *Physical Review A*, 65(2), 2002.

[FLMR04] J. M. Fernandez, S. Lloyd, T. Mor, and V. Roychowdhury. Algorithmic cooling of spins: A practical method for inclreasing polarization. *International Journal of Quantum Information*, 2(4):461–467, 2004.

[FPB+02] E. M. Fortunato, M. A. Pravia, N. Boulant, G. Teklemariam, T. F. Havel, and D. G. Cory. Design of strongly modulating pulses to implement precise effective Hamiltonians for quantum information processing. *Journal of Chemical Physics*, 116(17):7599–7606, 2002.

[FR86] E. Fukushima and S. B. W. Roeder. *Experimental Pulse NMR: A Nuts and Bolts Approach*. Westview Press, 1986.

[FVH+02] E. M. Fortunato, L. Viola, J. S. Hodges, G. Teklemariam, and D. G. Cory. Implementation of universal control on a decoherence-free qubit. *New Journal of Physics*, 4:5, 2002.

[GC97] N. Gershenfeld and I. L. Chuang. Bulk spin-resonance quantum computation. *Science*, 275(5298):350–356, 1997.

[Got97] D. Gottesman. *Stabilizer codes and quantum error correction*. PhD thesis, California Institute of Technology, 1997.

[Got98] D. Gottesman. A theory of fault-tolerant quantum computation. *Physical Review A*, 57:127–137, 1998.

[Gro96] L. Grover. A fast quantum mechanical algorithm for database search. *Proc. 28th Annual ACM Symposium on the Theory of Computation*, pages 212–219, 1996.

[GST+05] G. Gervais, H. L. Stormer, D. C. Tsui, P. L. Kuhns, W. G. Moulton, A. P. Reyes, L. N. Pfeiffer, K. W. Baldwin, and K. W. West. Evidence for skyrmion crystallization from nmr relaxation experiments. *Physical Review Letters*, 94(19):196803, 2005.

[GZ04] C. W. Gardiner and P. Zoller. *Quantum Noise: A Handbook of Markovian and Non-Markovian Quantum Stochastic Methods with Applications to Quantum Optics*. Springer, 2004.

[Haa01] F. Haake. *Quantum Signature of Chaos*. Springer Verlag, 2001.

[Han50] E. L. Hanh. Spin echoes. *Physical Review*, 80:580–594, 1950.

[Hav03] T. F. Havel. Procedures for converting among lindblad, kraus and matrix representations of quantum dynamical semigroups. *Journal of Mathematical Physics*, 44(2):534–557, 2003.

[HGW+07] M. K. Henry, A. V. Gorshkov, Y. S. Weinstein, P. Cappellaro, J. Emerson, N. Boulant, Jonathan S. H., C. Ramanathan, T. F. Havel, R. Martinez, and D. G. Cory. Signatures of incoherence in a quantum information processor. *Quantum Information Processing*, 6(6):431–444, 2007.

[HHH99] M. Horodecki, P. Horodecki, and R. Horodecki. General teleportation channel, singlet fraction, and quasidistillation. *Physical Review A*, 60(3):1888–1898, 1999.

[HJ85] R. A. Horn and C. R. Johnson. *Matrix Analysis*. Cambridge University Press, 1985.

[HJ91] R. A. Horn and C. R. Johnson. *Topics in matrix Analysis*. Cambridge University Press, 1991.

[HL08] A. Harrow and R. Low. Random quantum circuits are approximate 2-designs. *arXiv:0802.1919*, 2008.

[HRC02] A. Harrow, B. Recht, and I. L. Chuang. Efficient discrete approximations of quantum gates. *Journal of Mathematical Physics*, 43:4445, 2002.

[HRH+07] M. K. Henry, C. Ramanathan, J. S. Hodges, C. A. Ryan, M. J. Ditty, R. Laflamme, and D. G. Cory. Fidelity enhancement by logical qubit encoding. *Physical Review Letters*, 99(22):220501, 2007.

[HSVC01] T. F. Havel, Y. Sharf, L. Viola, and D. G. Cory. Hadamard products of product operators and the design of gradient-diffusion experiments for simulating decoherence by NMR spectroscopy. *Physical Review A*, 280(5-6):282–288, 2001.

[JK99] J. A. Jones and E. Knill. Efficient refocusing of one-spin and two-spin interactions for nmr quantum computation. *Journal of Magnetic Resonance*, 141(2):322–325, 1999.

[JL03] R. Jozsa and N. Linden. On the role of entanglement in quantum-computational speed-up. In *Proceedings of the Royal Society of London A*, volume 459, pages 2011–2032, 2003.

[JM98] J. A. Jones and M. Mosca. Implementation of a quantum algorithm to solve Deutsch's problem on a Nuclear Magnetic Resonance quantum computer. *Journal of Chemical Physics*, 109:1648–1653, 1998.

[Jon94] J. A. Jones. Fundamental limits upon the measurement of state vectors. *Physical Review A*, 50(3682-3699), 1994.

[JSC+04] B. Julsgaard, J. Sherson, J. I. Cirac, J. Fiurasek, and E. S. Polzik. Experimental demonstration of quantum memory for light. *Nature*, 432(7016):482–486, 2004.

[JSS04] T. F. Jordan, A. Shaji, and E. C. G. Sudarshan. Dynamics of initially entangled open quantum systems. *Physical Review A*, 70(5):052110, 2004.

[Kay07] P. Kaye. Cooling algorithms based on the 3-bit majority. *Quantum Information Processing*, 6(4):295–322, 2007.

[KCL98] E. Knill, I. Chuang, and R. Laflamme. Effective pure states for bulk quantum computation. *Physical Review A*, 57(5):3348–3363, 1998.

[KDvK+99] S. Kronmüller, W. Dietsche, K. v. Klitzing, G. Denninger, W. Wegscheider, and M. Bichler. New type of electron nuclear-spin interaction from resistively detected nmr in the fractional quantum hall effect regime. *Physical Review Letters*, 82(20):4070–4073, 1999.

[Kin63] J. F. C. Kingman. The exponential decay of markow transition probability. In *Proceeding of the London Mathematical Society*, volume s3-13, pages 337–383, 1963.

[Kit97a] A. Y. Kitaev. Quantum computations: Algorithms and error correction. *Russian Mathematical Surveys*, 52:1191, 1997.

[Kit97b] A. Y. Kitaev. Quantum error correction with imperfect gates. In A. S. Holevo, O. Hirota, and C. M. Caves, editors, *Quantum Communication, Computing and Measurment*, pages 181–188, New-York, 1997. Plenum Press.

[Kit03] A. Y. Kitaev. Fault-tolerant quantum computation by anyons. *Annales of Physics*, 303:2, 2003.

[KL97] E. Knill and R. Laflamme. Theory of quantum error-correcting codes. *Physical Review A*, 55:900, 1997.

[KL98] E. Knill and R. Laflamme. Power of one bit of quantum information. *Physical Review Letters*, 81(25):5672–5675, 1998.

[KLA+02] E. Knill, R. Laflamme, A. Ashikhmin, H. Barnum, L. Viola, and W. H. Zurek. Introduction to quantum error correction. *Los Alamos Science*, 2002.

[KLM01] E. Knill, R. Laflamme, and G. J. Milburn. A scheme for efficient linear optics quantum computation. *Nature*, 409:46, 2001.

[KLM07] P. Kaye, R. Laflamme, and M. Mosca. *An Introduction to Quantum Computing*. Oxford University Press, 2007.

[KLMN01] E. Knill, R. Laflamme, R. Martinez, and C. Negrevergne. Benchmarking quantum computers: the five-qubit error correcting code. *Physical Review Letters*, 86(25):5811–5814, 2001.

[KLMT00] E. Knill, R. Laflamme, R. Martinez, and C.-H. Tseng. An algorithmic benchmark for quantum information processing. *Nature*, 404:368, 2000.

[KLR+08] E. Knill, D. Liebfried, R. Reichle, J. Britton, R. B. Blakestad, J. D. Jost, C. Langer, R. Ozeri, S. Seidelin, and D. J. Wineland. Randomized benchmarking of quantum gates. *Physical Review A*, 77:012307, 2008.

[KLZ98] E. Knill, R. Laflamme, and W. H. Zurek. Resilient quantum computation: Error models and thresholds. *Philosophical Transactions of the Royal Society*, 454:365–384, 1998.

[Kra83] K. Kraus. *States, Effects and Operations*. Fundamental Notions of Quantum Theory. Academic Press, Berlin, 1983.

[Kri06] D. W. Kribs. A brief introduction to operator quantum error correction. *Contemporary Mathematics*, 414:27–34, 2006.

[KRK+05] N. Khaneja, T. Reiss, C. Kehlet, T. Schulte-Herbruggen, and S. J. Glaser. Optimal control of coupled spin dynamics: design of NMR pulse sequences by gradient ascent algorithms. *Journal of Magnetic Resonance*, 172(2):296–305, 2005.

[KSK+04] K. Kobzar, T. E. Skinner, N. Khaneja, S. J. Glaser, and B. Luy. Exploring the limits of broadband excitation and inversion pulses. *Journal of Magnetic Resonance*, 170:236, 2004.

[Lat98] B. P. Lathi. *Signal Processing & Linear Systems*. Berkeley Cambridge Press, 1998.

[LBF98] N. Linden, H. Barjat, and R. Freeman. An implementation of the Deutsch-Jozsa algorithm on a three-qubit NMR quantum computer. *Chemical Physics Letters*, 296(1-2):61–67, 1998.

[LBL06] M. Laforest, J. Baugh, and R. Laflamme. Time-reversal formalism applied to maximal bipartite entanglement: Theoretical and experimental exploration. *Physical Review A*, 73:032323, 2006.

[LCYY00] D. W. Leung, I. L. Chuang, F. Yamaguchi, and Y. Yamamoto. Efficient implementation of coupled logic gates for quantum computation. *Physical Review A*, 61(4):042310, 2000.

[LD98] D. Loss and D. P. DiVincenzo. Quantum computation with quantum dots. *Physical Review A*, 57(1):120–126, 1998.

[LE74] I. J. Lowe and M. Engelsberg. A fast recovery pulsed nuclear magnetic resonance sample probe using a delay line. *Review of Scientific Instruments*, 45(5):631–639, 1974.

[Lev86] M. H. Levitt. Composite pulses. *Progress in Nuclear Magnetic Resonance Spectroscopy*, 18(Part 2):61–122, 1986.

[Lev01] M. H. Levitt. *Spin Dynamics: Basics of Nuclear Magnetic Resonance*. John Wiley and Sons Ltd, New-York, 2001.

[Lib03] R. Liboff. *Introductory Quantum Mechanics*. Addison-Wesley, 2003.

[Lin76] G. Lindblad. On the generators of quantun dynamical semigroups. *Commun. Math. Phys.*, 48:119, 1976.

[Llo95] S. Lloyd. Almost any quantum logic gate is universal. *Physical Review A*, 75(2):346–349, 1995.

[LMPZ96] R. Laflamme, C. Miquel, J.-P. Paz, and W. H. Zurek. A perfect quantum error correction code. *Physical Review Letters*, 77:198, 1996.

[LSB+07] M. Laforest, D. Simon, J. Baugh, M. Ditty, and R. Laflamme. Using error correction to determine the noise model. *Physical Review A*, 75(012331), 2007.

[Lüt96] H. Lütkepohl. *Hanbook of Matrices*. Cambridge University Press, 1996.

[LVZ+99] D. Leung, L. M. K. Vandersypen, X. L. Zhou, M. Sherwood, C. S. Yannoni, M. Kubinec, and I. L. Chuang. Experimental realization of a two-bit phase damping quantum code. *Physical Review A*, 60(3):1924–1943, 1999.

[McC87] J. R. McConnell. *The Theory of NMR Spin Relaxation in Liquids*. Cambridge University Press, 1987.

[ME08] E. Magesan and J. Emerson. Personal communication, 2008.

[MFM+00] R. Marx, A. F. Fahmy, John M. Myers, W. Bermel, and S. J. Glaser. Approaching five-bit nmr quantum computing. *Phys. Rev. A*, 62(1):012310, 2000.

[MG58] S. Meiboom and D. Gill. Modified spin-echo method for measuring nuclear relaxation times. *Review of Scientific Instruments*, 29(8):688–691, 1958.

[MG75] P. Mansfield and P. K. Grannell. Diffraction and microscopy in solids and liquids by nmr. *Physical Review B*, 12(9):3618–3634, 1975.

[MJN+02] R. G. Mani, W. B. Johnson, V. Narayanamurti, V. Privman, and Y. H. Zhang. Nuclear spin based memory and logic in quantum hall semiconductor nanostructures for quantum computing applications. *Physica E-Low-Dimensional Systems & Nanostructures*, 12(1-4):152–156, 2002.

[MOL+99] J. E. Mooij, T. P. Orlando, L. Levitov, L. Tian, C. H. van der Wal, and S Lloyd. Josephson persistent-current qubit. *Science*, 285:1036–1039, 1999.

[NC00] M. A. Nielsen and I. L. Chuang. *Quantum Computation and Quantum Information*. Cambridge University Press, Cambridge, UK, 2000.

[Nie02] M. A. Nielsen. A simple formula for the average gate fidelity of a quantum dynamical operation. *Physics Letters A*, 303:249, 2002.

[NKL98] M. A. Nielsen, E. Knill, and R. Laflamme. Complete quantum teleportation. *Nature*, 396:52–55, 1998.

[NMR+06] C. Negrevergne, TS Mahesh, C. A. Ryan, M. Ditty, F. Cyr-Racine, W. Power, N. Boulant, T. F. Havel, D. G. Cory, and R. Laflamme. Benchmarking quantum control methods on a 12-qubit system. *Physical Review Letters*, 96(17), 2006.

[NP73] L. W. Nagel and D. O. Pederson. SPICE (simulation program with integrated circuit emphasis). Memorandum no. ERL-M382, EECS Department, University of California at Berkeley, 1973.

[NPT99] Y. Nakamura, Y. A. Pashkin, and J. S. Tsai. Coherent control of macroscopic quantum states in a single-cooper-pair box. *Nature*, 398:786–788, 1999.

[NR04] J. W. Nilsson and S. Riedel. *Electric Circuits*. Prentice Hall, 7^{th} edition edition, 2004.

[NSO+05] C. Negrevergne, R. Somma, G. Ortiz, E. Knill, and R. Laflamme. Liquid-state NMR simulations of quantum many-body problems. *Physical Review A*, 71(3, Part A), 2005.

[PBE+03] M. A. Pravia, N. Boulant, J. Emerson, A. Farid, E. M. Fortunato, T. F. Havel, R. Martinez, and D. G. Cory. Robust control of quantum information. *Journal of chemical physics*, 119(19):9993–10001, 2003.

[PCZ97] J. F. Poyatos, J. I. Cirac, and P. Zoller. Complete characterization of a quantum process: the two-bit quantum gate. *Physical Review Letters*, 78:390–393, 1997. Also arXiv, quant-ph 9611013.

[PDR88] A. P. Peirce, M. A. Dahleh, and H. Rabitz. Optimal-control of quantum-mechanical systems - existence, numerical approximation, and applications. *Physical Review A*, 37(12):4950–4964, 1988.

[Pec94] P. Pechukas. Reduced dynamics need not be completely positive. *Physical Review Letters*, 73(8):1060–1062, 1994.

[PTP46] E. M. Purcell, H. C. Torrey, and R. V. Pound. Resonance absorption by nuclear magnetic moments in a solid. *Physical Review*, 69:37–38, 1946.

[RB01] R. Raussendorf and H. J. Briegel. A one-way quantum computer. *Physical Review Letters*, 86:5188, 2001.

[RdVRMK00] H. Rabitz, R. de Vivie-Riedle, M. Motzkus, and K. Kompa. Chemistry - Whither the future of controlling quantum phenomena? *Science*, 288(5467):824–828, 2000.

[Rei05] B. W. Reichardt. Improved magic states distillation for quantum universality. *Quantum Information Processing*, 4:251–264, 2005.

[RLBL05] C. A. Ryan, M. Laforest, J.-C. Boileau, and R. Laflamme. Experimental implementation of discrete time quantum random walk on an nmr quantum information processor. *Physical Review A*, 72:062312, 2005.

[RLL08] C. A. Ryan, M. Laforest, and R. Laflamme. Randomized benchmarking of single and multi-qubit control in liquid state NMR quantum information processing. *arXiv:08083973*, 2008.

[RNL+08] C. A. Ryan, C. Negrevergne, M. Laforest, E. Knill, and R. Laflamme. Liquid-state nuclear magnetic resonance as a testbed for developing quantum control methods. *Physical Review A*, 78:012328, 2008.

[Sak85] J. J. Sakurai. *Modern Quantum Mechanics*. The Benjamin Cummings Publishing Company, New York, 1985.

[SB01] P. Stelmachovic and V. Buzek. Dynamics of open quantum systems initially entangled with environment: Beyond the kraus representation. *Physical Review A*, 64(6):062106, 2001.

[Sch95] B. Schumacher. Quantum coding. *Physical Review A*, 51(4):2738–2747, 1995.

[Sch96] B. Schumacher. Sending entanglement through noisy quantum channels. *Physical Review A*, 54(4):2614–2628, 1996.

[Sch07] M. Schlosshauer. *Decoherence and the Quantum-to-Classical Transition*. Springer, 2007.

[SCS+00] Y. Sharf, D. G. Cory, S. S. Somaroo, T. F. Havel, E. Knill, R. Laflamme, and W. H. Zurek. A study of quantum error correction by geometric algebra and liquid-state NMR spectroscopy. *Molecular Physics*, 98(17):1347–1363, 2000.

[Sha49] C. E. Shannon. Communication in the presence of noise. In *Proceedings of the Institute of Radio Engineers*, volume 37, pages 10–21, 1949.

[Sho94] P. W. Shor. Algorithms for quantum computation: Discrete logarithms and factoring. In *Proceedings of the 35th Annual Symposium on the Foundations of Computer Science*, pages 124–134, Los Alamitos, CA, 1994. IEEE Computer Society.

[Sho95] P. W. Shor. Scheme for reducing decoherence in quantum computer memory. *Physical Review A*, 52:2493, 1995.

[Sho96] P. W. Shor. Fault-tolerant quantum computation. In *Proceedings of the 37th Symposium on the Foundations of Computer Science*, pages 56–65, Los Alamitos, California, 1996. IEEE press.

[SKBF85] A. J. Shaka, J. Keeler, Smith M. B., and R. Freeman. Spatial localization of nmr signal in an inhomogeneous radiofreqeuncy field. *Journal of Magnetic Resonance*, 61(1):175–180, 1985.

[Sli96] C. P. Slichter. *Principles of Magnetic Resonance*. Springer, 96.

[SMW05] L. J. Schulman, T. Mor, and Y. Weinstein. Physical limits of heat-bath algorithmic cooling. *Physical Review Letters*, 94(12):120501, 2005.

[Sol00] R. Solovay. Lie groups and quantum circuits. Technical report, Math. Sci. Reas. Inst., 2000.

[Spi92] M. R. Spiegel. *Theory and Problems in Probability and Statistics*. McGraw-Hill, New York, 1992.

[Ste96] A. M. Steane. Error correcting codes in quantum theory. *Physical Review Letters*, 77:793, 1996.

[STH+99] S. Somaroo, C.-H. Tseng, T. F. Havel, R. Laflamme, and D. G. Cory. Quantum simulations on a quantum computer. *Physical Review Letters*, 82:5381–5384, 1999.

[Sti55] W. F. Stinespring. Positive functions on C*-algebras. *Proceedings of the American Mathematical Society*, 6:211–216, 1955.

[Str03] G. Strang. *Introduction to Linear Algebra*. Wellesly-Cambridge Press, 3^{rd} edition edition, 2003.

[SV99] L. Schulman and U. Vazirani. Molecular scale heat engines and scalable quantum computation. In *Proceeding of the 31^{th} Annual ACM Symposium on Theory of Computing*, 1999.

[SVC00] M. Steffen, L. M. K. Vandersypen, and I. L. Chuang. Simultaneous soft pulses applied at nearby frequencies. *Journal of Magnetic Resonance*, 146:369–374, 2000.

[THL+95] Q. A. Turchette, C. J. Hood, W. Lange, H. Mabuchi, and H. J. Kimble. Measurement of conditional phase shifts for quantum logic. *Physical Review Letters*, 75:4710–4713, 1995.

[TML03] J. M. Taylor, C. M. Marcus, and M. D. Lukin. Long-lived memory for mesoscopic quantum bits. *Physical Review Letters*, 90(20), 2003.

[Ton90] Y. L. Tong. *The multivariate normal distribution*. Springer Verlag, New-York, 1990.

[Tow00] J. S. Townsend. *A Modern Approach to Quantum Mechanics*. University Science Books, 2000.

[TPC94] P. Tekely, P. Palmas, and D. Canet. Effect of proton spin-exchange on the residual c-13 mas nmr linewidths - phase-modulated irraduation for efficient heteronuclear decoupling in rapidly rotating solids. *Journal of Magnetic Resonance A*, 107(2):129–133, 1994.

[TSS+00] C.-H. Tseng, S. Somaroo, Y. Sharf, E. Knill, R. Laflamme, T. F. Havel, and D. G. Cory. Quantum simulation of a three-body interaction Hamiltonian on an NMR quantum computer. *Physical Review A*, 61:012302, 2000.

[vdV98] A. W. vab der Vaart. *Asymptotic Statistics*. Cambridge Series in Statistical and Probabilistic Mathematics (No. 3). Cambridge University Press, 1998.

[Veg04] A. J. Vega. Controlling the effects of pulse transients and rf inhomogeneity in phase-modulated multiple-pulse sequences for homonuclear decoupling in solid-state proton nmr. *Journal of Magnetic Resonance*, 170(1):22–41, 2004.

[VES+72] R. W. Vaughan, D. D. Elleman, L. M. Stacey, W.-K. Rhim, and J. W. Lee. A simple, low power, multiple pulse nmr spectrometer. *Review of Scientific Instruments*, 43(9):1356, 1972.

[VFP+01] L. Viola, E. M. Fortunato, M. A. Pravia, E. Knill, R. Laflamme, and D. G. Cory. Experimental realization of noiseless subsystems for quantum information processing. *Science*, 293:2059, 2001.

[Vid03] G. Vidal. Efficient classical simulation of slightly entangled quantum computations. *Physical Review Letters*, 91(14), 2003.

[VK05] L. Viola and E. Knill. Random decoupling schemes for quantum dynamical control and error suppression. *Physical Review Letters*, 94(6):060502, 2005.

[VR89] K. Vogel and H. Risken. Determination of quasiprobability distribution in terms of probability distributions for the rotates quadrature phase. *Physical Review A*, 40(5):2847–2849, 1989.

[VSB+01] L. M. K. Vandersypen, M. Steffen, G. Breyta, C. S. Yannoni, M. H. Sherwood, and I. L. Chuang. Experimental realization of Shor's quantum factoring algorithm using nuclear magnetic resonance. *Nature*, 414(6866):883–887, 2001.

[War97] W. S. Warren. The usefulness of NMR quantum computing. *Science*, 277:1688–1689, 1997.

[Wei99] U. Weiss. *Quantum Dissipative Systems*. World Scientific, Singapore, 1999.

[WHE+04] Y. S. Weinstein, T. F. Havel, J. Emerson, N. Boulant, M. Saraceno, S. Lloyd, and D. G. Cory. Quantum process tomography of the quantum fourier transform. *Journal of Chemical Physics*, 121(13):6117–6133, 2004.

[Wim94] S. Wimperis. Broadband, narrowband, and passband composite pulses for use in advanced nmr experiments wimperis s. *Journal of Magnetic Resonance A*, 109:221, 1994.

[WJ06] J. Wrachtrup and F. Jelezko. Processing quantum information in diamond. *Journal of Physics-Condensed Matter*, 18(21, Sp. Iss. SI):S807–S824, 2006.

[WLC01] Y. S. Weinstein, S. Lloyd, and D. G. Cory. Implementation of the quantum fourier transform. *Physical Review Letters*, 86:1889, 2001.

[ZL96] W. H. Zurek and R. Laflamme. Quantum logical operations on encoded qubits. *Physical Review Letters*, 77:4683, 1996.

[ZLD+04] J. F. Zhang, G. L. Long, Z. W. Deng, W. Z. Liu, and Z. H. Lu. Nuclear magnetic resonance implementation of a quantum clock synchronization algorithm. *Physical Review A*, 70(6), 2004.

[ZLSD02] J. F. Zhang, Z. H. Lu, L. Shan, and Z. W. Deng. Realization of generalized quantum searching using nuclear magnetic resonance. *Physical Review A*, 65(3), 2002.

[Zur03] W. H. Zurek. Decoherence, einselection and the quantum origins of the classical. *Review of Modern Physics*, 75:715–775, 2003.